THE MECHANOCHEMISTRY IN HETEROGENEOUS REACTIVE POWDER MIXTURES UNDER HIGH-STRAIN-RATE LOADING AND SHOCK COMPRESSION

A Thesis
Presented to
The Academic Faculty

by

Manny Gonzales

In Partial Fulfillment
of the Requirements for the Degree
Doctor of Philosophy in the
School of Materials Science and Engineering

Georgia Institute of Technology
December 2015

Copyright © 2015 by Manny Gonzales

THE MECHANOCHEMISTRY IN HETEROGENEOUS REACTIVE POWDER MIXTURES UNDER HIGH-STRAIN-RATE LOADING AND SHOCK COMPRESSION

Approved by:

Professor Naresh N. Thadhani, Advisor
School of Materials Science and Engineering
Georgia Institute of Technology

Professor Arun M. Gokhale
School of Materials Science and Engineering
Georgia Institute of Technology

Professor Thomas H. Sanders
School of Materials Science and Engineering
Georgia Institute of Technology

Professor David L. McDowell
School of Materials Science and Engineering
Georgia Institute of Technology

Professor Laurence J. Jacobs
Department of Civil and Environmental Engineering
Georgia Institute of Technology

Date Approved: November 11, 2015

To my mother, Leonila, my aunts Galinda and Graciela, and my love,

Rachel,

the most important women in my life,

and the strongest, most courageous women on the planet.

Thank you for making my life worth living.

ACKNOWLEDGEMENTS

This work would not have been possible without the support and advisement of Professor Naresh N. Thadhani, who brought me to the group in 2010 and showed me the limitless potential for scientific advancement in the field of shock compression and high-strain-rate research. He never hesitated to offer his advice and always had his door open to me and everyone in the high-strain-rate (HSR) research lab, and indeed everyone at Georgia Tech. He allowed me the intellectual freedom and liberty that many students dream of. He offered an intellectually-stimulating environment and the resources that allowed me to explore a difficult problem. He also held me to a high standard and provided a critical eye, with the goal of making me a better scientist and engineer. I am indebted to him for this.

To the members of my committee, I offer my sincere thanks for serving as my advisors, for lending a bit of your intellect and sowing the seeds of curiosity, and for serving as inspirations to me, thus shaping my outlook. To Professor Arun M. Gokhale, whom I consider the very best of us, your intellect and scientific prowess are an inspiration, and your teaching is unmatched. I learned much from you and surely won't forget. We should all be so lucky to be your student. To Professor Thomas H. Sanders, a true paragon of the old school. To Professor David McDowell, whose encyclopedic knowledge and mathematical precision are to be admired. I gained a new appreciation for the state of the art in computational mechanics thanks to him. And to Professor Larry Jacobs, a true student advocate and awesome force for good. His encouraging words and priceless advice renewed my vigor on many occasions. I am lucky to have his enduring support.

There are many to whom I owe a debt of gratitude. To the many Seans that have graced the lab with their presence, I owe two in particular a great debt for their support of my work. To Sean Dixon whose delightful and inquisitive nature, made for great company. He

was a tour de force, and monumentally important to many – here's to you! May this minor recognition lift you as you deserve to be. To Sean Bradley, who has such great potential for growth as a researcher and engineer, helped me prepare many of my shock compression targets and shot the gun with me on more than one occasion. His attention to detail is admirable, and I am glad to have his support.

There are people whom I've taken to call "friend" who have served to stroke my intellect and have rekindled my faith in humanity.

- Dr. Ricardo Avila, you often reminisce as to the reason why I chose to associate myself with you. You silly man. You should know better! What better reason that to share a drink with a brilliant mind?

- Dr. Ashok Gurumurthy, you and I worked on this very difficult problem together. I'm glad to have worked with you as a collaborator and have enjoyed our time together.

- To my friend, Dr. Juan C. Noveron, who was my first chemistry professor. I still recall the day I went to your office and you tried to get me to change my major to chemistry. I remember that day fondly. You and I have developed a true friendship that I value.

- To my friend, Parveen Sood, who is the best example of what science should be, and how we should conduct ourselves. He is an inspiration to me. He has suffered for his craft and I know no one better. May you soon achieve the greatness you deserve.

- And lastly, to my friend Lance Williams, I offer my sincere thanks for your friendship. We have endured much together and your steadfast, continued friendship is one of my most valuable possessions. Like most people, there is a great geographical distance between us, and still we both know that we will be there when needed. You value loyalty to the end. That means a lot. Thank you for your friendship.

The following professors have undoubtedly changed my life and those of many others. They deserve my eternal gratitude –

- Peter “Pedro” Golding - An eternal student advocate, my biggest advocate, and my good friend. I’m sure he’s waiting even now to hear the good news that I finally finished! Thanks for always being there.
- Stephen W. Stafford - Another eternal student advocate, who helped me realize that I love my craft. I’m sure he’s waiting for me to return home and safeguard the most important resource - the students. Thanks as well for always being there.
- Laurence E. Murr - A savant and crown prince of metallurgy. He did it all and is truly an inspiration.
- Jack F. Chessa - My advisor from yesteryear, he sparked my curiosity for numerics and stimulated my intellect and thirst for knowledge. Thank you for helping get my feet wet!
- Ted Belytschko - Gone, but certainly never forgotten. May you rest in peace.
- Arturo Bronson - A misunderstood intellectual who shares much in common with me. Thank you for always offering your encouragement.

The HSR lab integrates all the aspects of science and research that I have come to love in a seamless manner, and it was a pleasure working here. I also wish to thank the members of the lab, especially Dr. Gregory Kennedy whose efforts and advice helped me understand the important and pervasive subtle nuances of experimental work in shock compression science. I’ve come to appreciate the new blood that flows through its veins. Alex Bryant, David Scripka, René Díaz, Sukanya Sharma, Stephanie Holguin, and Travis Voorhees – The future of this lab rests in your capable hands.

Lastly, I wish to acknowledge again (though they received due dedication) the most important women of my life: my mother Leonila Gonzales, my aunts Galinda and Graciela

Cabrera, and the love of my life and best friend, Rachel. They are my lifeblood and keep me going. I would also like to acknowledge Mr. Bulmaro Valencia and his wonderful family. Their unwavering support and friendship have brought our families together. I owe much to him and his family for their kind assistance and support. To all others whom I've forgotten, may I be forgiven for this transgression.

TABLE OF CONTENTS

LIST OF TABLES

LIST OF FIGURES

SUMMARY

This work presents a systematic study of the mechanochemical processes leading to chemical reactions occurring due to effects of high-strain-rate deformation associated with uniaxial strain and uniaxial stress impact loading in highly heterogeneous metal powder-based reactive materials, specifically compacted mixtures of Ti/Al/B powders. This system was selected because of the large exothermic heat of reaction in the Ti+2B reaction ($\Delta H_{rxn} = -320$ kJ/mol), which can support the subsequent Al-combustion reaction. The unique deformation state achievable by such high-pressure loading methods can drive chemical reactions, mediated by microstructure-dependent meso-scale phenomena. Design of the next generation of multifunctional energetic structural materials (MESMs) consisting of metal-metal mixtures requires an understanding of the mechanochemical processes leading to chemical reactions under dynamic loading to properly engineer the materials. The highly heterogeneous and hierarchical microstructures inherent in compacted powder mixtures further complicate understanding of the mechanochemical origins of shock-induced reaction events due to the disparate length and time scales involved.

A two-pronged approach is taken where impact experiments in both the uniaxial stress (rod-on-anvil Taylor impact experiments) and uniaxial strain (instrumented parallel-plate gas-gun experiments) load configurations are performed in conjunction with highly-resolved microstructure-based simulations replicating the experimental setup. The simulations capture the bulk response of the powder to the loading, and provide a look at the meso-scale deformation features observed under conditions of uniaxial stress or strain. Experiments under uniaxial stress loading reveal an optimal stoichiometry for Ti+2B mixtures containing up to 50% Al by volume, based on a reduced impact velocity threshold required for

impact-induced reaction initiation as evidenced by observation of light emission. Uniaxial strain experiments on the Ti+2B binary mixture show possible expanded states in the powder at pressures greater than 6 GPa, consistent with the Ballotechnic hypothesis for shock-induced chemical reactions. Rise-time dispersive signatures are consistently observed under uniaxial strain loading, indicating complex compaction phenomena, which are reproducible by the meso-scale simulations. The simulations show the prevalence of shear banding and particle agglomeration in the uniaxial stress case, providing a possible rationale for the lower observed reaction threshold. Bulk shock response is captured by the uniaxial strain meso-scale simulations and is compared with PVDF stress gauge and VISAR traces, thus validating the simulation scheme. The simulations also reveal the meso-mechanical origins of the wave dispersion experimentally recorded by PVDF stress gauges.

CHAPTER I

INTRODUCTION AND MOTIVATION OF THIS RESEARCH

The behavior of solids under extreme dynamic high pressure conditions is fascinating indeed, for physical states normally not accessible through conventional quasi-static processes are obtainable, and the full potential for probing materials under extreme conditions can be realized. Even states that are inaccessible under static high pressures are accessible under dynamic high-pressure and high-strain-rate loading conditions. The rapid, destructive nature of a high-strain-rate deformation process[1] leads to phenomena where the physical, chemical, and mechanical properties of the material no longer resemble that of a material loaded by any other means. The classic example is the shock wave, associated with a near-discontinuous change in physical and thermodynamic state, from the quiescent base state, to a higher energy "shocked" state. Shock waves are observable in day-to-day phenomena, e.g. aerodynamic compression during flight (helicopter rotors being a prime example) due to the facile compression of air. However, the shock compression phenomenon becomes even more complex in solids and liquids due to their incompressible nature. Here, a shock wave also leads to a near-discontinuous change in properties, but often brings with it a wave structure, with inelastic and nonlinear processes occurring during the rise to peak pressure. These processes are compounded by the heterogeneous nature of materials due to wave dispersion and nonlinear dissipative processes [1].

Solids subjected to high-strain-rate loading and shock compression experience sudden configurational changes, defect generation, and unique dissipative processes occurring

[1] A high-strain-rate process is generally viewed as one where the material system or component of interest is loaded rapidly, either through concussive impact, explosive interaction, etc. and the resulting physical processes are determined by traveling wave characteristics and limited by the acoustic properties of the material. These processes generally do not have enough time to achieve relaxation and equilibrium within the time scales associated with the induced loads, and so are very different from traditional quasi-static processes readily accessible in traditional laboratory settings.

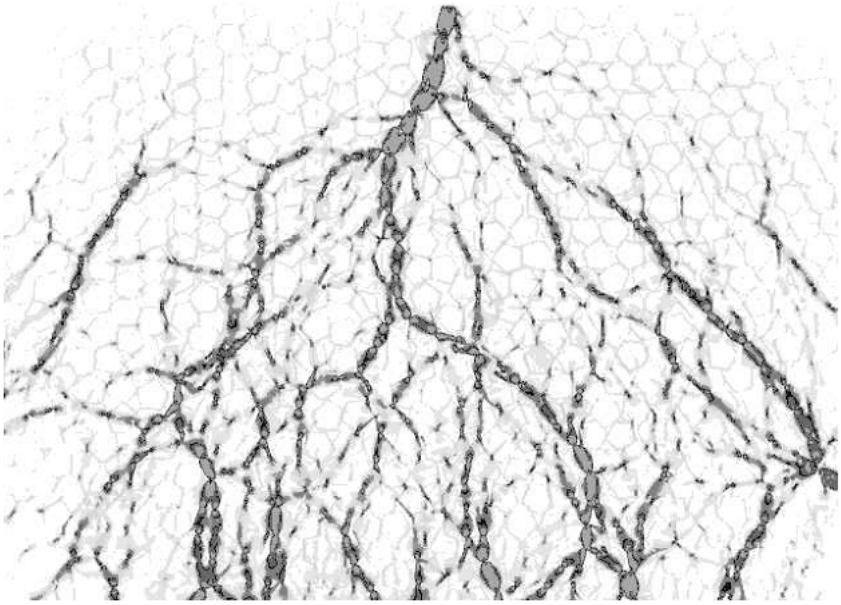

Figure 1: A two-dimensional collection of grains subjected to a vertical force which shows the transmission of the force in the form of chains across the medium. These chains can bifurcate depending on their stability. Forces transmit dynamically as characteristics of a wave equation and bifurcations are permitted in these solutions. Sustaining the force chain depends on the material properties (stability) and geometry of the grains, and is a characteristic of granular, heterogeneous materials [2].

behind the shock front [3]. This is exacerbated if the solid contains material-level heterogeneity, both spatially and through inhomogeneous property distribution. This heterogeneity, while complex, may prove to be a useful property if tailored properly. Sand is the quintessential example of a highly heterogeneous material, where large silica grains with varied size distributions and moisture or clay content can serve as a wonderful damping media for a speeding bullet. The force-chain mechanism [4, 5, 6] is understood as being the mediator of the damping effect inherent in the penetration-defeat process through granular media such as sand. Each grain must be in contact with an adjacent grain for the forces to be transmitted. This transmission is hyperbolic by its very nature and thus the forces are characteristics of a wave-type equation – a natural consequence of the equations of motion. Figure 1 shows such a characteristic transmitted along grain contacts in a granular media. A number of bifurcations are observed as a result of instability in the force chaining and preferential contact/re-orientation of grains. The dispersion at granular

free surfaces and the force-chaining that precedes material instability at the granular level invariably leads to projectile defeat. This is a simple example of a wave transformation as it propagates through a heterogeneous medium [7] and is integral to understanding the dynamic response in highly heterogeneous materials.

1.1 Heterogeneity at the meso-scale - Applications to reactive materials

It is indeed fascinating that the very distribution of microconstituents such as sand particles has such an effect on the bulk macroscopic behavior and the dynamic response of the system. Certain types of macroscopic behavior observed in sand are also inherent in generalized heterogeneous materials where microstructural inhomogeneity[2] serves as the primary source of heterogeneity. For example, bulk orientational anisotropy is common in highly textured materials, and polycrystalline solids can have an abundance of grain orientations[3], leading to meso-scale spatial heterogeneities in the form of oriented grain boundary systems. This is responsible for the different mechanical responses observed for a material under different processing conditions. Heterogeneous mixtures show a similar geometric distribution of constituents as a polycrystalline material, with greater disparity in mechanical and physical properties; the observed bulk response seems to rely on these microstructural properties. One would surmise that it is possible to extrapolate the effects of the heterogeneity[4] to the chemical stability and reactivity of materials, especially under dynamic loading conditions. These loading conditions and any induced reactivity caused by these conditions occur at time and length scales commensurate with the scales of the heterogeneity (within the meso-scale[5]) and thus it can be hypothesized that the bulk

[2] An inhomogeneity is defined by Mura [8] as the presence of a distinct phase in a material with different constitutive properties and morphology that, by its very nature, leads to inhomogeneous local strain fields produced under some prescribed external stress.

[3] Obviously, the multitude of grain orientations averages out the macro-level stress response, leading to the observed bulk isotropic behavior of typical polycrystalline solids

[4] Heterogeneity is now considered an umbrella term encompassing both inhomogeneities as defined by Mura [8] and any geometric or topological distribution of constituents that leads to the production of inhomogeneous strain fields

[5] The meso-scale is identified as the length scale between about 1 μm and 1 mm, i.e. where microstructural features are resolved

mechanochemical response will depend strongly on understanding the meso-scale response to dynamic loading.

A generalized heterogeneous material can also be considered as a material where there is some property-level heterogeneity in which the macro-level response is directly influenced by meso-level responses to an external stimulus in a volume-average sense. Such responses can manifest structural and chemical changes at the meso-scale under the influence of an appropriate external stimulus, which can lead to thermodynamically favorable conditions for reactivity (i.e. heating and material mixing through the conversion of microkinetic energy to heat via plastic deformation and friction [3, 7]). Indeed, the ability to control the meso-scale mechanical response and create from it a meaningful bulk chemical change is the very definition of mechanochemistry – chemistry driven by mechanical response or mechanical phenomena. Such chemistry becomes important when dealing with reactive materials (RMs), specifically those materials employed under dynamic load conditions such as explosives and munitions. The load configuration is also of importance, as generalized high-strain-rate events can produce triaxial states of stress much more complex than the idealized uniaxial cases, as in a rod-on-anvil impact (Taylor) test or a parallel plate-on-plate impact (shock compression) experiment. The interplay of the load configuration with the stress and strain state at the meso-scale is hypothesized to create the response that can radically alter the bulk behavior of the material even in the absence of microstructural heterogeneity. However, the microstructural heterogeneity may not be able to be decoupled from the critical interplay and indeed must play a critical role as has been observed in past works [9].

Microstructure-level heterogeneity is hypothesized to be of critical importance to the shock-initiation and overall shock compression response of reactive materials, particularly because the microstructure can be the driver for inhomogeneous stress/strain response and can exacerbate phenomena that serve as precursors to reaction. The inherent nature of a dynamic load requires wave propagation, which itself can be stable or unstable, the latter is

what has been found to be an essential element for dynamic reactivity and dynamic heating. Micro-level deformation will influence the overall bulk dynamic response, and it is crucial that this phenomena be studied to properly discern the effects of extrinsic microstructural variables on bulk dynamic response. This applies to any generalized heterogeneous material, especially energetic materials systems which are necessarily composite materials with many levels of heterogeneities [10]. Microstructure-level heterogeneity acts collectively in the meso-scale, where the variables of interest are particle-level interactions and the interactions of interfaces with traveling stress waves. The hierarchical complexity of heterogeneous materials makes understanding these particle-level interactions crucial to understanding chemistry driven by mechanical loads and facilitated by initial and evolving heterogeneities.

1.2 Multifunctional Energetic Structural Materials (MESMs) subjected to high-strain-rate loading conditions

A relatively new class of materials has emerged whose chemical energy content may be efficiently utilized under extreme conditions. The ever-evolving quest to usefully extract every last calorie of energy possible [11] from energetic materials has fostered the current interests in reactive composite materials, whose reaction response depends on the interplay between the constituent materials' physical, mechanical, and chemical properties. These materials systems are often produced as composites of metal particles or molecular explosives embedded in some kind of binder or matrix. Their initiation characteristics are dependent on the complex microstructures generated during processing, and the inhomogeneous meso-scale loading produced during high-strain-rate loading. Metallic powder-based reactive materials compacted to green strength or higher are also used due to the high exothermic energy release associated with the reaction on a per gram basis, and enhanced by the inherent porous nature of the compacts. These materials are stable, strong enough to handle, and have a substantial load-bearing capability, in addition to the ability to release high amounts of reaction energy upon demand, due to the nature of their microstructure

and physical/mechanical properties. This prompts their classification as Multifunctional Energetic Structural Materials (MESMs) – materials systems with energy releasing ability in addition to having some other desirable property, namely strength, without compromising energy density. MESMs are attractive since they retain structural and chemical stability at moderate loads and can be tailored to react under very specific conditions. Chemical reactions in MESMs may be mechanically-induced with the application of an impulsive load (e.g. impact) or under some other form of high-strain-rate deformation.

High-strain-rate loading conditions are typical in applications where the energetic material is subjected to impact. This can range from impact and penetration of a cylindrical projectile on an anvil, to the penetration of a projectile in a granular medium. If any inertial confinement is present, this can lead to the development of a shock wave within the solid material, which propagates mediated by the conservation laws. The shock compression of a material is accompanied by sudden configurational changes and defect generation [12], which can facilitate material mixing at the meso-scale. The mixing is by and large a bulk effect, but can be localized depending on the geometry and distribution of the microconstituents [13]. This localized mixing is theorized to be facilitated by the following:

- Microstructural topology which governs the relative location of reactants and materials with mismatched impedances. This includes particle orientation, topological connectivity, and contact proximity of reactant particles.

- Constituent morphology which can lead to reactant confinement in concave particle regions, leading to preferential deformation and mixing.

- Instability-driven material heating mediated by material properties and distribution of constituents. It is theorized that the very geometry of the loading relative to the particle distribution (microstructural topology) will lead to instability if the relative heating of the material overcomes any dislocation-driven strengthening effects [3].

- An adequate concentration of porosity which leaves open space for material mixing

to be facilitated, as well as heating due to pore collapse.

This does not take into account any exothermicity from a reactive species and what reactive transport may do to enhance this mixing. This is an active area of research and is beyond the scope of this work.

MESMs are naturally highly heterogeneous due to the need for combining reactive material components (a molecular explosive, or heterogeneous reactive powder) with a binder or matrix material in order to provide structural integrity. Precursor powders of the reactive material must be processed and combined in some way[6] so as to provide structural and chemical stability, while not compromising on the materials' functional properties, such as the chemical reactivity of the material under dynamic loading. Figure 2 shows a hypothetical rod made of a reactive material impacting an inert anvil. Zooming into the material, the expectation would be a highly complex microstructure, as in the case of the present work, a microstructure of a Ti+2B+Al mixture. Zooming further into the microstructure shows even greater topological complexity in the particles which is inherent in the processing and powder selection for this material. Understanding the effects at this particle level and meso-level, where collections of particles affect the bulk behavior of the material, is critical to understanding the response of heterogeneous reactive mixtures to dynamic loading. It is this very topological complexity and heterogeneity in size, morphology, and particle properties that is hypothesized to govern reactivity in reactive powder mixtures.

The unique thermodynamic conditions achieved during shock compression lead to interesting phenomena that cannot be observed under normal conditions. The concomitant shear and high pressure lead to complex triaxial states of stress and strain at the meso-scale. It is indeed a unique environment and tool to probe the physical, mechanical, and chemical properties of materials. However, the transient nature of the mixing phenomena and the disparate nature of the time and length scales involved complicates real-time measurements

[6]Consolidation of powders is a complex subject on its own and is beyond the scope of this work

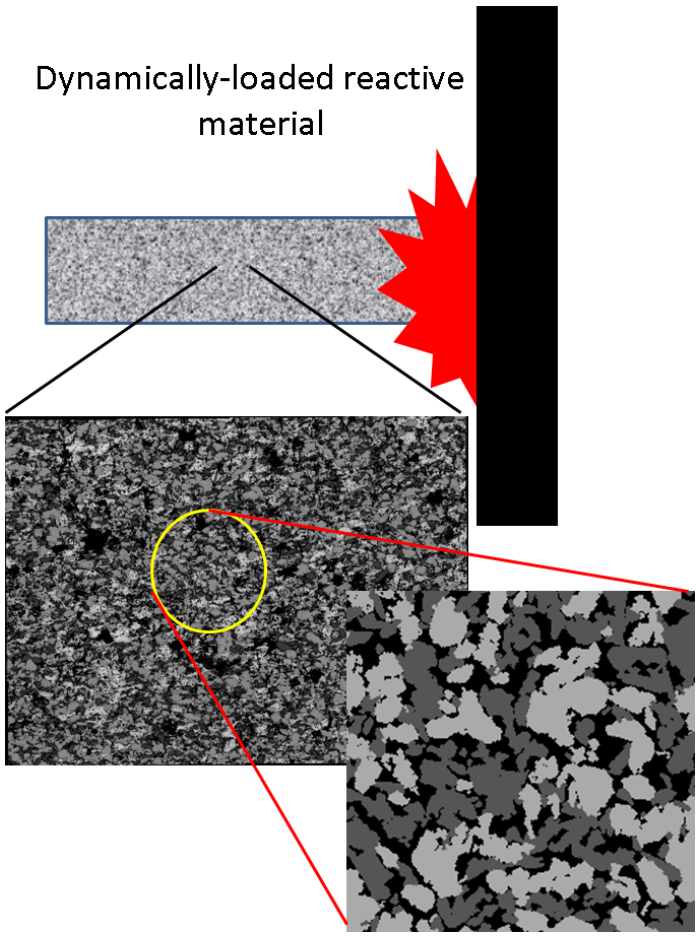

Figure 2: A reactive component, shown as a 2D rod impacting some inert anvil, leading to a chemical reaction. This hypothetical rod is made of a heterogeneous mixture (A Ti+B compacted mixture in this example) that shows meso-scale heterogeneity. In this case, the lighter-colored Ti particles and the darker-colored B particles have similar sizes, and are both topologically complex. It is the mixing, deformation, and mechanical behavior of the particles at the meso-scale that are theorized to be the most important variables to consider when tailoring reactive materials for optimum response under dynamic loads.

and leads to reliance on indirect observations of the phenomena of interest. The contributions from the effects of various length scales on the phenomena are equally difficult to resolve and decouple from the bulk material behavior. It is important to be able to discern the relative sensitivity of the bulk phenomena to microstructural variables to be able to identify the critical variables that can be manipulated to produce the desired bulk dynamic response of the material. Ultra-fast time-resolved measurements can reveal some aspects of the microstructural behavior manifesting itself at the bulk scale, but these measurements

remain indirect and the actual microstructural variables remain convoluted due to the disparate length scale that the device probes. However, the highly-resolved time scale probed by these measurements allows the capture of transient behavior that can provide clues as for phenomena occurring in the meso-scale.

MESMs present another dimension of complexity in that they are normally composed of metallic powder mixtures which, when compacted and pressed, become geometrically complex at the meso-scale due to the multitude of phases, sizes, and shapes that each material constituent may possess. However, the desirable bulk response in these MESMs is hypothesized to rely on this very complexity, which of course makes the investigation of the dynamic response of MESMs doubly complex. Furthermore, the characteristic heterogeneities can exacerbate material instability which is essential to reactivity [14, 15, 12]. Meso-scale plasticity of the component materials in the powder mixtures depends on the microstructural configuration and can lead to material instability, which is theorized to be critical to reactivity in MESMs.

Large amounts of heat can be released over a relatively small area during chemical reactions occurring in highly exothermic MESMs under shock compression, in contrast to an explosive detonation which typically leads to a large pressure buildup due to gaseous product generation and expansion. The high temperatures generated can influence the shock compressed state of the system due to the thermal pressure buildup, leading to anomalous thermodynamic behavior as described by the shock adiabat (Hugoniot) of the thermodynamic states in shock compression. Moreover, chemical reactions may affect the wave mechanics through dispersion effects at the shock front and can increase the shock velocity as a result of the formation of dense phase reaction products. These reactions have been postulated to occur via solid-phase or liquid-phase mechanisms, the kinetics of which depends on interfacial energetics and transport processes at the particle scale. If a chemical reaction does occur, it can propagate as a self-sustaining moving front [16]; the stability of the reaction front ultimately determines whether the reaction can be self-sustaining.

Mechanical stability at particle interfaces also influences the reaction initiation conditions [17].

1.3 Problems in understanding the shock-driven chemistry in reactive materials

The chemistry of reactive materials systems becomes unruly when considering their behavior under extreme conditions such as during shock compression. Meso-scale phenomena influence the onset and extent of chemistry in these systems, but are not adequately described in the framework of equilibrium thermodynamics. Indeed, there are transport phenomena occurring at the meso-scale that influence reaction initiation and can only be adequately treated in a non-equilibrium thermodynamic framework. The unique mechanical and thermodynamic conditions created under shock compression or during very high strain-rate deformations are not readily described by macroscopic equilibrium thermodynamics and are beyond the scope of this work. The theories of propagating singular surfaces[7] [1] have been applied with success in analyzing shock waves in materials. However, their limitations when applied to heterogeneous systems that disperse the shock front must be considered if they are to be used judiciously and with success. The shock compressed state of a material is given by the Hugoniot, which is a locus of shocked states that satisfy the Rankine-Hugoniot jump conditions. Therefore, any anomalous deviation from the theorized inert Hugoniot state must be assessed carefully to properly determine its origin and association with physical/chemical changes and whether this deviation can be used to describe chemical changes in highly heterogeneous materials.

Tailoring energetic materials to react under very specific dynamic conditions requires a-priori knowledge of the reaction mechanisms, as well as the shock compression behavior (in the form of an equation of state) of the system if the material is to be used for energy release applications. Understanding these conditions depends on the resolution of coupled

[7] The consequence of these theories are the famous Rankine-Hugoniot jump conditions

multi-scale phenomena, since experiments performed at high-strain-rates are extremely expensive and difficult. Furthermore, metal powder compacts obtained from cold isostatic compression have a complex microstructure that is highly heterogeneous and may contain a large amount of void space, the distribution of which is largely controlled by the compression method and the constitutive properties of the powders, along with extrinsic properties such as the powder size distribution and morphology. The defect state of the constituent particles in a metal powder-based energetic material also influences their reactivity. The myriad of variables involved in designing energetic powder mixtures complicates the isolation of each contributing phenomena.

Extrinsic properties of the constituent materials such as particle morphology, size distribution, volume fraction, particle condition, etc. and their effects on chemical reactions in powders have been explored in previous works [15, 18, 19, 20, 21, 22]. These works have concluded that the reactivity of powder mixtures is highly dependent not only on the extrinsic properties of powder mixtures, but also the intrinsic (strength) property differences due to meso-scale phenomena such as particle fracture, agglomeration, and viscous dissipation. These conclusions were based on experimental evidence of anomalous deviations in the shocked state (Hugoniot) and on the observed pressure profiles in the experiment along with microstructure-based simulations. Prior efforts have centered around describing the potential thermodynamic state achieved during shock wave propagation in reactive powder materials [23, 14, 24] solely due to the thermodynamic state variables such as pressure and volume, and on phenomenologically-based reactive flow models. Other works have discussed the effects of the constitutive models of the materials in meso-scale simulations [25], as well as the effects of pre-treating powders [26]. The transport processes linked to the meso-scale enhance localized shear deformation and interparticle contact which increases reactant availability and forces the materials to transition to a higher energy state due to the introduction of defects. These phenomena have yet to be decoupled and their

extent quantified. Furthermore, the wave mechanics at the meso-scale have not been satisfactorily explored.

The greatest challenge in understanding the shock-induced chemical reactivity of energetic materials lies in resolving the pertinent length and time scales. While measurements of the shock wave profile and stresses achieved during shock compression can provide important information on the consequences of a chemical reaction or of the very compaction process in powder compacts, these signatures cannot be used to describe the kinetics of the reaction nor its extent. Furthermore, the local sites of reaction initiation cannot be directly probed and the influence of extrinsic microstructural variables on shock-induced reaction initiation can only be inferred through post-mortem analysis, thermodynamic measurements, and through microstructure-based continuum simulations [27, 28].

The inertial response from a material undergoing a phase change or chemical reaction can indeed produce changes in a shock wave profile, but the influences of the contributing factors cannot be decoupled. These problems are exacerbated when dealing with highly heterogeneous materials, especially compacts of powders with large void spaces that support mechanically-driven mixing at high strain rates. The physical differences between the different mechanical phenomena at the particle- and meso-scales can be discerned through continuum-level simulations incorporating the proper physically-based constitutive models. The utilization of computational simulations is thus paramount in understanding the possible mechanical and thermodynamic states that lead to preferential reaction initiation.

1.4 Goal: Microstructural tailoring of energetic materials

The heterogeneous microstructures inherent to energetic powder compacts add an additional layer of complexity in the quest to unravel the understanding of shock-induced reaction mechanisms in these energtic materials. The influence of microstructure on the micromechanical and bulk response of the powders is theorized, with the right distribution of constituents, to enhance particle transport, promoting reactivity in the time duration

of mechanical equilibration which would be impossible through diffusional mechanisms alone. The loading configuration additionally affects the local stress/strain response at the particle level thereby affecting the reaction mechanism. The problem is exacerbated by the configuration of the reactants which is influenced by particle morphology, size effects, and reactant properties (specifically strength and impedance-mismatch between constituents).

The following questions have been identified as paramount to understanding shock-induced mechanochemistry in heterogeneous MESMs consisting of reactive powder mixtures:

- How does the heterogeneous microstructure affect the wave mechanics, particle deformation, localized strain distribution, and ultimately the mechanochemistry? Can this be generalized to a set of microstructural design parameters?

- Are so-called "hotspots," or regions of strain localization, as important in energetic powder mixtures as in composite molecular explosives (i.e. RDX)? If a reaction initiates at a hotspot, can it be sustained?

- Can continuum microstructure-based simulations using existing constitutive models predict the shock compression response in powder compacts? Can an improved microstructural representation help identify the effects of extrinsic meso-scale variables on the shock compression response in energetic powder compacts?

- Can any evidence of a chemical event be found in stress and velocity signatures recorded during shock compression? What can these signatures reveal about the heterogeneous deformation of the powder during shock compression?

- Are single-point properties such as shock speed U_s representative of the shock compression response of heterogeneous powder compacts?

- Can conventional techniques and assumptions applicable to shock compression phenomena be applied to highly heterogeneous materials in which wave dispersion and

mechanical dissipation processes prevail?

- Is there a preferred microstructural configuration which promotes shock-induced reactivity and can this state be tailored a priori?

The current work attempts to address these questions through a systematic study of the dynamic response of heterogeneous energetic powder mixtures. The prototype Ti/Al/B system is selected with the expectation that the components of the system support anaerobic chemical reaction by enhancing transport phenomena and producing a favorable thermodynamic state during deformation. The Ti/B reaction is highly exothermic and it was postulated (cf. chapter 4) that this exothermicity could enable and sustain a combustion reaction in Al under dynamic loading, a daunting proposition on its own. The powders have disparate mean sizes and have varied morphologies, from irregular/flake to spherical, in addition to having disparate shock impedances and constitutive properties. The boron particles are amorphous[8] while the titanium particles are sponge-like (irregular) α-Ti. The boron particles are also much harder than the titanium particles, and have an additional layer of complexity – boron has many stable crystalline allotropes and recent work has just begun to unravel the true complexity of this metal/metalloid [29].

The high enthalpy of reaction in the formation of TiB_2 from its elemental precursors makes this system attractive to support and sustain Al combustion. Enhanced mixing is expected from the straining of the softer Al phase, which can also lead to strain localization supported by the geometry of the microstructure and distribution of the constituents. For example, larger Ti particles are expected to deform much more readily than the harder B particles, but can still provide pathways for Al jetting (cf. for example Eakins and Thadhani [21]) especially if they are in close proximity to the surrounding Al. Furthermore, the Al

[8]Crystalline powders were used in some initial uniaxial stress experiments, but the transition was made to amorphous powders due to the higher reactivity and availability/cost of the powders. These experiments are noted when necessary.

can help carry B particles during deformation, potentially increasing reactivity by promoting intimate contact between the Ti and B. However, mutual plastic deformation between B and Ti proved to be the limiting factor in considering this system and even with the high energy of the system, reactivity remained elusive.

1.5 Approach to research

The shock compression (uniaxial strain) and high-strain-rate deformation response (uniaxial stress) of compacts of Ti/Al/B were assessed in this work using a combined experimental and computational approach. A variety of shock compression and high-strain-rate loading experiments were conducted to investigate the high-strain-rate deformation behavior of Ti+2B compacts in order to ascertain the potential shock-induced (under uniaxial strain) and strain-induced (under uniaxial stress) reactivity of the material as evidenced by deviations in the Hugoniot of the material or light emission, respectively. These experiments were repeated on different mixtures of Ti+2B+Al for a fixed material density to compare the effects of Al on the stress state in the case of uniaxial strain experiments, and the observed light emission response upon impact in the case of uniaxial stress experiments. The effects of extrinsic properties associated with the microstructure, as well as the intrinsic physical properties of the reactants were explored in this work via meso-scale simulations utilizing synthetic microstructures. These simulations study a variety of microstructural conditions and provide insight into the potential reaction meso-scale mechanism and the role that the microstructure and constitutive properties play in reaction initiation.

1.5.1 Mechanochemistry under shock compression conditions in Ti/Al/B

The ultimate goal of this work is to generate an understanding of the influence of microstructural variables on the mechanochemistry in a system that can react aerobically and anaerobically, and to determine the roles of the microstructure, constituent properties, and wave mechanics leading to shock-induced chemical reactions. This was done by probing

the shock compression response of Ti+2B powders in an effort to understand the thermodynamic state achieved during the passage of a shock wave and the potential effects caused by a shock-induced chemical reaction. The shock compression experiments were performed via parallel plate impact experiments on encapsulated powders using a variety of instrumentation, from poly-vinylidene fluoride (PVDF) stress gauges, to velocity interferometry to track the surface motion between the powder and a suitable containment window. The experiments probed the shock state of the powder from the crush-up state onward, up to pressures as high as 10 GPa. Anomalous response in the Hugoniot of the mixture manifesting as an expanded state was observed, due to a potential shock-induced chemical reaction.

Shock compression experiments were also performed on Al-containing Ti+2B mixtures to compare these mixtures with their non-Al-containing counterparts. The rise-time to peak pressure was found to decrease in the presence of Al due to the topological connectivity and the preferential plastic deformation in Al, but much of the intrinsic characteristics of the measured stress traces remained the same, indicating that the crush-up behavior governed much of the response of these mixtures. This was mainly due to the high hardness of B in relation to Ti, which increased the crush strength of the mixture. Furthermore, it was determined that Al mediates deformation and mixing in all loading cases, though reduces the overall heating in the material.

Continuum computational models at the meso-scale were used to elucidate the deformation mechanisms as a function of the loading configuration, strain rate, and microstructure and were validated by the time-resolved impact experiments in uniaxial stress and uniaxial strain loading configurations. The wave mechanics in these heterogeneous systems can be inferred as a function of extrinsic properties from these simulations. The effects of constitutive properties and equation of state (EOS) for each constituent were tested based on the correspondence to the experimental data.

In addition, temperature and strain fields were studied and their extent/distribution quantified in an effort to identify hotspot formation mechanisms and bulk thermal response

to shock compression in these systems. Stereological tools [30, 31] were employed to assess the microstructural evolution and its relationship to these field variables. This information was evaluated as a function of microstructure to help identify the microstructural condition which that can be expected to enhance chemical reactivity in these mixtures.

Lastly, the mechanochemistry of the combined Ti/Al/B system was studied with the help of the shock adiabat developed for the Ti+2B powders. This was done using a combined experimental and computational approach where a series of microstructures with varying extrinsic properties were studied via meso-scale continuum simulations. High velocity impact experiments were conducted at the Georgia Institute of Technology and at the Munitions Directorate at Eglin Air Force Base on both Ti+2B and Ti+2B+Al mixtures at impact velocities up to 1500 m/s. Diagnostics included PVDF stress gauges, the Velocity Interferometry System for any Reflector (VISAR), and Photon Doppler Velocimetry (PDV) to characterize the material velocity of the compacted powder mixtures and the arrival times of the stress waves through the powders.

1.5.2 Mechanochemistry in Ti/Al/B at high-strain-rates

High-strain-rate deformation experiments in the configuration of the modified rod-on-anvil Taylor impact setup were performed to investigate the occurrence of chemical reactions in the Ti/Al/B system[9]. The studies were supported through meso-scale simulations using both real and validated simulated microstructures. A range of Ti/Al/B stoichiometries were considered from 0% Al to 75% Al in 25% Al increments.

A lower velocity threshold for observing light-emission upon impact of the compact against an anvil was found for 50% Al-containing mixtures of Ti+2B. Meso-scale simulations showed a more uniform mixing of constituents in the presence of Al due to the preferential plastic straining in this softer material. Even though higher temperatures were observed in simulations at the same impact velocity, there were large, cold regions which

[9]Chemical reactions are identified by light emission events observed through high speed photography

potentially quenched any reaction.

1.6 Outline of this work

This dissertation is split up into eight subsequent chapters. Chapter 2 provides a brief background in shock compression and high-strain-rate deformation physics. A brief introduction to shock compression of solids is given and the mechanics and thermodynmaics pertinent to shock compression in powder mixtures is provided. The equations of state, mixture models, conservation equations, and relevant thermodynamics is also given. Chapter 3 provides a literature review of the state of the art in shock-induced chemistry of energetic materials. A historical overview of shock compression science leading to the current interest in phase and chemical transformations in heterogeneous powder mixtures is provided. The open questions in the field are also outlined. Chapters 4 and 5 describe the experimental and simulation techniques employed in this work. Chapter 6 outlines and discusses the results of the both uniaxial stress and uniaxial strain experiments and simulations; Chapter 7 attempts to connect the observed behavior in uniaxial stress and strain and correlates the bulk response with microstructural state. Chapter 8 gives a summary and conclusions of this work and provides recommendations for future work and

CHAPTER II

LITERATURE REVIEW

2.1 Brief historical overview - chemical reaction and phase transformation phenomena in shock compression

Shock compression science evolved out of the seminal works at Los Alamos after World War II. The focus of those studies was the behavior of shock waves in condensed matter produced by explosive-material interaction. The original works [32, 33] showed the effectiveness of shock compression in probing the high pressure equation of state of solid materials, and in particular discerning the α–ε martensitic phase transformation in iron [33], which was deemed physically impossible under shock compression by the preeminent high pressure physicist P. W. Bridgman[1].

The field was cemented with the landmark publication by Rice, McQueen and Walsh [34] in 1958 and shock compression science was legitimized as a systematic method of studying materials at high pressures. Interest in the field would soon explode with the synthesis of diamond particles from carbon [35]. Additional studies in shock synthesis [36, 37, 38, 39, 40, 41, 42] would eventually lead to the current interest in understanding the shock compression and high strain rate behavior of heterogeneous metal powder-based energetic materials. Improvements in computational and simulation technology have spurred an additional revolution which includes the predictive design of materials systems for improved performance under shock loading [43, 44]. This has been informed in large part by an improved capability of nanosecond-resolution instrumentation for shock wave measurement [45, 46, 47].

The importance of shock wave propagation in materials was beginning to be realized

[1] Of course Bridgman was later convinced of the transformation after the high pressure scale of his Bridgman device was re-calibrated with data from shock experiments

with the allotropic transformation of iron at 13 GPa, first observed by Minshall [33] under quasi-static conditions in 1954. As outlined by Duvall and Graham [48], phase transitions induced by shock wave loading were posed as possible by Schardin [49] as early as 1941. Bridgman showed that chemical reactivity and phase transformations were possible by imposing a shear stress simultaneously on a hydrostatic state of compression [50, 51, 52, 53, 54, 55]. However, he was skeptical that a chemical reaction or phase change was possible within the time scales to reach the peak pressure of a shock wave. An additional set of experiments and a refinement of the established high pressure scales provided unequivocal evidence of the α–ε martensitic phase transition of iron by shock compression [56]. Nellis [57] attributes Bridgman's standing as the world's leading high pressure physicist to fueling the debate over the existence of such transformations unobservable at quasi-static conditions, which propelled many experimental high pressure physicists to improve their experimental capability. Bridgman immediately recognized the importance of such a discovery and also found that much higher pressures could be achieved with explosives. These observations inspired Alt'shuler [58] to conduct the first underground nuclear test to generate shock waves at Arzamas-16 ("Los Arzamas") [59].

Much of the early research in shock compression materials synthesis was conducted in the Soviet Union [60, 61, 62]. Ryabinin [63] first observed evidence of possible chemical reactivity when subjecting materials to sudden shock loading. Dremin and Breusov [64] provided the first major review outlining the crucial role that shear plays in shock compression of materials, revealing possible shock-loading scenarios leading to chemical reactivity or transformation. Further experiments showed allotropic behavior in graphite (the famous graphite-to-diamond phase transition) [35] and in the cubic and wurtzite polymorphs of BN obtained through shock compression of hexagonal BN [65, 66, 48]. Kimura [67] followed by Horiguchi and Nomura [68, 69] in Japan were the first to chemically synthesize TiC from porous powder compacts under shock compression. These works also showed that the remnants of the shocked state were energetically activated, promoting further chemical

reactivity. Batsanov et al. [62] later demonstrated that potassium nitrate showed enhanced chemical reactivity after shock modification; this work is widely considered to have brought the subject of shock-induced reactivity into the limelight. Adadurov et al. [60] showed that polymerization of acrylamide and trioxane was possible with the passage of a shock wave, which was identified as a shock-induced phenomenon [70]. This early work revealed that the shock process could induce or enhance chemical reactivity in materials at incredibly short time scales, i.e. at the peak pressure of the shock wave. Future work would involve a critical assessment of the possibility of ultrafast chemical reactions occurring within the shock front [36]. These studies further exemplified the untapped potential of this new field of study.

2.1.1 Looking forward

The advent of massively-parallelized computing environments have enabled simulations of large-scale systems as well as intricate meso-scale simulations at smaller length scales. These simulations use continuum mechanics descriptions (field variables are describable by continuous functions permitting a finite number of discontinuities) of material behavior and can be used to resolve meso-scale phenomena contributing to the bulk behavior of the materials. Extrinsic properties such as particle size distribution and morphology can be investigated with precise numerical simulations, the validity of which may be correlated with experiments. This relatively new development permits the accurate microstructural description of the material and enables the decoupling of potential meso-scale phenomena responsible for shock-induced reaction initiation.

The following sections discuss recent pertinent works in the chemistry of powder materials under shock compression, the current efforts in modeling, simulation, and theory of shock-induced chemistry in heterogeneous energetic materials, and the current general trends in understanding the mechanochemistry at high-strain-rates. The role of meso-scale heterogeneity and its effects on bulk mechanochemical response is of particular interest in

this work. The proposed research seeks to illustrate the tailorability of metallic powder-based MESMs for use in high-strain-rate applications. Mechanochemistry of the Ti/Al/B system under shock compression loading is of interest and the mechanisms for reactions at various length scales will be explored in support of this goal.

2.2 Chemical reactions and synthesis of materials under shock compression

Elemental powder precursors can undergo chemical reactions under shock compression through mechanisms that are fundamentally different from first-order physical and chemical changes [48]. The turbulent state within the shock wave, facilitated by the local heterogeneity within the powder, leads to extreme deformation of particles and enhanced material mixing, which can cleanse oxidized surfaces and lead to conditions favorable to chemical reactions [9, 12]. The natural porosity in powder compacts (of green strength or higher) provides sites for mixing and thermal buildup due to pore collapse during the densification process. This is of particular importance in explosive materials [3, 71] where the energetic material is in the form of a molecular crystal embedded in some binder. Solid state bonding of particles is also possible during the deformation processes. The bulk mass transport of constituents may bring reactants into closer proximity where their reaction is more probable. Bulk heating due to the thermal pressure buildup in a shock compressed material can be sufficient to cause molecular decomposition or melting at interfaces. Extreme localized heating can also lead to the same phenomena at discrete locations within the material microstructure. The thermal pressure buildup may be sufficient to cause the reaction to be self-propagating [72]. Thus, chemical change and densification can concomitantly occur during shock compression and can lead to drastically different states of matter and microstructures unlike any that can be produced via normal materials processing routes [73].

Chemical reactions occurring as a result of the passage of a shock wave through a material can be characterized based on the time scale of occurrence [12]. *Shock-induced* chemical reactions occur in the time scale of mechanical equilibration during the peak

pressure of the shock wave front while the material is undergoing rapid changes in thermodynamic state variables. Reactions occurring or enhanced by the disordered and activated material left behind after the passage of a shock wave are considered to be *shock-assisted*. In contrast, for reactions induced by the shock wave, the shocked region becomes filled with activated states that lead to enhanced reactivity. Reactivity can also be induced by the massive shearing events, localization phenomena, and enhanced mass transport associated with high strain-rates at pressures below those of the shock wave regime. Such reactions may be considered to be *strain-induced* and are one of the principal focuses in this work along with shock-induced reactions. Highly heterogeneous materials systems can react in a combination of *shock-induced* and *strain-induced* manners, where localization phenomena becomes an important precursor for a reaction to occur. Chemical reactions occurring as a result of the passage of a shock wave through a material can be characterized based on the time scale of occurrence [12]. *Shock-induced* chemical reactions occur in the time scale of mechanical equilibration during the peak pressure of the shock wave front while the material is undergoing rapid changes in thermodynamic state variables. Reactions occurring or enhanced by the disordered and activated material left behind after the passage of a shock wave are considered to be *shock-assisted*. In contrast, for reactions induced by the shock wave, the shocked region becomes filled with activated states that lead to enhanced reactivity. Reactivity can also be induced by the massive shearing events, localization phenomena, and enhanced mass transport associated with high strain-rates at pressures below those of the shock wave regime. Such reactions may be considered to be *strain-induced* and are one of the principal focuses in this work along with shock-induced reactions. Highly heterogeneous materials systems can react in a combination of *shock-induced* and *strain-induced* manners, where localization phenomena becomes an important precursor for a reaction to occur.

Much of the early works in materials synthesis and decomposition involved displacement-type chemical reactions which were found not to depend on diffusive transport. Studies of

ultrafast chemical reactions (mainly decomposition occurring within the microsecond time scale of the high pressure state) were first conducted by Batsanov et al. [74] and showed that the decomposition of $CdCO_3$ was due to an intramolecular process not requiring diffusion of the reaction components. This was also later shown to occur with andalusite decomposing into an amorphous form of Al_2O_3 by Schneider and co-workers [75]. In contrast to the early works in materials synthesis and decomposition of covalent and molecular solids, the investigation of shock induced reactions in intermetallic-forming powder mixtures is a relatively young field. The mechanisms for reaction initiation in these systems is much different from molecular decomposition or displacive mechanisms mentioned previously. Indeed, the transport phenomena enhanced by the shock front has been found to be an essential ingredient [12, 14].

Horie et al. [36, 76] were the first to study intermetallic-forming powder mixtures of Ni/Al and Ti/Al under shock compression. They observed an ordered phase of Ni_3Al in the high temperature zones of the post-impact recovered material and various other stoichiometries interdispersed within the low temperature zones [36], as shown in figure 3. The high temperature regions were found near the periphery of the samples due to wave interactions at the edges of these regions. They also observed a region of a nearly homogeneous distribution of the Ni_3Al product dispersed alongside inhomogeneous, irregularly-shaped Ni, which was partly attributed to localized inhomogeneous distributions of starting particles. Finally, regions of NiAl and $NiAl_3$ grains were also observed. The $NiAl_3$ phase was postulated to have formed by precipitation from the liquid state, as the structure had the classic eutectic form [36]. They also identified numerous mechanisms thought to influence the initiation of a chemical reaction. Among these events are the high speed motion of dislocations, the consolidation of particles, viscoplastic deformation, and localized reactions leading to an exothermic energy release. They noted that the particles in the shocked region became mechanically activated and achieved intimate contact. This, along with high

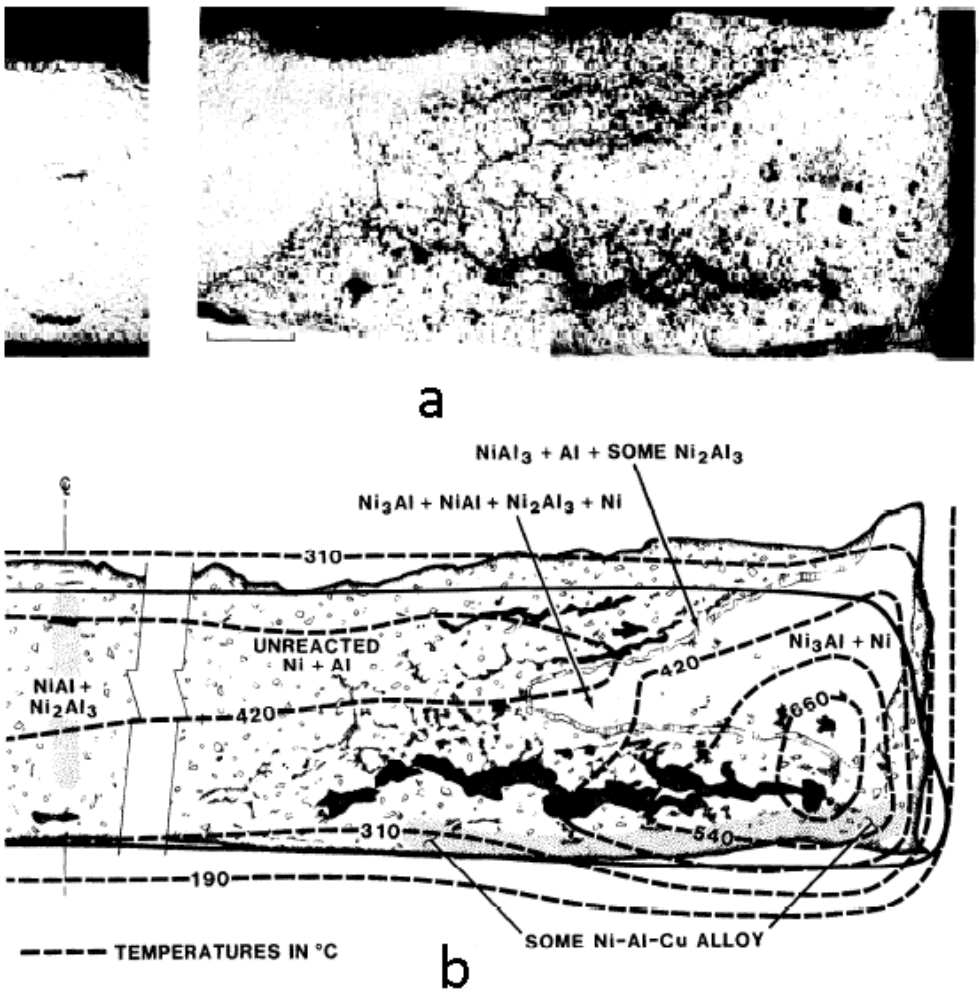

Figure 3: (a.) Recovered shock-compressed Ni/Al powder compact specimen (b.) Calculated temperature isotherms superimposed on a schematic image of the recovered specimen. The crack was caused by spallation. Adapted from Horie et al. [36]

local stress and thermal gradients were postulated to lead to reaction. However, the postulated mechanisms are based on conjecture and inferred from the stress traces recorded from experiments and are indirect in nature. Furthermore, the effects of these mechanisms on the reaction initiation are unknown. Computer simulations of shock processes were used to predict the temperature distribution within the powder compact. The results shown in figure 3b illustrate that the reacted regions achieve temperatures close to those for the initiation temperatures of Ni/Al powders under self-propagating high temperature synthesis (SHS) reaction. This initial work provided evidence for synthesis reactions from recovered

samples and post-mortem characterization, but without direct time-resolved measurements.

2.2.1 Direct observation of shock-induced reactions

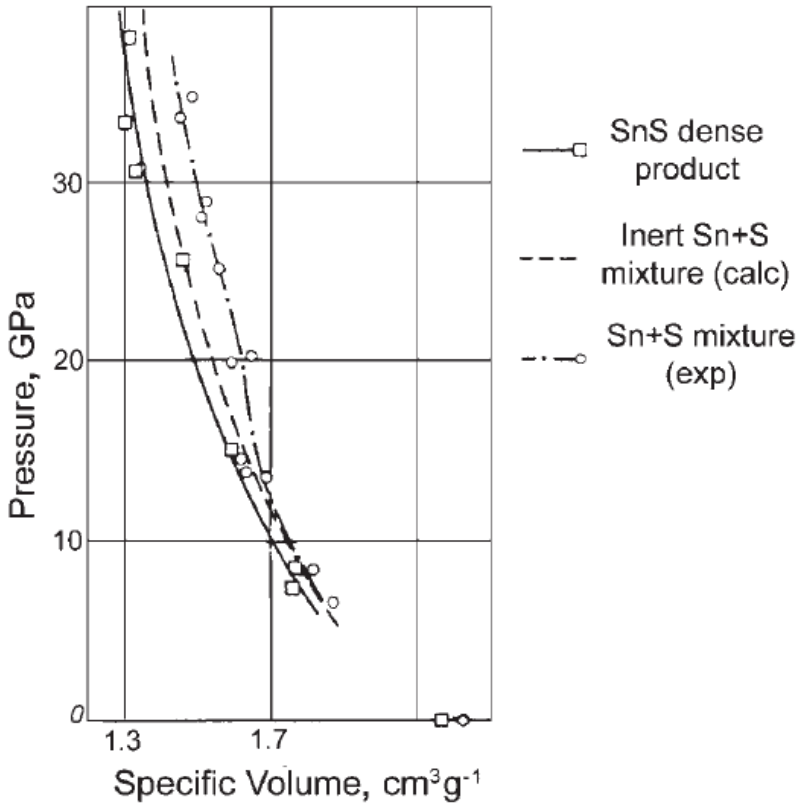

Figure 4: The shock Hugoniot obtained by Batsanov et al. [77] shows pronounced deviation from the calculated Hugoniot for solid SnS and an inert rule of mixtures Sn+S calculation, revealing a thermal back pressure created by the exothermic energy release by the reaction.

Batsanov et al. [77] analyzed the Sn-S system through Hugoniot measurements and found an anomalous behavior in the monotonic volume increase seen in the Hugoniot curve at around 15 GPa. The deviation was well beyond that expected for the shock compression of an inert porous mixture (see figure 4), indicating that a reaction had occurred within the equilibration time at peak pressure of the shock wave (near the shock front). They attributed the deviation to the reaction producing new products and to the disparity in particle velocities of material constituents at high pressures causing extreme material mixing

(mechanically-based transport phenomena enhancing the diffusion-controlled processes). They also concluded that if the specific volumes of the mixture and reaction product are close, then the shock adiabat will shift to the right (expanded state) in $P-V$ space as a result of the thermal back pressure exerted by the exothermic release of energy during reaction [77]. They postulated that a threshold pressure P^* had to be exceeded for such deviation to be observed in $P - V$ space. This study provided the first evidence of a chemical reaction in a powder mixture system, based on time-resolved Hugoniot measurements.

Graham et al. [78] provided a comprehensive overview of materials synthesis under shock compression and identified the uniqueness of the shock process which involves simultaneous shear and high pressure at very short time durations. Graham would later provide a new look at chemical reactions within the peak pressure state of the shock [79]. Batsanov's work [77] provided the first direct measurement of an anomaly that could be interpreted in the framework of a shock-induced chemical reaction. The "Hugoniot-based" observation of a chemical reaction prompted further analysis from Graham and co-workers [80] using the new Bauer piezoelectric PVDF stress gauges [81, 82, 83, 84]. This work identified the class of reactions occurring at high pressures and classified the Hugoniot deviations as "Ballotechnic" reactions [79]. Graham proposed that the heat of reaction evolves as a constant pressure process and the heat contributes to the expanding volumetric state, in contrast to Batsanov's constant volume correction to the energy equation [85]. This idea was further extended by Bennett and Horie [24] through a critical analysis of prior attempts in using the Mie-Grüneisen equation of state to predict the reaction product Hugoniot [15, 86, 87, 72]. The Ballotechnic model will be discussed in greater detail in section 2.3.1.

Bennett and Horie et al. [14] reported similar evidence of reactivity in a Ni-Al powder mixture and observed the characteristic "peculiarity" in the Hugoniot as witnessed by Batsanov in the nanosecond time scale. Their perspective on the reaction event is based on

an "excess pressure" recorded through a Manganin gauge embedded in their backer material away from direct contact with the compacted powder (shielded by a buffer material). Figure 5a shows a series of recorded pressure traces from two experiments performed at nearly the same impact velocity. A large excess pressure was recorded well above the 21 GPa (dotted line) predicted by an inert mixture calculation in both experiments, but was more pronounced for the slightly higher impact velocity of the 1075 m/s experiment versus that at 1064 m/s. This excess pressure is beyond the error bars of the experiment (cf. figure 5b) and remains nearly constant for higher impact velocities. The pressure is thought to arise from the exothermic nature of the reaction and subsequent effects of the volumetric expansion of the reaction products. Furthermore, the slightly higher velocity profile (1075 m/s versus 1064 m/s) reveals a pronounced excess pressure (58 kbar) above the baseline pressure, indicating that a reaction occurred within the first 100 ns of the impact event.

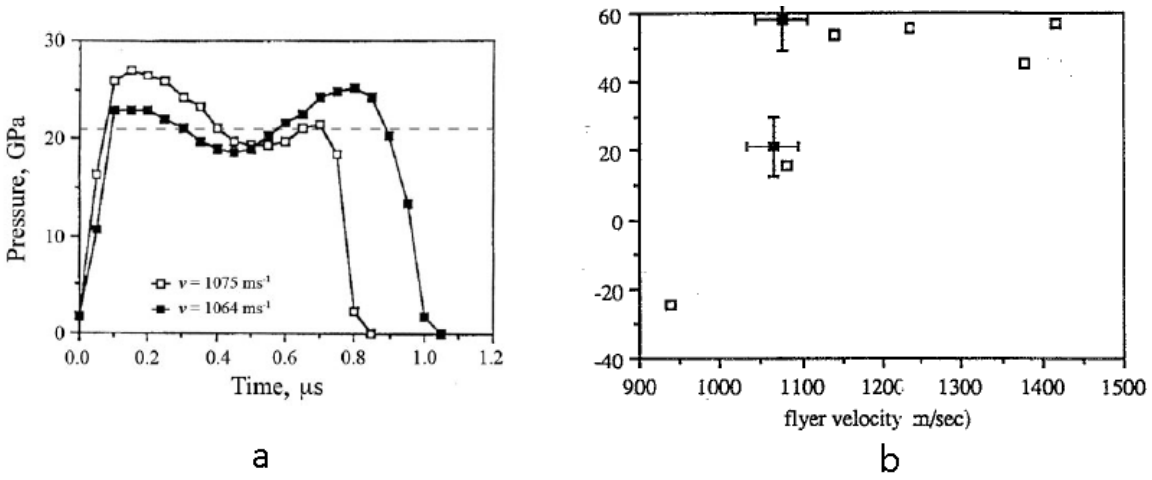

Figure 5: Evidence of shock-induced chemical reaction in Ni/Al provided by an "excess pressure" condition in the observed pressure profiles. (a.) Propagated pressure profiles (Manganin backer gauge) recorded at impact velocities of 1075 m/s (open squares) and 1064 m/s (filled squares) showed a peak pressure in excess of the predicted inert mixture pressure of 21 GPa (dotted line). (b.) Excess pressure ($P_E = P_{Measured} - P_{Inert}$) plotted versus impact velocity showing a clear threshold impact velocity (about 1100 m/s) where the excess pressure remained well above the error bar range for any subsequent experiments.

Bennett and Horie also provided metallographic evidence showing completion of the reaction of Ni and Al forming $NiAl_3$ around 1075 m/s impact velocity, in contrast with that

for the lower velocity profile which showed signs of a diffusive mechanism for reaction (potentially a shock-assisted reaction). They attributed this to a characteristic threshold velocity to reaction occurring at around 1075 m/s. These works provide conclusive evidence that shock-induced reactions can indeed occur within the peak pressure regime of a shock wave and as such are subject to different initiation mechanisms in stark contrast to traditional thermochemical mechanisms. The exact mesomechanical origins of the reaction are still unknown and many subsequent works have depended on these peculiarities to infer that a reaction event has occurred. These effects were not directly probed in these experiments since the gauge was shielded by a buffer material, leading to a steepening of the shock front and thus obscuring the meso-scale effects on the bulk response.

Other intermetallic-forming systems have been studied using time-resolved measurements as well as post-mortem recovery experiments. Dunbar et al. [88] were the first to study the Ti-Si system with time-resolved measurements using Bauer PVDF stress gauges [81, 82, 83] following Graham's initial work with PVDF gauge calibration [84]. The Ti-Si system was studied using powder mixtures in 5:3 molar ratios of Ti-Si with the intent of preferentially supporting the Ti_5Si_3 reaction pathway. Evidence of a shock-induced reaction event was found on the basis of an increase in measured shock speed as compared with a predicted value from an inert rule of mixtures calculation. Coupled with the nanosecond time resolution of the PVDF gauge, this provided evidence of an ultrafast event occurring within the rise to peak pressure in the shock wave. A subsequent study by Thadhani et al. [42] investigating the morphological effects on the shock response of Ti-Si powders showed that coarse (> 150 μm) and fine (< 10 μm) particle morphologies were detrimental to chemical reaction, owing to Si particle fracture and entrapment (coarse) and particle agglomeration (fine) during compaction, whereas a medium ($10 - 20$ μm) particle size led to greater shock speeds, indicating greater reactivity in these medium size particle mixtures. A greater expanded state in P-V space was observed for medium morphology particles, indicating a greater reactivity over the other sizes considered. Vandersall et al. [89, 90, 91, 92, 93] also

studied a Si-intermetallic system (Mo-Si) and found that melting of Si inhibited reaction and produced lower than expected shock speeds due to the density change in Si. This was manifested as a lower shock speed than what was predicted by a mixture equation of state for an expected reaction of Mo+Si. Melting was observed in post-shock samples as shown in figure 6. Moreover, similar evidence of melting and re-solidification was observed in [94, 95] which indicated reactivity to be mediated by liquid-phase mechanisms. Vandersall also observed highly dispersed wave profiles in Mo/Si powder mixtures during compaction which has implications in the Hugoniot analysis of this powder mixture, which will be discussed in connection with the present work.

The study of the intermetallic-forming Ni-Ti system by Xu and Thadhani [96] revealed a strong dependence of the deviation from the inert mixture Hugoniot state on processing condition (ball-milling time) and extrinsic properties. This work showed a drastically reduced threshold for reaction initiation due to the lowered activation barriers and higher energy state of the deformed powders, as well as the new topological configuration of the powders into a mechanically-induced alloyed system. This was evidenced in broader XRD traces and alloy phase (B2-NiTi-(110)) peaks present for longer ball milling times, as shown in figure 7. However, further ball-milling and mechanical alloying revealed a Hugoniot shock state on the inert mixture curve (see figure 8 a and b). The reduction in the expanded state is evidence of reduced extent of heat released during shock compression (less reactants available for chemical reaction) [96]. These works outline the importance of extrinsic component properties and the need for nanosecond time-resolved measurements.

2.2.2 Post-mortem evidence of shock-induced reactions

The shock-induced reactions and formation of silicides such as niobium and molybdenum silicides have been studied by Vecchio et al. [94, 95] and Yu and Meyers [86] in an effort to understand the reaction mechanisms. They tested powders of varying sizes and morphologies and closely controlled the experimental conditions to ensure that recovered

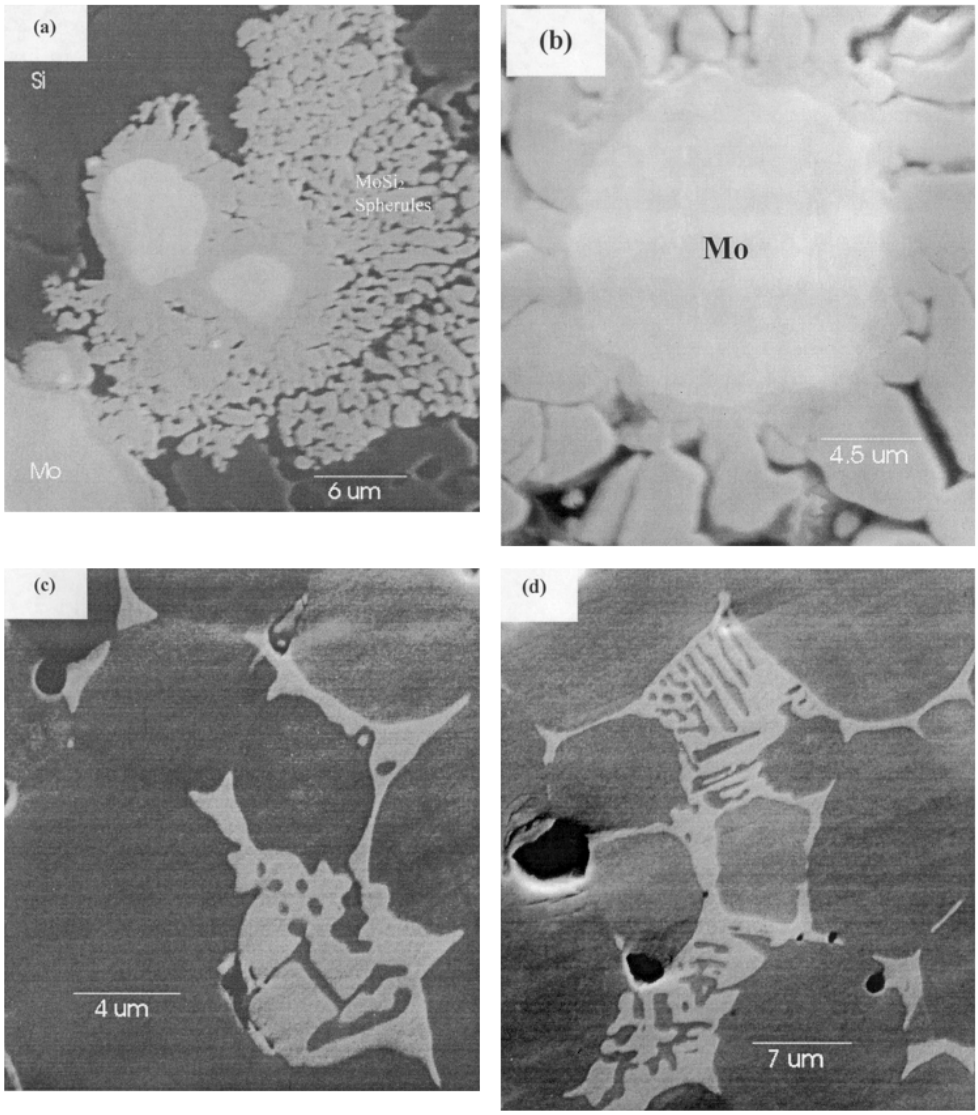

Figure 6: (a.) – (b.) Photomicrographs showing the partially-reacted eutectic phase of $MoSi_2$ in the presence of ejected Mo particles. (c.) – (d.) Fully reacted microstructure showing a eutectic $MoSi_2$ characteristic of a melt/re-solidification process. [93]

specimens would be in a partially-reacted condition similar to that near the onset of reaction. Their work concluded that a liquid-phase interfacial mechanism was responsible for reaction initiation based on post-mortem characterization of the shock compressed material. Figure 9 shows a recovered specimen of Nb+Si powder shock compressed at 1.2 km/s. A progression through the capsule thickness shows: a.) The fully compacted, though unreacted, region near the top of the capsule, b.) A transition region between the unreacted and partially-reacted regions, c.) A close-up of the partially-reacted region showing

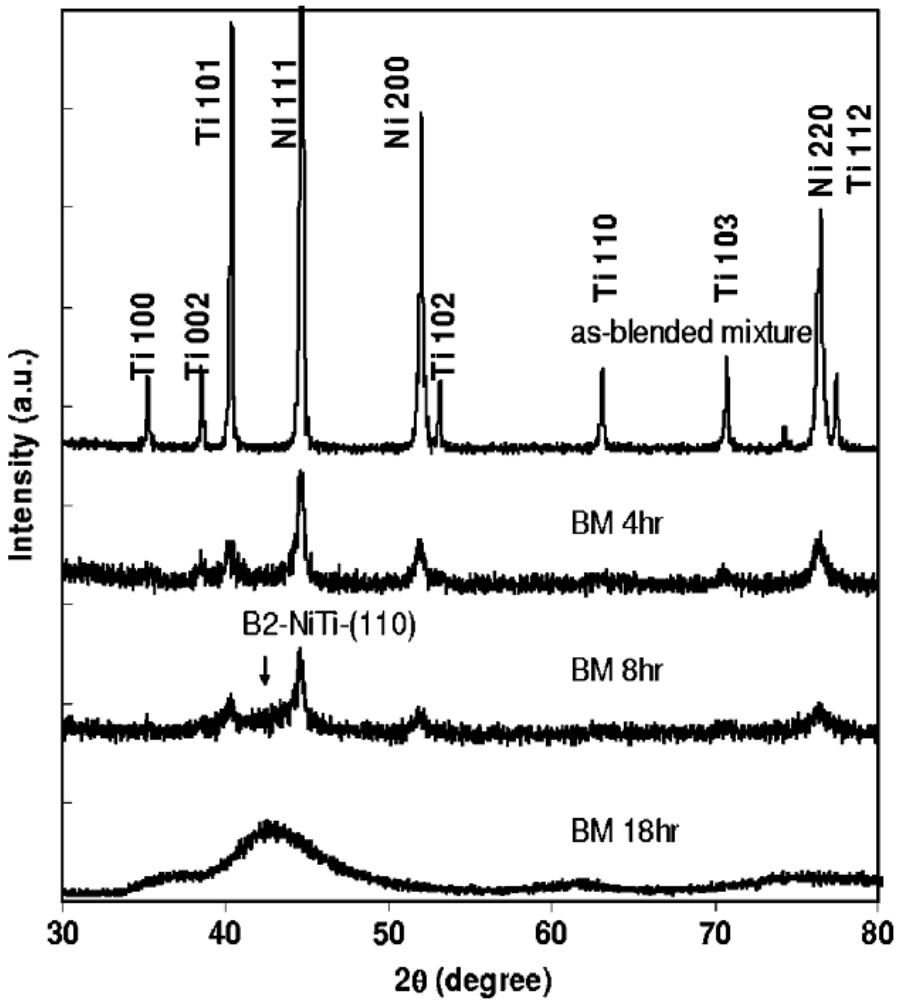

Figure 7: Ball-milling of Ni-Ti mixtures showed peak broadening of Ni and Ti peaks at 4 hours (due to particle straining) and alloying at greater ball milling times, producing an energetically active powder mixture [96].

$NbSi_2$ nodules surrounding unreacted Nb particles, d.) A transition region between the partially-reacted and fully-reacted material, e.) A close-up of an interphase region showing an equilibria between Nb metal, $NbSi_2$, and the potential transition interphase product Nb_5Si_3. The authors proposed a mechanism based on the melting of the Nb-Si interfaces leading to the removal of the activation and diffusion barriers to subsequent synthesis of Nb-Si intermetallics. Some eutectic product was observed at higher impact velocities and preheated samples. The high temperatures in the molten Si phase may have caused the dissolution of $NbSi_2$ and the subsequent turbulent mixing of the products gave a uniform

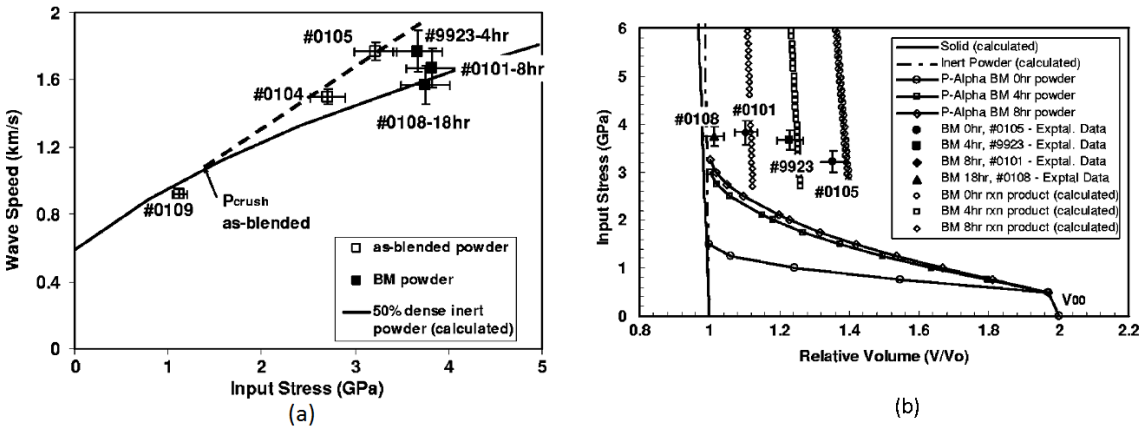

Figure 8: (a.) Shock compression experiments on as-blended Ni/Ti powder mixtures show pronounced deviations from the inert and porous Hugoniots at higher pressure, approaching the reaction product NiTi Hugoniot, indicating a Ballotechnic-type reaction. (b.) Increased ball-milling time had a dissimilar effect on the shock state of the Ni/Ti mixture, showing reduced deviation from the inert mixture Hugoniot [96].

re-solidified structure, reminiscent of equilibrium melting and solidification. This mechanism is a result of the aftermath of the shock process and does not represent the potential reaction occurring within the peak pressure state of the shock wave.

A similar progression for Mo-Si is shown in figure 10 where now the nodular particles are a $MoSi_2$ phase forming from a similar re-solidification from the Mo-rich Si liquid phase. Fracture is most prevalent in Mo particles along the internal grain boundaries, but it does not seem to disrupt the mechanism for the reaction. Indeed, the microstructures of the recovered Mo-Si compacts and Nb-Si compacts share many similarities. No interphase boundary was found in the Mo-Si compacts. The $MoSi_2$ particles likely form similarly as the $NbSi_2$ particles, i.e. at the molten Si and Nb(Mo) interface through solid-liquid mechanisms, whereupon further reaction is facilitated by the dissolution of these particles in the melted Si, saturating it with metal and further consuming the metal. This continues until the short-range forces in the liquid cause the agglomeration of Nb(Mo)-Si and the $Nb(Mo)Si_2$ solidifies in a spherule form. The kinetics of solid state diffusion are thus removed from the equation and the system can react within hundreds of nanoseconds through this dissolution

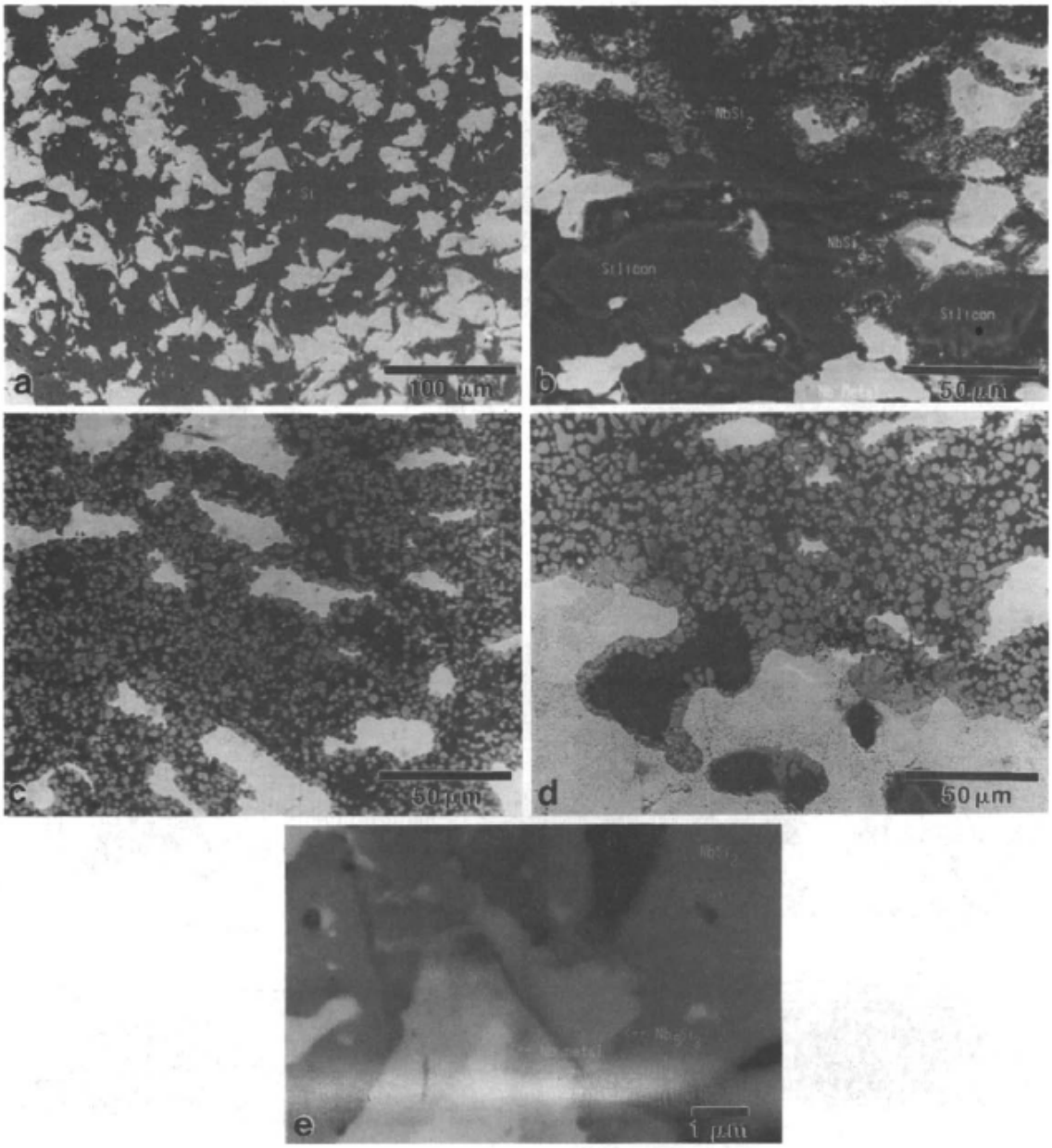

Figure 9: Post-mortem recovered samples of Nb/Si compacts. (a.) Unreacted, fully compacted region. (b.) Transition region between unreacted and partially-reacted zones. (c.) Close-up of partially-reacted zone. (d.) Transition region between partially-reacted and fully-reacted zones. (e.) Close-up of an interphase region comprised of the potential transition product phase Nb_5Si_3. Adapted from Vecchio et al. [94].

and re-solidification process[2]. This mechanism was further discussed in a companion paper

[2]The kinetics of first order transitions such as melting are incredibly fast, on the order of the phonon relaxation time of atoms [48]. Therefore, sustained reaction may be possible through mechanisms independent of diffusional processes.

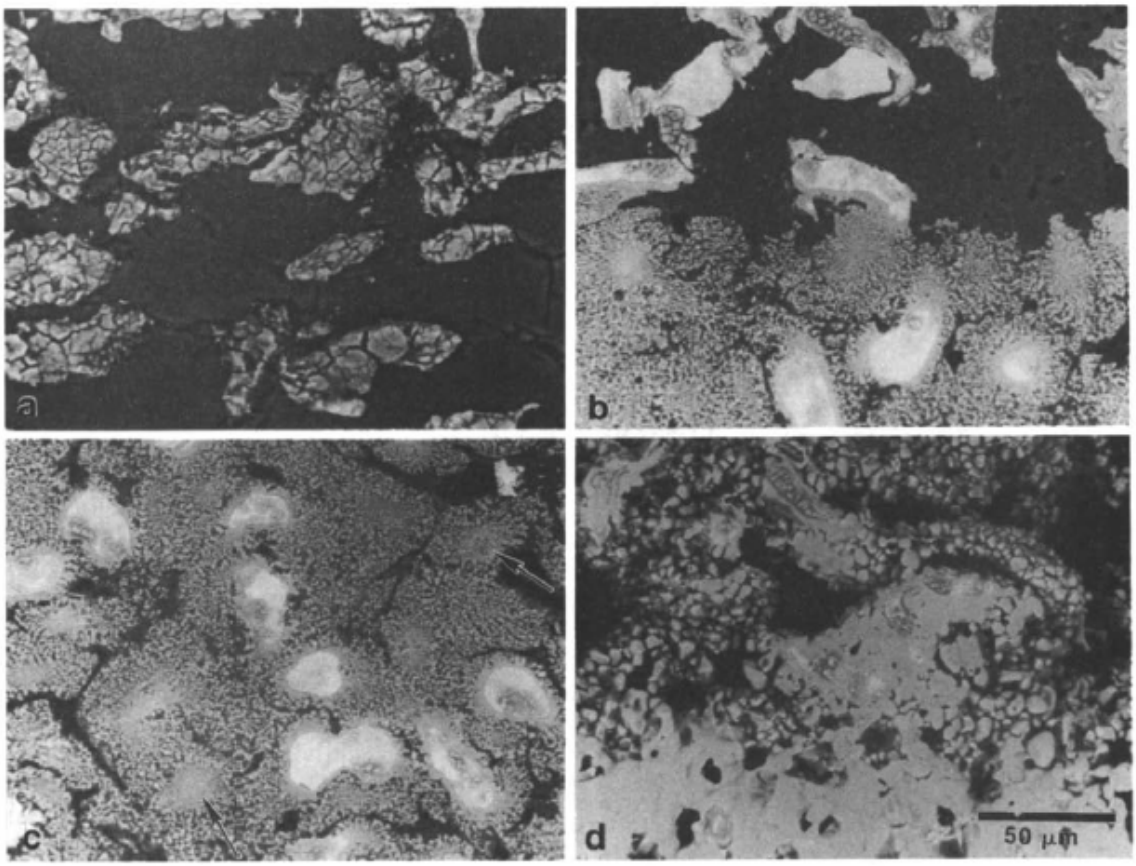

Figure 10: Post-mortem recovered samples of Mo/Si compacts following a similar progression as figure 9. Arrows in figure (c.) correspond to Mo particles that have been completely converted to $MoSi_2$. The Mo particles show considerable fracture (figure (a.)) whereas the Si particles heavily strain. Adapted from Veccio et al. [94]

to this original work [95].

2.2.3 Reactivity under uniaxial stress loading

Reactivity in powder mixtures subjected to uniaxial stress loading differs from shock compression loading in that there is no outer confinement of the powder mixture. This leads to excessive flow and plastic straining of the constituents and also leads to pronounced localization phenomena. Reactivity will be mediated by the plastic deformation of soft phases leading to strain localization as well as bulk heating necessary to sustain chemical reactions. Recent works studying the reactivity of metal powder-based energetic materials under uniaxial stress have revealed the importance of strain localization and topological

connectivity [97] in promoting reactivity.

Ames [10] studied a variety of energetic materials systems and found that the intense localized shearing observed during high-strain-rate loading in a Taylor rod-on-anvil impact configuration was an essential precursor to initiating chemical reactions. The Taylor bar was made entirely of the pressed energetic powder mixture. High speed photography reveals the onset of a chemical reaction event near the shear band formed at the impact site during the mushrooming of the projectile (Figure 11). Nesterenko [98] demonstrated through controlled shear experiments unaided by shock compression that reactivity in Nb+Si powder samples was indeed possible by strain alone (the strain-induced mechanism). Meyers et al. [55] attribute the reactivity to the large energy of deformation localized in the shear bands which exceeds the threshold values proposed by Krueger and Vreeland [99, 100]. Unfortunately, these studies do not provide a time scale for reactivity and only infer the reaction mechanism based on post-shock observation, postulating a liquid-phase reaction mechanism.

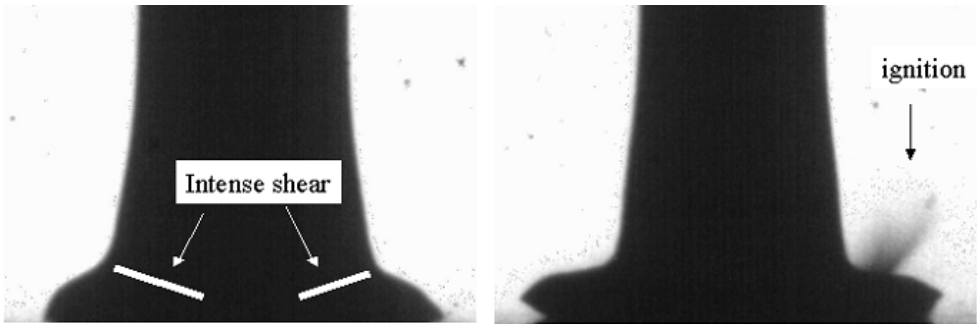

Figure 11: Photographic evidence of impact-induced chemical reaction showed ignition event happening until the onset of extreme shear localization (aided by uniaxial stress load geometry). Adapted from [10].

Du and Thadhani [101] studied the impact-initiated reactivity in a number of binary Al-based intermetallic-forming systems. They concluded that the chemical reactions (based on observed light emission) occurred during continued lateral straining of the reactive pellet beyond the consolidation point. The equilibrated stress between the anvil and pellet and the kinetic energy were found to not be independently controlling the reactivity. This showed

that the bulk straining and localization in the material were the most important factors leading to reactivity in this configuration.

Herbold et al. [26] presented corroborating evidence for the existence of a unique energy threshold for reaction initiation in ball-milled Ni+Al powder mixtures under uniaxial stress conditions. Pressed pellets of the Ni+Al mixture were mounted on a copper rod and fired as if in a modified Taylor setup. A chemical reaction was identified based on light emission observed in a framing camera. They found that there was a minimum reaction energy threshold for a certain ball-milling time and found the threshold to be lower for higher theoretical maximum density (TMD) compacts. This shows that pre-treatment of starting powders affects reaction initiation even if unaided by shock compression.

2.2.4 Current trends in shock-induced reactivity research

The intermetallic-forming Ni-Al system continues to be of great interest due to its energetic qualities and the attractive high-temperature properties of the Ni_3Al reaction product. A novel manufacturing approach has enabled Ni/Al laminates to be formed with precise bi-layer spacing (see for example [102]), exploiting the uniform contact between surfaces to enhance reactivity. These laminates have been found to be highly reactive at small (nano-scale) bi-layer spacings, possibly due to a more uniform availability of reactants in the system. A high-strain-rate event can cause localization phenomena due to the geometry of the system and the softening of the Al phase which likely mediates plastic deformation. The viscous dissipation near the localized region (shear band-like instabilities) is perhaps in competition with the interfacial phenomenon which behaves as an activation barrier to subsequent reaction [103].

Current interest in shock-induced reactions has focused on energetic materials, in particular MESMs. MESMs are relatively stable and only react when imparted with sufficient dynamic energy. These materials exploit the reactivity of the constituents and their relative

strengths, ultimately allowing for the tailoring of properties based on microstructural design. The National Research Council study of shock chemistry [104] highlighted the importance of continued research in the field of shock compression and the unanswered questions regarding the shock chemistry of powder precursors. It was noted that reactions in materials under shock loading can occur within the microsecond time scale of the peak-pressure regime of the shock and that the chemistry was enhanced due to transport processes such as material mixing due to extreme plastic flow [104, 12]. The design of MESMs depends on an understanding of these physical processes at the submicrosecond time scale. Studies into these mechanisms are complicated by the disparity in length and time scales and by the constitutive properties of the constituents, owing to the nucleation and growth processes during a chemical reaction, and the apparent role of shear on the reaction thermodynamics [48]. Nevertheless, accurate inferences of the reaction mechanisms in energetic materials can be made through a coupled experimental and computational approach, though lacking a generalized theoretical framework, as long as appropriate validation and correlations of the methods with experiments are made.

2.3 Thermodynamics of porous and distended composite mixtures

2.3.1 Ultrafast reactions - Thermodynamic models and computer simulations

The mechanisms governing the enhanced reactive state in a shocked material or the events leading to a reaction during the peak pressure state of the shock wave are still not understood. Various kinetic and phenomenological models have been developed based on metallurgical observations and existing continuum theory. Some thermodynamic models based on a Mie-Grüneisen correction to the inert Hugoniots of the powder mixtures have been developed to predict the shocked state during a shock-induced chemical reaction [15, 86, 87, 72, 24]. Many of these models depend on a pre-existing kinetic assumption and therefore do not consider the time-evolution of reaction-products using a true kinetic model. However, what is now known through experimental inference is that the complex

defect state created by a shock wave can induce a chemical reaction in the time scale of mechanical equilibrium [77, 105, 14, 12].

The first comprehensive phenomenological mechanism for such strain-induced reactions was given by the ROLLER model of Dremin and Breusov [64]. This model is based on mechanical displacement of two adjacent layers of material. If the traditional nucleation and growth kinetics are considered, the nucleating phase will arise between two moving layers of material and act as a kind of "roller" which traps constituent atoms of the adjacent materials, further increasing in size and concentration by acting as a mixer (Figure 12). Thadhani [12] notes that the time scale of electron shell rearrangement (around 10^{-13} s) is shorter than the time scale of atomic contact, indicating that atoms can indeed combine with the "roller" and form a new phase. The new phase forms through plastic deformation and enhanced mass transport without recourse to diffusion mechanisms.

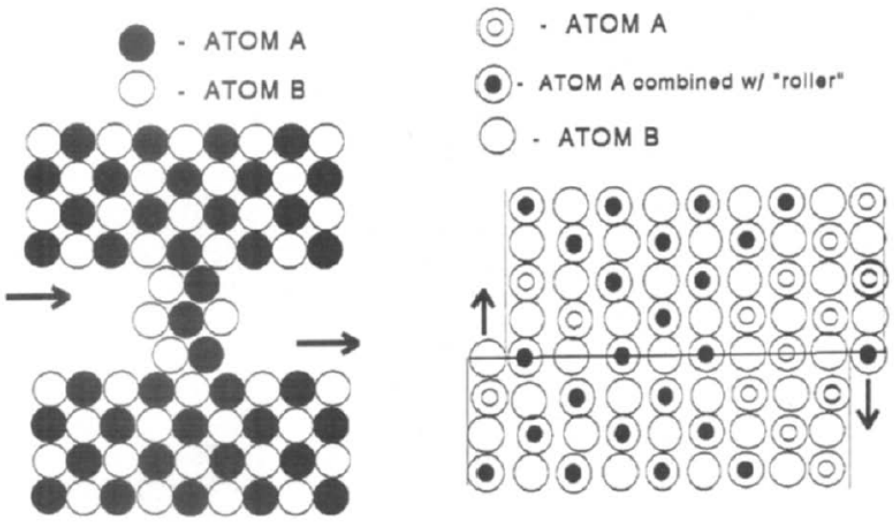

Figure 12: (a.) Schematic of the roller model where a small "roller" of nucleating material between two adjacent moving layers of material attracts and binds atoms without recourse to diffusive mechanisms. (b.) Top view showing multiple nucleation sites with rollers. Adapted from Thadhani [9].

The CONMAH model was developed by Graham [106] following the observation of the mechanochemical effects of the shock wave on the material. Although the ROLLER model

gives a satisfactory depiction of localized processes, large scale chemical reactivity is only possible through the coordinated mass transport facilitated through rapid plastic deformation. The passage of a shock wave leads to a great amount of energy release which can lead to localized melting at particle interfaces, polymorphic phase transformations (both high pressure and high temperature phases), defect formation, and chemical reactions. The reconfiguration of the reactant materials during shock loading along with the formation of defects greatly affect the solid state reactivity during shock loading. Graham's CONMAH model summarizes these important phenomenological effects caused by the shock wave via the following processes [106]:

- **CON**figurational changes in particle morphology and in crystal structure
- **M**ass mixing where particles are forced together and relative motion and friction enhances energy transport.
- **A**ctivation where the configurational changes and generation of defects lead to highly reactive structure.
- **H**eating due to strain localization and temperature gradients through the shocked medium.

2.3.2 Continuum thermochemical models

The first reaction kinetics model for shock-induced reactions was developed by Maiden and co-workers [107] inspired by the reactive flow model of Nutt [108] and applied to the Ti + 2B reaction. This model employed the mass fraction of the reactants as an internal state variable for the total energy. It considered the evolution of the mass fraction λ as an Arrhenius process [107, 9, 16] and coupled the kinetic evolution of the mass fraction with the conservation equations:

$$\frac{\partial \lambda}{\partial t} = k_N \lambda^N \exp\left(-\frac{E}{RT}\right), \tag{1}$$

where the pre-exponential factor k_N depends on the diffusion coefficient, N denotes the order of the reaction, and the variables E, R, and T take on the usual definitions of activation energy, gas constant, and temperature, respectively. The model also considers a separate equation for pressure evolution assuming a homogeneous decomposition of pressure contributions due to volumetric expansion and chemical changes. The reaction initiation mechanism in this model is governed by the thermal energy due to pore collapse, thus creating "hot-spots" where reactions potentially occur. Maiden and Nutt [109] subsequently developed a heterogeneous model based on this "hot-spot" assumption, triggering reaction when the surface temperature of a void reached a specified threshold. This model was contested by Enikolopyan et al. [110] who considered reaction initiation to be governed by the unique processes occurring during high-strain-rate loading irrespective of thermal mechanisms. These authors believed that it was the rapid mixing and mechanical disintegration [72] that led to reactivity based on observations that these shock-induced reactions occurred rapidly for both strongly *and* weakly exothermic systems without regard to the initiation temperature.

Horie and Kipp [23] developed a homogeneous phenomenological model describing the combined effects of dispersive mixing with the temperature and pressure that occurred during the passage of a shock wave. This model combines the law of mass action for the rate laws with a turbulent mixing reactor scheme and considers a possible transition phase leading to the final stable product from a shock-induced reaction. A strain rate dependence is included in the Arrhenius definition of the rate constant. Figure 13a shows a schematic of the model considering the passage of a shock wave through binary material with a void. Inhomogeneous temperature contributions to chemical reactivity were later added to the model by Taylor et al. [111]. Horie and co-workers subsequently developed what came known to be the VIR (voids, inactives, reactives) model [112, 16] which takes into account a system of voids, inactive materials, and reactive materials under pressure equilibrium (figure 13b, top). The system is considered closed, but heat transfer is permitted within

the components of the system in the extended version of the model, which is refined to better capture the dispersed wave mechanics due to heat transfer during reaction (figure 13b, bottom) The VIR model includes constitutive modeling of pore collapse through the $P-\alpha$ model of Hermann [113] and a description of chemical reactivity based on the original Horie-Kipp model [23]. This model essentially takes into account the internal quenching of the reactive species by the non-reactive species through thermal exchange, which is a feature not present in the original formulation. Figure 14a shows the extended VIR model simulating the reflected pressure profile in a Ni/Al experiment with remarkable fidelity.

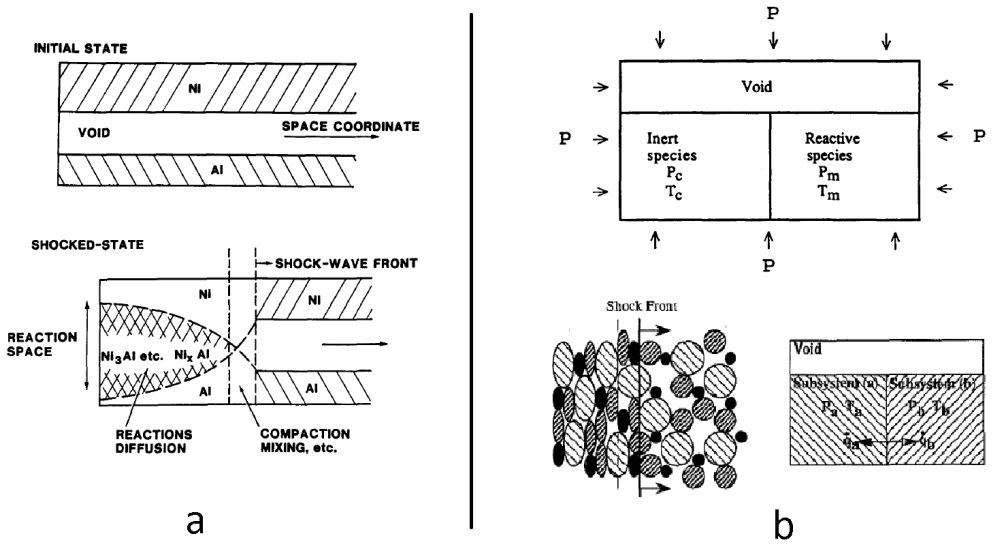

Figure 13: (a.) One-dimensional representation of the phenomenological model developed by Horie and Kipp [23]. The one-dimensional slab consists of Ni and Al with a void in the center. The void serves as a space for mass-mixing to take place and subsequently collapses under the action of the shock pressure. The resulting non-equilibrium mixture will react if the appropriate thermochemical conditions are met. (b.) Schematics of a VIR (top) and Extended VIR (bottom) reactor cells where inactive and reactive species can exchange heat and mix within a void area

Horie et al. [16] argue that due to the high exothermic energy release from synthesis reactions occurring during shock compression, there is little kinetic barrier opposing reactivity and once initiated, the reactions tend to go to completion. Therefore, any kinetic activation barriers serve only as initiation barriers and subsequently can be ignored, similar to Boslough's hot-spot criterion [72]. This permits the kinetic models to be applied without

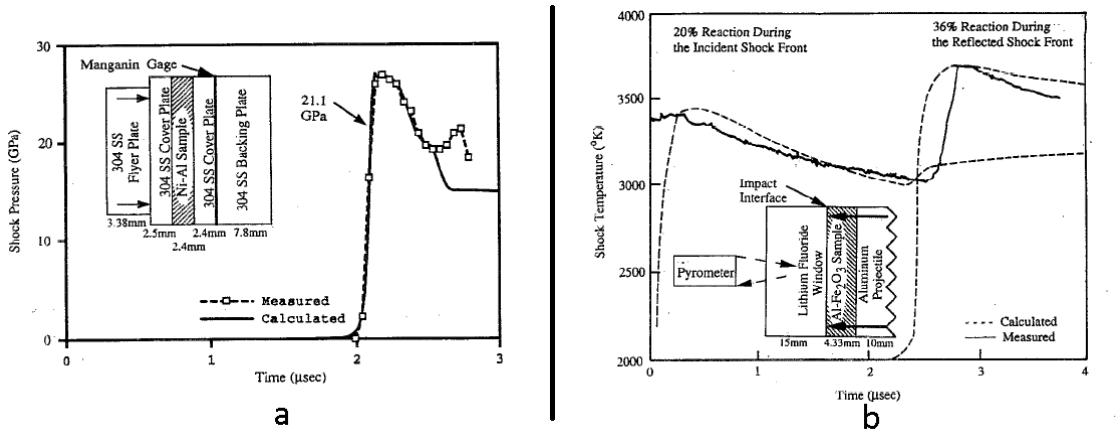

Figure 14: (a.) Simulated reflected pressure profile for the capsule setup (inset) as shown. The Extended VIR model prediction is in remarkable agreement with the experimental data reproducing the peak excess pressure condition. (b.) Predicted and measured (pyrometry) temperature profiles for the Al-Fe_2O_3 thermite system [72] again showing remarkable agreement. Chemical reactions accounted for the high bulk temperatures and the deviation from the inert calculations by Boslough.

remorse when analyzing the shock-induced reactions in powder compacts. Although the models show excellent agreement with experiments (at a condition with known excess pressure), they do not take into account the heterogeneous nature of the compact, instead resorting to a bulk continuum description and pore collapse through a phenomenological model. The chemistry is also not taken into account properly (law of mass action descriptions based on molar concentration, rather than activity) and thus the models should be used with caution when dealing with highly heterogeneous systems or systems with multiple or complex reaction pathways. Horie describes a heterogeneous reactive flow as a probable source for shock-induced chemical reactions [17]. This model was implemented in a continuum framework similar to his VIR model and reveals a dependence on extrinsic properties for such heterogeneous flow to lead to reactions. It also reveals that the hydrodynamic phenomena associated with shock compression can reduce the prevailing length scales through surface instabilities at particles, making it possible for even diffusion-controlled processes to prevail.

Two main schools of thought have been adopted to explain the initiation phenomena

in reactive materials under shock loading [55]: a solid-solid mechanism where reactions are driven by mechanochemical transport phenomena, and a solid-liquid mechanism which relies on the thermochemical energy release to be greater than the melting point of a constituent material. The efforts of Krueger et al. [114, 100, 99] showed that chemical reactivity occurred at a characteristic shock energy threshold, independent of the shock pressure. They observed minor surface reactions at energies below the threshold and nearly complete reaction for energies above the threshold in the Ni-Si system. These conclusions were substantiated by Meyers et al. [94, 95, 55] for the Nb-Si system. Localized melting of Si established the threshold energy and the proposed mechanism for product formation was a nucleation and growth phenomena. Furthermore, Vecchio et al. [94] observed that particles of $NbSi_2$ were constantly being nucleated and ejected from surfaces of Nb, indicating that an interphase boundary did not form and thus did not inhibit the reactivity. This is in stark contrast to the proposed mechanisms espoused in the ROLLER and CONMAH models which depend on solid-state mass mixing from the shock to initiate a reaction.

Recent work by Do and Benson [115] develops a computational framework for modeling chemical reactions using the discrete particle method (DPM). The chemical kinetic model was inspired by Kee et al.'s [116] CHEMKIN software package. These authors obtained a deformation structure for a uniaxial strain configuration of particles and also simulated the growth and evolution of reaction fronts using the kinetic models adopted. Figure 15 shows their results indicating the increase in reaction product over time reaching a saturation point. This model assumes the kinetics and employs the law of mass action (composition-based) in calculating the properties of the shocked material. However, the mechanism is improperly accounted for since the kinetics are assumed and only one reaction pathway is considered (no phase changes in the constituents).

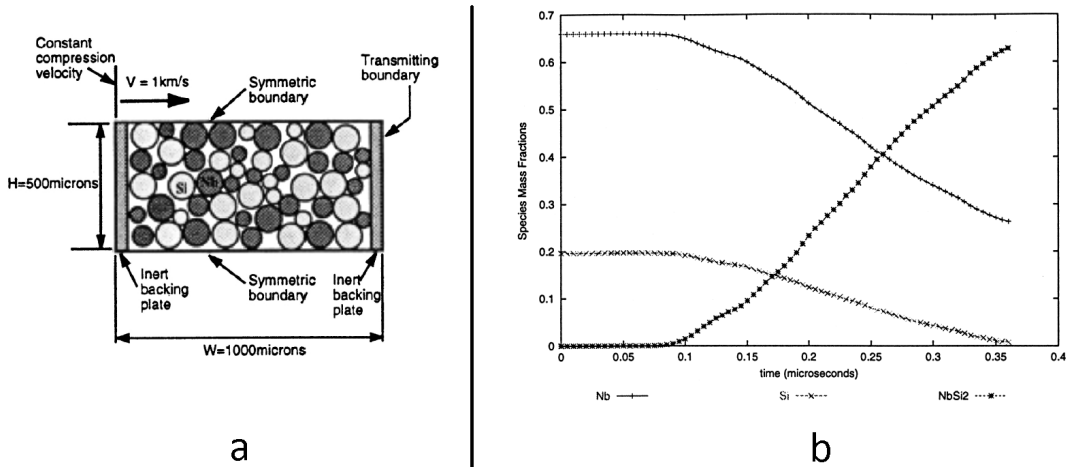

Figure 15: (a.) Model problem for Do and Benson's reactive discrete particle simulations at the meso scale (idealized particles). (b.) Concentration profiles showing exchange of constituents . Adapted from Do and Benson [115].

2.3.3 Recent developments and unresolved issues

Recent works by Eakins and Thadhani [19] have shown the effects of particle morphology and orientation on shock-induced reactions. They found that shock-induced chemical reactions depended on heterogeneous phenomena such as particle fracture, cleansing of surfaces, and void collapse and mixture. Meso-scale simulations [21] revealed complex hydrodynamic phenomena occurring during rapid deformation. A distinct size effect has been observed for mixtures of Ti and Si powders [42]. Dissipative mechanisms such as fracture were observed for coarse particle sizes (105-149 μm) while clustering was observed for fine particle sizes (< 10 μm), both inhibiting reaction. The intermediate particle sizes showed greater deformation and mixing, indicating an optimal particle size leading to reaction. This work served as a confirmation of the CONMAH model posited by Graham [106]. Herbold et al. [26] provided corroborating evidence for the existence of a unique energy threshold for reaction initiation in ball-milled Ni+Al under uniaxial stress conditions. They found that there was a minimum reaction energy threshold for a certain ball-milling time and found the threshold to be lower for higher theoretical maximum density (TMD) compacts. This shows that pre-treatment of starting powders affects reaction initiation even

if unaided by shock compression.

Although many satisfactory phenomenological and kinetic models exist, there still remain unresolved issues regarding the mechanisms governing reactivity and transformation of shocked materials. Also, previous studies do not reveal the time scale of reaction initiation and propagation since they depend on post-mortem analysis and theoretical calculation of the pressure and temperature conditions during reaction. The indirect observation of reaction through the Hugoniot shift or the excess pressure provides no indication of reaction pathway or extent. These models instead presuppose reaction goes to completion or assume an arbitrary reaction time. The phenomena occurring at the meso-scale is a combination of hydrodynamic mixing, geometric and material instabilities, and dissipative mechanisms. Reactions likely initiate through some interfacial mechanism, mediated by a liquid or solid state equilibria depending on the load state, and either quench or propagate depending on the stability of the reaction front.

It is believed that shock-induced reactions strongly depend on these contributing mechanisms and that microstructures can be tailored to optimize reactivity [13]. There is still no clear understanding of the reaction initiation mechanisms and their mechanochemical or thermochemical origins. Furthermore, the current models do not consider the hindrance of the reaction front by the formation of a reaction-product interface. Future efforts should be directed at addressing these issues so that the mechanisms preceding reaction initiation may be found, which also requires consideration of the micro-scale processes occurring near the interfaces during shock loading. The work presented in this dissertation aims to investigate this length scale along with the meso-scale processes that are affected by these micro-scale phenomena. An assessment of the manifested wave mechanics resulting from a shock-induced reaction will be also be provided.

CHAPTER III

BACKGROUND IN SHOCK COMPRESSION AND HIGH-STRAIN-RATE SCIENCE

This chapter presents the scientific background on shock compression science, starting with the derivations of the Rankine-Hugoniot jump conditions for solids under shock compression. These relations stem from the conservation relations and are completely general. The thermodynamics of powder mixtures under shock compression are discussed both for inert and reactive mixtures. The equations of state (EOS) and phenomenological compaction models used in the present work are discussed. A survey of various equation of state (EOS) models and phenomenological compaction models is provided, along with the thermodynamic models for shock-induced chemical reactions of the "Ballotechnic" form. The chapter concludes with a brief survey on the theory of errors employed in this work. The purpose of this chapter is to introduce the reader to the relevant background necessary to explore powder mixtures under shock compression and serves as a refresher. The reader familiar with shock compression science can skip this chapter and proceed directly to the next chapter.

3.1 Shock Compression of Solids

A shock wave is rigorously defined as a traveling discontinuity in a continuous medium induced by the sudden dynamic compression of said medium well into the plastic regime (or in the case of gases, into the highly-compressed regime). In solids, this is preceded by a non-conservative event whereby the dynamics induce permanent material deformation, i.e. the transformation of kinetic energy into permanent deformation with concomitant heating and entropy production in the material. A shock wave travels into the medium

and with it a discontinuous thermodynamic state, where state variables such as pressure, internal energy, and density vary in a near-discontinuous manner from their nascent values prior to the arrival of the wave. The conservation relationships still hold at the wave interface with modifications (the Rankine-Hugoniot jump conditions) and can be used to relate these thermodynamic variables through closure with an equation of state (EOS). The near-discontinuous nature of this wave is such that there is insufficient time for long range diffusion of atomic species to take place [3], and the rise time to the new thermodynamic state (i.e. the time that it takes to get to 90% of the equilibrium state achieved behind the shock) is incredibly fast, and is usually less than 100 ns [3].

In solid materials, any sudden loading is transferred hyperbolically as wave characteristics which travel at a specific limiting speed[1]. This speed depends on whether the underlying structure of the material is modified by the loading. The shock speed in the material is mediated by the bulk compressibility and is pressure-dependent. The elastic speed (the wave speed of a material that is not crystallographically modified and still within the elastic regime) is mediated by the elastic modulus and density of the material. However, porous and heterogeneous materials are typically a mixture of phases and the situation becomes more complex. Composite properties are used to predict the limiting wave speeds in these materials and are usually a first-order estimate; experiments are necessary to fully quantify the shock response of heterogeneous composite solids. Nevertheless, the knowledge of shock compression in solids will be extrapolated to these situations in this work in an attempt to better understand these complex materials, at least through the lens of the simpler thermodynamic framework of solids.

Because the material is compressible, a compression caused by a piston will create a highly compressed region[2] where the front disturbance ahead of the piston will travel at a

[1]The sound speed of the material, or the shock speed depending on the deformation state and compressibility of the material

[2]The compression is mediated by the compressibility of the material $|\partial P/\partial V|$, which can only promote a shock wave if the compressibility goes up as the stress P goes up [3].

velocity U_s faster than the material behind the disturbance, which is still constantly being compressed by the piston. This material will move at a velocity U_p which matches the velocity of the piston itself. This inertial separation between the propagating discontinuity and the material moving behind it is due to the continual addition of compressed material to the already compressed region [3]. The situation becomes complicated when dealing with powders or granular/porous materials because there are multiple regions and interfaces where the waves can reflect and therefore not fully develop into this inertially dissociated region of compressed material and traveling discontinuity. The front itself will have a structure associated with the distribution of constituents, their morphology, and the kinetics of densification (i.e. crush strength and dissipation associated with compaction) [7] and will not be perfectly discontinuous, in some cases dispersed over as much as 1 μs in the case of coarse ($\sim$ 400 μm) sand[3]. Nevertheless, theories based on this framework have been developed for powders and will be discussed herewith.

This chapter presents an overview of the theory of shock compression of solids and porous mixtures. A detailed exposition of pertinent equations presented in chapter 2 is presented to develop context for the investigation of the shock compression of Ti/Al/B reactive powder mixtures. It is by no means a complete exposition, but every attempt will be made to outline the pertinent equations that are employed in this work as well as their limitations. The conservation relations (i.e. the Rankine-Hugoniot jump conditions) are first formulated and presented as applied to solid materials, and are further extended to porous solids. The treatment of shock waves in powder mixtures and porous solids is further discussed in section 3.3.2 and the current models for the equations of state for powder mixtures are provided. Next, the thermodynamics of shock-induced chemical reactions and the predictive models used to estimate the product Hugoniot for a reacting mixture under shock compression are discussed in section 3.4. This chapter concludes with a word on statistical analysis as it was applied in this work.

[3] G. Kennedy and N. N. Thadhani unpublished results, Georgia Tech, 2014

3.2 Conservation relations in shock waves

This section will develop the conservation relations and implement them for the special case of a shock wave. The conservation relations are ubiquitous and essentially axiomatic, and are based on the assumption that certain field quantities can be defined as single-valued continuous functions over the spatial domain of interest. The field quantities of interest are displacement, velocity, acceleration (displacement-based quantities), pressure/stress (force-based quantities), and temperature and density (thermodynamic continuum-level quantities linking the statistical mechanics of a large number of moving particles).

Consider a one-dimensional body Ω that has been stressed such that the rapid application of the load caused a moving discontinuity to form in the body. Any applied stress will travel throughout the body in the form of a characteristic due to the form of the conservation of momentum (to be derived below). At the continuum level, the conservation relations are assumed to be valid and to govern all field variables in the domain of interest, in this case, some material medium Ω. If the stress applied to the body is rapid and high enough, a shock wave may form where the material behind the traveling wave will be at a higher stress, velocity, density, etc. relative to the material ahead of the way. This variation is nearly discontinuous, as is shown in figure 16.

3.2.1 Conservation of Mass

The conservation of mass, for example, asserts the balance of mass in an open system with accumulation, assuming that a piecewise continuous function of density $\rho = \rho(\mathbf{x}, t)$ exists and fills some volume of space Ω [117]. The density is a measure of how matter is distributed across the space Ω, where $\Omega \in \mathbb{R}^3$. The total mass in the space for a distribution of matter $\rho(\mathbf{x}, t)$ is:

$$M = \int_{\Omega} \rho(\mathbf{x}, t) d\Omega. \tag{2}$$

If matter is changing in some way, the rate of increase of total mass as a result of this

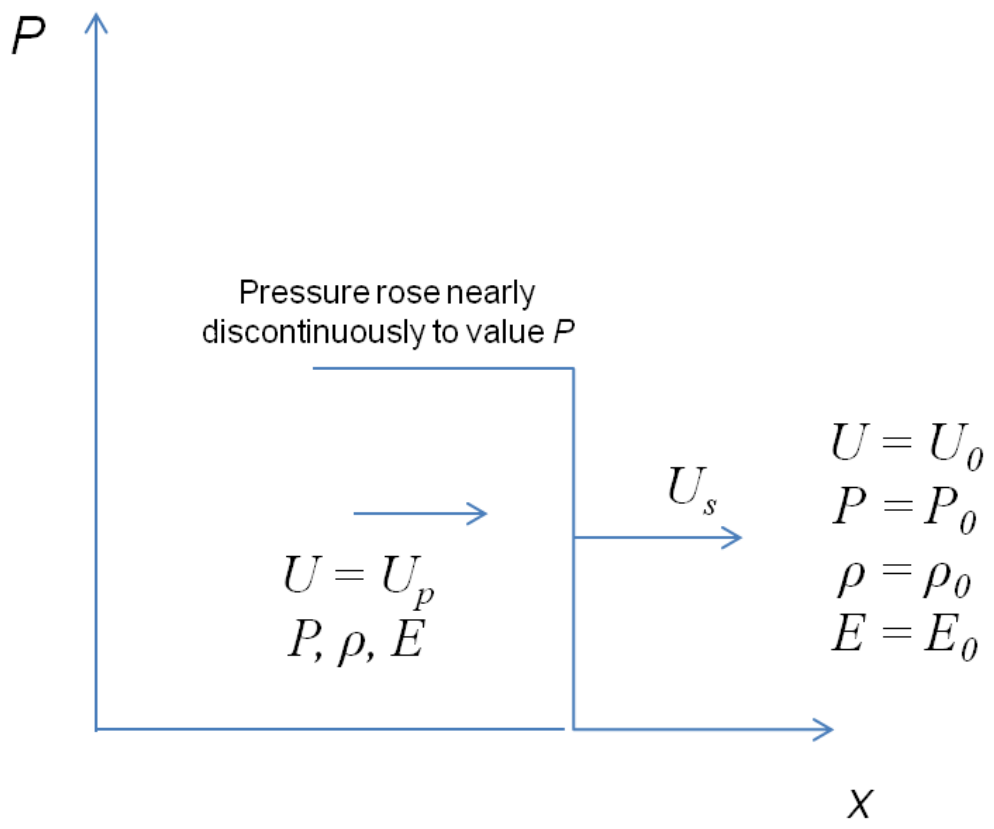

Figure 16: Consider the stress amplitude plotted over the distance through a continuous medium. After a sufficiently large and rapid application of load on a material, a shock wave will develop which is a traveling discontinuity in thermodynamic state variables. The state variables behind the shock wave depend on the conservation relations and an equation of state.

change is:

$$\frac{\partial M}{\partial t} = \int_{\Omega} \frac{\partial \rho(\mathbf{x}, t)}{\partial t} d\Omega. \tag{3}$$

However, if there is no change in mass, i.e. if mass is not created or destroyed in the space Ω, then the rate of increase in mass must equal the rate of mass inflow through the surface Γ.

The mass efflux across the bounding surface of the medium volume is based on the movement of material with a spatial velocity field v. The material moving across some infinitesimal area $d\Gamma$ having a normal vector $\mathbf{n}$ is carried by the velocity field v whose

component is in the normal direction (with a negative sign to reinforce the fact that it is a mass outflow):

$$-\rho v_n dS = -\rho \mathbf{v} \cdot \mathbf{n}. \tag{4}$$

Therefore, the total amount of mass outflow through the entire bounding surface is:

$$-\int_\Gamma \rho v_n d\Gamma = -\int_\Omega \nabla \cdot (\rho \mathbf{v}) d\Gamma, \tag{5}$$

where the last term arises from the divergence theorem. Since the rate of mass inflow must equal the rate of mass outflow, equating terms gives:

$$-\int_\Omega \nabla \cdot (\rho \mathbf{v}) d\Gamma = \int_\Omega \rho(\mathbf{x}, t) d\Omega, \tag{6}$$

or:

$$\int_\Omega \left[\rho(\mathbf{x}, t) + \nabla \cdot (\rho \mathbf{v})\right] d\Omega = 0 \qquad \forall d\Omega. \tag{7}$$

This expression is valid for all possible integration volumes, and can thus only be true if the integrand is exactly zero, i.e.

$$\frac{\partial \rho}{\partial t} + \nabla \cdot (\rho \mathbf{v}) = 0, \tag{8}$$

or in indicial notation:

$$\frac{\partial \rho}{\partial t} + \frac{\partial (\rho v_i)}{\partial x_i} = 0, \tag{9}$$

where the density of the material ρ is a continuous function of space and time – $\rho = \rho(x, y, z, t)$ and v is the spatial velocity of the medium[4].

[4]More details on the difference between material and spatial coordinates can be found in Malvern's text [117]

3.2.1.1 *Conservation of mass in a shock wave*

In the case of a discontinuous change in state variables, the continuity equation 8 must take into account a moving discontinuity at velocity U_s relative to the disturbed material moving at a different material velocity U_p which propagates into a medium moving at a velocity U_0. Considering the shock wave front as the moving reference frame, the mass of material exiting the wave (to the left of the shock front in figure 16) will have a new density ρ and will be moving at a velocity $U_s - U_p$ relative to the shock front. This mass will be the product of the density and the amount of volume traversed in time δt, which is equal to the cross-sectional area multiplied by the velocity and time: $\rho A(U_s - U_p)\delta t$. The amount of material entering the shock front (the nascnent material that is being compressed) has an initial density ρ_0 and may be moving with an initial velocity U_0. Mass conservation must be satisfied (eq. 8), which for a one-dimensional case, simplifies to equating the mass entering and leaving the front. Considering the mass conservation through the shock wave as the moving reference frame, the general expression becomes (after cancelling the cross-sectional area and δt terms which are the same across the shock front) [118]:

$$\rho_0(U_s - U_0) = \rho(U_s - U_p). \tag{10}$$

This equation is completely general and valid for any infinitely sharp discontinuity in thermodynamic state. It is used as an approximation to the highly dispersed compressed states observed in this work in the context of distended powder mixtures.

3.2.2 Conservation of Momentum

The conservation of momentum relates the momentum change of a body to an applied impulse. This equation can be cast in differential form relating incremental stresses applied to a body and a variety of forces. The force equilibrium on a body must be such that all external forces must add to the product of the body's mass and its acceleration (Newton's second law). If the forces are applied over some time δt, then a momentum change must

occur. In the case of a shock wave, the thermodynamic pressure changes discontinuously from P_0 to P, and thus a momentum change must follow.

Impulse is defined as:

$$\int F(t)dt, \tag{11}$$

which equals $(P - P_0) \cdot A \cdot \delta t$ in the case of a shock wave. This must equal the momentum change:

$$\rho A \delta t (U_s - U_p) U_p - \rho_0 A \delta t (U_s - U_0) U_0. \tag{12}$$

Equating terms gives:

$$\rho A \delta t (U_s - U_p) U_p - \rho_0 A \delta t (U_s - U_0) U_0 = (P - P_0) \cdot A \cdot \delta t, \tag{13}$$

whereupon cancellation of common terms yields:

$$\rho (U_s - U_p) U_p - \rho_0 (U_s - U_0) U_0 = (P - P_0). \tag{14}$$

This equation is commonly combined with the conservation of mass to obtain the typical form of the conservation of momentum by noting that $\rho_0 U_s = \rho(U_s - U_p)$:

$$\rho_0 U_s U_p - \rho_0 (U_s - U_0) U_0 = (P - P_0). \tag{15}$$

If the initial momentum is zero (stationary body impacted by a shock wave), the equation becomes:

$$P - P_0 = \rho_0 U_s U_p. \tag{16}$$

This is the form of the conservation of momentum that will be used to analyze the compressed state of the powder in this work.

3.2.3 Conservation of Energy

The conservation of energy considers the work done by all external forces balancing the internal energy and the kinetic and potential energies:

$$\Delta E = \Delta KE + \Delta PE + \sum \Delta W, \tag{17}$$

where ΔE represents the change in internal energy of the system, KE and PE are the kinetic and potential energies of the system, and $\sum \Delta W$ is the sum of all sources of work done on to/by the system. This is similar to the classic definition of the First Law of Thermodynamics:

$$dE = \delta Q - \delta W, \tag{18}$$

where the differential δ denotes path dependence, i.e. the total differential of internal energy E, path independent by definition of a total differential (Pfaffian form), can be composed of path dependent changes in heat Q and work W. The work done by the passage of the shock wave is composed of the force term (PA) and displacement ($U\delta t$). Using intensive quantities, each term becomes [3, 118]:

$$\Delta KE = KE_2 - KE_1 = \frac{1}{2}[\rho A(U_s - U_p)\delta t]U_p^2 - \frac{1}{2}[\rho_0 A(U_s - U_0)\delta t]U_0^2, \tag{19}$$

$$\Delta PE = 0^5, \tag{20}$$

$$\Delta E = EA\rho(U_s - U_p)\delta t - E_0 A\rho_0(U_s - U_0)\delta t, \tag{21}$$

$$\Delta W = PAU_p\delta t - P_0 AU_0\delta t. \tag{22}$$

[5] No electromagnetic, or gravitational effects considered

Equating terms in the conservation of energy (eq. 17) yields, after taking $U_0 = 0$:

$$PAU_p\delta t = \frac{1}{2}\rho A(U_s - U_p)\delta t U_p^2 + EA\rho(U_s - U_p)\delta t - E_0 A\rho_0 U_s \delta t. \tag{23}$$

Cancelling like terms ($A\delta t$) gives:

$$PU_p = \frac{1}{2}\rho(U_s - U_p)U_p^2 + E\rho(U_s - U_p) - E_0\rho_0 U_s. \tag{24}$$

The common form of the conservation of energy in a shock wave is obtained by modifying this general form noting that the conservation of mass must also apply:

$$PU_p = \frac{1}{2}\rho_0 U_s U_p^2 + \rho_0 U_s(E - E_0). \tag{25}$$

Re-arranging the equation by dividing through by $\rho_0 U_s$ to isolate the energy term gives:

$$E - E_0 = \frac{PU_p}{\rho_0 U_s} - \frac{1}{2}\rho_0 \frac{U_s U_p^2}{\rho_0 U_s}. \tag{26}$$

Invoking the conservation of momentum, eq. 16 for the U_p term gives:

$$E - E_0 = \frac{P(P - P_0)}{(\rho_0 U_s)^2} - \frac{1}{2}\frac{(P - P_0)^2}{(\rho_0 U_s)^2}, \tag{27}$$

thus obtaining a common denominator. Considering again the conservation of mass:

$$\rho_0 U_s = \rho(U_s - U_p) \tag{28}$$

$$\frac{\rho_0 U_s}{\rho} = U_s - U_p \tag{29}$$

$$U_p = U_s - \frac{\rho_0 U_s}{\rho} \tag{30}$$

and the conservation of momentum:

$$P - P_0 = \rho_0 U_s U_p \tag{31}$$

$$U_p = \frac{P - P_0}{\rho_0 U_s} \tag{32}$$

$$\therefore \quad U_p = \frac{P - P_0}{\rho_0 U_s} = U_s - \frac{\rho_0 U_s}{\rho} = \frac{U_s(1 - \rho_0)}{\rho}. \tag{33}$$

Isolating the $\rho_0 U_s^2$ term by rearranging equation 33 gives:

$$\rho_0 U_s^2 = \frac{-\rho(P - P_0)}{\rho_0 - \rho}. \tag{34}$$

The specific volume is by definition the inverse of density, i.e. $1/\rho = V$. Substituting gives:

$$\rho_0 U_s^2 = \frac{-(P - P_0)}{V(1/V_0 - 1/V)} \tag{35}$$

$$= \frac{-(P - P_0)}{(V - V_0)/V_0} \tag{36}$$

$$= \frac{(P - P_0)}{(V_0 - V)/V_0} \tag{37}$$

$$= \frac{(P - P_0)}{\rho_0(V_0 - V)}, \tag{38}$$

and thus:

$$(\rho_0 U_s)^2 = \frac{(P - P_0)}{(V_0 - V)}, \tag{39}$$

which is the slope of the Rayleigh line drawn in $P - V$ space. This equation is substituted back into equation 27 to obtain:

$$E - E_0 = \frac{P(P - P_0)}{(P - P_0)} \cdot (V_0 - V) - \frac{1}{2}\frac{(P - P_0)^2}{P - P_0} \cdot (V_0 - V) \tag{40}$$

$$\therefore \quad E - E_0 = \frac{1}{2}(P + P_0)(V_0 - V), \tag{41}$$

which is the commonly-used form of the conservation of energy. Equation (41) is integral to this work, as it is the partition of energy between the compaction of the loose powder

and the shock compression that leads to the complex behavior of powder mixtures (i.e. the long rise-times and dispersed wave fronts) under shock compression. The conservation equations are completely general and there are five variables [3]: pressure P, material (particle) velocity U_p, shock velocity U_s, specific volume V, and energy E. Thus, a fourth equation is necessary for closure. This equation is in the form of a thermodynamic equation of state (EOS) which relates state variables, usually $U_s - U_p$ or some other equation. These equations are dealt with in the next section.

3.3 Thermodynamics of Shock Waves in Powder Mixtures

The thermodynamic and mechanical properties of materials are important variables when considering the shock compression of solids. The compressibility of a solid material indeed gives rise to the steep shock front observed upon rapid and strong compression. The conservation equations require an additional expression connecting thermodynamic state functions to provide a complete description of the solid under shock compression. This additional expression is in the form of an equation of state, typically relating the pressure to the volume and energy or temperature of the material on some thermodynamic surface, typically on a Hugoniot (locus of shocked states), isentrope, isotherm, etc. The equation of state can connect a locus like the Hugoniot to some other thermodynamic path. This equation is usually taken as the linear relationship between U_s and U_p, and many materials show this behavior, although Kerley has recently written a counter-argument to this paradigm [119] which should be critically assessed. Still, the linear $U_s - U_p$ relation remains a powerful tool used by many researchers.

The popular Mie-Grüneisen equation of state relates the pressure and internal energy thermodynamic states of two paths (typically an isotherm and a Hugoniot) through an isochore:

$$P_H - P_T = \frac{\Gamma}{V}(E_H - E_T) \tag{42}$$

where the subscripts H and T refer to the Hugoniot and Zero-Kelvin Isotherm of the material and the constant Γ is the Grüneisen constant which is defined by:

$$\Gamma = V\left(\frac{\partial P}{\partial E}\right)_V = \frac{3\alpha}{C_v \beta_T}, \tag{43}$$

where α is the linear thermal expansion coefficient (hence the factor of three to obtain the volumetric expansion coefficient), C_v is the specific heat at constant volume, and β_T is the isothermal compressibility, which is the inverse of the isothermal bulk modulus:

$$\beta_T = \frac{1}{K_T}. \tag{44}$$

Other analytical equations of state exist which relate the pressure to the bulk modulus. One such equation is the Murnaghan equation [16]:

$$-V\left(\frac{\partial P}{\partial V}\right)_T = K_T = K_{T0}\left(\frac{V_0}{V}\right)^n, \tag{45}$$

which can be integrated on the isotherm to give the pressure as a power function in the relative volume V_0/V:

$$P_T = P_0 + \frac{K_{T0}}{n}\left[\left(\frac{V_0}{V}\right)^n - 1\right]. \tag{46}$$

Horie and Sawaoka [16] derived the thermodynamically-consistent EOS from the Murnaghan equation and the entropy function:

$$ds = \left(\frac{\partial s}{\partial V}\right)_T dV + \left(\frac{\partial s}{\partial T}\right)_V dT, \tag{47}$$

recalling the Maxwell relations:

$$\left(\frac{\partial s}{\partial V}\right)_T = \left(\frac{\partial P}{\partial T}\right)_V = \left(\frac{\partial P}{\partial E}\right)_V \left(\frac{\partial E}{\partial T}\right)_V, \tag{48}$$

and:

$$\left(\frac{\partial P}{\partial E}\right)_V = \frac{\Gamma}{V} \tag{49}$$

$$\left(\frac{\partial E}{\partial T}\right)_V = T\left(\frac{\partial s}{\partial T}\right)_V = C_v \tag{50}$$

$$\therefore \quad ds = \frac{\Gamma}{V} C_v dV + \frac{C_v}{T} dT \tag{51}$$

From the definition of the Helmholtz Free Energy F

$$dF = \left(\frac{\partial F}{\partial V}\right)_T dV + \left(\frac{\partial F}{\partial T}\right)_V dT \tag{52}$$

$$= -PdV - sdT, \tag{53}$$

integration yields the following expression for free energy:

$$\begin{aligned} F = F_0 + P_0(V_0 - V) + \frac{K_{T0}V_0}{n(n-1)}\left[\left(\frac{V_0}{V}\right)^{(n-1)} + (n-1)\frac{V}{V_0} - n\right] - s_0(T - T_0) \\ + C_v\left\{(T - T_0)\left[1 + \left(\frac{\Gamma}{V}\right)_0 (V_0 - V)\right] + T\ln\frac{T_0}{T}\right\}, \end{aligned} \tag{54}$$

whereupon derivation gives the following EOS for pressure:

$$P = \left(\frac{\partial F}{\partial V}\right)_T = P_0 + \frac{K_{T0}}{n}\left[\left(\frac{V_0}{V}\right)^n - 1\right] + C_v\left(\frac{\Gamma}{V}\right)_0 (T - T_0). \tag{55}$$

This equation may be related to the Hugoniot state of the material by application of the Mie-Grüneisen EOS.

3.3.1 Thermodynamics of inert mixtures under shock compression

An inert mixture equation of state is necessary to predict the possible shock state of a powder mixture fully compacted by the shock wave. The inert mixture equations of state depend on the homogeneity of thermodynamic extensive quantities, specifically:

$$E = \sum_i m_i e_i \tag{56}$$

$$V = \sum_i m_i v_i \tag{57}$$

$$M = \sum_i m_i, \tag{58}$$

where intensive state variables are represented by lowercase letters, and the variable m_i denotes the mass of the i^{th} constituent in the mixture. The energy, $E = E(S, V, n_i)$ where n_i is the mole number of constituent i, can be defined as an Euler homogeneous function:

$$E(\lambda s, \lambda V, \lambda n_i) = \lambda E(s, V, n_i). \tag{59}$$

For homogeneous functions of degree 1 ($\lambda = 1$), the Pfaffian derivative of the energy functional gives:

$$dE = \left(\frac{\partial E}{\partial s}\right)_{V,n_i} ds + \left(\frac{\partial E}{\partial V}\right)_{s,n_i} dV + \left(\frac{\partial E}{\partial n_i}\right)_{s,V} dn_i, \tag{60}$$

which can be related to measurable state variables [120, 16, 121]:

$$\left(\frac{\partial E}{\partial s}\right)_{V,n_i} = T, \qquad \left(\frac{\partial E}{\partial V}\right)_{s,n_i} = -P, \qquad \left(\frac{\partial E}{\partial n_i}\right)_{s,V} = \mu_i. \tag{61}$$

Similar relationships can be determined for all thermodynamic functions using the appropriate Legendre transform and Maxwell relation. These derivations can be found in any standard text on chemical thermodynamics [120, 16, 121]. The thermodynamic relationships are used when developing appropriate thermodynamic models for mixtures and are completely general.

A mixture EOS can be formulated through a linear combination of contributions from the constituents to some state variable. The extensivity of state variables allows for the linear combination of specific volumes by mass fraction. McQueen et al. [122] developed a thermodynamically-consistent method of mixing thermodynamic state variables to

develop a suitable Hugoniot EOS. This process is necessary because mixture internal energies are heterogeneous due to different structures leading to mixing free energy ΔG^M and configurational entropy differences. Although mechanical equilibration can be accounted for if ordinary interpolation procedures are taken, thermal equilibrium (and thus thermodynamic equilibrium) is not guaranteed due to this heterogeneity [3]. Therefore, a different procedure is necessary which resolves this temperature discrepancy.

The procedure involves developing suitable cold curves (zero-Kelvin isotherms) in $P - V$ space for each constituent. This is necessary to avoid inhomogeneous thermal effects between the constituents.

$$P_{OK} - P_H = \frac{\Gamma_0}{V_0}(E_{0K} - E_H). \tag{62}$$

The procedure to obtain the zero-Kelvin isotherms for each component is outlined in Meyers [3] and the resulting differential equation will be reproduced below. This involves defining the pressure as a function of volume and energy for each constituent and relating the resulting differential function to the Hugoniot energy.

$$\left(\frac{\partial P}{\partial V}\right)_{0K} + \left(\frac{\Gamma_0}{V_0}\right) P_{0K} = \frac{\Gamma_0}{2V_0}\left[P_H + \left(\frac{V_0}{\Gamma_0} + V - V_0\right)\left(\frac{\partial P}{\partial V}\right)_H\right] \tag{63}$$

This equation may be numerically integrated using the definition of the Hugoniot shown below for the individual constituent assuming a linear $U_s - U_p$ relation to obtain the zero-Kelvin isotherms.

$$P_H = \frac{C^2(V_0 - V)}{[V_0 - S(V_0 - V)]^2} \tag{64}$$

$$\left(\frac{\partial P}{\partial V}\right)_H = \frac{C^2 + 2S[V_0 - S(V_0 - V)]}{V_0 - S(V_0 - V)]^4} \tag{65}$$

The new mixture EOS is obtained by relating the energy at the Hugoniot and the energy along the zero-Kelvin isotherm. These isotherms are "mixed," i.e. the isotherm for the mixture is the mass-fraction-weighted sum of the component isotherms, and then the isotherms

are related to the Hugoniot state using the Mie-Grüneisen EOS.

$$V = \sum_i m_{f,i} V_i \tag{66}$$

$$\left(\frac{V}{\Gamma}\right) = \sum_i m_{f,i} \left(\frac{V}{\Gamma}\right)_i \tag{67}$$

$$E = \sum_i m_{f,i} E_i \tag{68}$$

After mixing, the Hugoniot is obtained by numerically integrating the inverse differential equation:

$$\left(\frac{\partial P}{\partial V}\right)_H + \frac{P_H}{2V_0/\Gamma_0 + V - V_0} = \frac{(2V_0/\Gamma_0)(\partial P/\partial V)_{0K} + 2P_{0K}}{2V_0/\Gamma_0 + V - V_0} \tag{69}$$

Equation 69 provides the Hugoniot of a mixture avoiding the problem of heterogeneous temperature effects. Other mixture theories were analyzed by Garg and Kirsh [123, 16] on the basis of either mechanical or thermal equilibrium. The McQueen mixture theory is acceptable for the current work and is employed to analyze the shock compressed state of the mixture.

3.3.2 Thermodynamics of powder mixtures under shock compression

The shock compression of monolithic solid materials (without chemical reaction or phase change) is well-understood and describable to a high degree of fidelity by the Rankine-Hugoniot jump conditions. The situation becomes complicated in composite mixtures of metal powders due to the potential chemical reaction induced by shock compression and complex thermodynamics associated with the mixture state. A good first approximation of the shock compression response of a powder mixture can be obtained by making a number of equilibrium thermodynamic assumptions. The following treatment follows that of Horie and Sawaoka [16] and is also based on the mixture theory of McQueen and a variety of modifications for porous solids.

Porous solids (powder compacts with some normal distribution of voids/pores) will invariably go through a compaction process during dynamic compression (either through uniaxial strain or stress loading). The compaction process is a non-equilibrium transient state where the shock wave is not fully developed as it propagates through the powder. In an infinitesimal region within the compaction front, many models presume a fully developed shock state (e.g. the ubiquitous Snow plow model) for the purposes of predicting the compaction response. These models are phenomenological in nature and depend on the definition of some evolution parameter that describes the compaction process. Compaction is normally considered to be a three-stage process:

- Stage 1: The bulk and localized re-orientation and relative movement of particles to fill as much space as possible. Frictional forces (static friction constantly being broken, as in stiction phenomena) dominate transient equilibrium states.

- Stage 2: Complex deformation processes take over when the elastic limit within the particles is exceeded and plastic deformation becomes significant. The softer particles begin to deform to fill the rest of the space left over from stage 1. If the particle geometries (i.e. particle size distributions and morphology distributions) and constitutive properties allow, the plastic deformation regime can be quite pronounced, leading to complex phenomena mediated by deformation-induced heating and flow (solid-state bonding).

- Stage 3: Fracture is the natural consequence of continued plastic deformation of the particles due to continual shearing along critically-resolved shear stress directions. The fracture process can lead to agglomeration of the newly-formed particles, thus repeating the cycle.

The aforementioned processes are in stark contrast to the ideally-locking solid which compresses to full density for any positive pressure. Any model that has predictive capabilities of the final state of a porous solid must take into account the compaction process in

some way. The following section outlines models for the compaction process of powders and porous solids.

3.3.2.1 Continuum-based compaction models - P-α and variants

The compaction behavior of porous solids was empirically studied by Hermann [113] where he introduced an evolution parameter relating the porous volume to the solid volume and assuming that the pressure was a function only of the solid volume and energy. He also assumed that the elastic and plastic response of the powder is directly relatable to this parameter. He defined the distention parameter α as:

$$\alpha = \frac{V_{00}}{V} = \frac{1}{\Phi}. \tag{70}$$

The pressure relationship to the distension was modified by Carroll and Holt [124] to account for stress averaging effects in the powder [16]:

$$P = \frac{1}{\alpha} f(V/\alpha, E) \tag{71}$$

The elastic and plastic behavior of the powder is modeled separately. For the elastic response, the compaction relationship related the evolution of the distention α to the bulk elastic sound speed and isentropic bulk modulus:

$$\left(\frac{d\alpha}{dP}\right)_{elastic} = \frac{1}{K_{s0}}\left[\left(\frac{C_{por}}{C_s}\right)^2 - 1\right], \tag{72}$$

which was cast in a simple form for numerical expediency by Hermann [113, 16], which is an integrated form using properties at zero pressure:

$$\left(\frac{C_{por}}{C_s}\right) = 1 + \frac{1-\alpha}{1-\alpha_0}\left(\left(\frac{C_{por}}{C_s}\right)_0 - 1\right), \tag{73}$$

The subscripts "*por*" and "*s*" refer to the porous and solid conditions respectively, and the subscript 0 indicates the zero pressure condition. The plastic response was derived by Butcher and Karnes [125] assuming a simple polynomial expression for the distension:

$$\frac{\alpha - 1}{\alpha_e - 1} = \left(1 - \frac{P - P_e}{P_{cr} - P_e}\right)^2 . \tag{74}$$

This expression may be modified to isolate the distention parameter:

$$\alpha = 1 + (\alpha_e - 1)\left(1 - \frac{P - P_e}{P_{cr} - P_e}\right)^2 . \tag{75}$$

This form is used in the present work to predict the resulting distension as a function of applied hydrodynamic stress P, the distension at maximum elastic compression α_e for a maximum applied stress P_e (where the particles have reached their elastic limit), and the crush-up critical stress P_{cr} where all particles are assumed to have fully consolidated.

The crush-up stress, P_{cr}, must be estimated in some way, or be determined experimentally by curve-fitting to measured stress data. This value can be estimated for the mixtures using the Fischmeister-Artz method [126] which treats the packing and deformation of idealized particles through the deformation of their contact points. Thus, the pore collapse is a natural consequence of the deformation of the particle contact points, mimicking reality as shown in figure 17. Their expression provides the critical crush stress P_{cr} of a powder mixture required to compress a powder of bulk yield strength σ_y to density ρ:

$$P_{cr} = 2.97\rho^2\left(\frac{\rho - \rho_0}{1 - \rho_0}\right). \tag{76}$$

A more complex expression for higher relative density regions was developed [16] considering both the low stress compaction mode (particle re-arrangement) and high stress compaction mode (particle deformation) in linear combination:

$$P_{cr} = \sigma_y\left[\frac{3aZD}{4\pi R^2}f_s + 2\ln\frac{a(1)Z(1)}{a(1)Z(1) - a(D)Z(D)}f_h\right], \tag{77}$$

where $a(i)$ and $Z(i)$ represent the contact area and contact points at a relative density ($D = \rho/\rho_0$) value of i, and f_s and f_h are the volume fractions of particles undergoing elastic

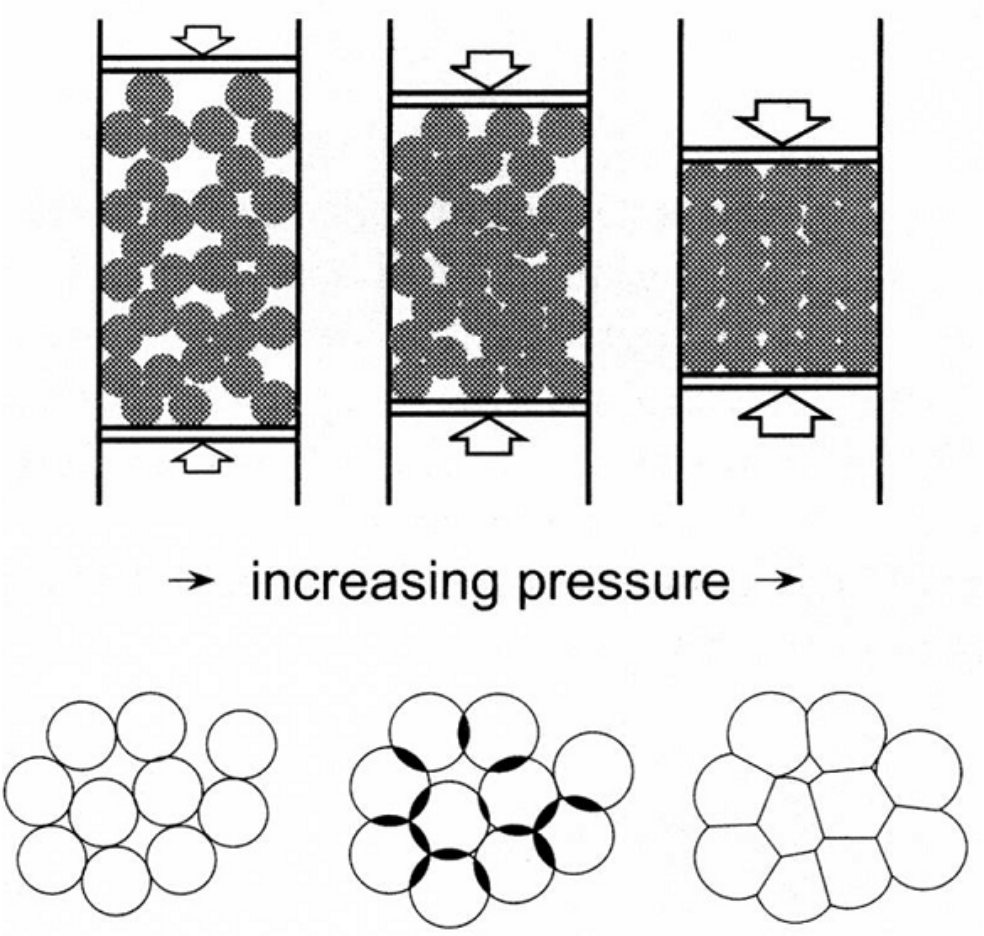

Figure 17: In a quasi-static compaction of idealized spheres, the contact points between the spheres naturally create a statistical distribution of porosity. It is the compaction and deformation of these points (which can be modeled as Hertzian) which leads to the pore collapse. Particle re-arrangement and bridging dominates low pressure compaction, whereas particle deformation dominates the higher pressure regime. Fischmeister and Artz [126] derived the crush stress for deformation limited to contact points on average. Figure is adapted from Horie and Sawaoka [16].

(subscript "s") and plastic (subscript "h") deformation respectively [16]. Expression (76) is a direct consequence of Equation (77) assuming greater than 90% relative density.

An alternative mechanistic treatment of particle compaction was developed by Carroll and Holt [124] who used continuum plasticity theory to assume the entire compaction process could be modeled as the compaction of a hollow sphere containing the properties of the powder (The hollow-sphere model). They solved the equations of equilibrium in radial coordinates ($r - \theta$) for a hollow sphere under hydrostatic load:

$$\frac{d\sigma_r}{dr} + \frac{2}{r}(\sigma_r - \sigma_\theta) = 0 \tag{78}$$

$$\sigma_r = -P \quad : r = b \tag{79}$$

$$\sigma_r = 0 \quad : r = a, \tag{80}$$

where b and a are the outer and inner radii of the hollow sphere. They then formulated a stress-strain relation based on the Generalized Hooke's law and employed a Tresca Yield criterion:

$$\sigma_r - \sigma_\theta = \sigma_y, \tag{81}$$

and defined the relative density based on the dimensions of the hollow sphere:

$$D = \Phi = 1 - a^3/b^3 \tag{82}$$

$$\alpha = 1/D. \tag{83}$$

The solution to the differential equations depends on the location of the elastic-plastic boundary, which evolves as a function of the distension by definition:

$$P = \begin{cases} \dfrac{4\mu(\alpha_0 - \alpha)}{3\alpha(\alpha - 1)} & \alpha_0 \geq \alpha \geq \alpha_e; \\ \dfrac{4}{3}\mu + \sigma_y - \dfrac{2\mu\alpha_0}{\alpha} + \sigma_y \ln \dfrac{2\mu(\alpha_0 - \alpha)}{\sigma_y(\alpha - 1)} & \alpha_1 \geq \alpha \geq \alpha_{pl}; \\ \dfrac{2}{3}\sigma_y \ln\left(\dfrac{\alpha}{\alpha - 1}\right) & \alpha_{pl} \geq \alpha \geq 1; \end{cases} \tag{84}$$

A simplified version of the Carroll-Holt model was derived [124, 127] which does not take into account the transitional region between elastic and plastic deformation of the particles. The elastic behavior is thus reckoned as the initial distension at ambient conditions α_0, and the equations may be solved for α:

$$\alpha = \begin{cases} \alpha_0 & 0 < P < P_e; \\ \dfrac{1}{1 - \exp(-3P/2\sigma_y)} & P_e < P < \infty \end{cases} \tag{85}$$

In the Carroll-Holt model, the shear modulus for the powder mixture μ arises naturally from the stress-strain relationship, and the compaction stages are accounted for by the three expressions for the given regimes of the distension α, including the transitional region until the deformation is uniformly plastic, i.e. above α_{pl}. This model provides a mechanistic way to predict the compaction and densification response of a powder mixture assuming some mixture law (Voigt/Reuss, etc.) for the constitutive properties, and can be incorporated into a suitable EOS through the distension parameter α to determine the intermediate state of the mixture during compaction to full density.

3.3.2.2 Porous equation of state models

The hydrodynamic (no shear effects) continuum-based models all presuppose that the final state is related to state variables such as pressure, volume, internal energy, etc. The Hugoniot for the powder should be describable by the same equations as for a solid material, assuming that continuum-level assumptions hold, i.e. response is governed by variables such as pressure and internal energy in some averaged sense [16]. This also means that the jump conditions can be applied if indeed a steady shock wave develops [118]. The Hugoniot for a solid can be determined with the aid of the Mie-Grüneisen EOS:

$$\left(\frac{dP}{dV}\right)_H = \frac{\left(\frac{\partial p}{\partial V}\right)_s + \frac{\Gamma}{2V}(P - P_0)}{1 - \frac{\Gamma}{2V}(V_0 - V)}. \tag{86}$$

However, now the specific volume V_0 is an adjustable parameter and can be tailored to account for the crush-up phenomena irrespective of shear (only considering bulk energy partitioning of dynamic shock energy to crush-up energy). In the Mie-Grüneisen EOS, assuming the snow-plow model, there will be positive volume increases for certain values of

pressure due to increases in internal energy. In this model, it is assumed that once compaction occurs, the resulting solid compacted mixture is indistinguishable from a composite solid that has been shocked to a similar state. A reference thermodynamic state (such as an isentrope) can be used along with the Mie-Grüneisen EOS to determine the final state, and it is common for the reference volume to be the solid volume. In the case of an isetrope, the EOS becomes:

$$P = P_r + \rho\Gamma(E - E_r) \tag{87}$$

$$E_r = -\int_{V_0}^{V} P_s dV \qquad \text{For Isentrope} \tag{88}$$

$$E_r = \frac{1}{2} P_r (V_0 - V) \qquad \text{For Hugoniot,} \tag{89}$$

where the subscript "0" refers to the solid mixture reference. Figure 18 shows the resulting Hugoniot prediction from the reference curve assuming an isentropic reference. If using the reference Hugoniot, the equations become:

$$P = P_r \frac{1 - (\rho\Gamma)(V_0 - V)/2}{1 - (\rho\Gamma)(V_{00} - V)/2} \tag{90}$$

$$P_r = \frac{\rho_0 C_0^2 \epsilon_V}{(1 - S\,\epsilon_V)^2} \tag{91}$$

$$\epsilon_V = 1 - \frac{\rho_0}{\rho} = 1 - \frac{V}{V_0} \tag{92}$$

and C_0 and S are the coefficients of the linear $U_s - U_p$ relationship. Defining the porosity ratio as the %TMD from solid:

$$\%TMD = \Phi = \frac{\rho_{00}}{\rho_0} = \frac{V_0}{V_{00}}, \tag{93}$$

the critical condition for an anomalous Hugoniot (positive densities at positive pressures) was derived by Simons and Legner [128, 16] for the snow-plow model assuming that all thermal energy was due to pore collapse:

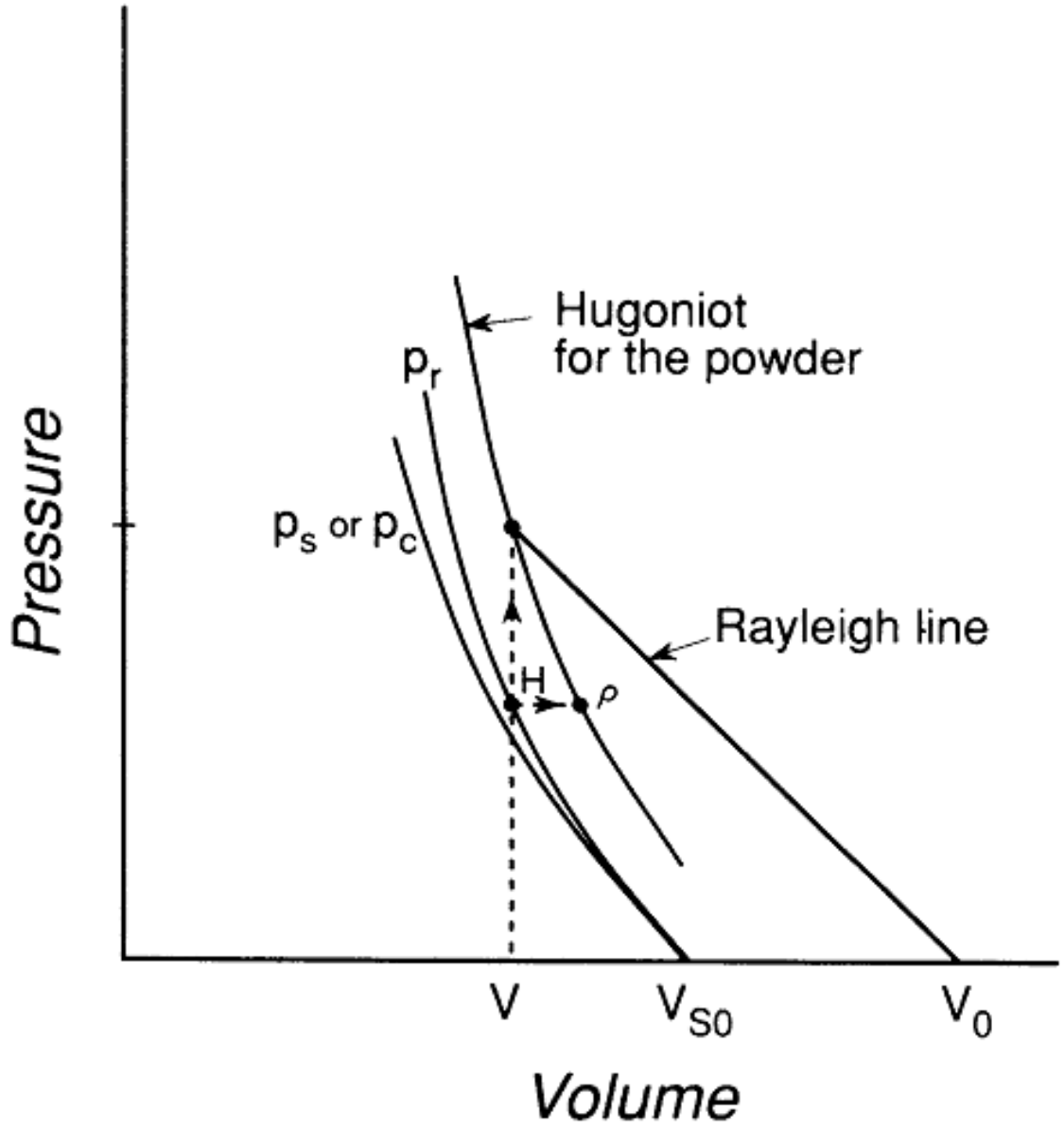

Figure 18: The snow-plow model assumes compaction occurs in a one-step process for any positive pressure. Therefore, the predicted Hugoniot state may be derived from a suitable reference state assuming the reference to be in the zero-pressure solid state (fully dense).

$$\Sigma = \Phi_{cr} = \frac{\rho_{00}}{\rho_0} = \frac{\Gamma}{2+\Gamma}, \tag{94}$$

which was found to be in good approximation with data as shown in figure 19.

It is thus very important that the mixture does not exceed these critical values, lest the excess internal energy developed by the crush-up of the powder confound any other

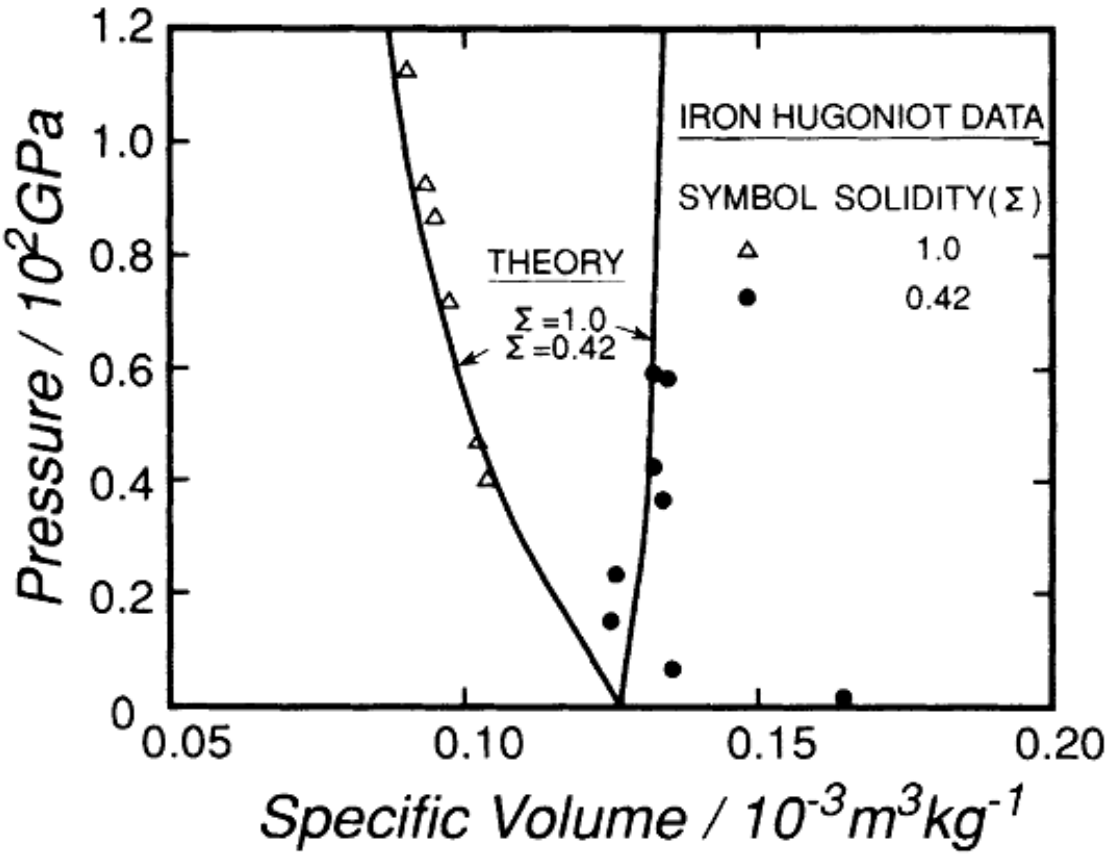

Figure 19: Simons and Legner computed Hugoniot predictions for select porous solids and confirmed through their simplifying assumptions that a porosity $\Phi = 0.5$ is around the critical value for the Hugoniot to become anomalous as a result of the pore collapse heating [128].

signature which produces anomalies in the $P - V$ or $U_s - U_p$ spaces. This model does not consider the pore collapse phenomena since the compaction of the pores happens at any positive pressure. More complex continuum-level calculations incorporate an evolution parameter for the density which accounts for the compaction of pores. These models are considered in the present work for the Ti/Al/B ternary mixture.

A similar prediction comes from assuming the Hugoniot of the solid mixture as the reference state. By writing an expression for the powder Hugoniot using the Mie-Grüneisen EOS, the following expression may be derived:

$$P = \frac{[2V - \Gamma(V_0 - V)]C^2(V_0 - V)}{[2V - \Gamma(V_{00} - V)][V_0 - S(V_0 - V)]^2} \tag{95}$$

which is conceptually similar to Equation (91).

3.3.2.3 A non-multi-valued porous EOS - The Wu-Jing EOS

The equations of state applied to powders can lead to multi-valued solutions as in the case of the Mie-Grüneisen equation of state. Various efforts have been made to evaluate the shock state of a powder along different thermodynamic paths to ensure thermodynamic consistency. Rice and Walsh [129] presented an equation of state based on an isobaric thermodynamic path in contrast to the isochoric path used by the Mie-Grüneisen equation of state. The form of the equation was later derived from thermodynamic arguments by Wu and Jing [127] and it became a new equation to investigate the thermodynamics of shock compression of porous solids.

Wu and Jing started by first considering an isobaric process, in contrast to the Mie-Grüneisen approach which is an isochoric process. Along an isobaric path, the enthalpy H becomes the relevant energy term. They considered the volume and enthalpy to be composed of the cold term (at zero-kelvin) and the thermal part:

$$V(P,T) = V_C(P) + V_T(P,T), \tag{96}$$

$$H(P,T) = H_C(P) + H_T(P,T), \tag{97}$$

where the thermal contribution to the enthalpy is obtained from:

$$dH_T = C_P dT. \tag{98}$$

Invoking the Maxwell relation:

$$\left(\frac{\partial H}{\partial P}\right)_T = -T\left(\frac{\partial V}{\partial T}\right)_P + V \tag{99}$$

and substituting the definitions of volume and enthalpy gives the Wu-Jing EOS upon integration:

$$V - V_C = \frac{R(P)}{P}(H - H_C), \tag{100}$$

where R is merely an integration constant and a function solely of pressure. Its thermodynamic meaning can be determined from the differential of Equation (100):

$$R = P\left(\frac{\partial V}{\partial H}\right)_P. \tag{101}$$

Invoking the following thermodynamic relations:

$$\left(\frac{\partial V}{\partial H}\right)_P = \frac{1}{C_P}\left(\frac{\partial V}{\partial T}\right)_P, \tag{102}$$

$$\left(\frac{\partial C_P}{\partial P}\right)_T = -T\left(\frac{\partial^2 V}{\partial T^2}\right)_P, \tag{103}$$

$$K_S = \left(\frac{C_P}{C_V}\right)K_T = \rho C^2, \tag{104}$$

$$\Gamma = \left(\frac{K_T}{C_V}\right)\left(\frac{\partial V}{\partial T}\right)_P, \tag{105}$$

leads to a tractable form of the integration constant R in terms of common physical properties[6]:

$$R = \frac{P\Gamma}{K_S} = \frac{P\Gamma}{\rho C^2}. \tag{106}$$

To find the Hugoniot for the powder material, the equations for the cold enthalpy and thermal contribution are written explicitly for both the solid phase (fully compacted), and powder phase (with the superscript ’):

[6]Further details can be found in the original work by Wu and Jing [127]

$$V - V_C = \frac{R(P)}{P}(H - H_C), \tag{107}$$

$$V' - V'_C = \frac{R(P)}{P}(H' - H'_C), \tag{108}$$

$$\tag{109}$$

The cold enthalpy H_C for the powder is defined by:

$$H'_C = E'_C + PV'_C, \tag{110}$$

$$H' = E_{00} + \frac{1}{2}P_e(V_{00} - V_e) + \frac{1}{2}P(V_e + V'_H), \tag{111}$$

where the transition from elastic (subscript e) to plastic deformation in the powder is accounted for by the additional energy terms in the enthalpy. Wu and Jing assumed that the porous and solid material both had the same starting energy, which gives the following relationship when combining terms:

$$\begin{aligned} V'_H =& \frac{1-(R/2)}{1-(R/2)[1-(P_e/P)]}V_H \\ &+ \frac{(R/2)}{1-(R/2)[1-(P_e/P)]}\left((V_e - V_0) + \frac{P_e}{P}V_{00} + \frac{1-R}{(R/2)}(V'_C - V_C)\right). \end{aligned} \tag{112}$$

Recent work by Vogler and Grady et al. [130] uses the Grady P-λ compaction model in conjunction with the Rice-Walsh EOS to analyze a variety of porous powder mixtures and determine their off-Hugoniot shock compressed states. They noted that the extent of solid-state phase transitions in the porous mixtures were a function of starting distention state which was aided by the enhanced shearing rates typical of the compaction process in highly porous materials. This work shows the utility in using a consistent thermodynamic EOS to predict the shock compression of porous mixtures.

However, the applicability of the Wu-Jing and Rice-Walsh equations of state may still be limited to applications where the meso-scale heterogeneity effects are not significant

enough to greatly affect the bulk response. For example, any meso-scale heterogeneity which forces the shock wave to become highly dispersed due to the multitude of internal surfaces in a powder or due to property disparity can invalidate any continuum mixture theory-based analysis due to the non-equilibrium effects and inhomogeneity of the thermodynamic functions [1, 131]. Dai et al. [132, 133] for example found that the Wu-Jing equation of state did not successfully describe the shock response of extremely small nano-iron powders due to the high crush strength effects and the interfacial forces which become significant at very small particle sizes and large porosities. With this in mind, the efficacy of these models was tested in the present work to help predict the shock compression response of the Ti/Al/B powder mixtures. Further details are discussed in chapter 4.

3.4 Thermodynamic models for reactive mixtures under shock compression

A composite mixture composed of reactive metal powders isostatically compacted (green strength) can undergo shock-induced chemical reaction [16, 9, 12, 41]. The thermodynamics of the reaction and the ensuing wave stability were analyzed by Boslough [87, 72] where he found that metal powder mixtures behaved like explosives and their reactions were like "heat detonations" and proceeded to immediate thermodynamic equilibrium if the reaction was initiated. This chemical reaction will evolve heat and displace the thermodynamic state achieved due to shock compression by some value in either V or P. This is due purely to heat evolution and mass transport of constituents during chemical reaction.

If thermodynamic equilibrium is achieved within the shock front (i.e. the Hugoniot end state is reached within the time scale of mechanical equilibration), then the thermodynamic end state will be off the Hugoniot due to this volumetric/pressure change. The inherent porosity of the powder mixture will also be at a higher Hugoniot energy state than the solid mixture due to the pore collapse energy. The high heat generated by the pore collapse can lead to a convex Hugoniot in $P - V$ space due to the volumetric expansion [134].

Hugoniot-based models forgo detailed heterogeneous descriptions at the meso-scale

and instead opt to lump the energetics of the reaction within the conservation relations irrespective of their mechanochemical origins. These models are truly end-state models and cannot provide the necessary details to infer a mechanism. Rather, they depend on deviations in the measured pressure or particle velocity and ascribe these deviations to the formation of a reaction product disrupting the wave mechanics of the otherwise inert system. While the models have been used to infer the possible reaction in many systems, they should be critically evaluated to determine the cause of the deviations.

Boslough and Graham [135] performed shock compression experiments on Ni/Al powder mixtures using a radiation pyrometer to probe the temperature evolution at the surface of the powder compact and the window backer in an effort to provide real-time observations to substantiate the earlier observations by Horie et al. [36, 76, 136]. They observed spectral radiance producing extremely high temperatures at localized regions where hydrocode calculations predicted temperatures sufficiently hot enough to cause ignition. A streak camera recorded the luminescence which produced temperatures well in excess of the camera sensitivity, providing compelling evidence for an ultrafast reaction occurring within 100 ns of the peak pulse.

Boslough [72] later provided a thermochemical model for shock-induced chemical reactions, which he likened to detonations in explosives[7]. He lumped the effects of the reaction (a complete reaction) into the Rankine-Hugoniot energy equation

$$E_H - E_0 = \frac{1}{2}(P_H - P_0)(V_{00} - V_H) - \Delta H_{rxn} \tag{113}$$

where the subscript H refers to the shocked state (Hugoniot state, or the state where thermodynamic equilibrium is achieved behind the shock wave). The effects of pore collapse energy and reaction energy are implicitly contained in this equation through the V_{00} and ΔH_{rxn} terms. He then proceeded to outline the conditions necessary for reaction wave

[7]He termed these reactions in solids as "heat detonations" and noted that the reactions shared many common traits with conventional detonations, without the sudden expansion.

stability based on the Courant-Friedrich Fourier analysis [137] and showed the similarity between a heat detonation and conventional detonation. Boslough [72] then determined the Hugoniot of the reaction product by combining the reaction energy with the thermal energy contribution along the isentrope, to arrive at:

$$P_H(V) = \frac{-\Delta H_{rxn} - \int_{V_0'}^{V} P_S\, dV - \frac{V}{\Gamma'} P_S}{\frac{1}{2}(V_{00} - V) - \frac{V}{\Gamma'}} \tag{114}$$

where V_0' is the specific volume of the reaction product at standard state, Γ' is the Grüneisen constant of the product, and the subscript S refers to the isentropic state. This model assumes kinetically-favorable conditions (complete reaction within the shock rise time). It is crucial that the energy released by the reaction is in excess to the thermal pressure buildup to avoid anomalous Hugoniot behavior (cf. Zel'dovich and Raizer [134]). However, there is inconsistency in the definition of the initial states as well as the sign of the heat of reaction term.

Batsanov et al. [85] considered a constant volume reaction and predicted the extent of reaction from the energy difference between a reaction product and inert mixture and comparison with experiments. This procedure did not adequately account for the specific volume expansion as a consequence of the reaction. The method focused on Ballotechnic reactions as described by Bennett and Horie [24] which provide both a constant volume and constant pressure adjustment of the Hugoniot based on a suitable reference state. Figure 20 presents schematics showing these adjustments to the expected dense product Hugoniot. This derivation uses the Hugoniot of the dense product as the reference state for the Rankine-Hugoniot conditions. The predicted pressure is given by:

$$P = \frac{(E_0^* - E_0) + P_H^*[1/2 \cdot (V_0^* - V) - (V/\Gamma)^*]}{1/2 \cdot (V_{00} - V) - (V/\Gamma)^*} \tag{115}$$

where the starred variables refer to the dense product reference state. A similar derivation was given using the isentrope of the dense product as the reference state and gives a result similar to Boslough's (cf. equation 114). In the constant pressure adjustment (Figure 20b),

the isentrope serves as the reference state and gives the following equation, on applying the Rankine-Hugoniot jump conditions:

$$V = \frac{V_S^* \left[(V/\Gamma)^* (K_S/V_S)^* - P_S^* \right] + P_S^* V_{00}/2 + \int_{V_0^*}^{V_S^*} P_S^* dV_S^* - (E_0^* - E_0)}{(V/\Gamma)^* (K_S/V_S)^* - P_S^*/2} \tag{116}$$

where the isentropic bulk modulus K_S comes from the thermodynamic relation: $K_S = -V(\partial P/\partial V)_S$. Thus, a Hugoniot may be predicted in the case of a chemical reaction through this Mie-Grüneisen adjustment.

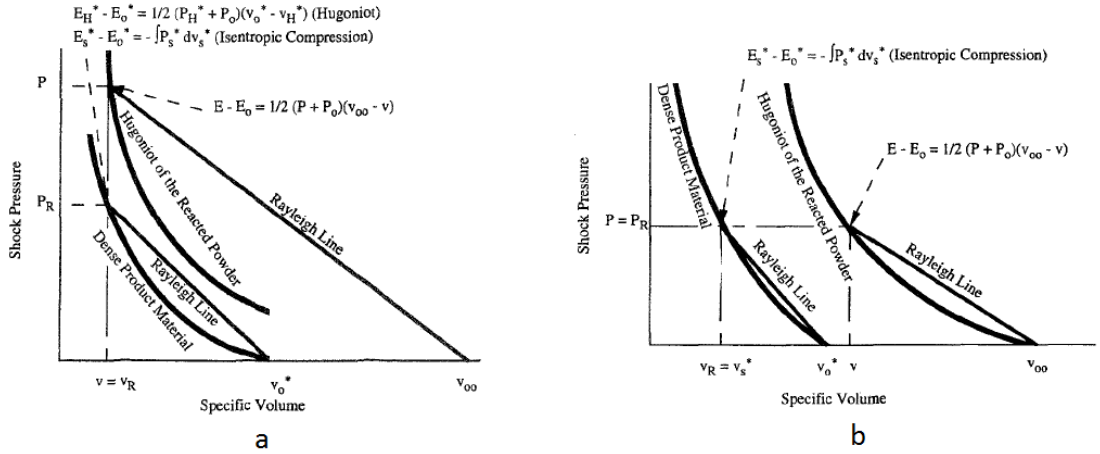

Figure 20: (a.) Schematic of the constant volume adjustment to the dense product Hugoniot reference state. (b.) Constant pressure adjustment. The isentrope refers to the dense product reference state. Adapted from Bennett and Horie [24].

These Hugoniot analyses have been used to evaluate experimental observations of potential shock-induced reaction phenomena in a variety of systems.[8] The principal ideas underlying the analysis are that the reaction and pore collapse occur in a predictable fashion, i.e. reactions go to completion within the shock front and the powder mixture fully densifies behind the shock front. However, the irreversible nature of the reaction (i.e. heat dissipation due to transport phenomena) is not incorporated in this end-state analysis. Further analysis is suggested to determine these effects and how to incorporate them into this framework.

[8] See for example the review article by Eakins and Thadhani [13]

Recent work by Zhang et al. [138] explored the implications of shock-induced chemical reactivity in the context of deviations from the inert Hugoniot state. This is in an effort to provide a predictive model for shock-induced reactivity, based on assumed reaction kinetics. They used the Wu-Jing EOS [127] and the Born-Mayer potential to approximate the EOS for the cold material. The authors also incorporated a simple kinetic model assuming a linear reaction rate for the extent of reaction y:

$$\frac{dy}{dt} = kf(y), \tag{117}$$

where the rate constant k takes on an Arrhenius form:

$$k = A \exp\left(-\frac{E_a}{R_u T}\right), \tag{118}$$

where A and E_a are material constants, R_u is the universal gas constant, and T is the absolute temperature. They used the functional form:

$$f(y) = n(1-y)\left[-\ln(1-y)\right]^{(n-1)/n}, \tag{119}$$

where n is related to the boundary conditions. Zhang et al. then predicted the Hugoniots for a variety of materials in the published literature based on combining these assumed kinetics with the constant volume adjustment to the Hugoniot pressure presented by Bennett and Horie [24]:

$$P = \frac{-y\Delta H + P_H\left[\frac{V_0 - V}{2} - \frac{V}{\Gamma}\right]}{\frac{1}{2}(V_{00} - V) - \frac{V}{\Gamma}}. \tag{120}$$

The results of this Hugoniot analysis are presented in Figures 21 (a) and (b). The analysis showed close agreement with the shock compression response of the Ni/Ti mixture investigated by Xu and Thadhani [139] (figure 21a). This result shows that the potential deviant shock response from the inert Hugoniot of the Ni/Ti mixture was due to an incomplete shock-induced chemical reaction of Ni+Ti powder to the NiTi intermetallic. Similar

results were obtained for the Ni/Al mixtures analyzed by Eakins et al. [140], but all lie on the inert mixture line. Zhang et al. concluded that there was no evidence of shock-induced chemical reactions, in similar agreement with Eakins' findings for spherical morphology Ni/Al powders. The deviations from the inert Hugoniot were not substantial in the Ni/Ti case, casting doubt on whether a shock-induced chemical reaction event took place. However, the analysis by Zhang et al. shows that such deviations are possible with incomplete chemical reactions. Such analysis was conducted previously in an ad-hoc manner by Eakins and Thadhani [13]. These analyses must be conducted carefully to assess whether shock-induced chemical reaction events actually took place beyond the small deviations possible by incomplete chemical reactions as was shown in Zhang et al. [138]

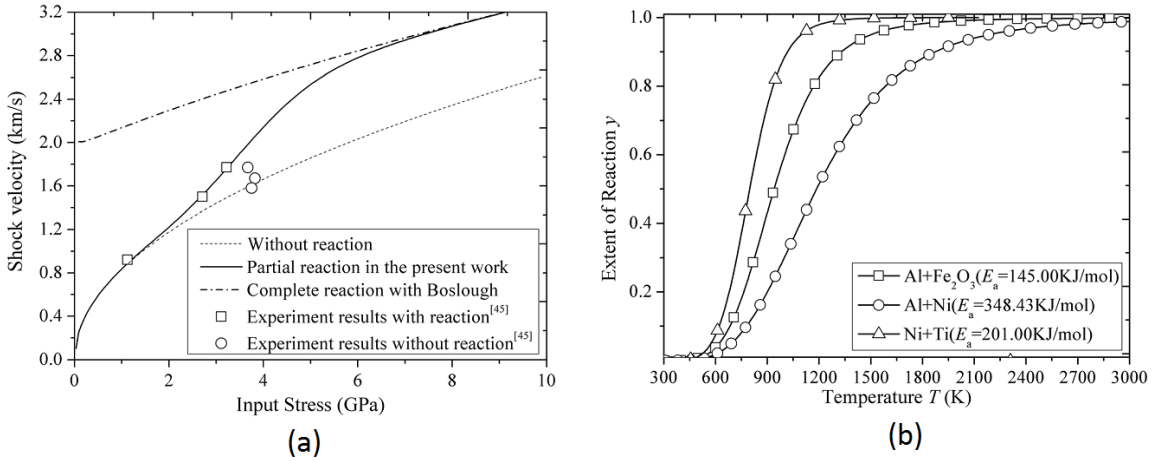

Figure 21: (a.) Predicted shock compressed state of Ni/Ti mixtures [139] employing the assumed kinetics model in Zhang et al.'s work [138]. The predicted shock state shows good correspondence with the experimental results, revealing that the shock-induced chemical reaction was incomplete in nature. (b.) The predicted extent of reaction y as a function of shock temperature for three different mixtures as analyzed by Zhang et al. [138].

3.5 A word on statistical analysis of data

Shock compression experiments are inherently expensive and due to the rapid and destructive nature of the loading environment, there is little room for error. Each component must be meticulously prepared to ensure planarity during the impact, as well as the proper shock compression behavior during experimentation. This entails repeated measurements of the

dimensions and properties of the components in each target to be shot. Errors propagate in such measurements and increase the overall uncertainty of any measurement, no matter how refined the instrument and how much resolution is quoted in the measurement.

The theory of errors [141, 142, 143, 118] is used in this work to quantify the extent of uncertainty of each measurement. The propagation of uncertainty involves combining all sources of systematic and random errors in the experiment and quantifying their contribution to the overall uncertainty of the system. Errors propagate according to the theory of errors in an RMS fashion based on a Pfaffian derivation of some measurement F with functional dependence on variables x_i:

$$\delta F(x_i) = \sqrt{\sum_i \left(\frac{\partial F}{\partial x_i}\right)^2 w_i(x)^2}, \tag{121}$$

Equation (121) is a direct consequence of a first-order Taylor expansion about the error $w_i(x)$ in variable x_i for the functional form F. This functional form must be first-order analytic [141, 144, 143] and the errors may be an RMS combination of both random and systematic errors of each independent variable x_i of the functional form. Consider the simple case of the shock speed measurement through a material U_s, which involves the measurement of transit time δt through some material thickness δh. The formula for direct computation of shock speed is a function of these two variables and may be expressed multiplicatively:

$$U_s = \frac{\delta h}{\delta t}. \tag{122}$$

As an example, the thickness of the sample may have been measured at five different locations within the area impacted, providing five independent measurements of thickness ($n = 5$ samples, using the same measuring device/technique). There will be inherent randomness in the material, which will manifest itself in the random distribution of the measurements, which will take the form of a t-distribution [143, 145] since the sample number is low. The central-limit-theorem (CLT) may be invoked to determine the most probable

value of $\delta h = \mu_h$, where μ_h is the arithmetic mean of the independent measurements of δh[9]. Each measurement will have an inherent systematic error w_{sys} arising from the inherent uncertainty in the measurement device/technique. Quantifying the systematic error requires intimate knowledge of the system and assumes the measurement itself does not introduce systematic bias from an improper technique or user error. The random error will be the standard error for n number of measurements:

$$w_{rand}(x) = \left(\frac{s}{\sqrt{n}}\right), \tag{123}$$

where s is the standard deviation of the sample set. For a more precise description of the random error, the sample standard error is t-corrected (can also be "Z"-corrected if the distribution is Gaussian) to create the proper confidence interval:

$$w_{rand}(x) = \pm\left(\frac{t_\nu s}{\sqrt{n}}\right), \tag{124}$$

where the t_ν-value for ν degrees of freedom ($\nu = n - 1$) is selected for some confidence level. Usually a 95% confidence interval is selected ($\alpha = 5\%$ uncertainty level). The more stringent the confidence level, the greater the uncertainty in the measurement. Stated another way, there will be 95% certainty that the measurement will lie within $\pm w_{rand}(x)$ confidence interval, and there is a 95% confidence in the measurement itself being a true representation of the "true" value of the measurement. Therefore, the error bar for this measurement is expected to be as small as possible to ensure the random error does not dominate the uncertainty.

Assuming the systematic error is quantifiable[10], one merely combines the random error

[9]The average of the thickness measurements (or any measurement for that matter) will approach the "true" statistical value for an infinite number of measurements. The CLT guarantees that the mean approaches the "true" value of the measurement and that the independent measurements are distributed in a Gaussian fashion. For a smaller number of measurements, these will behave in a t-distribution. Proofs for these statements may be found in any advanced text on statistics.

[10]The systematic error is usually set through instrument calibration by the manufacturer, and is taken to be $1/2$ the smallest detectable unit increment for the instrument [143]

in the measurement with the systematic error in an RMS fashion to arrive at the total error in the measurement. Linearly combining the systematic uncertainty with each measurement improperly conflates the errors, and the RMS combination has been shown to properly describe the total uncertainty in the measurement. Any measurement whose uncertainty is properly quantified that shows wide variability either showcases a perhaps unknown phenomena, an improper measurement, or perhaps reveals the inadequacy of the theory itself. Every effort is made to properly conflate errors in this work, as the assessment of shock-induced reactivity depends on the relative value of the measured thermodynamic state relative to a baseline theory. Proper error quantification allows for comparison and helps rule out gross missteps in the experiment.

Mitchell and Nellis [142] presented a methodology based on the theory of errors to quantify the uncertainties in the thermodynamic shock properties of standard materials. They generated uncertainty bands which propagated the errors of the thermodynamic variables C_0 and S through the impedance-matching method. The overall uncertainty in each independent thermodynamic shock property is propagated appropriately for all measurements and techniques in this work, including the impedance-matching technique (method of characteristics) based on Mitchell and Nellis's work.

Any error bar shows the range of uncertainty in the measurement and depends on the propagation of uncertainty, and nothing else. The error bar cannot express a range, or band, of uncertainty that is arbitrarily assigned based on extracting a single value from a data set. Interpretation of stress measurements or VISAR particle velocity measurement from peaks is largely subjective and based on criterion set by the experimenter. The uncertainty inherent in these assumptions can only be approximately quantified. This uncertainty propagates based on the theory of errors as a *systematic* uncertainty which is combined in an RMS-fashion with all systematic and random uncertainties in the measurement. This will generate error bars that more accurately represent the true uncertainty range of the measurement; this is the approach taken in the present work. This produces consistent error

bars which quantify the uncertainty of the *particular methodology* used to arrive at some measured thermodynamic property or state of the system.

CHAPTER IV

MATERIALS SYSTEM AND EXPERIMENTAL METHODS

Dynamic compression of powder mixtures requires careful sample preparation so that consistent mixtures (and by extension consistent microstructures) are created for experiments. The violent nature of the loading environment necessitates time-resolved diagnostics capable of capturing ultra-fast events. Transient events are very sensitive to environmental variables, so great care must be taken to ensure and that the experimentalist does not bungle and further confound the experiment. Be it photographic/videographic evidence, or quantitative evidence obtained from gauges/interferometry, the resulting data must reveal the dynamic response of the powder to the load. This becomes an ambitious task when considering reactive powder mixtures because of their inherent heterogeneity, and because discerning evidence of chemical reactivity is still indirect with conventional measurement techniques. Using this evidence to tease out a mechanistic and causal explanation for dynamically-induced reactivity is a Herculean task, and in the context of shock compression (uniaxial strain) and rod-on-anvil Taylor impact (uniaxial stress) loading, it requires careful experiment preparation and an eye to detail.

Typical shock compression experiments usually consist of measuring the transit time of the shock wave through the material, or some measurement of velocity/motion that can be related to the thermodynamic shock state (a point on the Hugoniot) through the appropriate impedance-matching technique and with the aid of equations of state for the materials used to impart the shock. This becomes complicated because the impedance-matching technique requires that the Rankine-Hugoniot jump conditions be rigorously satisfied. Of course, the measurement technique must be able to capture the behavior manifested in a true shock state to be able to assert the validity of the impedance-matching technique. Nevertheless,

these methods have been employed in past works [36, 14, 12, 41, 42, 13] to compare the mixture thermodynamics of an "ideally-locking" powder compaction process (assuming a fast rise to peak pressure) to the experimentally-observed behavior of the powder. In the present work, these techniques are judiciously applied with an adequate thermodynamic analysis to explore the implications of deviant measurements on the reactivity of the Ti/Al/B system.

The Ti/Al/B mixture is not without its unique challenges. In addition to being a ternary mixture[1], the constituents have complex material states. Boron has multiple allotropes that are thermodynamically stable at the pressure regimes accessible by the experiments; these challenges will be described in detail in section 4.1.2. These states may also be easily achieved by simply varying the starting state of the mixture under the same external influences to encourage local pressure and temperature gradients. The problem is circumvented at least in part by using amorphous boron powders.

This chapter discusses the experimental design adopted for exploring the dynamic response of Ti/Al/B compacts subjected to two different loading scenarios. In one scenario, the powder is isostatically compacted; the compact is propelled by a carrying rod into an anvil, producing a state of uniaxial stress upon impact (the classic Taylor rod-on-anvil impact test). In the other scenario, the compact is encapsulated and subjected to shock compression using parallel-plate impact, creating a state of near uniaxial strain limited by the bulk compressibility of the powder mixture (the classic Gas-Gun shock compression test). High speed imaging and ultrafast diagnostics are employed in the experiments to measure the transient response in the compact during loading. The experiments were designed with the main goal of identifying the onset of chemical reaction in the material, reckoned by comparison with appropriate baselines which will be outlined in the following sections. The shock response of Ti+2B powder mixtures distended to 50% TMD does not

[1]Binary mixtures are complex in both the underlying thermodynamic descriptions (i.e. an appropriate mixture theory) and due to meso-scale heterogeneities manifesting bulk behavior (i.e. force-chaining and instability effects)

exist in the open literature and therefore it was of utmost importance to fully characterize it to obtain a baseline response to assess shock-induced reactivity. The limitations of the experimental setup are discussed with particular attention given to the data reduction and its implications on chemical reaction and transient compaction behaviors in this mixture.

The motivations for selecting amorphous boron powders as a material of interest are discussed herewith in the context of promoting greater overall chemical reactivity. These implications are explored via meso-scale simulations using highly-resolved microstructures (cf. chapter 5). Furthermore, the constituents (namely boron) have dissimilar material properties, namely greatly dissimilar strengths, compared to Ti or Al. The extremely high hardness of boron (especially amorphous boron), coupled with the small size of the particles led to challenges in measurement – the front gauges (and potentially the back gauges) showed evidence of premature failure well before a stable stress state was reached. Nevertheless, the gauges provided valuable transit time measurements of the stress imparted into the powder and valuable information about the compaction process.

4.1 The Ti/Al/B Materials System

The Ti/Al/B materials system is a ternary intermetallic-forming system with unique characteristics stemming from the varied properties of the components and the inherent property-level and meso-level heterogeneity observed when creating pressed powder compacts of these constituents. Dynamic reaction initiation can unlock a number of viable reaction pathways. Understanding the mechanochemistry of Ti/Al/B under dynamic loading is paramount to ensure proper bottom-up design of MESMs utilizing this system. In the present work, the Ti+2B reaction pathway is considered due to the large exothermic energy release of the intermetallic reaction, which can support the subsequent combustion reaction of Al. The physical and mechanical properties of the constituent materials will ultimately influence the thermochemistry under dynamic loading and are discussed in this section.

4.1.1 Motivation for selecting the Ti/Al/B system

The ternary Ti/Al/B system was selected with the expectation that the highly exothermic reaction between Ti and B would ignite and sustain aluminum combustion. There are a variety of reaction pathways in this ternary system that are thermodynamically favorable and can ignite Al combustion. Moreover, the intermetallic reactions between Ti and Al can also compete with the Ti/B reactions and can aid, or be detrimental to, Al combustion. The interplay between the reactants will ultimately influence the bulk reactivity of this materials system. The reaction behavior is assumed to be a strong function of the mixture ratio, meso-scale distribution of constituents, and extrinsic component properties. Very little research in the open literature currently exists on the shock-induced reactivity of Ti/B.

The extraordinarily high heat of reaction for the Ti+2B reaction ($\Delta H_{rxn} = -320$ kJ/mol) was the main motivator for selecting the Ti/Al/B system for this work. The extensive research into binary intermetallic-forming systems (cf. section 2) has revealed the influence of meso-scale phenomena on their shock-induced reaction behavior. However, the mechanics of integrating these materials in a system that will form a multiple-reinforcement composite (i.e. multiple dispersed phases of reinforcement in one matrix material) has yet to be explored (a natural consequence of this ternary mixture). Furthermore, the effects of component preparation have not been studied in the Ti/Al/B system. These effects lead to differences in microstructural topology which can affect the bulk shock response by modifying the degree of heterogeneity in the compact. The disparate sizes, morphologies, and physical properties of the Ti/Al/B system create a unique, highly heterogeneous energetic mixture which contains, in theory, all the elements necessary to promote shock-induced and strain-induced reactivity. Each component contributes to the reactivity of the system in a different way and it will ultimately be the interaction of the constituents that will determine whether reactivity is enhanced, or diminished by combining these materials.

However, a key challenge became apparent when considering the influence of boron on

the mixture. Boron is an ill-characterized element with fascinating, yet enigmatic properties. This is of great consequence as there is a lack of Equation of State (EOS) data for boron in the pressure ranges considered, especially because of recent evidence of the existence of complex allotropes of boron at pressures achievable by gas-gun experiments at low velocities (i.e. Cu impact up to 1000 m/s) [29]. Existing EOS data is extremely scattered and only available for extremely high pressures (> 40 GPa), rendering extrapolation impossible. The recent discovery of these stable allotropes (within the last 8 years) explains the discrepancies of the shock data on boron published in the LASL shock compendium [146]. This was a key motivator for using amorphous boron particles instead of crystalline forms. The use of small particles of amorphous boron was hypothesized to increase reactivity in the Ti+2B mixture[2], but evidence was mixed, particularly under conditions of uniaxial strain loading.

4.1.2 Thermodynamic and physical properties of Boron

Boron is a highly complex semi-metal due to its five-fold coordinated symmetry (icosahedral distribution of atoms in a lattice structure) and is just beginning to be understood. The thermodynamic properties of boron relevant to this work include the Hugoniot shock properties (C_0 and S in the linear approximation of the shock speed and particle velocity behavior) and the Grüneisen constant Γ. These properties have not been measured in the published literature to the author's knowledge (in Amorphous Boron) and the stable allotropes of boron are still not well-understood. The shock Hugoniot data in the Marsh compendium [146] show wide deviations from the typical linearity observed in most metals, hinting at a potential phase transformation around a shock speed of 11-12 mm/μs as shown in figure 22a. There is also a complete lack of data up to a shock pressure of 40 GPa (Figure 22b), propagating the error in the mixture theory approximation even further.

[2]This may potentially avoid the problem of allotropy due to the enhanced stability of the frozen liquid structure of amorphous boron. However, recent calorimetry data [147] shows that crystallization may be possible at the conditions achievable in this work.

Extrapolation to atmosphere conditions of the high pressure data does not correlate well with measured properties, indicating a potential high-pressure transformation. Furthermore, there was question as to the phase that was being tested in the data presented in the compendium [29]. This is because the stable allotrope at atmospheric conditions has been a contentious issue for decades [148, 29]. The extremely high strength of boron in addition to its physical character simply compounds the difficulty in understanding the shock compression response of boron in this complex 1:2 stoichiometric mixture[3].

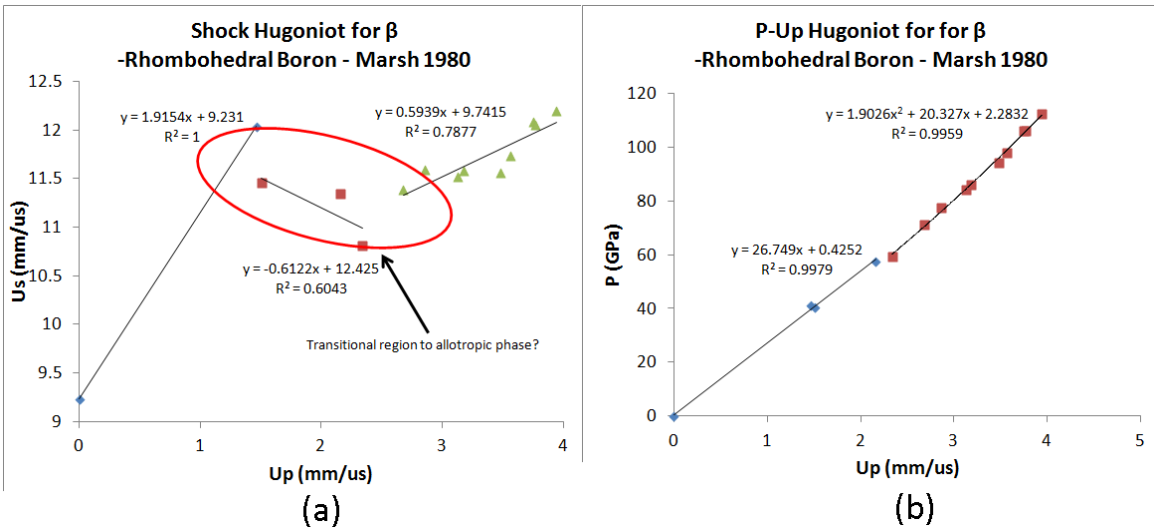

Figure 22: (a) The shock Hugoniot for what is assumed to be β-Rhombohedral Boron in U_s-U_p space as reported in the Marsh compendium [146]. There is some doubt as to whether the phase tested in this work was truly β-Rhombohedral boron. (b) The shock Hugoniot in P-U_p space shows two distinct regions with a kink around 40 GPa. The lack of data at lower shock pressures casts doubt on any shock Hugoniot constants (C_0 and S) obtained from this data.

Even with the increased interest and bolus of new work investigating this fascinating semi-metal, boron remains an ever-challenging enigma, known since 1808, but with grand fundamental questions still being addressed. For example, the stable ground state crystal phase had yet to be established until very recently [148]. This work established the α-B-to-β-B phase boundary between ~4 GPa and ~8 GPa with a linear extrapolation to ambient

[3]The 1:2 stoichiometry by its very nature creates a nearly 1:1 by volume mixture of Ti:B. Ergo, much of the microstructure volume is taken up by boron, a constituent not well-understood by the scientific community.

conditions. Their analysis concluded that it is actually the α-B phase that is the stable room temperature phase. Much of the uncertainty in the data from the Marsh compendium [146] can certainly be attributed to this fact, being that these experiments were conducted very early on with primitive knowledge of this element. There is also speculation that the high pressure data probed the γ-phase. The gas gun experiments performed in the present work are able to achieve stresses in the boron particles which straddle the phase boundary line, which merely compounds the difficulty in analysis. Figure 23 shows the new phase diagram with extrapolated boundary lines to atmospheric conditions. The boundary lines between the α and β phases are accessible in the shock compression regimes probed in the present work.

The problem becomes even more complex when considering mixtures of boron with titanium and aluminum. Boron on its own is highly reactive [29] and the possible reaction pathways (especially when also considering Al) become even more complex. Consider the Ti-B phase diagram in figure 24. The TiB_2 phase is a stable congruent line compound with melting temperature of 3215°C. Excess B above 31 wt. pct. will lead to an equilibrium of boron with TiB_2. Thus, an ample supply of boron will always be available for reaction. A smaller percentage of boron leads to other stoichiometric compounds, but these are largely metastable relative to TiB_2 [149]. The Ti-Al and B-Al phase diagrams (figures 25 and 26, respectively) also show increased complexity with large stability regions in the case of the TiAl (α) intermetallic and other stoichiometries possible. The AlB_3 intermetallic is a stable line compound with a relatively high kinetic barrier for transformation, although there has been much controversy over the existence of complex B-Al polymorphs [150]. While there may be multiple reaction pathways possible, the present work focused solely on Ti-B reactivity and Al-combustion, with the assumption that the reactivity is greater in the Ti+2B case.

What was thought to be the stablest room-temperature allotrope of boron, namely the β-Rhombohedral form, was extensively studied in the Former Soviet Union by Tsagareishvili

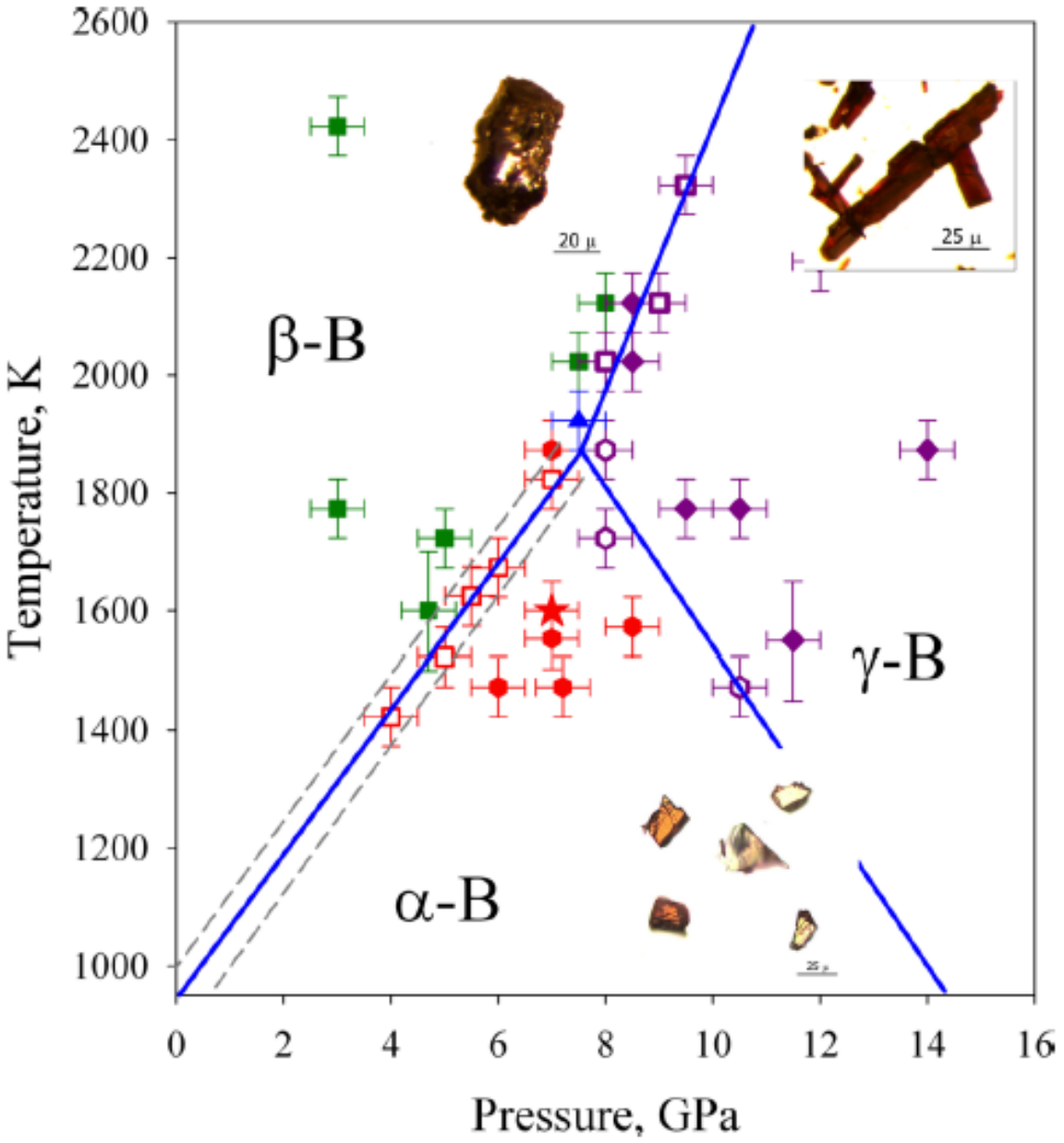

Figure 23: Experimentally-resolved P-T phase diagram of boron, showing the α-boron phase as the stable ground phase crystal.

and co-workers [151]. The higher pressure/temperature allotrope α-rhombohedral boron was also studied by that group [152]. The sound velocities were determined by Uno et al. [153] and Medwick et al. [154] using the resonant frequency method. The linear thermal expansion coefficients were investigated by Lundström et al. [155] and Tsagareishvili et al. [151]. Nelmes et al. [156] determined the pressure derivative of the isothermal bulk

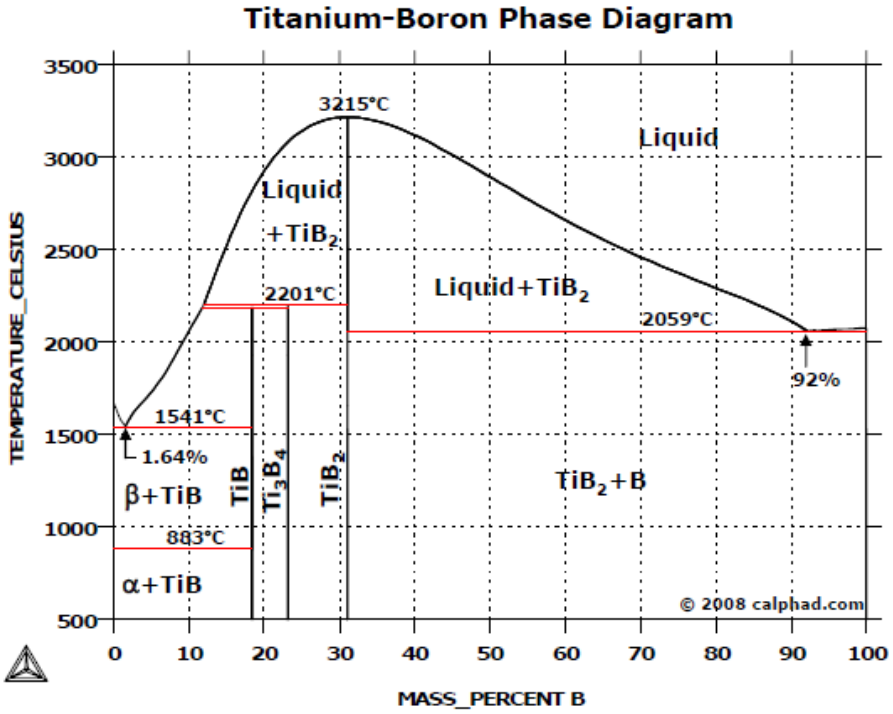

Figure 24: Updated Ti+B compositional phase diagram - Calphad database (ThermoCalc 2008).

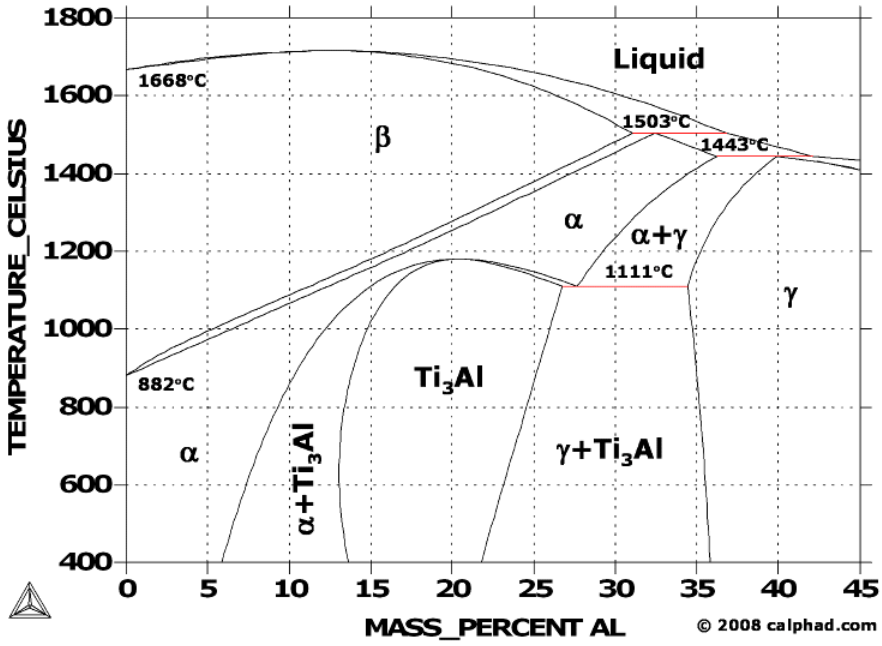

Figure 25: Ti-Al compositional phase diagram - Calphad database (ThermoCalc 2008).

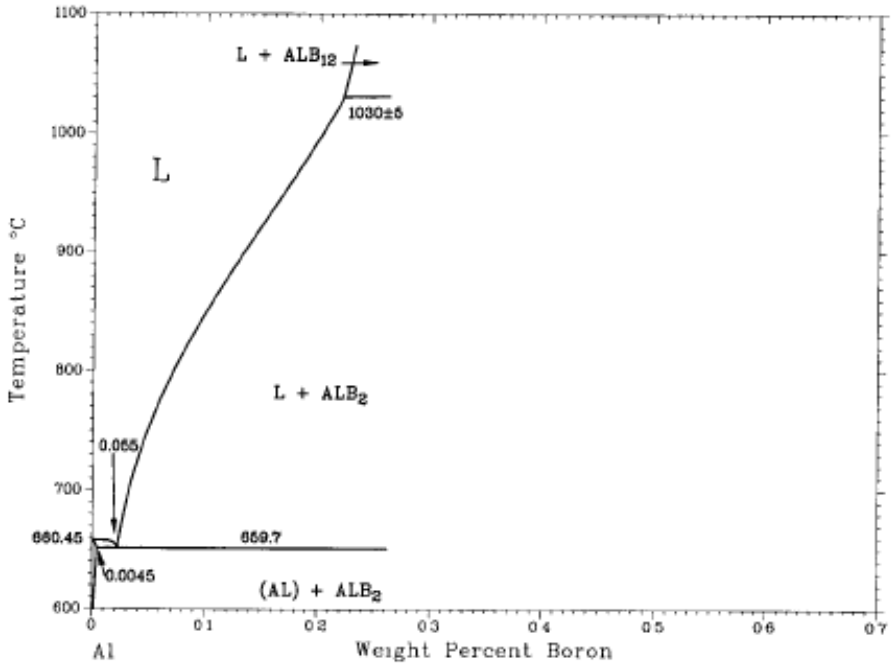

Figure 26: B-Al compositional phase diagram [150].

Table 1: Acoustic and physical properties for the materials studied in this work.

Material	C_0 (mm ·μs^{-1})	S	ρ (g·cm^{-3})	Γ	$Z = \rho_0 C_0$ (MN·s m^{-3})	σ_Y (MPa)
Boron	9.033	0.8337	2.338	1.61	21.1	**5364**
Titanium	5.22	0.767	4.5	1.09	23.5	140
Aluminum	5.35	1.34	2.7	2	14.4	35

modulus K_T' using x-ray diffraction measurements for changes in the c/a ratio of the lattice. The acoustic properties relevant to shock compression studies are summarized in table 1. The yield strengths are included in this table for comparison. Amorphous boron has one of the highest strengths of any material and the value reported in the table is based on the work by Wawner and Satterfield [157]. By far the greatest difference in properties between constituents stems from the strength difference.

Amorphous Boron is an exciting material as it possesses incredible strength [157, 158, 29] and as mentioned previously, has been shown to be highly reactive when thermally-ignited in the presence of Ti powders. Talley et al. [159] presented a synthesis method to produce “massive” amorphous boron in filament form through a hot-wire technique, which involves the reduction of a boron halide by hydrogen [160]. Wawner and Satterfield [157]

studied the tensile strength of amorphous boron filament produced by chemical vapor deposition (CVD) onto a tungsten filament, which was later etched away in hot 30% hydrogen peroxide. This involved a similar reduction process of a boro-halide, in this case BCl_3. They observed incredible tensile strengths, on the order of 400-600 ksi[4].

Unfortunately the amorphous boron EOS has not been studied, and only recent work has probed its transformation thermodynamics to the crystalline phases in calorimetry [147]. Therefore, much of the modeling and EOS properties for amorphous boron performed in the present work were an amalgamation of available properties. For example, a reliable EOS was not obtainable from the Marsh compendium, so Crockett's work [161] modeling the EOS of boron and boron carbides was used to obtain EOS properties for boron. The predicted Hugoniot from his EOS models is shown in figure 27. Crockett used the Thomas-Fermi-Dirac (TFD) models to obtain the thermal-electronic contribution to the EOS of boron and based the cold curve on diamond anvil cell work [161]. The Hugoniot in P-U_p space provided the acoustic properties shown in table 1, except for the bulk modulus, which was taken to be that of β-rhombohedral boron. This unfortunately compounds the uncertainty of the predicted EOS used to compare experimental data.

4.2 Exploring the mechanochemistry of Ti/Al/B powder mixtures

A variety of studies on shock compression of pressed powder compacts have been conducted (cf. chapter 2) exploring the transient compaction behavior, equation of state, and ultra-fast chemical reactions behind the shock front in metal powder mixtures. The early studies relied on fast measurement techniques such as Manganin stress gauges shielded from direct contact with the powder using some kind of buffer material. This was done to protect the gauge from the extreme heat generated by the chemical reaction and shock wave itself, in addition to providing some damage protection from the onslaught of the porous mixture on the gauge. The advent of nanosecond-resolution stress gauge measurements

[4]These were the values used for the constitutive models employed in meso-scale simulations.

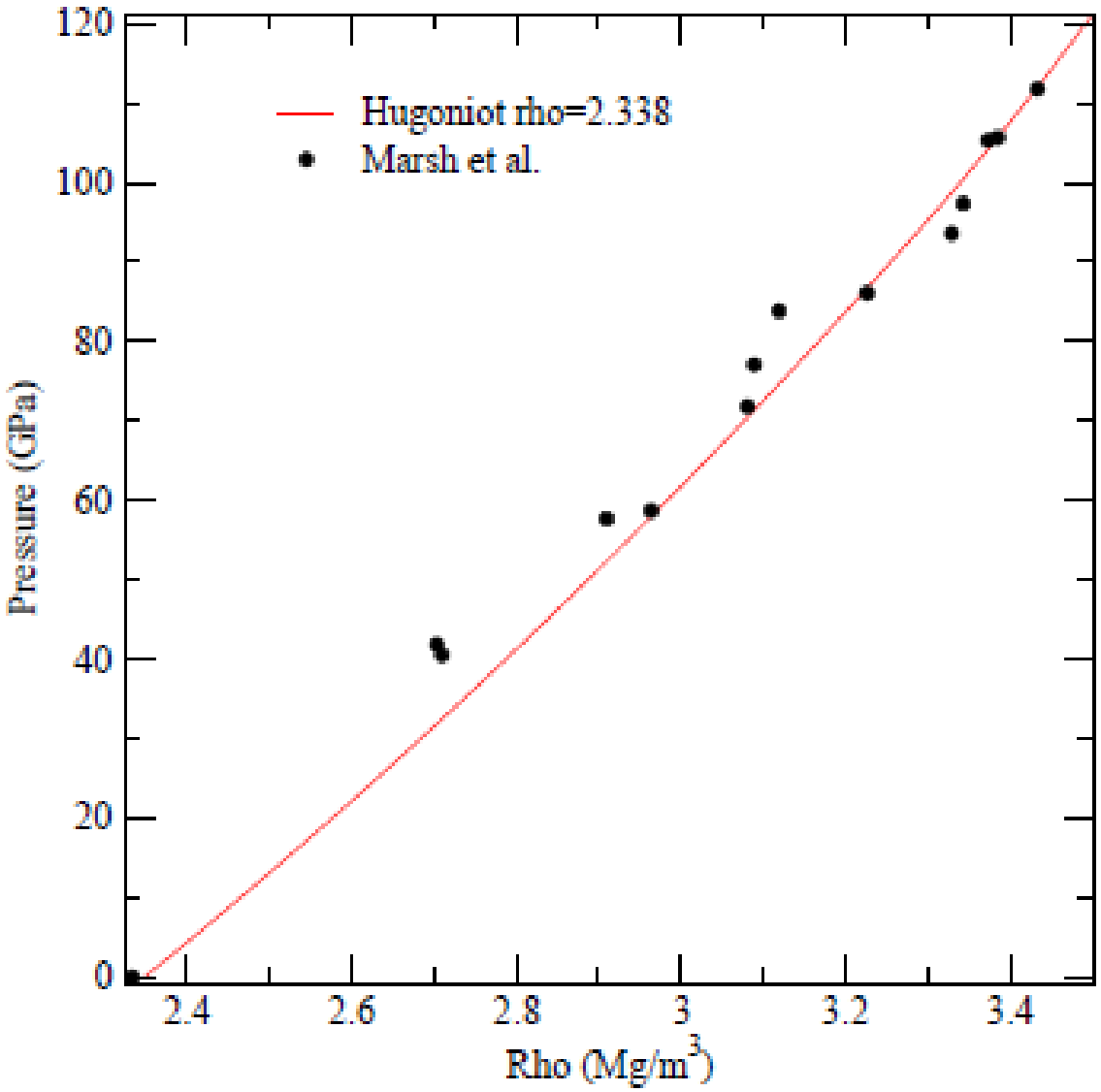

Figure 27: Hugoniot prediction from Crockett's work [161] on boron and boron carbide. This prediction was based on EOS simulations using Thomas-Fermi-Dirac (TFD) models.

employing piezoelectric (self-powered) gauges provided the opportunity to explore the transient compaction response and potential ultra-fast signals generated in a shock-induced chemical reaction. These gauges were utilized successfully by many workers investigating shock-induced reaction phenomena in reactive powder mixtures [9, 41, 42, 93, 92, 13].

As stated previously, the disparate nature of the time and length scales involved during a chemical reaction complicates experimental measurement. Furthermore, it becomes difficult to isolate and decouple the individual phenomena occurring through the length

scales with the traditional experimental techniques used in shock compression science (e.g. free surface velocity measurements with VISAR, stress measurements using piezoelectric gauges, etc.); the effect of each phenomena will invariably be smeared by the measurement device.

These techniques, while extremely useful and proven to be robust, still only provide an indirect observation of the prevailing phenomena. However, they remain a powerful tool and an integral part of any investigation into material behavior under shock compression and high-strain-rates. Integrating computational techniques and in-situ spectroscopic diagnostics with traditional measurement techniques can help resolve the phenomena and provide insight into the material behavior through a variety of length and time scales. Implementing a tool with improved spatial and temporal resolution such as the streak-camera-assisted Line-VISAR can further improve our understanding of the processes involved, but will still only yield indirect information about how the wave propagation mechanics are potentially disrupted by a reaction event.

The ternary mixture investigated in the present work was found to be much more complex than originally thought, and an adequate equation of state approximation from conventional mixture theories was found to be intractable; the EOSs generated were a first-order approximation. PVDF stress gauges were difficult to implement as measurement devices in direct contact with the powders due to the vastly different strengths and sizes of the boron particles relative to the gauge and adjacent titanium and aluminum powders. This led to extreme deformations of the gauge as evidenced from simulations. Many experiments did not produce equilibrated stress profiles at the input gauge; in these cases, the gauges served mainly as time-of-arrival (TOA) sensors, whereas other researchers were able to obtain equilibrated profiles[5]. VISAR traces were found to provide a more reliable measurement of the peak velocities, but measurements were highly convolved with

[5]Ni/Al mixtures were extensively studied using PVDF stress gauges and reliable profiles were obtained, especially when the particle morphologies facilitated a flatter shock-wave profile (i.e. closer to an idealized shock)

the compaction phenomena which was obscured by fringe contrast loss. Early compaction events were captured by both sensors, but added an extra level of noise to the data because of the uncertainty in the wave arrival time.

4.3 Powder Mixture Preparation

4.3.1 Mixture details

Different mixture stoichiometries for the powders were made based on either a pre-set specific volume fraction for a certain mass of powder or based on a desired molar ratio of the constituents. A variety of mixtures were also created for the purposes of material characterization (particle extraction for use in simulation). The ternary mixtures were designed to be volume-fraction-based, with some constituent (namely Al) making up some volume fraction of the mixture, with the rest of the mixture being made up of the remaining constituents in a particular ratio. As in Horie's work [36], a stoichiometric mixture was selected, in this case a 1:2 molar ratio of Ti:B in the hopes that the molar ratio would provide enough boron to support the Ti+2B reaction pathway. Similar approaches have been taken in other works [162, 163, 42, 92]. Other mixture stoichiometries were considered (1:3 and 1:4 molar ratios of Ti:B) hypothesizing the need for excess boron to be available for reaction. An excess of boron was initially thought to be helpful because it would permit an abundance of a reducing element to be present. However, this idea was discarded because the form of the boron (small amorphous boron particles) would cause it to have a much greater surface area than Ti (sponge Ti morphology at a mean particle size of around 20 μm), and would lead to boron agglomeration during mixing and pressing. This was shown by the author in a published work [164]. The 1:2 molar ratio of Ti:B is the baseline mixture for all experiments in this work.

Other works (See Eakins' review article for more information [13]) have revealed that different mixture ratios are better suited for the development of a dynamically-induced chemical reaction and have also been selected to isolate a specific phenomenon. Horie et

al. [14], for example, selected a non-stoichometric Ni/Al mixture, with a molar ratio of 2.604 Ni:Al, because a fully densified compact of the Ni/Al powder would have a similar impedance to the impactor that was selected for the experiments (304 stainless steel). The impedance-matching permitted any chemical reaction signatures in the form of "excess pressure" to be captured since a consistent baseline stress can be measured and compared with the inert mixture pressure (McQueen's method) without any overshoots due to impedance mismatch. Thus, the authors selected this mixture stoichiometry to specifically test whether excess pressure was present as a function of input stress, irrespective of impactor impedance. In contrast, the present work tests the shock compression response of a particular mixture stoichiometry and uses baseline mixture theory to infer a reacted state due to a Ballotechnic-type expanded state. While this is an accepted method to discern if a potential reaction event occurred, the method infers this indirectly.

Initial uniaxial stress experiments used a ~325 mesh equiaxed Ti powder acquired from Cerac and a ~325 mesh β-rhombohedral B powder supplied by Alfa-Aesar mixed in a 1:2 molar ratio. Preliminary characterization work and initial exploratory uniaxial stress loading experiments were performed with these powders, henceforth called *Set 1* after Gurumurthy [165]. However, these mixtures were discarded in subsequent experiments in favor of using a ~5 micron average particle size amorphous boron powder obtained from Alfa-Aesar (irregular/flake morphology) mixed with a sponge Ti powder (~625 mesh) from Atlantic Equipment Engineers (AEE); mixtures derived from these powders are henceforth known as *Set 2* mixtures. This was due to the larger reactivity of the amorphous boron powders observed in tests conducted by the Navy[6]. All experimental results described in the work were conducted on the sponge Ti and amorphous B powders and the subsequent descriptions pertain to *Set 2* mixtures. Every mixture considered in this work also maintains the Ti:B molar ratio at 1:2 in order to simplify comparisons between Al-containing mixtures. Any mixture containing Al is volume-fraction-based (A specific volume fraction

[6]These experiments have revealed a lower energy threshold for reaction in the context of thermal ignition.

of Al) with the remaining mixture consisting of the 1:2 molar ratio for Ti:B.

Table 2 summarizes the powder mixtures that were used in the present work. The shock compression experiments were focused on Mixture A and C due to the limited resources and time required for the experiments. The uniaxial stress loading experiments employed mixtures A-D.

Table 2: The powder mixtures used in this work. Mixtures A and C were the principal focus of the uniaxial strain experiments. The mixture stoichiometries were identical for sets 1 and 2. More information on the characterization methods is provided in chapter 5.

Mixture Label	Constituents	V_f (Al)	Experiments
A	Ti+2B	0%	Uniaxial Stress/Strain
B	Ti+2B/25%-Al	25%	Uniaxial Stress
C	Ti+2B/50%-Al	50%	Uniaxial Stress/Strain
D	Ti+2B/75%-Al	75%	Uniaxial Stress

The powders were weighed relative to a 100 g total mass basis for Ti such that the 1:2 molar stoichiometry was achieved for Ti and B. All weight measurements were accurate to ± 0.01 g and every effort was made to prevent any powder loss during transfer from containers, weigh boats, and mixing apparatuses. Any powder loss was accounted for by weighing the container pre and post powder transfer. The powders were first dried in an 110°C oven for 24 hours prior to mixing and later transferred to sealed containers under an Ar atmosphere. These containers were then transferred into a V-Blender for an additional 24 hours mixing to ensure a uniform-random mixture of powders. Figure 28 shows the starting powders imaged by an SEM. The Al powders are spherical and equiaxed with an average particle size of ~6 μm max. The boron powders were very difficult to image and were of an irregular/flake morphology. The Ti powder was composed of topologically-complex particles and were sieved using a ~625 mesh.

4.3.2 Isostatic compaction and imaging of powder compacts

The powder mixtures were prepared for experimentation and characterization via isostatic compaction in cylindrical M-2 tool steel dies of various diameters. The powder mixtures

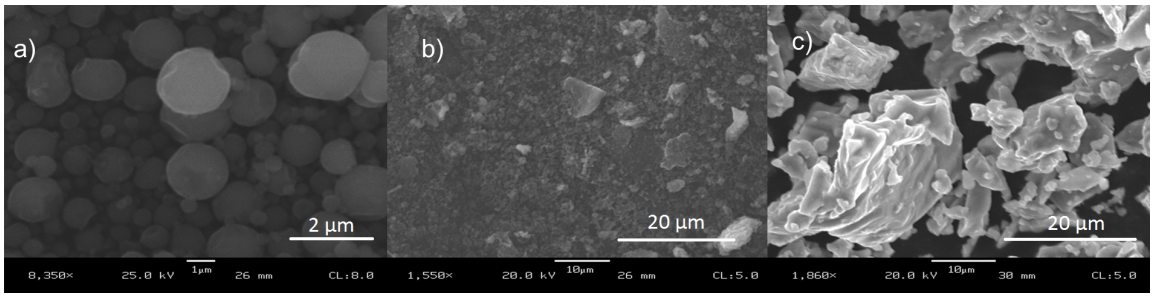

Figure 28: (a.) Valimet H-2 atomized Al powders are spherical and equiaxed, with an APS of ~3 µm max. A large number of particles are observed to be nanometer sized. (b.) Alfa-Aesar amorphous boron with an APS of < 5 µm shows an irregular/flake morphology. The low atomic number of B made it particularly difficult to image in the SEM. (c.) Atlantic Equipment Engineers (AEE) sponge Ti powder with a sieve rating of ~625 mesh shows jagged, topologically-complex particles.

were compressed in a Carver 50,000 lb capacity hydraulic press through a load-controlled setting for a variety of load durations. The load cycles were selected based on trial and error, with the final dimensions of the powder compact being the controlling factor. Powder was weighed depending on the desired %TMD post-compaction, assuming a final compact height (cylinder height) and constant die diameter:

$$m_{powder} = \rho_{th} \Phi V_{compact}. \tag{125}$$

The theoretical density of the powder was based on a rule-of-mixtures:

$$\rho_{th} = \sum_{i} V_{f,i} \rho_i, \tag{126}$$

where the density ρ_i and volume fraction $V_{f,i}$ of each component i are known a priori. Table 3 summarizes the volume and mass fractions for each mixture considered in this work. The load necessary to compact the powders to the desired compact dimension (height) is a function of the powder crush strength. The Fischmeister-Artz model (equation 76) was used as a baseline theory to help predict the load required to compact the material assuming the third stage of compaction (i.e. fracture) was reached upon load saturation. In other words, when further load application was unable to produce measurable change

in the punch-depth within the cylinder, it was assumed that any further load would lead to particle fracture. This model was used to obtain a ballpark estimate of the load required to achieve the dimensions required for the compact (to within ±4% TMD).

Three distinct compact sizes were considered. A 0.5 in-diameter compact (5 mm height) was created for the purposes of microstructural characterization for the various mixtures. A $\frac{1}{8}$"-diameter compact (2 mm height) was used for the uniaxial stress loading experiments in order to fit onto the 7.62-mm-dia. copper rods. Lastly, 50.8 mm diameter (4 mm height) compacts were pressed into the copper capsules used in the shock compression experiments. These dimensions were selected to ensure a compact aspect ratio of at least 15:1 to minimize potential edge effects on the wave propagation through the powder. Limitations in gun bore size for the high velocity experiments later conducted at Eglin AFB required compact diameters of 38 mm. The compact thickness also reduced somewhat to ensure that the %TMD was obtained consistently for each load condition, but still maintaining a large aspect ratio to limit edge effects during shock compression. This only affected three experiments. The powders were weighed based on the same assumptions stated above. Table 4 summarizes the load recipes used to compact the powders depending on the compact size and powder mixture.

Compact characterization was done to assess the constituent distribution and extract the individual particles through a montage serial sectioning method and create a library of individual particles. This allows for precise microstructural representations to be simulated to determine their effects on the bulk response observed in the experiments. Further details on the characterization are described in chapter 5.

Table 3: The theoretical densities and volume/mass fractions for each constituent and its corresponding mixture.

Mixture Label	Theoretical Density (g/cm^3)	V_f (B)	V_f (Ti)	V_f (Al)	m_f (B)	m_f (Ti)	m_f (Al)
A	3.52	0.46	0.54	0	0.31	0.69	0
B	3.32	0.35	0.40	0.25	0.25	0.55	0.20
C	3.11	0.23	0.27	0.50	0.18	0.39	0.43
D	2.91	0.12	0.13	0.75	0.09	0.21	0.70

Table 4: Load recipes employed in the preparation of powder compacts in this work. A Carver hydraulic press (50,000 lb max capacity) was used to compress the powders in M-2 steel dies or directly into the copper capsules for the uniaxial strain experiments. These recipes produced compacts with consistent %TMD (to within ±4%). The achievable %TMD varied based on mixture and was typically limited by the pure Ti+2B mixture. The Al-containing mixtures had to be pressed at lower loads to consistently produce the same %TMD as the pure Ti+2B mixture.

Compact type	Compact dimensions (mm)	Φ (%TMD)	Load dwell time	Max Load (lb)
Mixture A - Uniaxial Stress	$\phi = 3.175$, $h = 2$	75	30 s dwell	5000
Mixture B - Uniaxial Stress	$\phi = 3.175$, $h = 2$	75	30 s dwell	2700
Mixture C - Uniaxial Stress	$\phi = 3.175$, $h = 2$	75	30 s dwell	2000
Mixture D - Uniaxial Stress	$\phi = 3.175$, $h = 2$	75	30 s dwell	1200
Mixture A - Uniaxial Strain	$\phi = 50.8$, $h = 4$	50	100 s dwell	25000
Mixture C - Uniaxial Strain	$\phi = 50.8$, $h = 4$	50	100 s dwell	14000
Mixture A - Uniaxial Strain (Eglin)	$\phi = 38$, $h = 3.2$	50	100 s dwell	25000
Mixture C - Uniaxial Strain (Eglin)	$\phi = 38$, $h = 3.2$	50	100 s dwell	14000
Mixture B - Characterization	$\phi = 12.2$, $h = 5$	75	60 s dwell	20000
Mixture C - Characterization	$\phi = 12.2$, $h = 5$	75	60 s dwell	15000
Mixture D - Characterization	$\phi = 12.2$, $h = 5$	75	60 s dwell	10000

4.4 Uniaxial Stress Experimental Setup

Uniaxial stress loading conditions are produced when a long slender rod impacts a flat anvil, producing unconfined deformation in the radial direction of the rod. The deformation travels through the rod in the form of a plastic wave, which eventually stops propagating (or slows down/speeds up) when it interacts with a free surface or different impedance material. The extreme strains and strain rates experienced by a bulk solid under high velocity impact can lead to strain localization (material-driven), increased bulk heating due to plastic dissipation, and catastrophic fracture. The rod-on-anvil Taylor impact test provides the quintessential test to access these dynamic conditions. A rigorous analysis of the plastic wave propagation has been provided independently by Rakhmatulin, Taylor, and Von-Karman and Duwez [166, 167, 168]. The configuration can be modified slightly to include a reactive material under the uniaxial stress conditions unique to the Taylor test. Compacts of reactive powder mixtures may be analyzed such a Taylor rod-on-anvil impact setup and evidence of the deformation characteristics of the impact event may be found through high-speed imaging. In-situ chemical analysis through spectrography can provide an intimate picture of the chemical event, including the delineation of the possible reaction pathway and location of reaction initiation point [169].

Uniaxial stress experiments were conducted via photographic and videographic evidence of the post-impact deformation of the material and the observation of light emission as a potential descriptor of chemical reaction in the material. The camera settings became a crucial controllable variable in these experiments because the lower intensity of light emission in the Ti+2B reaction was obscured by the flashing mechanism of the camera. This had to be fine-tuned to be able to capture the light emission evidence necessary to assess whether an impact-induced chemical reaction potentially occurred in the material under consideration. This method could not discern whether the light emission came from

heating, impact flash[7], or any other source and thus only serves as a potential indicator of a reaction event. Further spectroscopic evidence is needed to clarify the source of light emission and whether a chemical reaction occurred as well as its cause.

Pellet-mounted rod-on-anvil impact experiments were conducted with mixtures ranging from pure Ti+2B (1:2 molar ratio), to mixtures containing Al in 25% by volume increments up to 75% Al. Figure 29 shows the configuration of the camera and light gas gun used for these experiments. Pellets 1/8" in diameter were isostatically compressed to a density of about 75% TMD ±4%, which was the maximum consistently achievable density for the Ti+2B powders (the limiting factor in pressing these pellets) within the stress tolerances for the M-2 steel dies. Higher pressures were required for greater densification, but were unobtainable due to the high crush strength of the mixtures and the higher B content required to achieve the Ti+2B stoichiometry. The same powder sources were used for each mixture, which consisted of the sponge Ti powder (AEE ~ 625 mesh), a spherical atomized Al powder (Valimet H-2), and amorphous boron (Irregular/flake Alfa-Aesar ~ 5 μm). These pellets were epoxy-mounted to a lapped copper rod ~30 mm long and were fired onto a maraging steel target. The impact events were recorded on a Hadland IMACON framing camera and NAC high speed video camera[8]. A laser-interrupt system (figure 29) was used to measure the velocity of the projectile based on the separation distances of the laser beams and an up-down counter recording the triggering times of the laser interruption by the projectile.

The experiments were performed both in air and in a < 100 mtorr vacuum to obtain a baseline response (i.e. to successfully capture luminescence with the cameras, without the camera flash interfering with the event.) and set the flash and gain values for the camera.

[7]The very nature of the impact led to light emission, possibly due to air ionization or plasma emission at the instant of impact. This was observed even in cases where light emission was not expected, as in a baseline experiment using only a copper projectile machined to look like the reactive pellet mounted experimental setup. Details are provided herewith.

[8]The high speed video camera was added for later experiments to confirm earlier observations

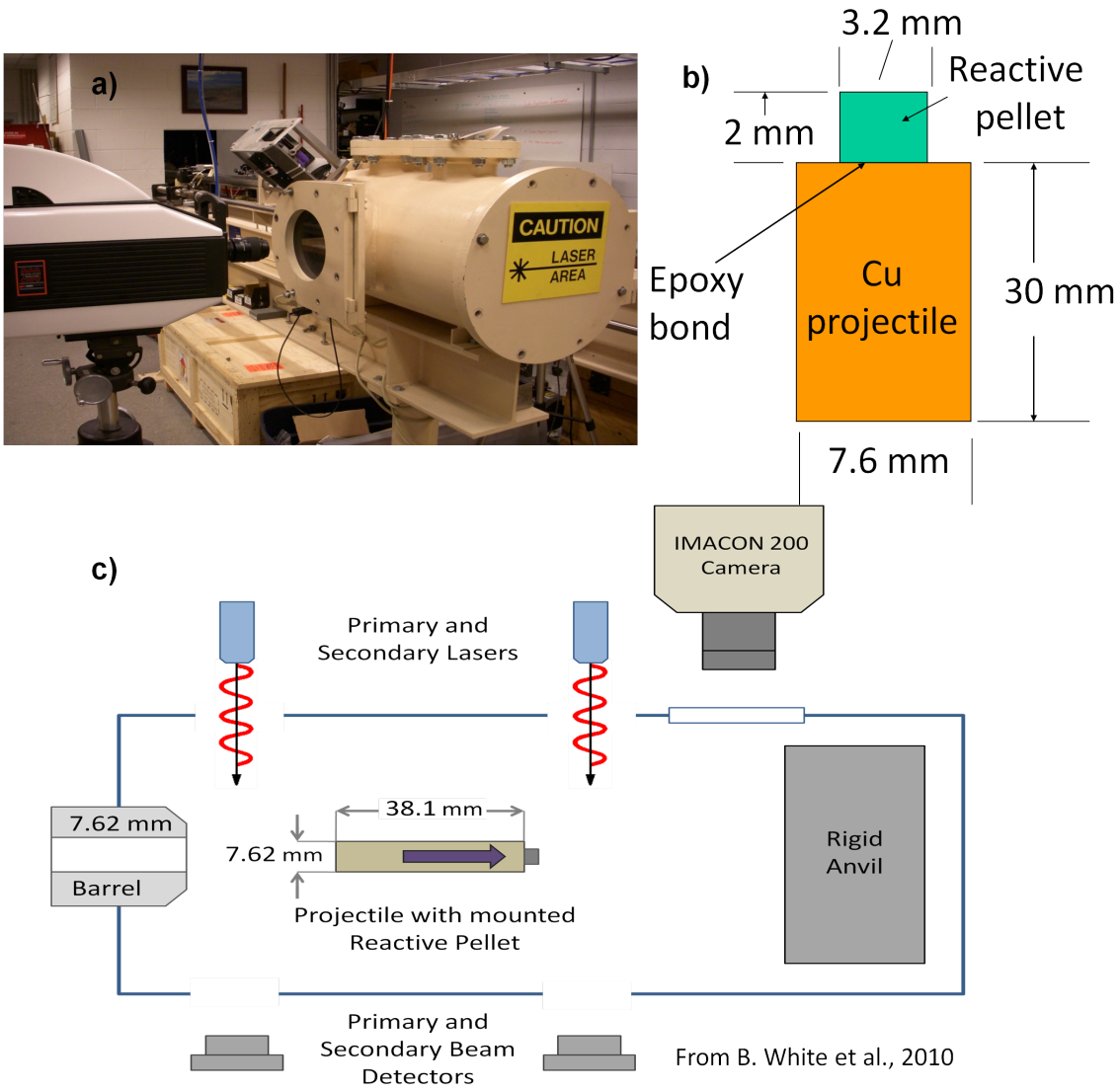

Figure 29: The 7.62 mm light gas gun at Georgia Tech was used to fire reactive pellets mounted on 7.6 mm diameter rods onto a maraging steel target. This system uses a laser-interrupt system to measure the impact velocity of the projectile. An IMACON framing camera and NAC high speed video camera (not shown) were aligned to capture images of the impact event.

Multiple experiments were conducted at higher gain and flash values to capture the rod/-compact silhouette geometry. Unfortunately, camera and flash triggering and timing issues plagued initial experiments, rendering the results unreliable. Furthermore, initial experiments used greater flash bulb values ($>$ 144) and gain to capture a crisp projectile image,

but at the cost of potentially obscuring faint light emission from a potential chemical reaction. It was decided to forgo the camera flash for the finalized go/no-go experiments so that the only light captured was unequivocally from the impact event and not the camera flash.

4.4.1 Discerning reactivity from light emission

The initial uniaxial stress impact configuration relied solely on photographic evidence of light emission from the IMACON framing camera. Timing issues coupled with the potential for the external camera flash to obscure light from a chemical reaction motivated the use of a longer recording window camera. The utilization of the NAC high speed video camera greatly aided the uniaxial stress impact experiments due to the broader recording window versus the IMACON framing camera. This is crucial as there is potential for light emission from impact heating alone or from other sources such as oxidation and air entrapment/-jetting between the projectile and anvil surfaces. It was assumed that chemical reactions arising from the reactive pellet would emit light for longer durations than the light from impact heating alone, as heat dissipation through heat conduction/radiation in the air would rapidly decay the emission intensity. The light from a chemical reaction would also show up in a debris cloud at later times, which was difficult to capture with the IMACON camera alone.

Experiments conducted on pure copper projectiles with the impact side machined (as a stepped projectile) to simulate a mounted pellet showed a substantial amount of light emission similar to that observed for a pellet-mounted experiment as shown in figure 30. These images show pure copper emitting a flash of light right at the impact and after the crush-up of the copper "pellet" (the stepped-part of the copper rod) at an impact velocity of 367 m/s (Camera gain at 7 with 44 flash intensity). This may be due to the actual geometry of the impact configuration, which promotes high speed jetting and material instabilities at the impact site, leading to large temperature localization and even oxidation of the copper projectile. However, the light emission in this case did not last beyond two NAC frames

spaced 5.2 μs apart, which helped distinguish it from actual chemical reactivity produced from a reactive pellet. Again, it is important to note that chemical reactions from reactive powder compacts emit a long-duration light which can last tens to hundreds of microseconds. The continual mixing of components in the debris cloud that forms subsequent to the full the leading to subsequent reactions can also be captured by the long recording window of the NAC camera. Only a large recording window allows these events to be discernible.

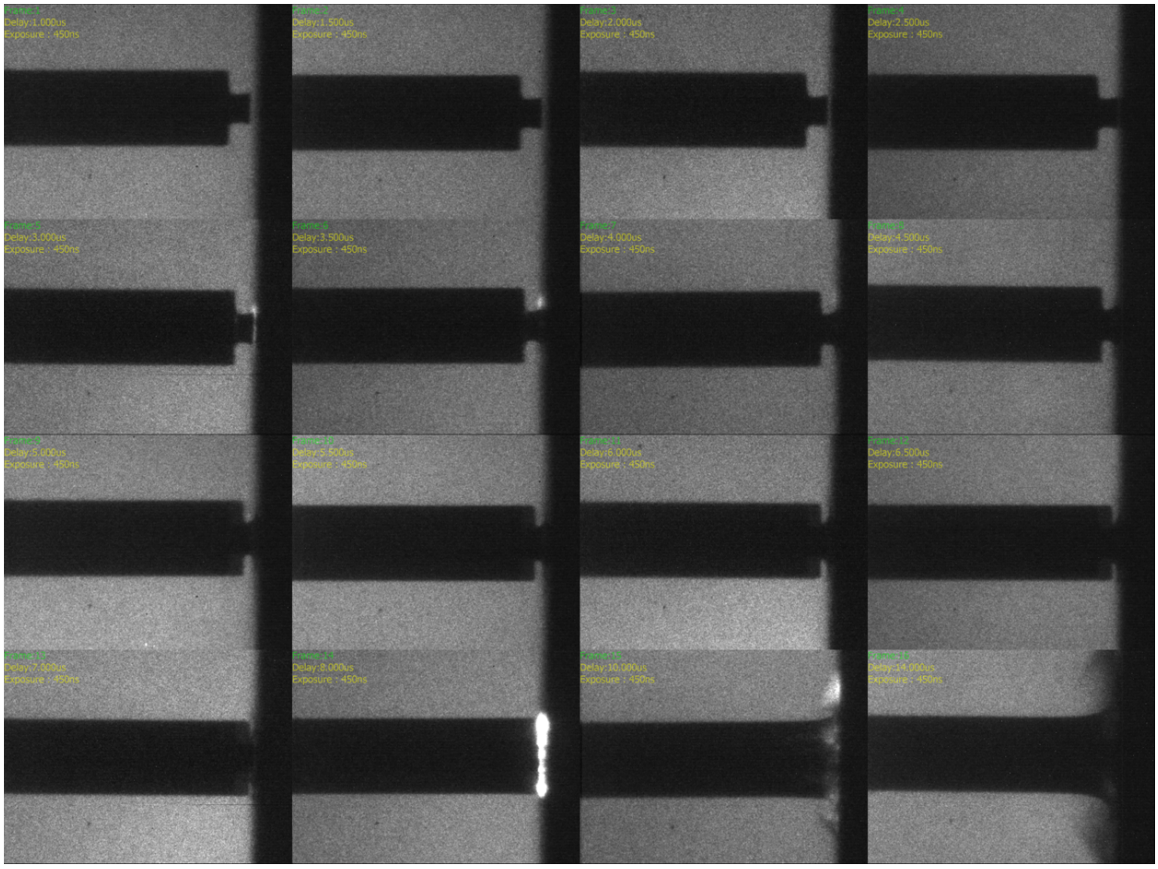

Figure 30: IMACON capture of a copper projectile impact test. The copper rod is lathed at the impact side to simulate a reactive pellet. The experiment was conducted at an impact velocity of 367 m/s and showed pronounced light emission both at the crush-up phase and right at impact. The emitted light dissipates after about 5 μs and is no longer subsequently observed. The same camera settings were used for these pure copper projectile experiments.

It should be noted that the light emission from the copper rod alone was not observed for velocities lower than the sound speed of air, as shown in figure 31. An initial hypothesis explaining this light emission was made, wherein a small air pocket entrapped by the

projectile generates a small shock wave due to the pressure difference, heating the air in the vicinity. Light emission observed right at impact may be due to this heating, resulting in air ionization. Luminescence was observed even when helium was back-filled along with the air in the chamber and also under evacuated conditions (< 150 mtorr). It can be therefore inferred that the light emission phenomena can arise from sources that normally would not interfere with the physical phenomenon of chemical reaction in the powder.

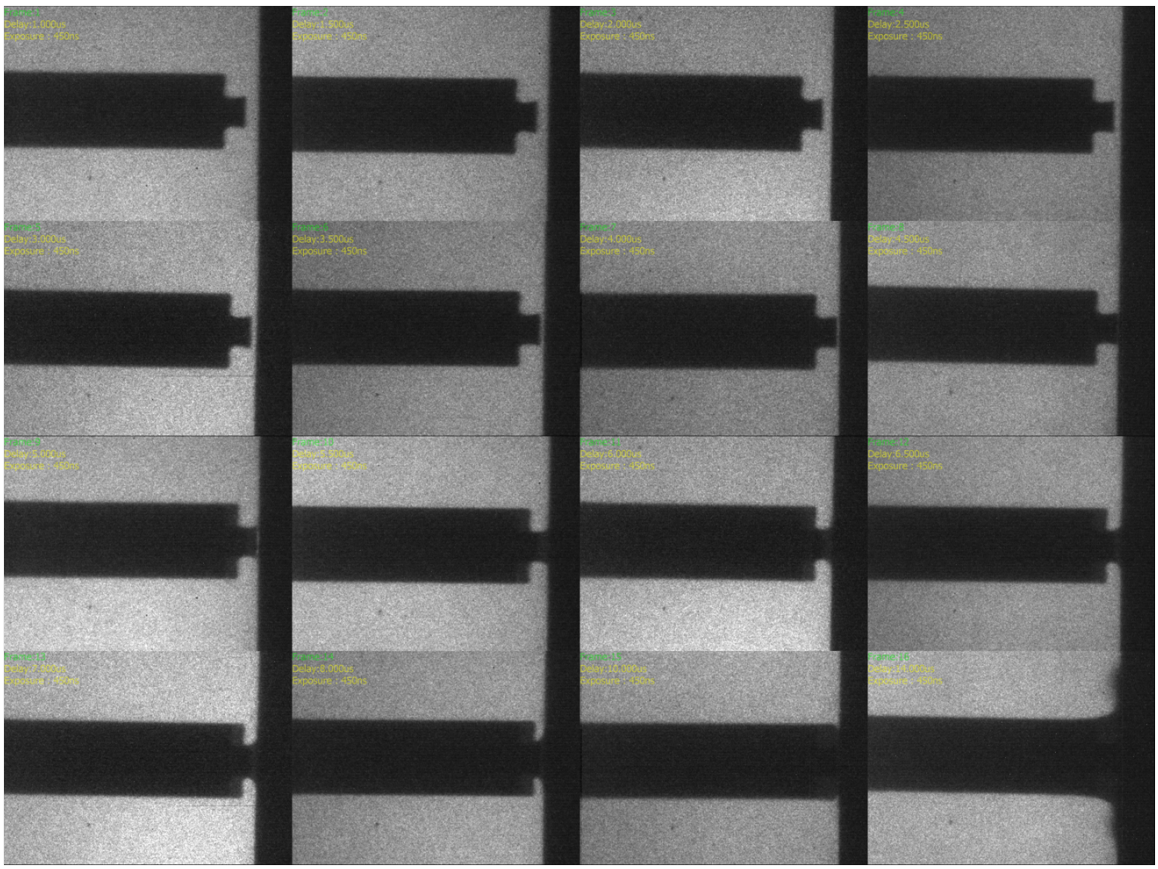

Figure 31: IMACON capture of a copper projectile impact test. The copper rod is lathed at the impact side to simulate a reactive pellet. No luminescence was observed for an impact velocity of 338 m/s (below the sound speed of air). Impacts of lower velocities showed similar results.

The occurrence of chemical reactions can be better assessed by distinguishing long-duration light emission from short duration events such as from heating/oxidation of the copper. Though the experimental configuration as it currently stands cannot causally link the chemical reaction, nor its source to the light emission, the long-duration light emissions

(reckoned as chemical reactions) can definitively be captured and distinguished from short-duration events. The go/no-go results presented in this work were collected by assuming any long-duration light emission was caused by the reaction in the pellet irrespective of whether or not the event occurred pre or post-impact with the copper rod, which was intended to only serve as a sabot to carry the reactive material to the anvil. Thus, the criterion selected in the present work to consistently assess the occurrence of impact-induced chemical reactions under uniaxial stress dynamic loading (on a go/no-go basis) is **if the observed luminescence lasted for more than two NAC frames, spaced 5.2 μs apart.**

4.5 Uniaxial Strain Experimental Setup

The shock compression of powder compacts made of Ti/Al/B powders was probed in this work via parallel-plate impact experiments using ultrafast time-resolved diagnostics to measure the signal arrival times of the imparted wave as it travels through the powder. These techniques provide a highly accurate measurement of transit time of a disturbance as it passes into the powder and arrives at the back surface of the powder, where it interacts with a backing material. The disturbance at the backing material interface can be tracked using laser interferometry (VISAR) and directly with the in-situ stress gauges used to measure wave transit time, and can be directly compared with calculations using impedance-matching techniques. The measurements also provide insight into the rise-time response of the powder, its eventual steepening at higher shock pressures, and the actual structure of the wave front. The wave front structure was found to be associated with the compaction response of the powder mixture and became less important at higher pressures, but nevertheless created difficulties when attempting to calculate transit times using these signals.

4.5.1 Capsule design and preparation

Copper capsules were constructed to encapsulate the powders. These capsules consisted of a copper ring (O.D. = 2.25 in, I.D. = 2 in.) and a copper driver faceplate that fastens

onto the ring using countersunk screws. The powder is pressed directly into the ring with a dummy copper driver attached, and a backing window (in this case, fused silica) is press-fit into the assembly. Previous experiments conducted in this lab used the same capsule design wherein the powder was pressed directly into the capsule and the driver plate already had the gauge attached. A key difference for the present work is that because of the high crush strength of the Ti+2B mixture (requiring 25000 lb load to press to 50% TMD), there was concern for the integrity of the gauge. Therefore, the powder was pressed into the "dummy" copper plate. The dummy plate was then removed and the driver with the attached gauge was carefully fastened into the ring. The fused silica window allowed for rear surface measurement of particle velocity between the powder/window interface. A 50% TMD was selected because it was the highest density achievable for Ti+2B without deforming the ring assembly. The experimental configuration is shown in figures 32 and 33, where the rear of the target assembly (figure 33b) shows two current-viewing resistors (CVRs) soldered onto the PVDF stress gauges. The PVDF gauges manifest a charge, which can be converted to a pressure as a result of the sensitive biaxial-stretching and poling process developed by Bauer [170, 171, 172, 83].

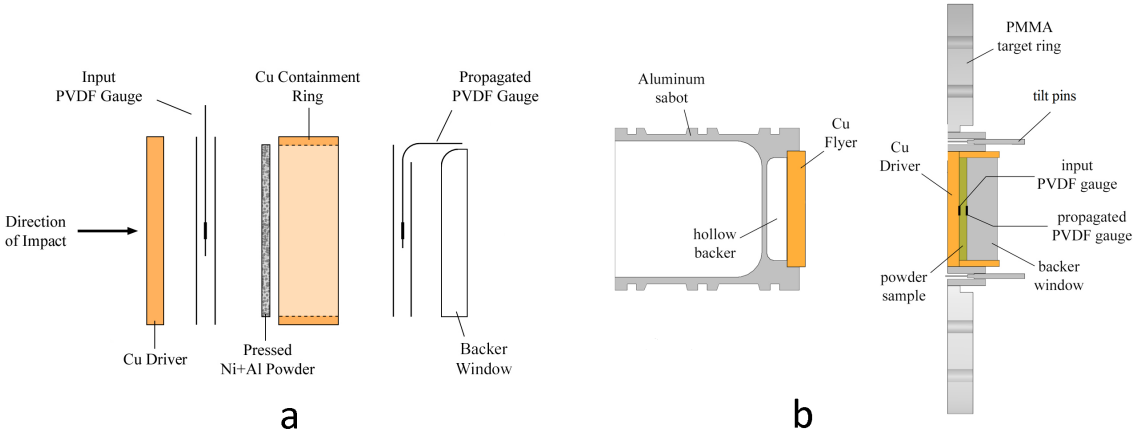

Figure 32: (a.) Schematic of the powder containment capsule used in the experiments. The gauge package is exploded showing the sandwiching layers of PTFE and the PVDF gauge. The last layer of PTFE is coated with 150 nm of Al (or 17 μm of foil in later experiments) to reduce pyroelectric interference. (b.) Impact experiment setup showing an Al sabot carrying the flyer plate (either copper, tungsten, or tungsten heavy alloy) [20]

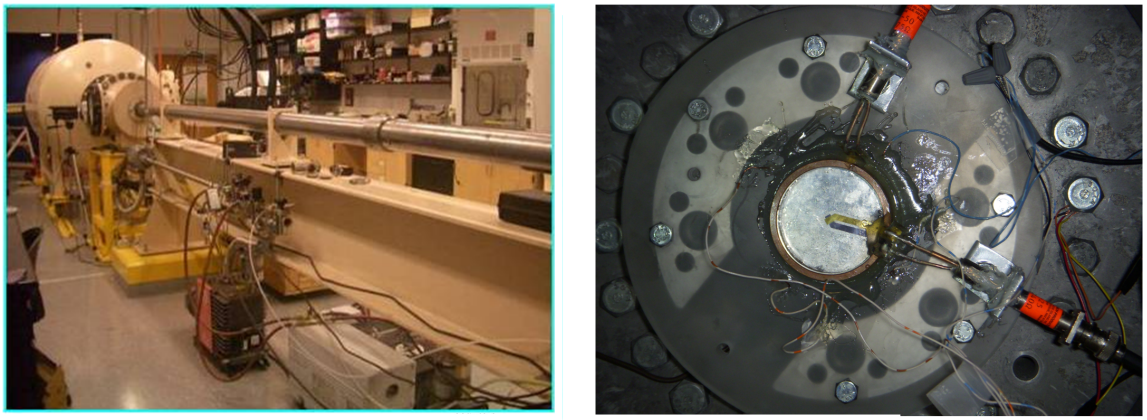

Figure 33: (a.) Georgia Tech Helium-driven 80 mm light gas gun used in highly reproducible shock compression studies. (b.) Typical target assembly showing the powder capsule (center) surrounded by tilt pin wires which provide time signatures of the wave arrival - an indirect measure of tilt during impact. The CVRs solder onto the PVDF gauges as shown and are held on L-brackets using 5 min non-sagging epoxy.

4.5.2 Diagnostics

The PVDF stress gauges (Piezotech S.A.S. - Hesingue, France) are epoxied onto sandwiching layers of 0.001 in. polytetrafluoroethylene (PTFE) sheets to isolate them from the copper and fused silica surfaces (Figure 32a). A 150 nm thick Al coating was sputtered over the sandwiching layers of PTFE to protect the gauge from pyroelectric interference due to shock heating of the PVDF [88, 83]. Two later experiments substituted 17 μm thick Al foil in place of the Al coating. However, an anomalous reading was recorded in the input trace for these two experiments (Experiments 1309 and 1310), due perhaps to the ringing up to the pressure in the higher impedance Al versus the lower impedance PTFE, being that the thickness in the foil is similar to the PTFE. The gauge was only able to record about 20-40 ns of data, concomitant with the travel time of the shock through the gauge package. It was therefore decided to use the sputter process on the subsequent experiments. The CVRs are connected via shielded cabling to a Tektronix DPO70804 8 GHz oscilloscope with a time resolution of 40 ps per data point and the signals from each gauge are split through 50 Ω power tees into low and high resolution channels, requiring a recombination step during

post-processing to combine the signal peaks with the reduced-noise fine resolution data. Four shorting pins provided three independent measurements of impactor velocity with an overall uncertainty of better than 0.5%.

The particle velocity of the powder is impedance-matched using the Rankine-Hugoniot conditions based on the shock speed and measured impact velocity. The stress value measured from the gauge is then correlated with this value using impedance-matching and if a direct measurement of stress is possible, the error bar is augmented by the calculated value when presenting the data[9]. Preliminary analysis of the data evaluated shock speed based on an average of three distinct transit time measurements of the wave through the thickness of the powder compact: at 10%, 50% and 90% rise times to the peak stress values recorded in the experiment for both the driver and backer gauges. However, the highly-dispersed nature of the propagated stress wave created enormous scatter and uncertainty in the measured shock speed. **In the present work, the wave speeds were calculated measuring the transit times between the toes of the waves (i.e. the first detectable arrival signal at the gauge), which provided the most consistent methodology and avoided dispersion effects of the compaction of the powder mixture. This is the methodology adopted for shock speed measurement in the present work.** Further details are provided in chapter 6.

The stress measurement from the PVDF gauges provides the hydrostatic component as a function of charge. Each experiment provides a pressure trace (pressure v.s. time) at the interface between the gauge and the powder on the driver and backer sides. A pressure value is selected based on the time at which the average voltage trace (smoothed with 50 points) first reaches a zero steady-state value. The error bar for the pressure is selected based on the pressure values recorded at times equal to the transit time of the shock wave

[9]All quantities arising from more than one independent measurement have a random error that follows a t-distribution. They are corrected with the appropriate t-value and are RMS combined with the systematic errors to give a total uncertainty for each measurement

through the gauge package if the whole package was modeled as PTFE. This error is augmented by the impedance-matched pressure obtained from the shock speed measurements and recorded impact velocity. In the event that the gauge provides an anomalous trace or fails prematurely, the pressure is taken as the impedance-matched value from the conservation of momentum. The associated error will be a result of the propagation of uncertainty of the powder density, shock, and particle velocity, along with their associated random and systematic errors.

VISAR interferometry was utilized after the first four experiments because input and propagated gauges were showing anomalous behavior in both the rise-time response and peak pressures recorded. The VISAR system uses a beam splitter which takes the reflected beam from the sample surface and runs a portion through a delay leg in the system, recombining to form an interference pattern that is directly proportional to the disturbance velocity. Etalon lenses are used in the VISAR system which determine the delay length, and were selected based on the expected peak velocity at the powder/backer interface. The VISAR approximation is coded into *PlotData* (Sandia National Laboratories) and the program is used for data reduction of both the PVDF and VISAR data.

CHAPTER V

MESO-SCALE SIMULATION TECHNIQUES PROBING THE DYNAMIC RESPONSE OF TI/AL/B POWDER MIXTURES

The shock compression and high-strain-rate loading regimes produce rapid material deformation and complex thermodynamic changes in materials which have been found to be microstructure-dependent. It is currently impossible to probe microstructural evolution in real time at scales that can provide information on how the bulk response manifests from meso-scale behavior. In such cases, numerical simulations can provide valuable insight into how the microstructure behaves and evolves when subjected to high-strain-rate deformation. Accurate meso-scale representations using realistic microstructures can provide an additional level of insight that other more simplistic simulations (or perhaps simplistic microstructural representations) may obfuscate. The highly resolved microstructural representations may also shed light on mechanistic explanations for observed bulk response as well as reveal design pathways for future material optimization once the fundamental questions are answered.

This chapter describes the simulation platform that was developed to simulate impact on microstructures of Ti/Al/B powder compacts in an effort to connect the measured bulk response with meso-scale phenomena. The simulations use continuum-based methods (i.e. finite difference calculations using the multi-material hydrocode CTH 9.0 - Sandia National Laboratories 2009) and material models in conjunction with high-fidelity microstructural representations to simulate the evolving microstructure as the rapid loading is applied. Field variables such as temperature and stress can be tracked as a function of time and position and can be compared directly to experimental measurements to tailor the model and understand how the starting microstructural configuration affects measured stress/velocity,

and how the evolving microstructural configuration can lead to preferential arrangement which has all the elements favorable for reaction initiation. The simulations also provide a look at what may be happening at the particle scale during shock compression and high-strain-rate deformation to provide some explanation as to the critical ingredients necessary to promote chemical reactivity under dynamic loading of reactive powder mixtures.

5.1 Developing digital microstructural representations for simulation

Prior work (cf. Chapter 2 and works by Do and Benson [115] and Austin and McDowell et al. [25]) investigating shock compression of reactive powder mixtures using meso-scale simulations utilized continuum-level models and more recently crystal plasticity models [25] to describe the constitutive behavior of binary mixtures at the particle-level. These simulations used simplistic geometric descriptions which, while preserving primitive stereological metrics of the microstructure such as constituent volume fraction, but did not consider the complex geometry and distribution of constituents common to heterogeneous reactive powder mixtures. Recent works have showcased the importance of a precise microstructural representation when performing these meso-scale simulations (cf. the review article by Eakins and Thadhani [13]), as important information is smeared out when using simplistic microstructural representations. Gurumurthy [165] outlines the importance of realistic microstructure descriptions when investigating meso-scale phenomena, especially if the available material models are primitive/empirical in nature.

In the present work, the investigation of mechanochemistry in reactive powder mixtures was approached by considering precise microstructural representations using an in-house method [165] to generate statistical volume elements (SVEs) of the binary and ternary microstructures typical of Ti/Al/B powder mixtures. These detailed descriptions were able to capture compaction-stage response observed in experiments and are a great first step to describing the meso-scale contributions to the measured bulk response in these mixtures under shock compression and high-strain-rate loading.

5.1.1 Metallographic preparation and analysis

Microstructures of powder compacts were obtained using conventional metallographic preparation and processing to image the constituent particles as they would be distributed in a compact deployed either under a uniaxial stress or strain loading configuration. The compact design was as described in chapter 4 and summarized in table 4. The powder compact was sectioned with a diamond abrasive saw by selecting a vertical section with a vertical direction oriented with the compaction direction. This was done to ensure unbiased microstructural sampling and avoid anisotropic effects [31, 164, 165]. The compact was then mounted in Bakelite and prepared metallographically by fine grinding with SiC emery paper (320-1200 grit, 100 rpm wet grinding speed, 60 s by hand) and polishing with Al_2O_3 solutions at 1 μm, 0.3 μm, and 0.05 μm, for 3 min at each stage to produce a scratch-free surface. Further details are contained in the companion thesis to this work by A. Gurumurthy [165].

Metallographic analysis was conducted on a variety of stoichiometries for the Ti/Al/B system (summarized in table 4). Initial characterization was conducted using the ~325 mesh Ti powder (Cerac) and crystalline (β-rhombohedral) boron powder employing the mixture configurations presented in table 4. With the switchover to amorphous boron, the mixtures were reformulated as described in chapter 4. Images were obtained both by optical microscopy and scanning electron microscopy (SEM). The Ti+2B compacts presented the greatest difficulty in characterizing; the boron particles were too small and proved difficult to image properly and segment/derive stereological properties.

Figure 34 shows the 75% Al, 75% TMD, Ti+2B rem. *set 1* microstructure which used the β-rhombohedral boron, obtained through optical microscopy. Higher Al-content is necessary for adequate metallography, as it inhibits excessive particle pullouts. The aluminum forms a pervasive matrix (white phase) with a random distribution of seemingly undeformed Ti and B particles. This is due to the relative hardness differences between Al, Ti, and B leading to Al preferentially filling any void space during compaction. Grinding and

polishing invariably led to particle pullouts which confounded the void and particle characterization. Polishing artifacts in the form of a speckle/haze were apparent in many of the compacts. Volume fraction calculations became more consistent with greater Al-content and higher %TMD which led to a greater compact strength (i.e. higher resistance to particle pullout). This further motivated the creation of a particle library to generate synthetic microstructures that are consistently tailorable in any form, and contain the real shapes of commercial powders (which can vary by vendor).

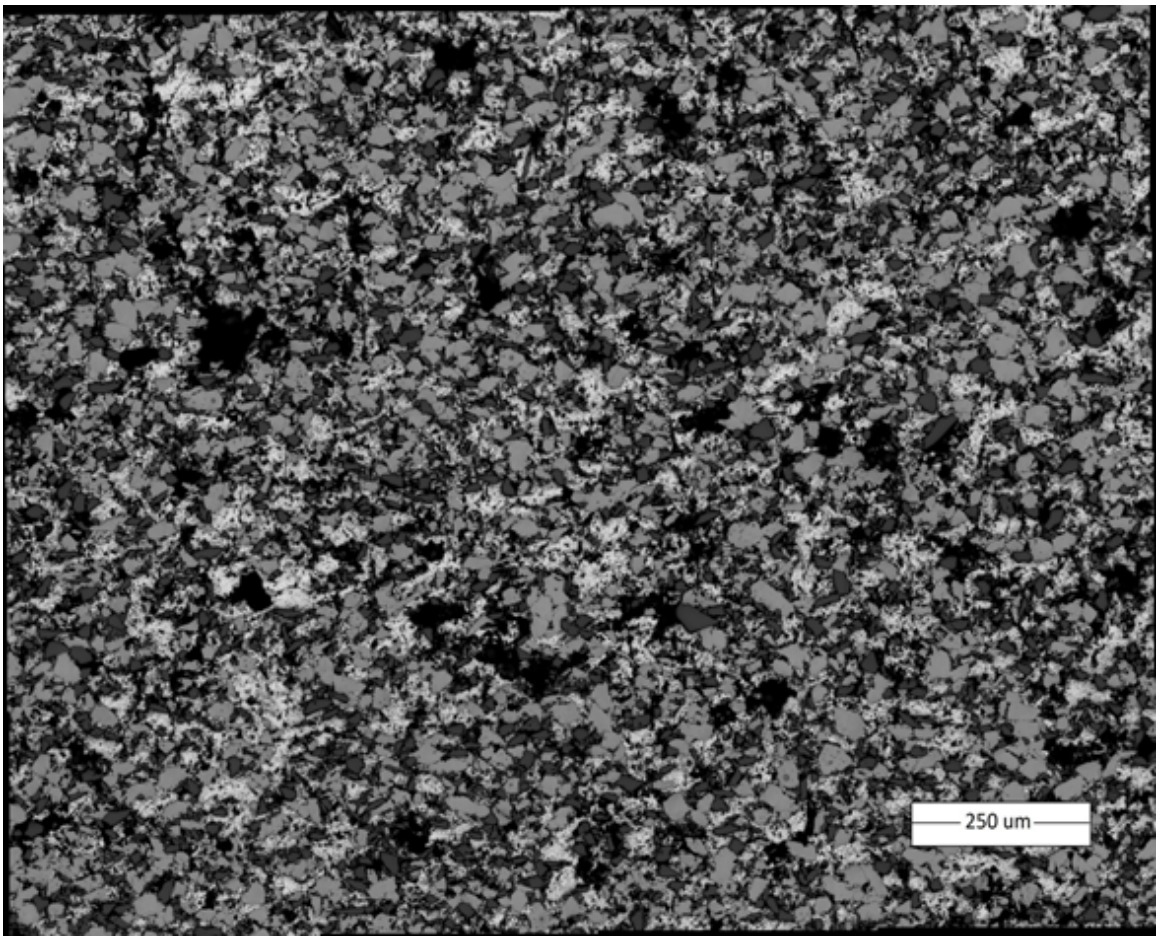

Figure 34: Microstructure for 75% Al mixture (75% TMD), Ti+2B rem. shows a random distribution of clearly defined Ti and B particles, and an Al-matrix without clear boundary definitions. A slight haze resembling a speckle pattern is observed throughout the Al-matrix which made for difficult segmentation and extraction of particles.

The initial goal was to generate real microstructures for use in direct meso-scale simulations. This proved challenging as consistent microstructures were not obtainable for

Al-content less than 75% and densities lower than 75% TMD. Even at 75% TMD, which was the highest consistently achievable for 1/8" compacts used in uniaxial stress experiments (the limiting factor being the pure Ti+2B mixture), stereological characterization showed highly variable constituent volume fractions and large particle pullouts. This inconsistency is inherent in these mixtures due to their low green strength, which limited the microstructural characterization to high %TMD compacts[1]. Prior workers [173] have manually processed images to artificially fill particle pullouts and correct these metallographic artifacts. However, these techniques were deemed inconsistent and were not pursued in this work.

This challenge became further apparent when characterizing the Ti+2B compacts, which were very difficult to press at high loads, leading to a lower density compact. Many attempts were made to section and metallographically characterize Ti+2B compacts, but this proved to be impossible. Adding aluminum improved the handling strength and provided opportunities to image the particle morphologies, at the expense of full microstructural characterization of pressed Ti+2B compacts[2]. Consistent microstructural representations were obtained, however, by simulating the microstructure using *real* particles extracted from particle libraries, which became the cornerstone of the simulation platform employed in this work.

The *set 2* powders used for the main experiments in this work also proved very difficult to characterize at the same volume fractions and densities considered in the dynamic loading experiments. The small boron particle size also caused an unexpected problem: the small size and relatively high hardness/strength of boron led to large agglomeration zones aligned to the axis of loading. Figure 35 shows the microstructure for Mixture D, 75% Al, Ti+2B stoich., pressed to nearly full density. The zoomed-in view (Figure 35, right) reveals

[1] These nuances are discussed in [165, 164]

[2] The distribution Ti+2B under uniaxial compression and its topological complexity were unable to be characterized due to these difficulties. By adding Al, a suitable compact was obtainable, but now the compaction was modified by the presence of a third component. This characterization effort was abandoned in favor of using synthetic microstructures for meso-scale simulations.

the character of the boron particles - agglomerated sets of stringers aligned normal to the vertical axis. The particle boundaries are more difficult to distinguish compared to the set 1 powders. Long-range heterogeneity was observed in these mixtures (as evidenced by the lack of convergence in the two-point correlation functions), and a satisfactory statistical volume element was unobtainable using conventional montages. Furthermore, the boron particles exhibited an orientational anisotropy effect arising from the compaction response of the powders [165, 164]. The agglomeration is stochastic in nature and automatic routines were unable to segment the particles. The boron particles for set 2 were thus simulated [165].

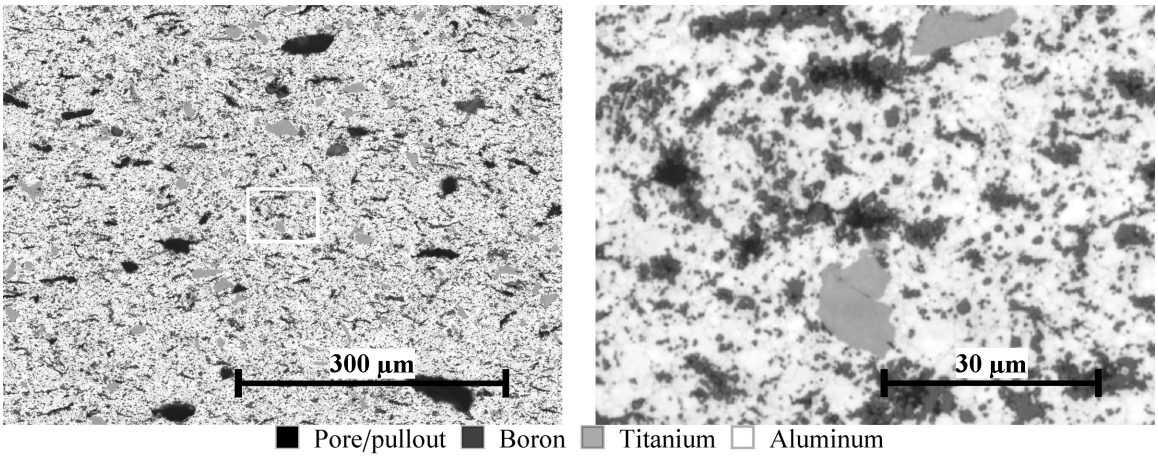

Figure 35: Mixture D microstructure showing bulk-orientational anisotropy [165]. Long-range heterogeneity was observed in these mixtures (as evidenced by the lack of convergence in the two-point correlation functions), and a satisfactory statistical volume element was unobtainable using conventional montages.

5.1.2 Synthetic microstructure generation

The main purpose of this metallographic analysis was not only to characterize the microstructure of powder compacts and provide representative microstructures for direct numerical simulation, but also to extract the individual particles through a segmentation process and thus build a set of particle libraries which precisely describe the true particle geometries in any tailorable microstructural distribution desired. This was deemed necessary because of the bulk orientational anisotropy during pressing, which made direct

microstructure-based simulations difficult. Therefore, generating tailorable microstructures utilizing a library of real particles became very attractive. A montage serial sectioning method was pioneered by the Gokhale research group at Georgia Tech [30, 165] to segment and extract the particle geometries. The method generates a library of vendor-specific particles that can be easily vectorized for use in computer simulations. The libraries are reusable and may be employed to generate any number of 2D microstructures. The technique was extended to generate three-dimensional microstructures as described by Gurumurthy [165].

There are many advantages to such an approach. As stated previously, imaging individual microstructures produces metallographic artifacts which are difficult, if not impossible, to avoid. Furthermore, the stochasticity inherent in microstructures cannot be captured through individual imaging; long-range heterogeneity is inherent in these powder mixtures [165, 164]. It is therefore an exercise in futility to precisely image each microstructure and presume to capture the salient features of the microstructure. The framework employed in this work and developed by Gurumurthy [165] permits the parametric study of individual microstructural variables and their effects on the bulk response of the materials to dynamic loading, and is the principal methodology employed in this work. Figure 36 provides a flowchart detailing the synthetic microstructure scheme. Montage serial sections obtained from pressed powder compacts can be used to extract individual particles through a segmentation routine. These particles are stored in a library for later use in simulations. The particles can be inserted into a simulation volume (in the 3D case) or be treated as 2D sections randomly selected from the many serial sections of a powder compact. Further details are provided by Gurumurthy [165].

5.1.3 Simulating 2D microstructures

The microstructures used for meso-scale simulations were simulated using the library of particles generated via montage serial sectioning. These were successfully generated for titanium and boron set 1 particles. However, difficulties with the segmentation process

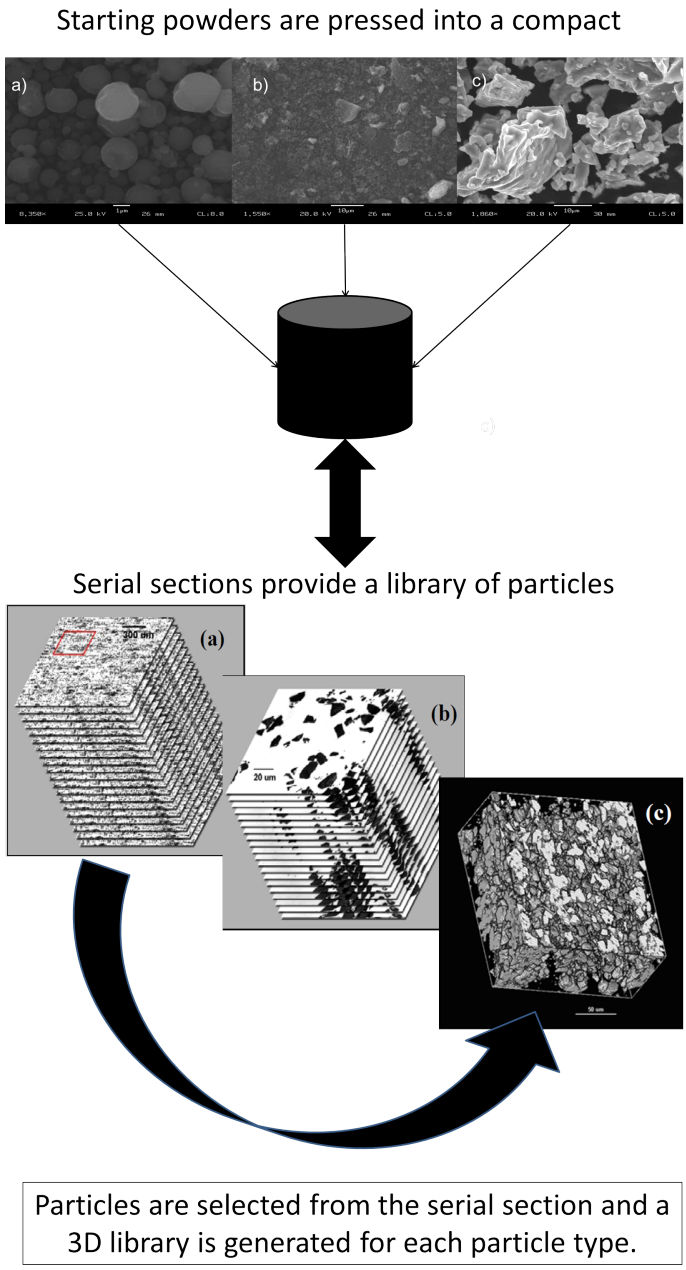

Figure 36: A library of real particles extracted from compacts can be generated through a montage serial sectioning technique. Systematic removal of material through polishing and subsequent imaging over the thickness of the compact can be used to precisely extract each particle for later use. More details may be found in ref. [174].

prevented extraction of the boron particles for set 2; titanium particles were successfully characterized and segmented for the set 2 powders. Aluminum and boron were therefore simulated using a polar plot of a Fourier sine series [165]. The Al-boundaries could not be

resolved, so it was opted to describe these domains as random shapes as described in [165].

Figure 37 summarizes the microstructure simulation method. Particles are added to a simulation volume one after another, taking a random 500 step walk until they reach an appropriate configuration, keeping a strict overlap criterion and ensuring the Ti+2B 1:2 molar ratio is preserved. This involves a simulated annealing protocol [165]. For the ternary microstructures (involving Al particles), the Al is simulated via the polar Fourier series plot and is inserted in a similar manner, but without overlap control (cf. Figure 38). Because the Al forms a pervasive matrix throughout, the harder particles are likely to merely be carried by the Al during deformation/compaction and will thus be found dispersed throughout the Al domains.

The microstructures were validated by Gurumurthy [165] through a statistical analysis of the two-point correlation functions relating the real microstructures and the simulated microstructures. The validation showed that there was some unavoidable, inherent long-range heterogeneity and non-periodicity, but overall the two-point correlations for each constituent in the simulated microstructures remained within two standard error bands ($\pm\frac{t_\nu s_e}{\sqrt{n}}$) of the sampled regions in the real microstructures [165]. Figure 39 shows a number of these two-point correlation functions for micrographs oriented perpendicular to the applied load direction for the compact. The two-point correlation function lies within the standard error bands, which begin to diverge as the parameter r increases, demonstrating the effects of long-range heterogeneity.

Figure 40 compares the real and resulting synthetic microstructures for samples from set 1 and 2 powders for Mixture C. There is good visual correspondence between the microstructures, and two-point correlation functions and lineal-path probability functions confirm this [165]. The simulated microstructures capture the shape of the particles along with their spatial distributions. This validation demonstrates that accurate microstructural representations may be obtained with this method.

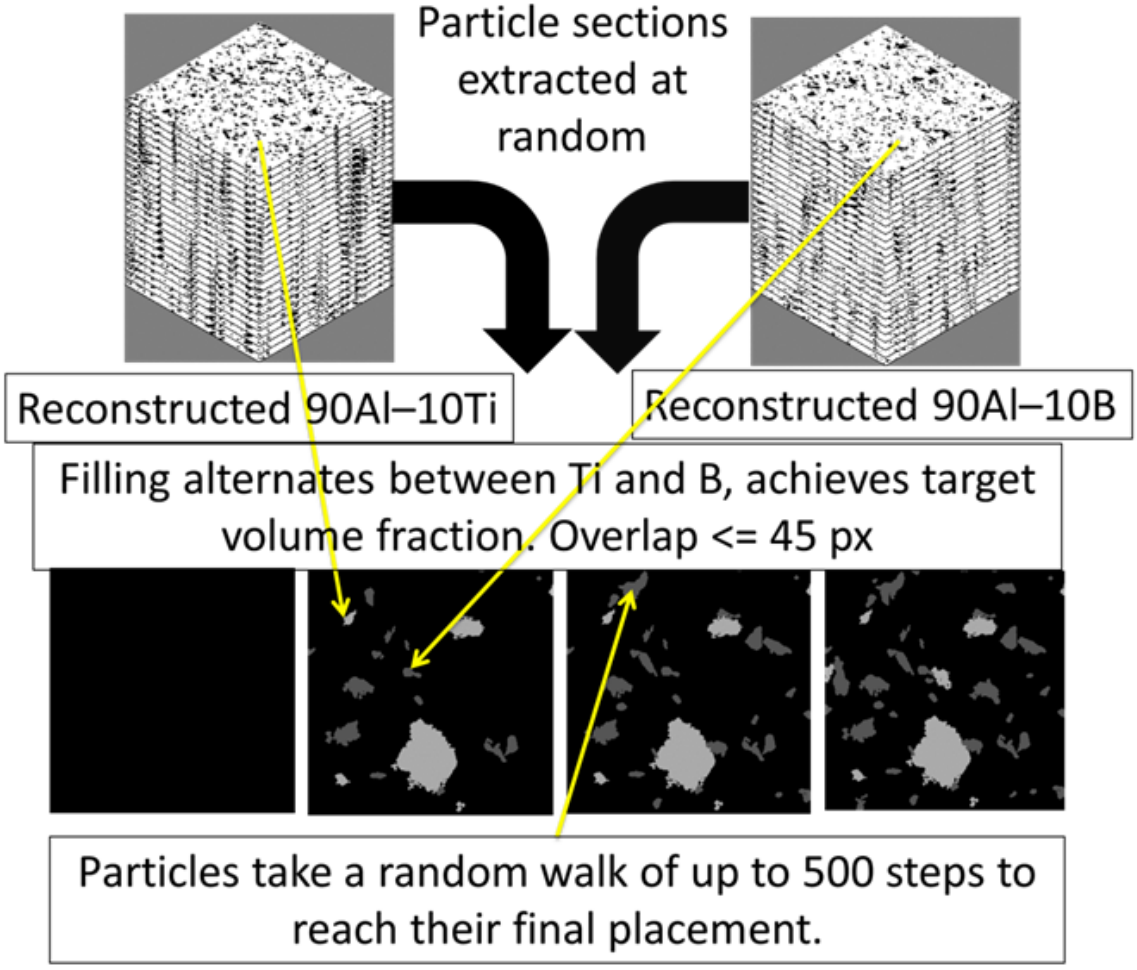

Figure 37: The microstructure simulation scheme adopted for this work. Titanium and boron particles are either obtained from montage serial sectioning (set 1 for both Ti and B) or are simulated. Each particle is inserted into a simulation volume and allowed to take a random walk of 500 steps to reach a final position. This method was used to simulate binary microstructures (90-Al, 10-Ti/B) for validation with two-point correlation and lineal-path probability functions.

The synthetic microstructure simulation scheme was used to generate the stoichiometries for Mixtures A-C for direct meso-scale simulation. Limitations in the hydrocode used for this work required large particle domains to be split up when the number of points describing the particle boundaries exceeded 2500. Larger particles were split manually in narrow locations where connectivity was deemed unimportant. The boundaries of the particles were left in extremely close proximity (but with well-defined boundaries of separation) that the mechanical behavior would not be altered. Uniform-random distributions

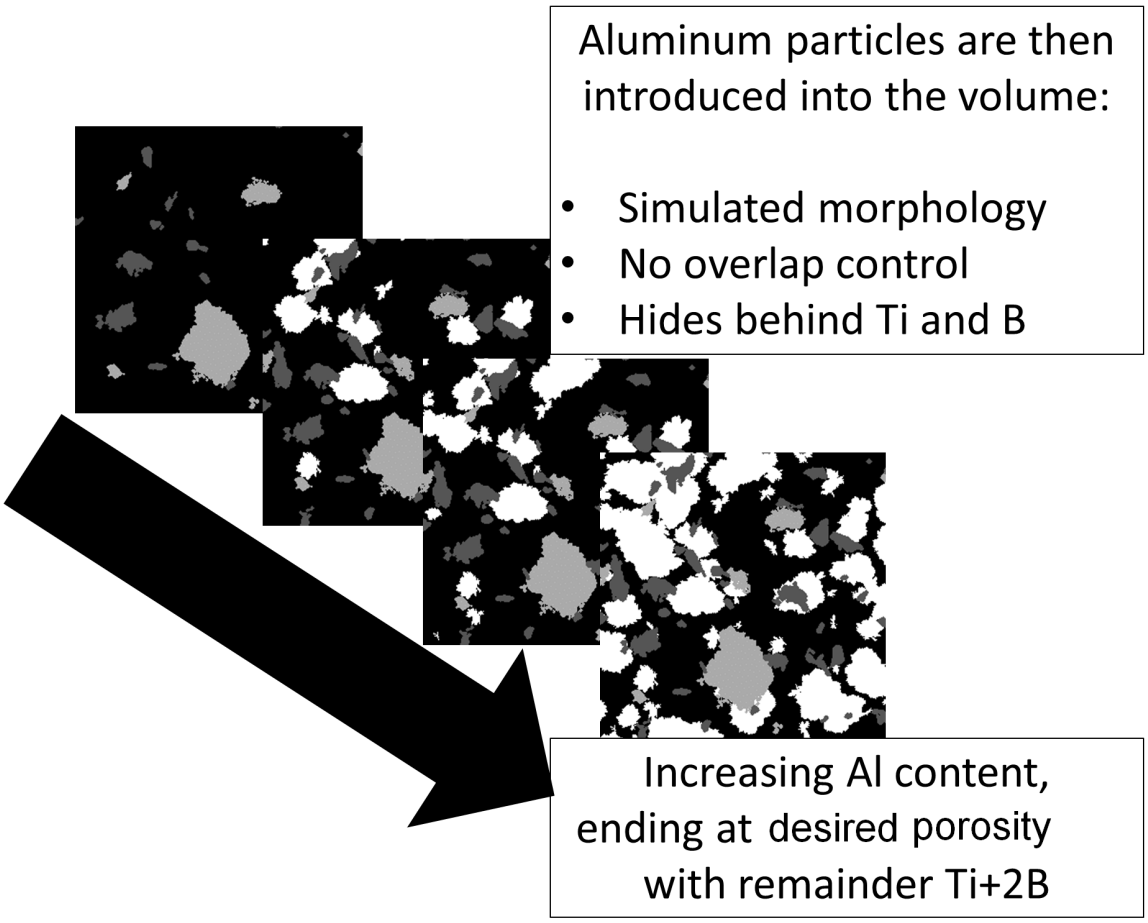

Figure 38: Systematic additions of Al into the simulation volume ensure that the stoichiometry of Ti+2B is preserved while maintainting strict control over the volume fractions. Unfortunately, no overlap penalty was built into this method since Al had "last-in" precedence in CTH. This meant that Ti/B particle positions and geometry were protected and Al was there to fill the void space as a matrix. Therefore, strict overlap control was deemed unnecessary.

were considered in this work, as precise microstructural characterization of each stoichiometry was intractable. Uniform-random distribution of constituents was deemed a good first approximation that would at least help capture the stoichiometric effect of the mixture on the bulk response.

The chief variables controlled in these synthetic microstructures were the stoichiometries and the densities. The stoichiometries were fixed by the mixture configuration, and

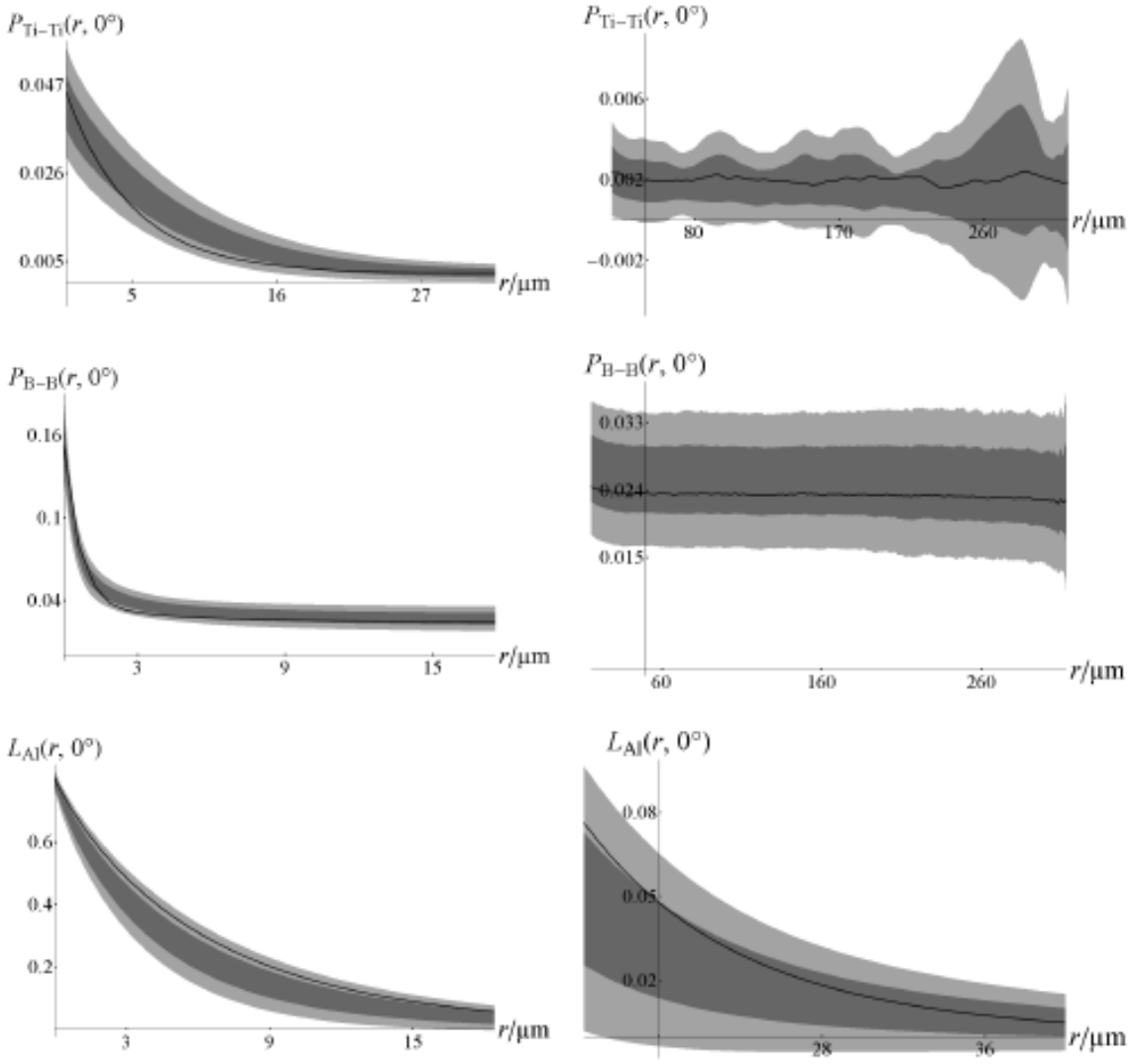

Figure 39: Two-point correlation function validation of simulated microstructures for micrographs oriented perpendicular to the applied load direction for the compact [165].

the density, $\Phi = 1/\alpha$, was set based on the application to replicate the experimental conditions. Only 2D microstructures were considered and some groundwork was developed for 3D microstructure-based simulations. Figure 41 shows a synthetic microstructure created for set 2 powders of Ti+2B-75%-TMD (uniaxial stress simulations).

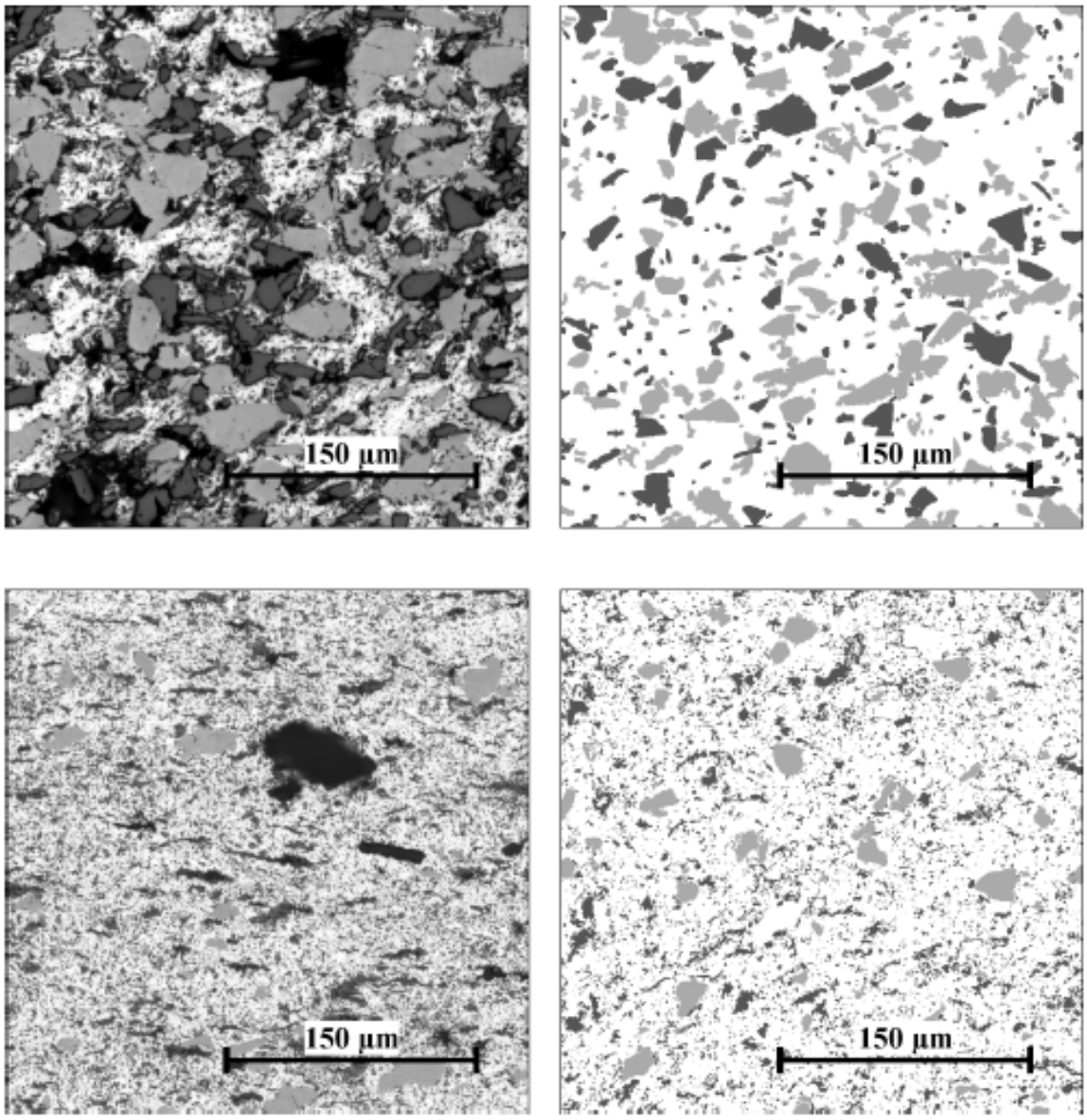

Figure 40: Comparison of real (left) and synthetic (right) microstructures for set 1 (top) and set 2 (bottom) powders. There is good visual correspondence between the microstructures, and two-point correlation functions and lineal-path probability functions confirm this to a high degree [165].

5.2 Impact and shock compression simulation using the multi-material hydrocode CTH

5.2.1 Diatom generation

The synthetic microstructure generation framework allowed for precise microstructure-based simulations of the dynamic processes induced by uniaxial stress/strain loading. Scale

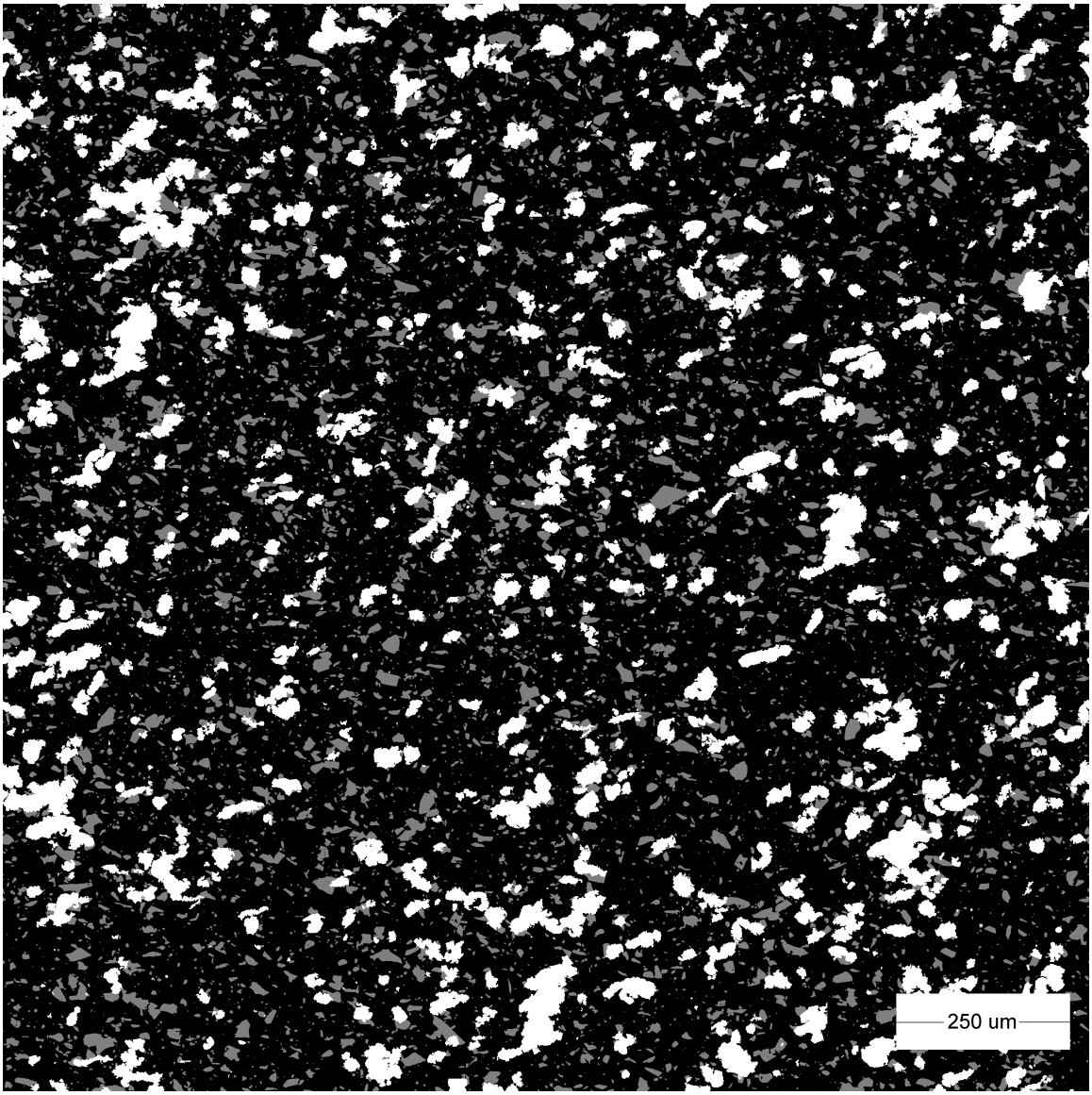

Figure 41: Synthetic microstructure for Ti+2B - 75%TMD generated for uniaxial stress simulations. A uniform-random distribution of constituents was selected because the actual microstructure could not be characterized and validated. Initial validation of the method was based on higher density (higher Φ) microstructures.

models of the impact scenarios considered in this work were created to determine the influence of meso-scale phenomena on bulk response. A simulated microstructure (cf. section 5.1.3) may be inserted into CTH by first thresholding and binarizing the individual phases and considering each phase (i.e. particle) separately. These particles are read into an in-house code (courtesy of Paul Specht, 2013) which vectorizes the domains and generates

boundary definitions readable by the *User-Defined Shape (UDS)* diatom environment in CTH. Each particle is vectorized and assigned a material ID, as summarized in figure 42; there is a 20 material limit in CTH that is considered when assigning material IDs. Each component is then assigned a constitutive model and equation of state depending on the material ID.

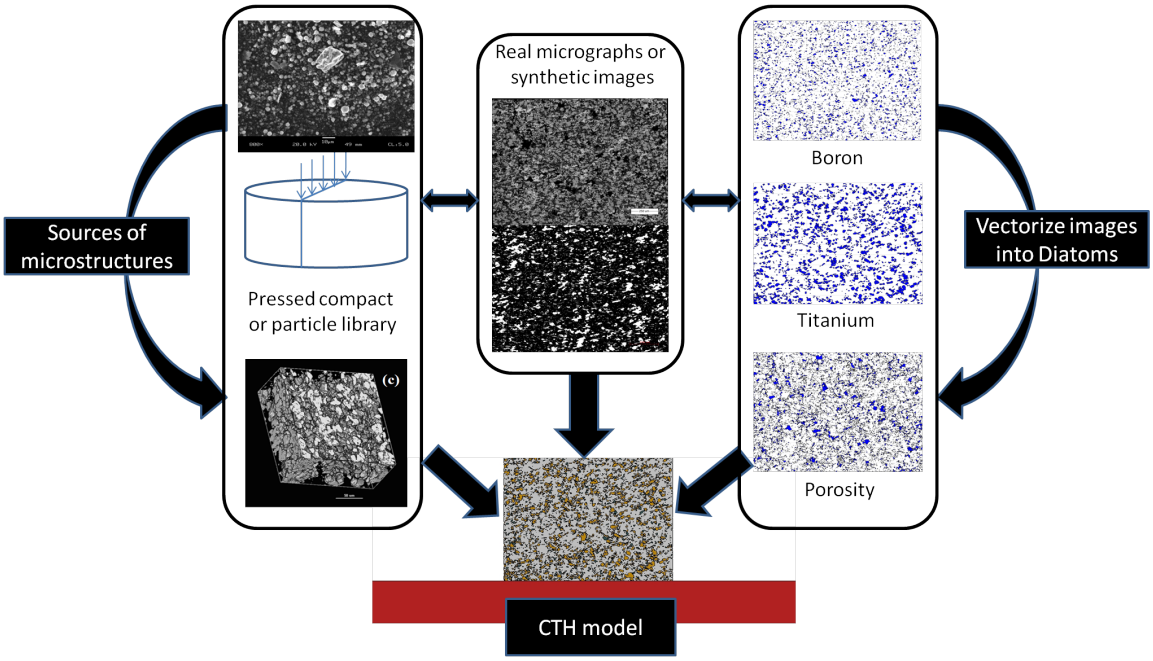

Figure 42: Microstructure-based simulation flowchart displaying the steps in generating a suitable microstructure for insertion into CTH. Structures are obtained from a montage serial sectioning technique and are either obtained from real images or via microstructural simulation. These structures are vectorized and inserted as diatoms into a CTH input file.

5.2.2 Equations of State and Constitutive Models

Precise EOS models are required for closure of the thermodynamic state under shock compression as discussed in chapter 3. There are many EOS models to choose from, and this work employs the equations of state defined internally by CTH. Each diatom is assigned a material ID which is associated with a constitutive model and EOS. A variety of EOS models are included in CTH, including the Mie-Grüneisen EOS and the Los Alamos SESAME EOS, that can describe the thermodynamic pressure as a function of volume and energy

or other variables such as compaction parameters. The possibility of simulating chemical reactions based on EOS models used in explosives (Baer-Nunziato, Jones-Wilkins-Lee, etc.) was explored early in this work. However, the models were deemed unsatisfactory to describe the unconventional Ti/Al/B mixture system, and thus were abandoned in favor of a purely mechanical (inert) analysis of the particle-level deformations unique to the microstructures and load scenarios considered in this work. The Los Alamos SESAME EOS was determined to be the best possible EOS to describe the materials and was used for Ti, Al, and the impactor materials Cu, and W. Other materials used the Mie-Grüneisen EOS built-in CTH models, except for boron, whose parameters were obtained from Crockett [161]. The boron EOS is further discussed in chapter 4.

The mechanical behavior of the constituents is described by rate-independent plasticity models tested in the dynamic loading regime. These include the Steinberg-Guinan-Lund (SGL) and Zerilli-Armstrong models which are physics-based constitutive equations that can model the effects of dislocation dynamics during high-strain-rate deformation [3]. These models were employed in prior works using microstructure-based simulations [21] and were reasonably effective at capturing the bulk response of the microstructures under shock compression. The effectiveness of these models was studied in detail by Austin et al. [25] and it was found that while the models could capture the wave propagation response satisfactorily, microstructure-sensitive properties and meso-scale plasticity were best captured by a more advanced physics-based model. Still, these models were considered satisfactory to investigate the meso-scale effects on bulk response in powder mixtures. Table 5 summarizes the constitutive and EOS models implemented in this work.

5.2.3 Uniaxial stress and strain simulations

The simulations differ chiefly in the boundary conditions and microstructures that were implemented. The constitutive equations and EOS models remained the same for each simulation. Each loading condition (uniaxial stress/strain) had a different microstructure

Table 5: The material models employed in CTH simulations. The boron EOS was modeled as a Mie-Grüneisen EOS using the values from Crockett's work [161].

Material	EOS	Constitutive Model	Comments
Ti	SESAME	Steinberg-Guinan-Lund	All internal models
B	Mie-Grüneisen	von-Mises yield surface	Models from [161, 157]
Al	SESAME	Steinberg-Guinan-Lund	All internal models
Cu	SESAME	Zerilli-Armstrong FCC	All internal models
W	SESAME	Johnson-Cook	All internal models
WHA	SESAME	Johnson-Cook	All internal models
Fused SiO_2	SESAME	Johnson-Cook	See Kerley [175]
Teflon/PVDF	SESAME	Hydrodynamic	All internal models

based on the scaling of the simulation to the experiment. The uniaxial stress simulations replicated the modified rod-on-anvil Taylor impact experiments employed in this work; the simulations are 1:2 scale models of the actual experimental setup. The top boundary simulates a rigid target by employing a symmetry boundary condition. The left and right boundaries set the pressure to zero and allow material in/out-flow. Lastly, the bottom boundary is sound-speed absorbing to simulate a half-space (cf. figure 43).

Simulations were performed on stoichiometric Ti+2B+(0, 25, or 50% Al) microstructures at impact velocities ranging from 175 m/s to 400 m/s. These simulations use 2D uniform-random distribution of particles and the simulated Al and B particles in the microstructures. These microstructures are then placed on a copper projectile which prescribed the impact velocities as initial conditions (cf. figure 43). Automatic Mesh Refinement (AMR) was employed with a refinement level of 4 to yield a square mesh 0.8 μm in size. A stress-based fracture criterion was employed for all materials, where the interfacial fracture strength was modeled as a fraction of the lower-strength constituent within the simulation cell. All material interfaces were prescribed a sliding condition whereby the relative shear velocity rates were set to zero.

The uniaxial strain simulations used the same material models as the uniaxial stress simulations with the addition of a simulated PVDF gauge on the front and back surfaces of the powder. This simulated gauge was added to later simulations to better capture the

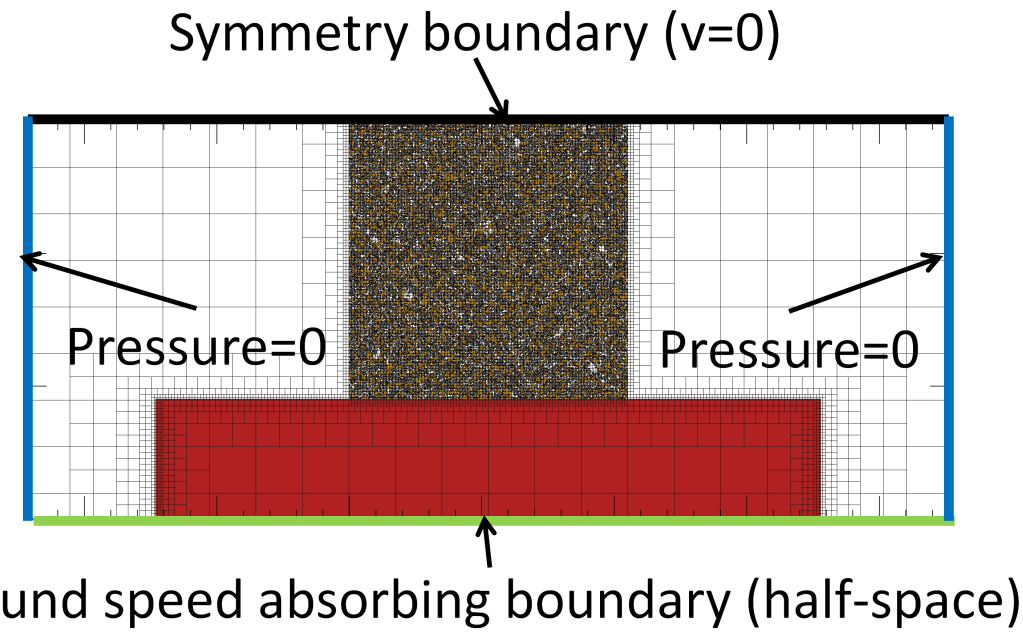

Figure 43: Schematic of the boundary conditions employed in all uniaxial stress simulations. The top boundary simulates a rigid target while the left and right boundaries permit material to exit and set the pressure to zero. The bottom boundary is sound-speed absorbing so that no wave interactions from the back surface of the copper rod interfere with the pellet.

anomalous signals observed in the rise time to peak pressure at the propagated gauge. This gauge was simulated at the same dimensions as in the experiments to simulate the effects of the particle shapes/sizes on the stress equilibration within the gauge. The simulations used copper and tungsten flyers with impact velocities ranging from 200 - 1055 m/s to match the experimental velocities. Figure 44 shows the simulation domain for the shock compression simulations. A 1.048 $\times$ 1.048 mm microstructure (1:4 scale model of the experimental setup) is sandwiched between simulated PVDF gauges (actual size using a hydrodynamic assumption), a Cu driver plate (Red) and Fused Silica (Tan) backer plate.

The uniaxial strain simulations used tracer points distributed along the midplane of the PVDF gauge to record the field variable histories (pressure, temperature, velocities) through the entire gauge. Ten tracer points were used along the input and propagated

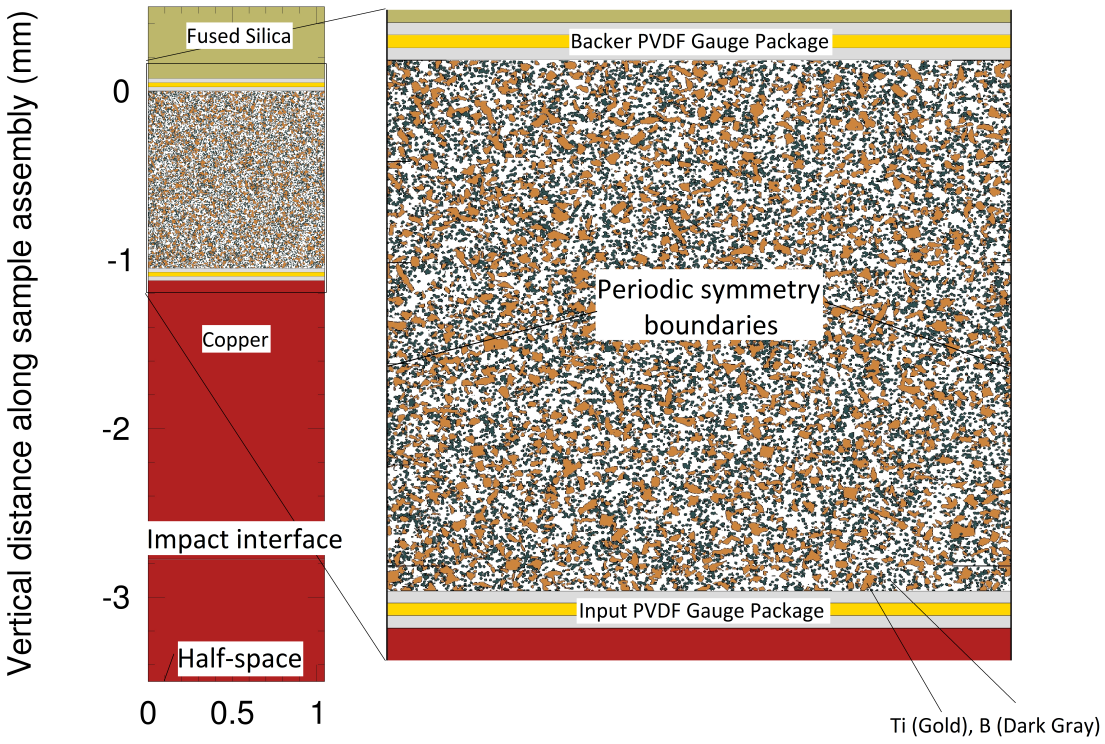

Figure 44: Simulation domain used for the parallel-plate shock compression impact simulations. A 1.048 × 1.048 mm microstructure (1:4 scale model of the experimental setup) is sandwiched between simulated PVDF gauges (actual size using a hydrodynamic assumption), a Cu driver plate (Red) and Fused Silica (Tan) backer plate. An interchangeable flyer was used (either Cu, W, or WHA) to generate different stress levels at the same impact velocities as the experiments.

gauges to track the average values of the field variables as they evolved through the simulation. These values were compared with the recorded experimental traces to evaluate the effectiveness of the microstructure-based simulation method. These values were also used to obtain an equation of state for the particular stoichiometry considered. A preliminary validation of this simulation method was based on capturing the shape and peak values of the recorded stress/velocity profiles. These results are presented in chapter 6.

CHAPTER VI

EXPERIMENTAL AND SIMULATION RESULTS

This chapter presents the results of the uniaxial stress and uniaxial strain dynamic loading experiments conducted on the Ti/Al/B powder mixture system, along with the accompanying microstructure-based simulations exploring the meso-scale phenomena inherent in the dynamic loading environments. The rod-on-anvil impact experiments reveal a stoichiometry effect on the optimal configuration promoting impact-induced reactivity. Meso-scale simulations show highly strained regions typical of uniaxial stress loading, but which change in character based on the stoichiometry of the mixture. The uniaxial strain impact loading raw experimental data is also presented and the results are cast in thermodynamic Hugoniot space. The unique wave profiles observed in the experiments are analyzed with key features delineated. The chapter concludes with a presentation of the uniaxial strain simulation results which show the bulk response obtained from the microstructure-based simulations and how meso-level heterogeneity manifests in bulk response.

6.1 Ti/Al/B stoichiometry effects under uniaxial stress loading

Uniaxial stress loading experiments were conducted using the set up described in chapter 4. Initial work considered set 1 powders, but were subsequently abandoned in favor of set 2 powders (see chapter 4). As a reminder, the set 2 powders consisted of sponge Ti powder (Atlantic Equipment Engineers, ~625 mesh), amorphous boron powders (Alfa-Aesar < 5 μm), and Valimet H-2 spherical atomized powders. The mixture stoichiometries considered are presented in table 2. Both the IMACON framing camera and NAC high speed video cameras were used to collect images of the impact event for the range of stoichiometries shown in table 4.

The reaction events usually appeared after the full crush-up of the pellet, when the plastic flow from the pellet forced it to nearly reach the outer diameter of the copper projectile. The ensuing pressure exerted by the copper and the subsequent anviling and confining effects during the copper deformation create excessive heating at the interface between the copper and reactive densified pellet. This heating is due to plastic straining and severe jetting, bringing about unique transport conditions. Meso-scale simulations performed using CTH substantiate this observation and show instabilities at the interfaces due to the relative shearing between the different materials at the pellet/copper interface.

In other, more bizarre cases, the impact conditions were just right to promote a "welding" or cladding of the copper rod (with reactive material mounted wedged between the rod and anvil) onto the anvil, as seen in Figure 45. The welding scenario was reproduced with a variety of impact conditions depending on the stoichiometry of the material, for a narrow range of impact velocities between 350 and 400 m/s. The observations merit further study because careful control of the impact dynamics and reactant configuration can make this a reproducible phenomena that can be studied systematically. Also, the weld interface may have interesting properties in common with other dynamic welding techniques. Further studies are merited to investigate the reproducibility of this welding process and to ascertain the dynamic mechanisms associated with the phenomenon.

The experiments involved two distinct impact stages due to the experimental setup. Stage 1 involved the impact of the reactive compact onto the anvil without any influence of the sabot (i.e. the copper rod). Stage 2 involves the sabot/copper rod as the compact is entrapped between the anvil and the rod, leading to a "re-shock" event where the impedance mismatch between the compact and rod creates a ring-up stress which increases the heat generated by the impact. Light emission was mainly observed during stage 2; the interaction between the copper rod with the steel anvil certainly contributes to the potential chemical reactivity in the compact.

Figure 46 presents the results of all uniaxial stress loading experiments performed on

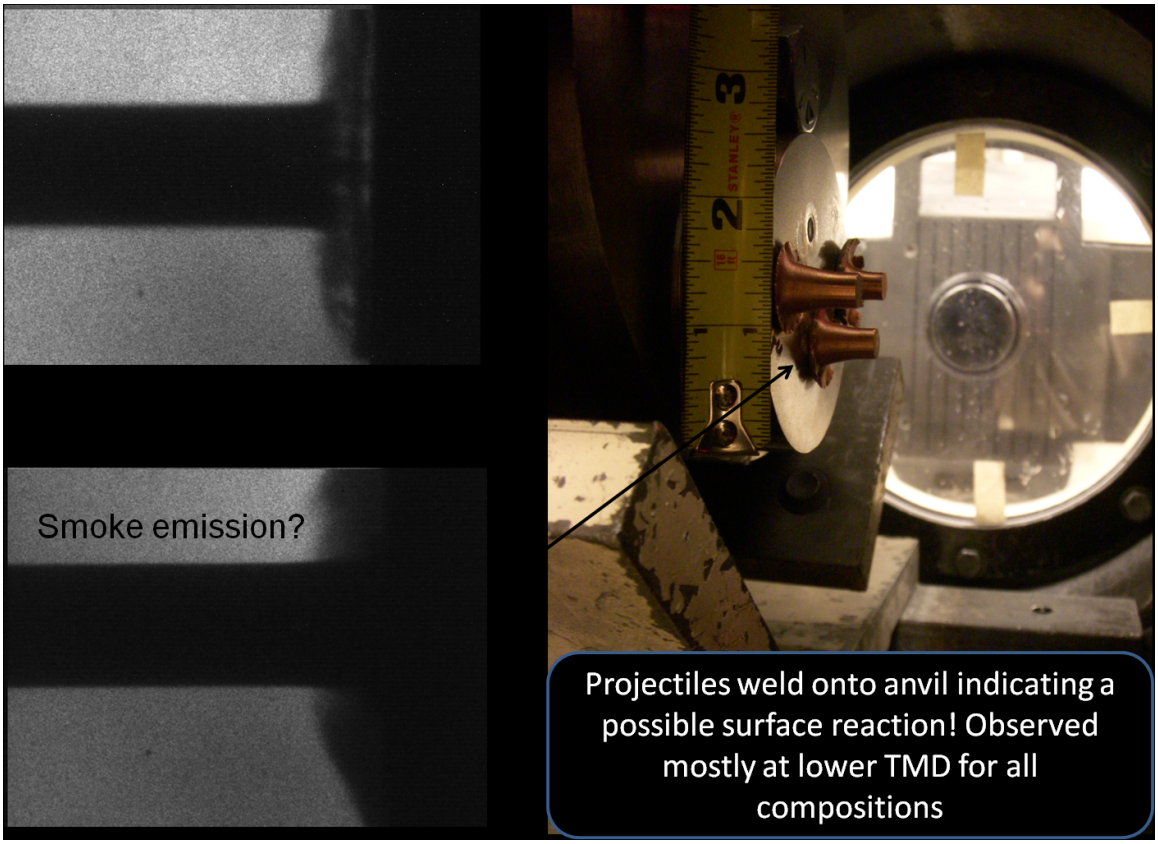

Figure 45: Some impact experiments showed a welding phenomena where the projectile either welded or cladded strongly onto the steel anvil. Some images showed either faint light signatures or smoke/debris emission. Further investigation is needed to quantify the dynamic conditions and consistency in reproducing this phenomenon.

Ti/Al/B powder compacts with a similar %TMD. The results are presented as "go" (reacted, filled symbols) or "no-go" (unreacted, unfilled symbols) based on the criterion outlined previously. The density was controlled by varying the compaction load during powder pressing as shown in table 4. A %TMD of 75% ±4% was considered because it was the highest %TMD achievable for the 0%-Al mixtures at the load capacity of the M-2 steel die used for compaction. Impact energy is plotted for each stoichiometry considered to outline potential trends in reaction "threshold" (the impact energy that must be exceeded to guarantee luminescence based on the aforementioned criteria) as a function of Al additions. The impact energy threshold for reaction initiation decreases to an optimal value of around 200 J (or around 175 m/s impact for the 30 mm rod considered) in the case of 50% Al. Further

additions of Al increase the threshold, and ultimately the pure Al experiments showed the greatest difficulty in reacting.

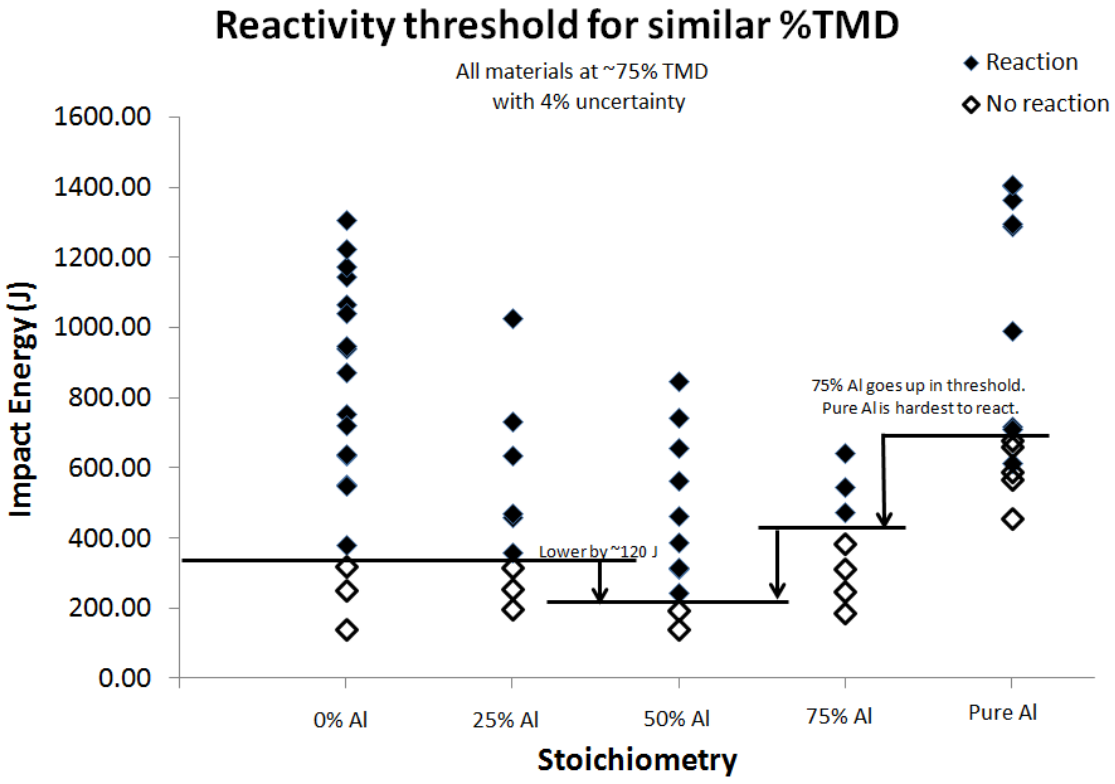

Figure 46: Go/no-go data for the rod-on-anvil uniaxial stress experiments. The impact energy required to observe a luminous event decreased for the 50% Al stoichiometry. This energy increased substantially as more Al was added.

The enhanced reactivity may be due to a potential liquid-phase mechanism resulting from the plastic heating of the softer Al phase enhancing the kinetics of any Ti/B reaction [176] for the 50% Al stoichiometry. The overall bulk heating is sufficient in the vicinity of the strained Al for any reactions between Ti and B to be sustained. However, the bulk heating in greater Al-containing structures (i.e. 75% Al) is reduced which may quench any further reaction at that stoichiometry. These observations were further explored through microstructure-based simulations (cf. section 6.2). The enhanced reactivity of the 50%-Al mixture (Mixture C) is an astonishing discovery as it hints at potential optimal microstructural configurations that can enhance the reactivity of this mixture. Ti+2B alone is

suspected to be highly reactive, but did not exceed the reactive potential that the 50%-Al mixture had. This points to a potential synergy beyond what is possible with Ti+2B alone at the densities considered.

6.2 Meso-scale uniaxial stress loading simulations

Microstructure-based simulations without consideration of chemical reaction were performed using simulated microstructures to study the impact conditions observed in the pellet-mounted rod-on-anvil experiment at the meso-scale. Microstructures were obtained by conventional metallographic techniques and through montaging of many fields of view to obtain a large representative field. The inherent difficulty in resolving the < 5 μm amorphous boron particles prompted the use of simulated microstructures for these simulations (cf. chapter 5). Further details are described in chapter 5.

Impact simulations of a fully dense microstructure (without grain-boundary definition in the Al) were initially conducted at two impact velocities using both real and synthetic microstructures [28] for the 75% Al microstructure. These simulations showed pronounced banding of the Al near the center of the projectile. A graded mesh with an element size of 5 μm growing to 10 μm at the outer edges was employed in these preliminary simulations. The higher velocity impact simulations showed Kelvin-Helmholtz instabilities as expected for two regions shearing at different rates. Figure 47 shows the results from a 400 m/s impact simulation performed on a real microstructure obtained from a 75% by vol. Al mixture. The temperature fields are plotted at two separate times in the simulation. The greatest heating is observed at the boundary between the pellet and copper rod.

Greater mesh refinement was employed in subsequent simulations, relying on the Automatic Mesh Refinement (AMR) capability of CTH giving a mesh size of 0.8 μm at the most refined point. The simulations used synthetically-generated microstructures where the Ti particles were the only components that came from a particle library. The Al and B particles were simulated using a polar plot of a 30 term Fourier sine series [177]. The %TMD

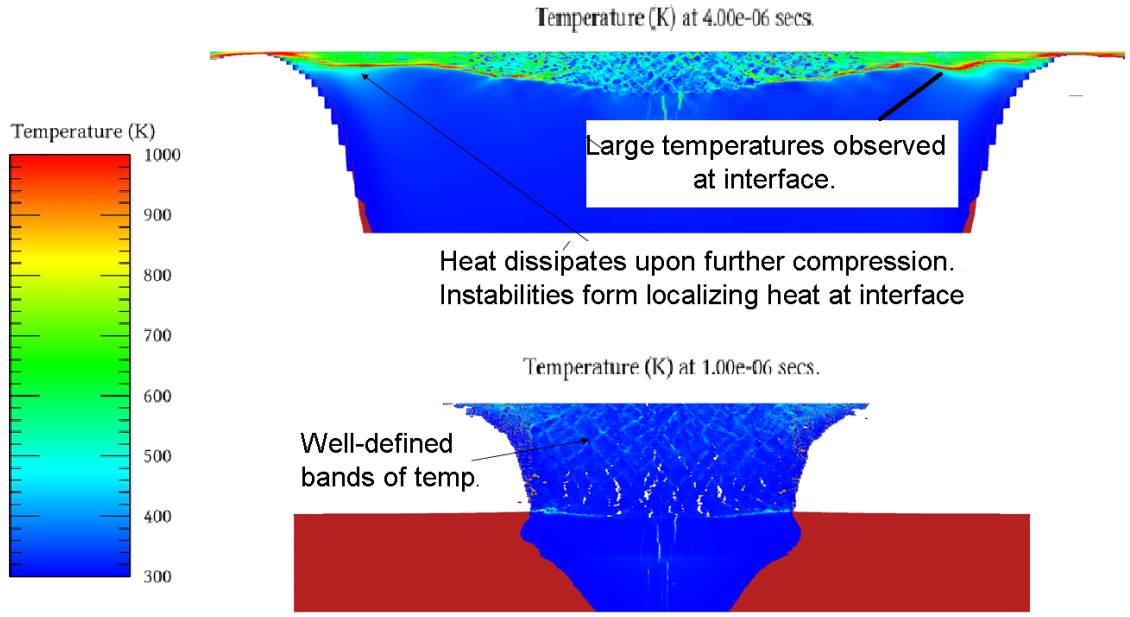

Figure 47: Temperature distribution from a 400 m/s impact simulation conducted using a real microstructure montage of the 75% Al microstructure. Pronounced banding was observed near the center of the structure as a result of the geometrical configuration of the constituents and the impact. The largest temperatures were observed at the interface between the microstructure and copper projectile upon crush up.

was closely controlled and each simulated microstructure had a uniform random particle distribution. The size distribution matched the reported sizes from the powder vendors.

The results of the refined simulations showed startling evidence of boron agglomeration in bands, coincident with the expected 45° shear bands typical of this loading configuration. The banding was observed for all structures at the stoichiometries simulated, from 0% Al content to 50% Al content[1]. The smaller boron particles rearranged themselves to fill empty space and flowed between the larger and softer Ti particles. Figure 48 shows two frames of an impact simulation for the 0% Al structure at a velocity of 400 m/s. The dark black bands actually contain many small boron particles that are either agglomerated or fractured and re-segregated. The boron particle boundaries coalesce and lead to the formation of the dark black region. This can be further appreciated in figure 50 which shows a zoomed-in

[1]The %TMD was kept constant for each structure at 75% to emulate the experiment %TMD

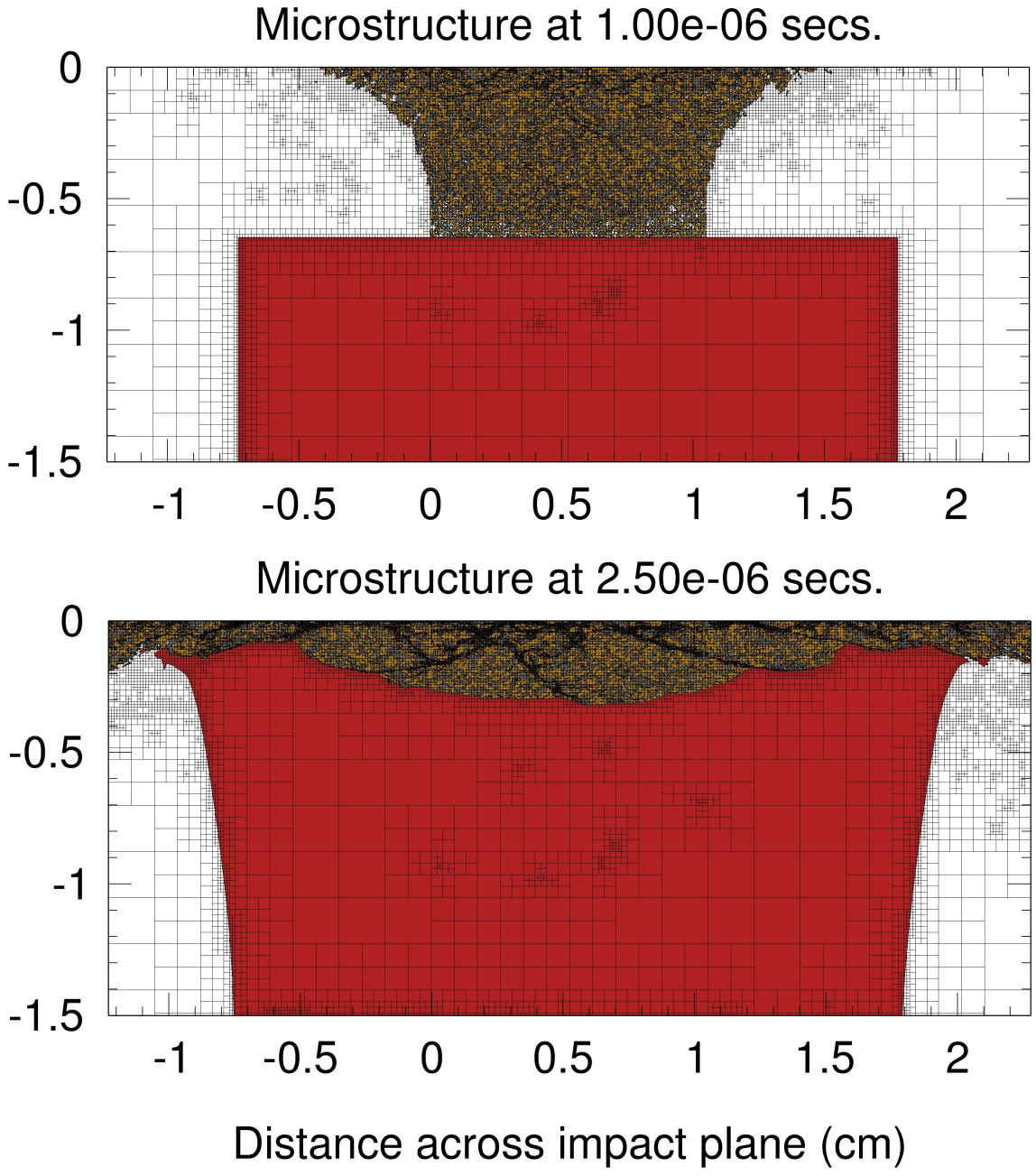

Figure 48: Microstructure snapshot at two different frames for 0% Al microstructure under rod-on-anvil test. V_{impact} = 400 m/s. Clear evidence of shear banding is observed. The bands consist of boron agglomerates which preferentially align with the shear band.

view of a shear band region.

The agglomerated structure can be better appreciated from a zoomed-in view with the superimposed temperature field. A half-view field was generated improving the overall resolution of the image with two frames displayed for the 0% Al and 50% Al structures at an impact velocity of 200 m/s (Figure 49). Both structures show pronounced banding and agglomeration. However, the number of small boron agglomerates is much higher for the 0% Al structure, indicating that the presence of Al somewhat reduces the boron agglomeration. This may be due to the Al preferentially shearing and filling the empty space, whereas the 0% Al structure depends on the shearing of the Ti and the movement of the smaller B particles to fill the empty spaces during crush-up.

A zoomed-in view shown in figure 50 compares regions near the middle of the structure for two different times. The structure of the agglomerates is revealed as colonies of boron particles, stretched and in some cases pulverized (most prevalent in the 0% Al structure). The boron particles are much more equiaxed in the 0% Al structure than in the 50% structure. The Al in the 50% structure carries boron along as it deforms, whereas the 0% structure leaves greater open spaces since the Ti does not deform as readily. These open spaces do not permit boron deformation. Instead, boron agglomerates and fractures during the mixing phase within these open spaces (i.e. pores). The bulk temperature is also much greater in the 0% Al structure where the heating is based on the plastic dissipation in the Ti and the interparticle friction between Ti and B surfaces.

6.3 Uniaxial strain loading on Ti/Al/B powder mixtures

This section presents the results of the shock compression (i.e. uniaxial strain parallel-plate impact) experiments performed on the Ti+2B mixture. A full characterization of the Hugoniot of this material was determined to be crucial to understanding the dynamic properties of this mixture. Since the boron equation of state is so ill-characterized in the literature, the shock Hugoniot was deemed paramount to this work in order to discern any shock-induced

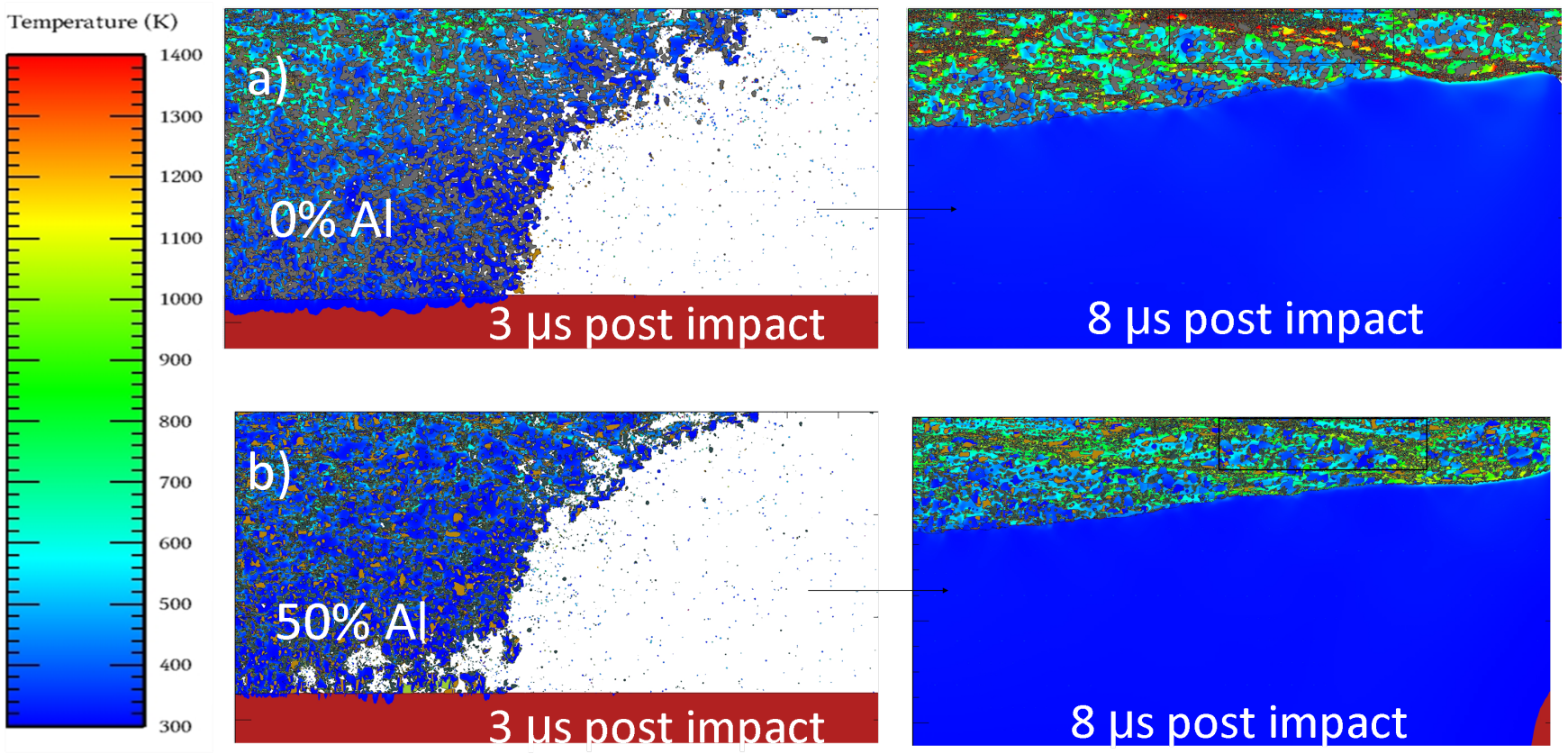

Figure 49: Half-view of the rod-on-anvil impact simulations at 200 m/s impact velocity. The temperature distribution shows that the majority of the heat localizes in bands coincident with the agglomerated boron. This is in stark contrast with the fully dense structure simulations where the majority of the heating was at the interface between the copper and powder.

chemical reaction event. The microstructure-based simulations of the shock compression response of the Ti+2B mixture using the uniform-random simulated microstructures generated for the uniaxial stress simulations are also discussed in this section. The simulations serve as a validation for the methodology by comparing the measured stress and velocity profiles with the predicted profiles. The simulations are able to successfully capture the stress and velocity profiles at the back surface of the powder and thus validate (to a first-order) the methodology and constitutive models employed.

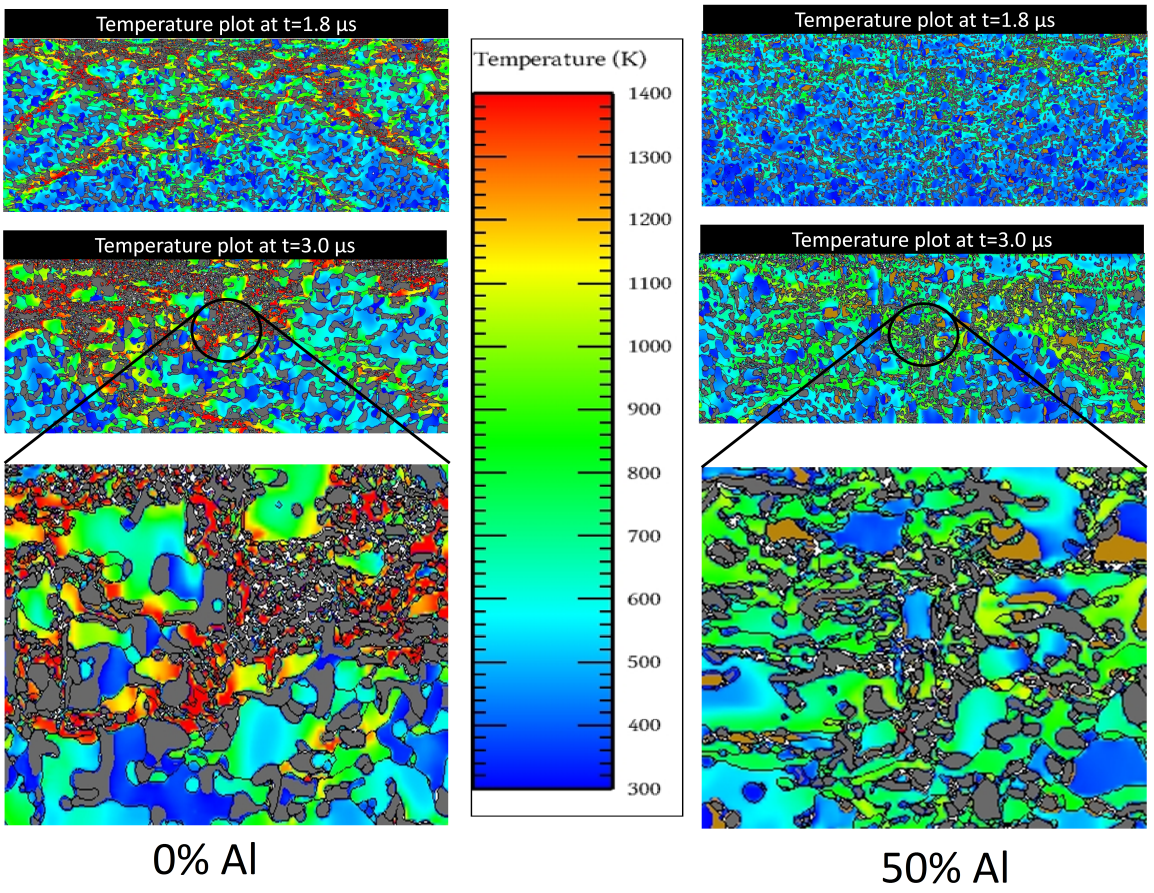

Figure 50: Zoomed-in view comparing the 0% Al and 50% Al microstructures at two different times for an impact velocity of 200 m/s. There are much more agglomerates in the 0% Al structure and their shape is more equiaxed since they pulverize and rotate in empty pores during crush-up. Temperatures are also much greater for the 0% Al structure, but shows lower bulk heating of the Ti particles, which may account for the discrepancy in the threshold condition observed in figure 46.

The shock compression behavior of the Ti/Al/B system must be ascertained if any predictions are to be made of the optimal reactive configuration or if any conclusions can be made as to the reactive behavior of the binary or ternary mixtures. The Hugoniot of the Ti+2B powder system has not been reported in the literature. The initial work investigating the chemical reactivity of this energetic system must begin by fully characterizing the Hugoniot of the powder mixture at a variety of pressures. Potential chemical reactions occurring within the mechanical equilibration phase of shock compression are reckoned through increased shock speeds measured by timing signatures from the PVDF stress gauges, an excess equilibrated stress at the backer gauge, or via an expanded state in P-V space consistent with the Ballotechnic hypothesis. The work then progressed to explore the effect of systematic Al additions, focusing on 50%-Al microstructures to compare with the "optimal" microstructure from the uniaxial stress experiments. The measured stress from the PVDF gauges (in cases where available) also provides an additional thermodynamic variable which reduces the uncertainty of probing the Hugoniot of the powder. Successful measurement of the pressure at the impact side of the powder surface is crucial in identifying a potential shock-induced reaction event.

6.3.1 Shock compression experiments performed on Ti+2B reactive powder mixtures

A number of shock compression experiments were conducted on Ti+2B molar mixtures, pressed at 50% TMD (±3%) using PVDF stress gauges and VISAR diagnostics[2]. The experiments were conducted using an 80 mm helium-driven light gas gun driving a sabot containing either a copper, tungsten, or tungsten heavy alloy flyer plate, as shown in figures 32 and 33. The projectile impacts a copper capsule assembly consisting of a copper driver plate and fused silica backer disk sandwiching the pressed powder compact. The impact velocity was measured via a sequential shorting pin technique and the impact tilt

[2]VISAR diagnostics were added to later experiments giving an additional measurement of the shocked state of the powder. VISAR only probes the back surface of the powder.

was measured using shorting pins lapped flush with the target ring.

The full experimental matrix is shown in table 6. The table distinguishes the diagnostics and relevant properties of the powder necessary for Hugoniot-based calculations, including the powder compacted thickness h, density ρ, and impedance-matched particle velocity U_p. Comparison of the shock Hugoniot of a porous powder compact with EOS models requires the starting density of the distended powder and measured shock speed. The stresses σ_I and σ_P correspond to the stresses at the input and propagated sides of the powder. The input stress for all experiments was impedance-matched using the shock speed U_s, impact velocity V_{Imp}, and known EOS of the flyer because the input PVDF gauge signal was deemed unreliable or most experiments. The propagated stress σ_P was taken as the peak stress based on Eakins' method [20] and outlined in section 6.3.2. Further details on the calculation of the Hugoniot parameters U_s, U_p, σ_I, and σ_P are presented in section 6.3.4.

6.3.2 Unique wave profiles in Ti/Al/B powder mixtures

Heterogeneous materials, specifically compacted powder mixtures, show highly-dispersed shock wave profiles due to compaction and other nonlinear processes (cf. Chapter 2). Dynamic compression of loosely-packed powders will be mediated by the topological connectivity of the powders, evolving heterogeneity, and wave reverberations across multiple impedance-mismatched surfaces. The compacted material achieves a compressed state and acts as an anvil pushing on the loosely-packed powder ahead of it. Waves continue to ring up to pressure mediated by conservation of momentum. Stress waves propagate through particles and can reflect at free surfaces, or transmit as wave characteristics if the topological connectivity permits. Impedance mismatch between constituent particles can ultimately influence the propagating wave structure.

The measurement tools implemented in the present work measure transient signals generated by the interaction between a stress gauge, or VISAR laser light beam, and moving particles. However, the size of the measurement probe influences the shape and structure

Table 6: The experimental matrix for the uniaxial strain loading experiments performed on Ti/Al/B outlining key properties and features of each shot. All experiments shown in the table were performed on the binary Ti+2B mixture, with the exception of shot Eglin 1, which was performed on the Ti+2B+50%Al mixture. All compacts are pressed to 50%TMD ±2%. The experimental error was plotted in the accompanying figures and not included in the table. Each experiment used the PVDF gauges as time-of-arrival devices to obtain the shock speed U_s, except in the case of the Eglin experiments, which relied on shorting pins. The particle velocity, U_p, and input stress, σ_I, were obtained by impedance-matching with the impactor of known EOS and measured impact velocity. The propagated stress σ_P was obtained from the recorded pressure trace using the method described by Eakins [20]. The compression V/V_{00} was calculated from the impedance-matched particle velocity U_p and input stress σ_I. Further details are discussed in section 6.3.2.

Experiment Setup Details					Experiment Results				
Shot #	Flyer	V_{Imp} (mm/µs)	ρ (g/cm^3)	%TMD	U_s (mm/µs)	U_p (mm/µs)	$\sigma_I(GPa)$	$\sigma_P(GPa)$	V/V_{00}
1205	Cu	0.513	1.76	50.1	1.29	0.486	1.1	2.3	0.623
1228	Cu	0.818	1.78	50.7	1.83	0.759	2.5	4.1	0.586
1302	Cu	1.044	1.78	50.7	2.24	0.954	3.8	5.7	0.574
1307	Cu	0.832	1.72	49.1	1.78	0.775	2.4	4.4	0.565
1309	WHA	0.911	1.71	48.6	1.85	0.965	3.0	6.0	0.479
1310	W	0.932	1.79	51.0	2.19	1.03	4.0	6.9	0.531
1314	W	0.890	1.75	49.9	1.97	0.992	3.5	6.2	0.486
1319	Cu	0.386	1.77	50.4	*[a]	*	*	*	*
1320	Cu	1.055	1.76	50.1	1.97	0.974	3.4	5.0	0.505
Eglin 1	Cu	1.221	1.58	50.6	2.46	1.34	5.12	1.8	0.444
Eglin 2	Cu	1.510	1.68	48.0	3.32	1.60	8.92	1.8	0.519
Eglin 3	Cu	1.225	1.70	48.3	2.9	1.31	6.46	1.8	0.547

[a] * Denotes failed PVDF gauges for shock speed calculation or other missing data

of the measurement and is a critical factor to consider when analyzing data. Unfortunately a proper meso-scale probe does not exist which extracts particle-level information and thus larger-scale gauges invariably smear the meso-scale effects. Development of meso-level sensors is a current effort in the HSR lab at Georgia Tech. The wave structures observed in the present work are thus a product of both the topological complexity of the microstructure and the nature of the measurement instruments used to obtain them.

In the present work, stress measurement was performed mainly at the back surface of the powder via the propagated stress gauge. The method for obtaining a single stress measurement from the gauge trace is based on the methodology outlined by Eakins [20]. Equilibrated stress values for the input PVDF gauge were not used in the Hugoniot analysis of the data because of the uncertainty in gauge integrity. The input stress values were impedance-matched based on the impact velocity and known EOS for the impactor. For all measurements of the propagated gauge stress, the values were determined by first finding the point at which the fluctuations in the voltage/current for the gauge reach zero. The transit time through the gauge package at the impact stress was used to determine maximum and minimum possible stress values as ringing and reverberations in the gauge package would eventually diminish and equilibrate. Eakins [20] took this as the stress value to plot in a thermodynamic space. However, since many of the input gauge traces failed to equilibrate, this technique was reserved specifically for the propagated gauge. The error bar for each measured stress was calculated from the RMS combination of the random, systematic, and uncertainty range similar to that used in Eakins' method for the recorded stress measurement.

The typical stress traces recorded for a shock compression experiment exhibit the following behaviors:

- The driver signal as recorded by the input PVDF gauge overshoots (see Figure 54) to the impedance-matched stress between the PTFE and the powder. This signal eventually rings down and equilibrates with the initial compressed powder layer. Small

perturbations in the ringing signal reflect the heterogeneous nature of the powder surface and smear these effects over the sensing area of the gauge (3 mm $\times$ 3 mm). Therefore, large heterogeneities commensurate with the sensing area of the gauge cannot be smeared and thus, each experiment will show a random deviation in these fluctuations beyond the uncertainty of the measurement. Getting a single stress reading that represents the Hugoniot state of the compressed powder becomes ambiguous as a result.

- The input gauge may capture re-shocks driven by a wave reflected from the powder/backer interface. The reflected wave travels through the fully compressed powder as the gauge equilibrates with the powder. This is likely to be observed if the experiment is conducted at lower impact velocities. However, it cannot always be captured due to premature gauge failure or interferences from the other sensing elements in the setup.

- The input gauges likely fail due to interfacial shearing between the hard boron particles and the protective PTFE layers. The shearing involves unstable flow of the PTFE layers, eventually leading to the premature failure of the gauge. Spurious results were common in the input gauges, and meso-scale simulations of the gauge package substantiate this hypothesis.

- The backer (propagated) gauge signal shows dispersive rise time effects (see figure 51) due to a two-stage compression event between loosely-bound particles near the surface of the gauge/backer interface and the compacted powder preceding this loosely-bound layer. This is accentuated by the impedance-mismatch between the backer, gauge, and powder. The rise-time effects have been captured by simulations and manifest the heterogeneous nature of these compacts. It becomes exceedingly difficult to compute a shock speed from three rise time values obtained from a backer signal at lower impact velocities due to the greater dispersion in the wave.

Greater insight may be obtained from the observation of the measured propagated (backer) stress traces as shown in figures 51 and 54. Figure 51 in particular shows a two-wave structure in the rise time of the backer gauge signal for a high pressure experiment. Meso-scale simulations reveal a similar response which has to do with the arrival of the loosely packed layer initially perturbing the gauge package. The equilibration event takes around 50 ns, well above the transit time of a shock wave through the package. Therefore, two independent events generate the signal: the arrival of the initial particles and the subsequent crush-up by the avalanching layer that follows. The peak pressure becomes less ambiguous at the backer gauge due to the equilibration between a dense packed powder (only surface heterogeneities are of significance) and the backer; this is reminiscent of two solids in contact. Other dispersive rise-time signals have been observed to occur well before the peak stress state at the backer and have been ascribed to a crush-up process or potential fracture of particles at the surface of the gauge package.

The propagated (backer) stress gauge traces captured for all successful experiments performed in the present work on Ti+2B compacts are plotted in figure 52. The 50%-Al powder compact experiments are also included in the figure. It can be seen that the stress gauges are able to capture rise-time structure for both the pure Ti+2B and the Ti+2B+50%Al (mixture C), indicating that the compaction response is strong in boron-containing mixtures. This structure seems to disappear at higher shock stresses, undoubtedly because the rise-to-peak stress will be much sharper for higher shock stresses. There is a regime between about 700 m/s and 1000 m/s impact speeds (Cu flyer) where the rise-time structure shows the distinct hump. The two-wave structure prevails at these intermediate shock stresses and represents a two-stage compaction event, to be discussed shortly.

The higher velocity experiments performed at the Munitions Directorate at Eglin AFB are also included in this data set. Three experiments were conducted at Eglin AFB to achieve higher stresses than with the helium-driven gas-gun at Georgia Tech. The experimental setup is a slightly modified version of the Georgia Tech setup, where the main

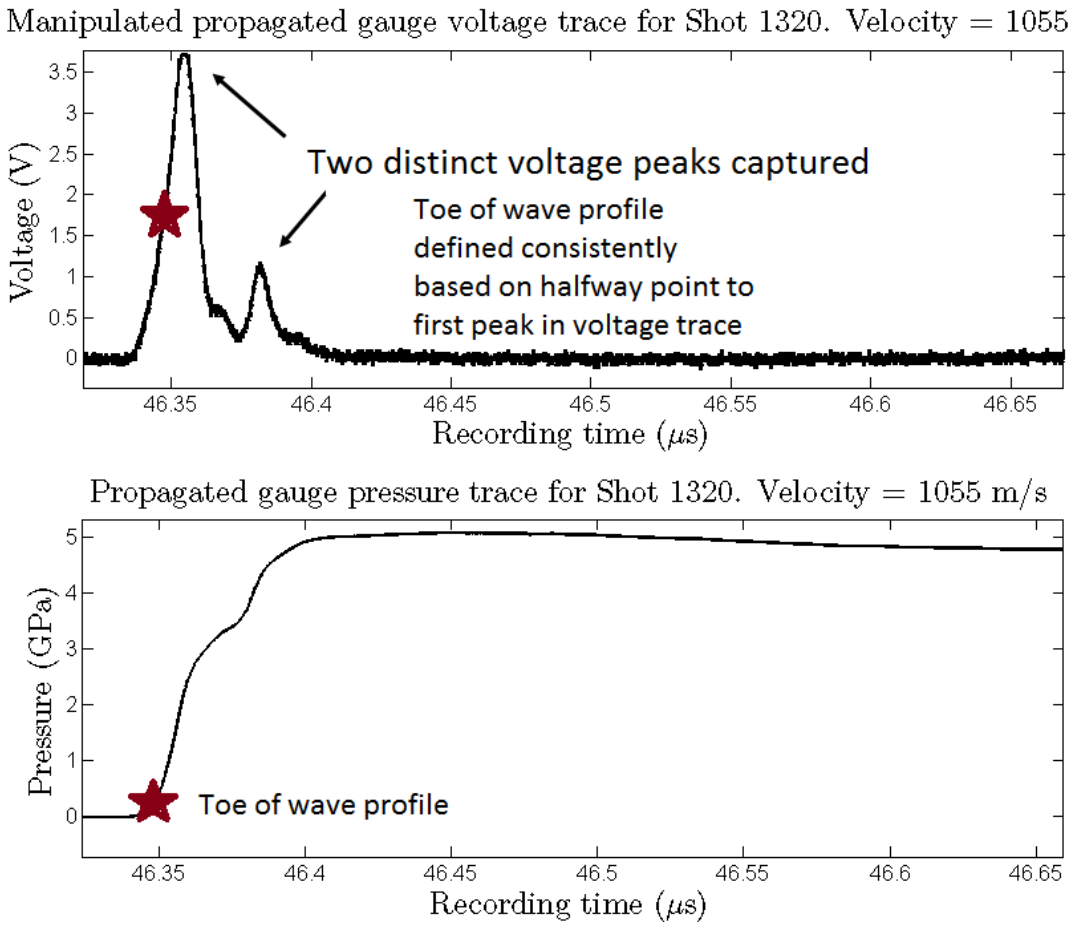

Figure 51: Backer stress trace showing a clear "hump" in the rise time to peak pressure. This is likely due to an initial equilibration from loosely packed powders near the powder/backer interface, followed by a subsequent compression by the fully compacted particles trailing this loosely-packed front. Two distinct voltage peaks are captured by the PVDF gauge. This hump was also captured by meso-scale simulations (cf. section 6.4). A star marks the toe of the wave, measured halfway to the first voltage peak in the raw voltage output from the PVDF stress gauge.

difference is a smaller diameter capsule, yet maintaining an appropriate aspect ratio to ensure one-dimensional wave propagation along the center of the sample. Dynasen PZT pins were used to measure the impact tilt and the target fixture is extensible to include other diagnostics such as photon doppler velocimetry (PDV).

The PVDF stress gauges were adapted to the Eglin target setup by machining a slot (cf. figure 53) so that the PVDF leads could protrude out from the capsule and through the aluminum target. However, the slot, though machined adequately, can interfere with

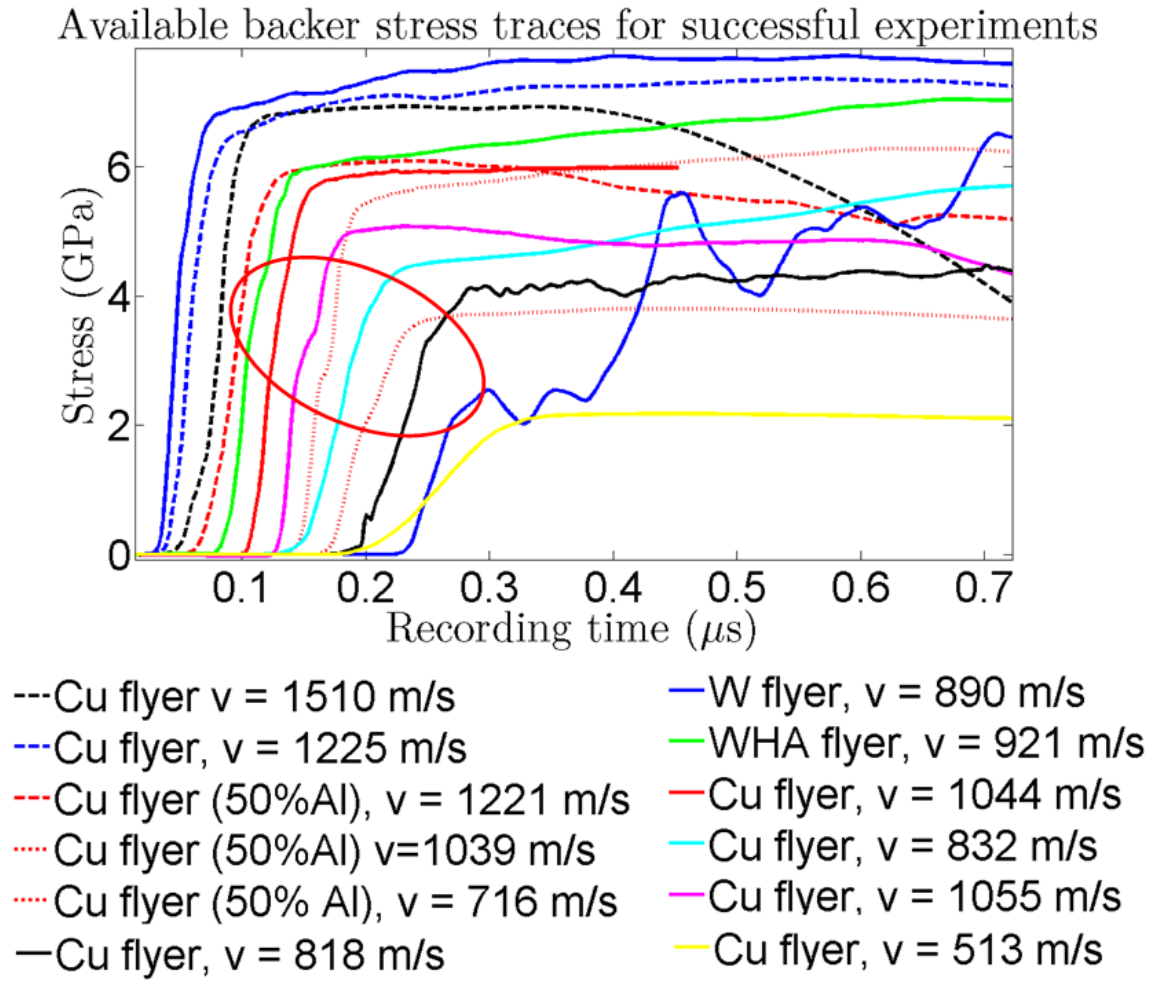

Figure 52: Compilation of every successfully acquired backer trace for the Ti/Al/B system. A propagated gauge trace was not available for all experiments due to oscilloscope or gauge failure (True for two experiments). The gauges were all able to capture rise-time structures and the characteristic "humps" indicative of a crush-up process.

the gauge leads due to an elastic wave propagating through the Al-capsule holder, causing motion between the slot and the gauge leads. This can result in premature shorting the PVDF gauge leads and subsequent shearing of the input PVDF gauges in all experiments performed at Eglin AFB. Therefore, reliable input signals (for peak stress and timing) for wave speed are not obtained for these experiments. The shock speeds were therefore obtained by cross-timing the PZT pins and calculating the transit time through the copper driver to arrive at the gauge package. This increases the uncertainty in the shock speed measurement, although the error propagated by the calculated shock speed through the

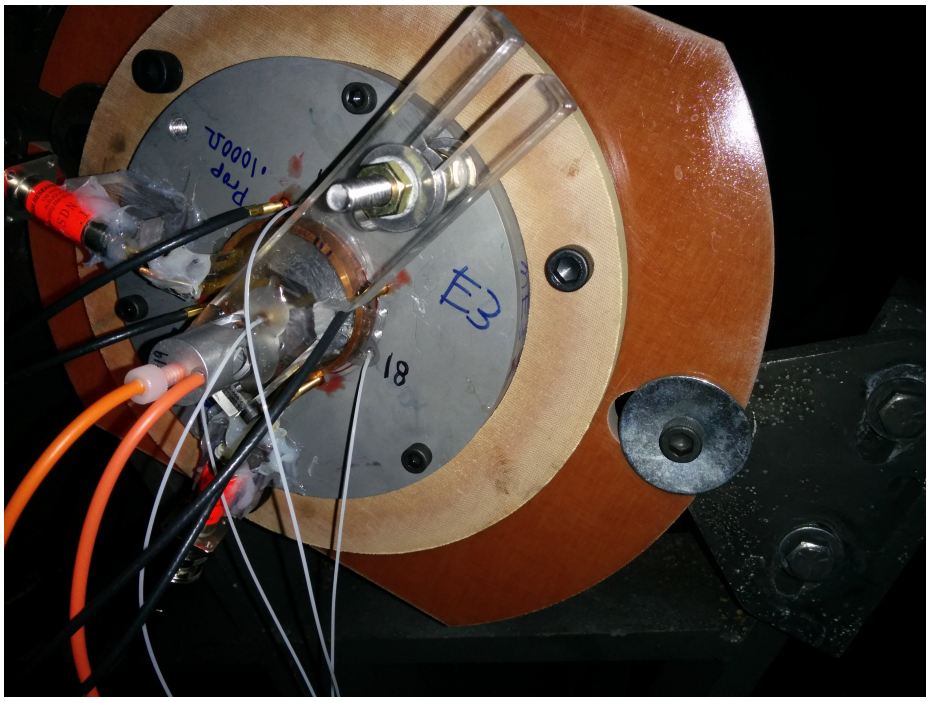

Figure 53: The target setup in the powder-driven gas-gun at the Munitions Directorate - Eglin AFB. Three experiments were conducted using Eglin's powder gun to achieve shock pressures up to 10 GPa. A number of difficulties were encountered when adapting the capsule design to the Eglin target setup.

copper is miniscule.

6.3.3 Calculating wave transit speed in Ti/Al/B powder mixtures

The PVDF propagated stress gauges were able to capture highly dispersed stress waves with interesting rise-time structures. Specifically, a characteristic "hump" was observed in many experiments at intermediate impact velocities (700 - 1000 m/s using Cu-flyers). It should be noted that these "humps" are similar to the classic two-wave kink observed due to phase transformation phenomena. However, the "hump" is actually a direct consequence of the smearing of the meso-level information by the gauge and the heterogeneous nature of the compaction of the constituents of the powder mixture (cf. section 7.3). The presence of this dispersed structure complicates Hugoniot-based analysis.

The Rankine-Hugoniot conditions require that a near-discontinuous change in thermodynamic state take place to be rigorously satisfied. The wave structure inherent in porous

powder compacts due to densification phenomena, particle agglomeration/comminution, and particle fracture, reveals important information about the compaction response at a specific applied pressure. However, the dispersed nature of the propagated wave through the powder, especially for highly distended powder mixtures, makes it difficult to apply the Rankine-Hugoniot conditions to the analysis.

Calculating the shock speed becomes difficult as well due to the variability in potential wave transit time measurements in highly dispersed propagated waves. A different time-of-arrival measurement is deemed necessary because the waves recorded by the propagated gauge often showed the rise-time anomalies and dispersion described previously, which can lead to a large random error in shock speed measurements taken during the rise time of the wave. Figure 51 shows the voltage output for Shot 1320 (V_{imp} = 1055 m/s, Cu impactor) along with the stress trace calculated through the PVDF gauge reduction program in PlotData. The time-of-arrival of the wave was taken at the half-max of the first peak in the voltage/current trace for the gauge, and was recorded as the "toe" value of the transit time (marked by a star in voltage trace). This value corresponds to the first rise. A small, but finite curvature can be observed at the toe of the wave, and represents a slight delay in the pressure rise due to the initial current buildup in the gauge. Thus, by taking the time-of-arrival at the half-max value of the first voltage peak, this allows enough time for an unambiguous non-zero signal to be recorded. Consistent time-of-arrival measurements of the propagating wave through the powder compact were obtained using this technique, and it represents the first arrival of the wave where the recorded stress first becomes non-zero, as shown in Figure 54. **All shock speed measurements presented herewith are reckoned from the toes of the waves, which correspond to the time at half-max for the first voltage spike recorded by the PVDF gauge.**

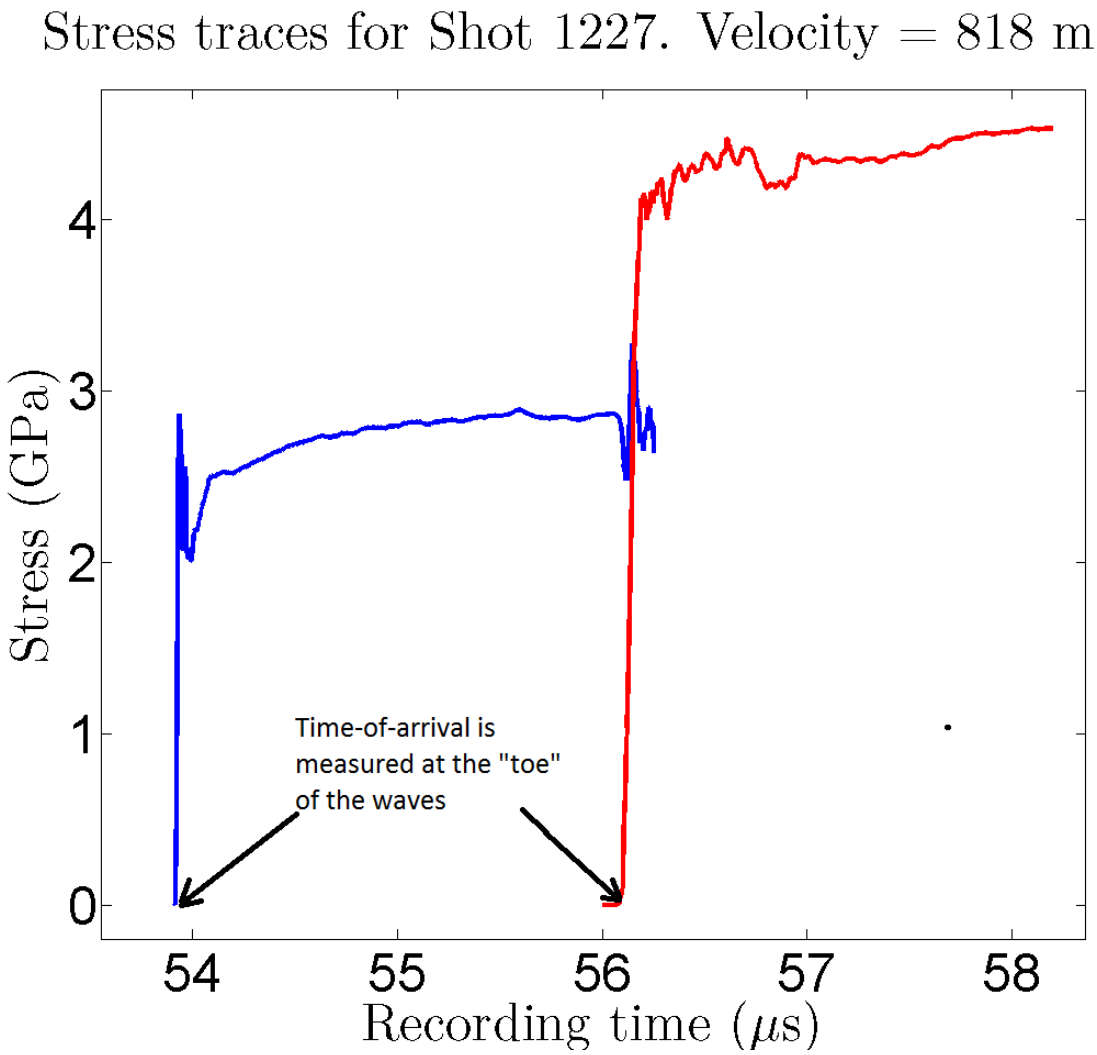

Figure 54: Stress traces for shot 1227 (V_{impact}=818 m/s) showing the driver (blue) and backer (red) stresses. The shock speed measurement is reckoned at the "toe" of the wave, measured at half the peak voltage value of the PVDF gauge. This gives values roughly when the wave becomes non-zero.

6.3.4 Hugoniot analysis of the Ti+2B powder mixture

The recorded wave profiles allowed for a shock speed to be obtained for the Ti+2B and Ti+2B+50%Al powder mixtures at a variety of impact conditions. Using the values of the shock speed and impact velocity (given in table 6), and known EOS for the impactor, impedance-matching was used to obtain the input stress (equivalent to pressure P), σ_1, particle velocity in the powder mixture, U_p, and relative volume V.

Figure 55 plots the measured shock speed versus the calculated particle velocity. The

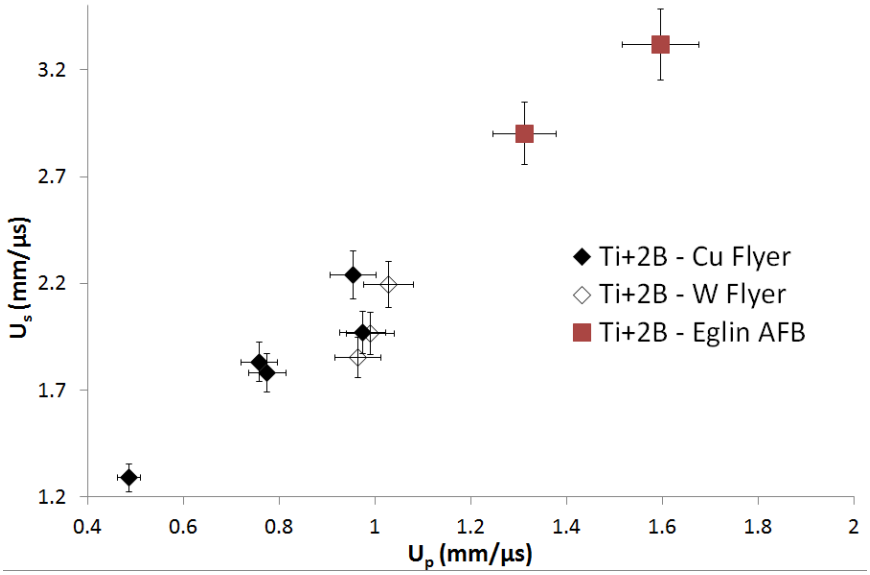

Figure 55: Experimental data cast in thermodynamic $U_s - U_p$ space. The data shows considerable scatter, likely due to compaction effects on the particle velocity.

data is also plotted in $U_s - P$ (only one calculated quantity) space, and $P - V$ (both calculated quantities) space as shown in figures 56 and 57, respectively. The $P - V$ thermodynamic space is particularly significant, as small changes in shock speed or applied pressure can lead to large changes in volume. In general, considerable scatter is observed in the $U_s - U_p$, $U_s - P$, and $P - V$ plots. Further analysis (presented in chapter 7) will be needed to compare the data with EOS models to evaluate trends in shock compressed states observed in the experiments.

A set of experiments were also conducted on the Ti+2B+50%Al mixture (mixture C) as shown in table 6. The experiments were conducted identically to the Ti+2B mixtures. However, all experiments conducted at Georgia Tech (3 of 4) suffered shortcomings in data acquisition. Either one (or both) gauges did not record a signal, or the oscilloscope trigger did not work. Cross-timing with the tilt pins allowed for an estimation of shock speed, although with a larger uncertainty. Therefore, these data points have a large error bar in the shock speed, which propagates to the rest of the calculated variables. A representative error bar is included for the data plotted in figure 58, plotted in $U_s - P$ space, with shock velocity measured using cross-timing, and pressure being obtained by impedance-matching.

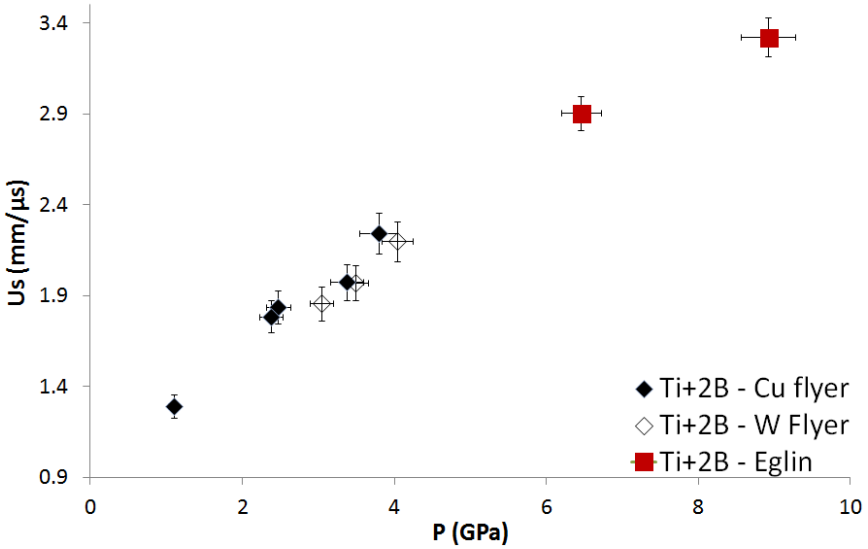

Figure 56: Experimental data cast in thermodynamic $U_s - P$ space shows less scatter than the $U_s - U_p$ data.

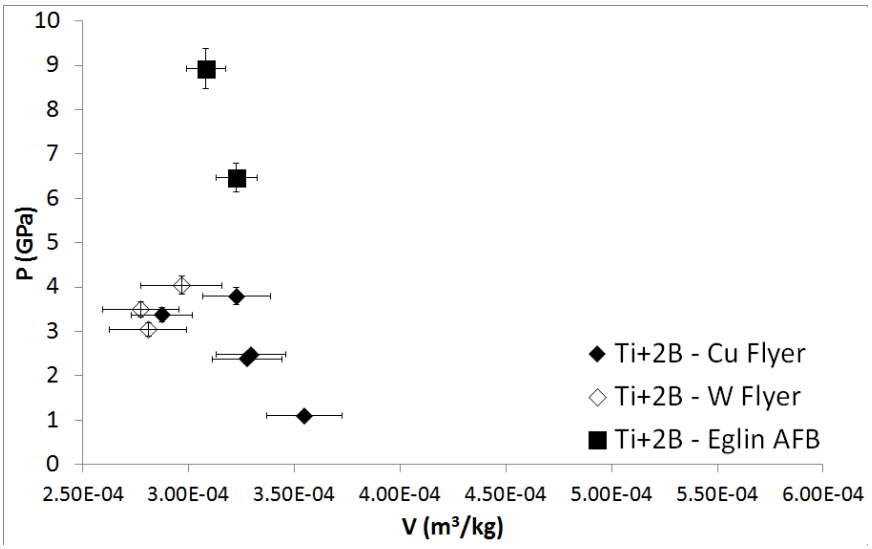

Figure 57: Experimental data cast in thermodynamic $P-V$ space. The data shows considerable deviation at higher stresses, indicating a potential expanded state. Further comparison with EOS predictions is required for verification.

6.3.5 Equation of state predictions for Ti+2B and Ti+2B+Al

The equation of state of the Ti+2B powder mixture (inert state, 50%TMD) was predicted from the McQueen mixture theory and using the Wu-Jing EOS as discussed in chapter

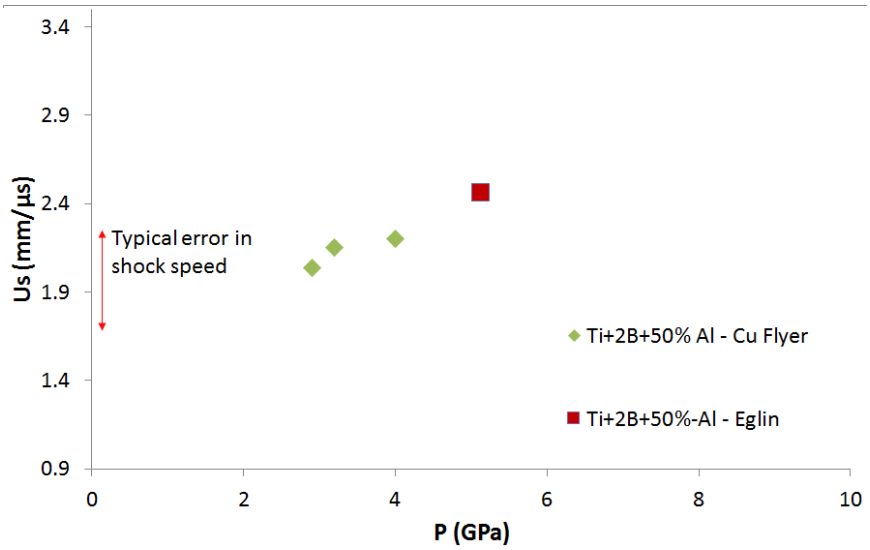

Figure 58: Experimental data cast in thermodynamic $U_s - P$ space for Ti+2B+50%Al powder mixture.

3. The shock speed and particle velocity relationships were obtained by mixing the zero-kelvin isotherms and heating them through the Mie-Grüneisen reference EOS. The resulting Hugoniot predictions for the Ti+2B mixture (mixture A) are shown in figure 59. The predicted U_s-U_p Hugoniot of the ternary Ti+2B+50%Al mixture (mixture C) lies nearly collinear with the Hugoniot of binary Ti+2B mixture. The reaction product curve was calculated using the Ballotechnic hypothesis, and is considered for the reaction of Ti+2B = TiB_2 ($\Delta H_{rxn} = -320$ kJ/mol), as described in chapter 3. The EOS predictions were also cast in $U_s - P$ (figure 60) and $P - V$ space (figure 61). The $P - V$ plot also includes the $P - \alpha$ approximation of the densification response of the Ti+2B mixture, for a crush-strength of 3.5 GPa.

The predicted inert mixture Hugoniot for the 50% TMD Ti+2B powder mixture, and the TiB_2 reaction-product Ballotechnic cast in linear U_s-U_p space have the following forms: Inert Ti+2B Mixture Hugoniot:

$$U_s = 0.1734 + 1.8397 U_p \tag{127}$$

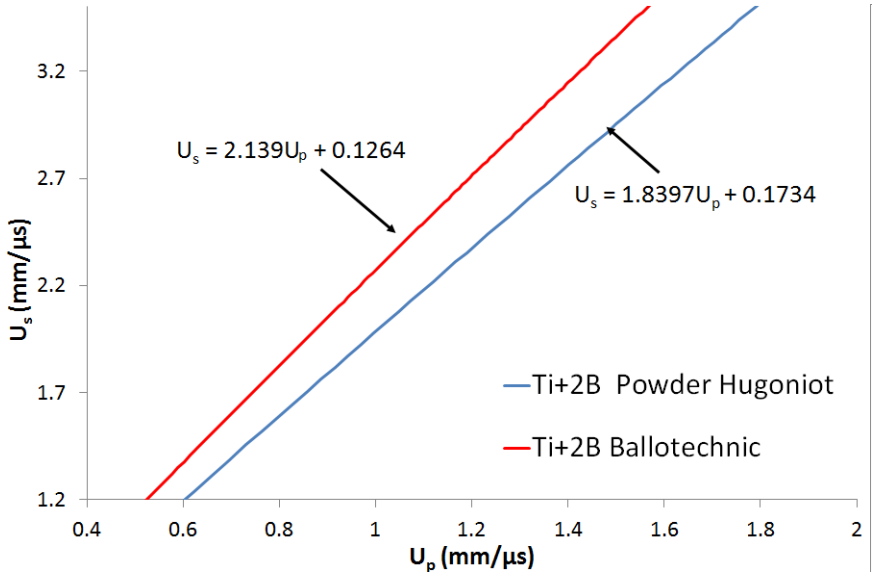

Figure 59: The U_s-U_p Hugoniot space for Ti+2B, showing the inert mixture Hugoniot and the Ballotechnic prediction. Linear $U_s - U_p$ relationships were obtained by curve-fitting.

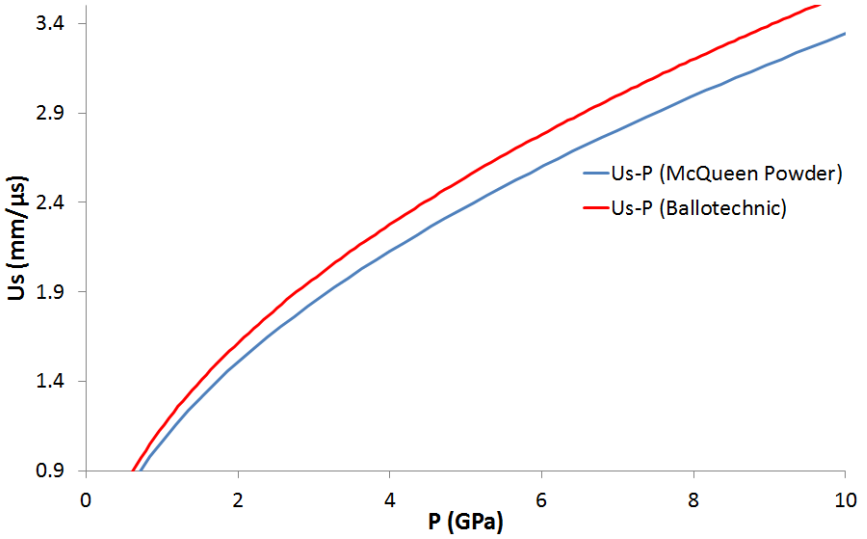

Figure 60: Predicted EOS (inert and Ballotechnic) in $U_s - P$ space for Ti+2B.

TiB_2 reaction-product Ballotechnic:

$$U_s = 0.1264 + 2.139U_p \tag{128}$$

The EOS for the Ti+2B+50%-Al mixture (Mixture C) was also determined and is plotted in $U_s - P$ as shown in figure 62.

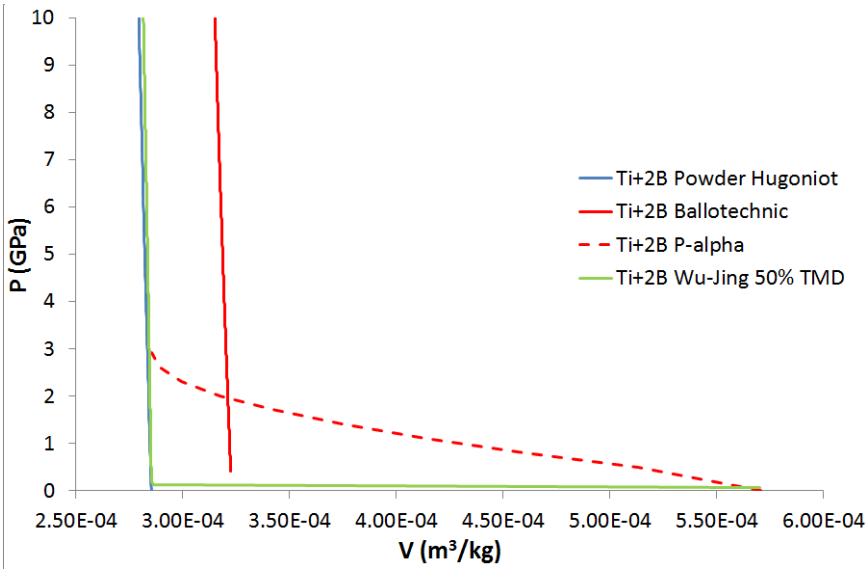

Figure 61: Predicted EOS (inert and Ballotechnic) in $P - V$ space for Ti+2B.

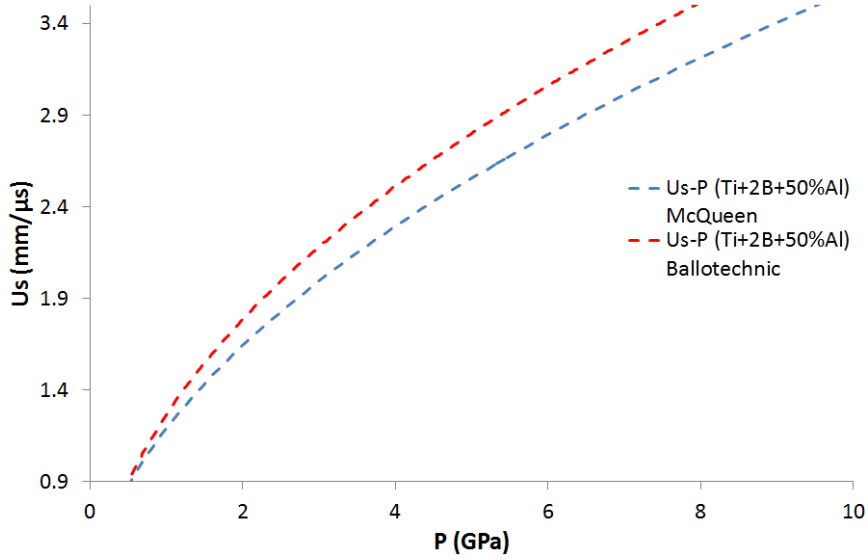

Figure 62: The $U_s - P$ EOS predictions (inert and Ballotechnic) for the ternary Ti+2B+50%Al powder mixture.

6.4 Meso-scale uniaxial strain simulations

A simulation platform was employed as described in chapter 5 where simulated microstructures with highly resolved features are studied using the continuum Eulerian hydrocode CTH. The simulations used the same properties as described previously and all employed AMR set up to track shock wave progression through the material (i.e. refine at boundaries

and at large gradients of pressure). Initial simulations explored different porosity levels, stoichiometries, and Al content. Initial simulations involved a movable piston (Cu) against the microstructure backed by a fused silica window (figure 63).

Subsequent simulations focused on reproducing the experimental conditions, including the 50% TMD achieved for each powder compact that is shock compressed. The simulations used microstructures with a 1:2 ratio of Ti to B, to mimic the powder mixtures used in the experiments. A set of uniform-random microstructures at 50% TMD were generated, with Ti particles sourced from a library of real particle shapes, and using simulated boron particles to match the size distribution quoted from the supplier. Initial simulations were conducted at variable Al and porosity content (shown in figure 64) to plan experiments. These microstructures used a library of titanium particles and the boron and aluminum particles were simulated using polar plots of a Fourier Sine series with a random size and morphology distribution.

Initial simulations used a fused silica backer (modeled using the Fused Quartz SESAME table) and a copper flyer directly impacting the microstructure (figure 63). The microstructure is a square domain 1.047 mm across a side. The left and right boundaries are periodic non-stick symmetry boundaries to simulate a large domain and the confinement observed in a uniaxial strain condition. The top and bottom boundaries are sound-speed absorbing to prevent release effects from affecting the shock front structure. Subsequent simulations incorporated a copper driver and separate flyer to match experimental conditions and vary the flyer material between copper, tungsten, and tungsten-heavy-alloy (cf. figure 44). A 50% TMD microstructure of Ti+2B was used for these simulations. Heat conduction was not included in these simulations due to the quadratic dependence of the time step to the mesh size.

Shock pressure was analyzed in pressure maps for variable porosity and Al content as shown in figure 65. The large pore space in the 50% structure yields the lowest peak pressure due in large part to wave release at pores. Greater Al content increases large

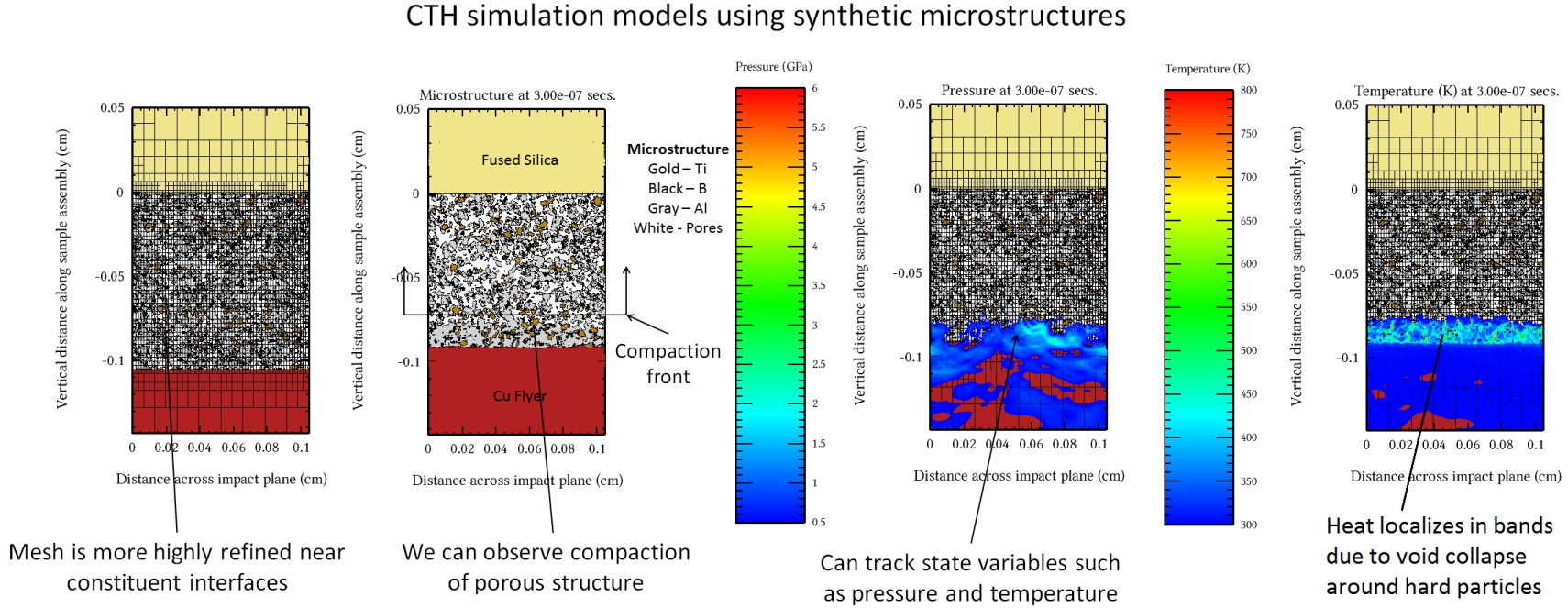

Figure 63: CTH models can be used to obtain field variables and microstructure evolution under shock compression.

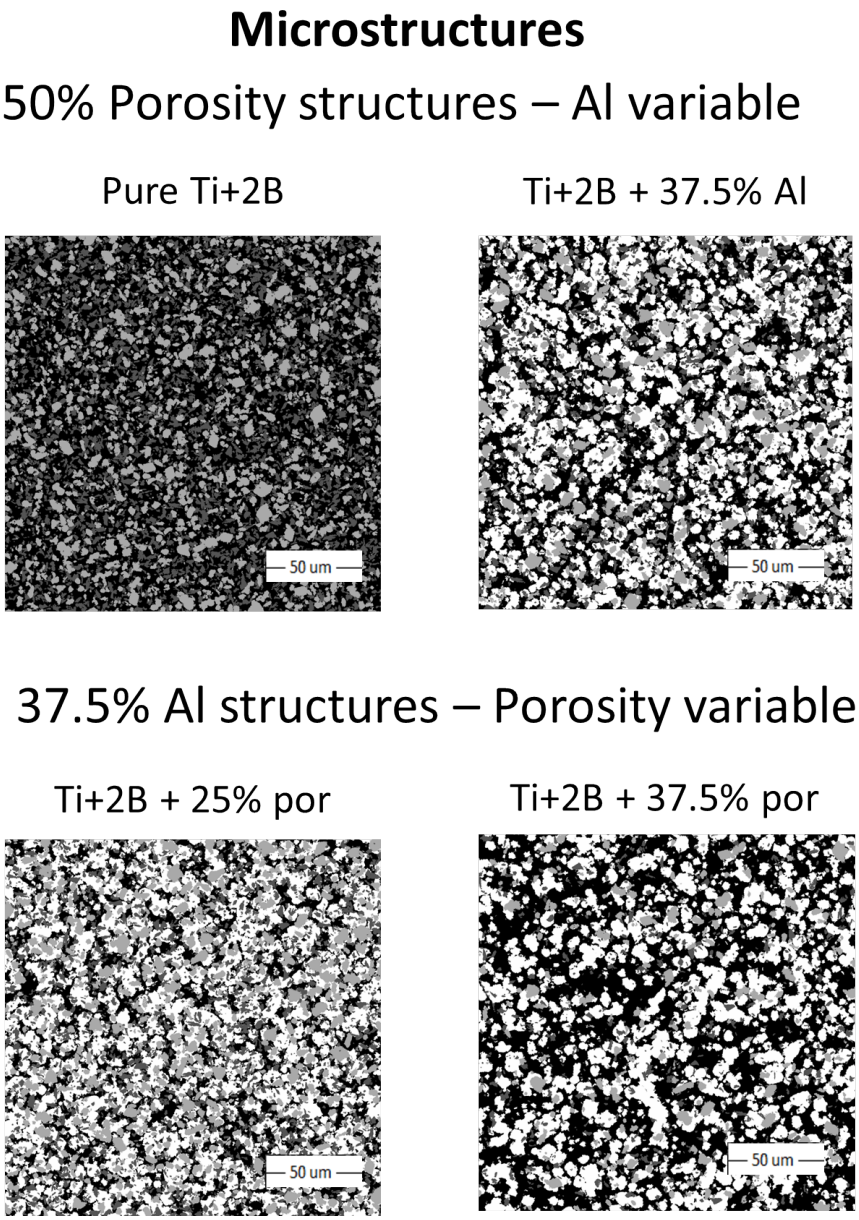

Figure 64: Initial microstructures generated for shock compression simulations. These microstructures explored the 50% TMD regime for the Ti+2B mixture along with the 75% TMD mixture. Porosity and Al content was varied to explore the effects on field quantities such as pressure and temperature. White - Al, Light gray - Ti, Dark gray - B, Black - Porosity

pressure zones, but actually creates some release pockets near the interface with the copper impactor. Furthermore, the Al-containing structures have lower overall pressure due to the lower overall impedance relative to pure Ti+2B.

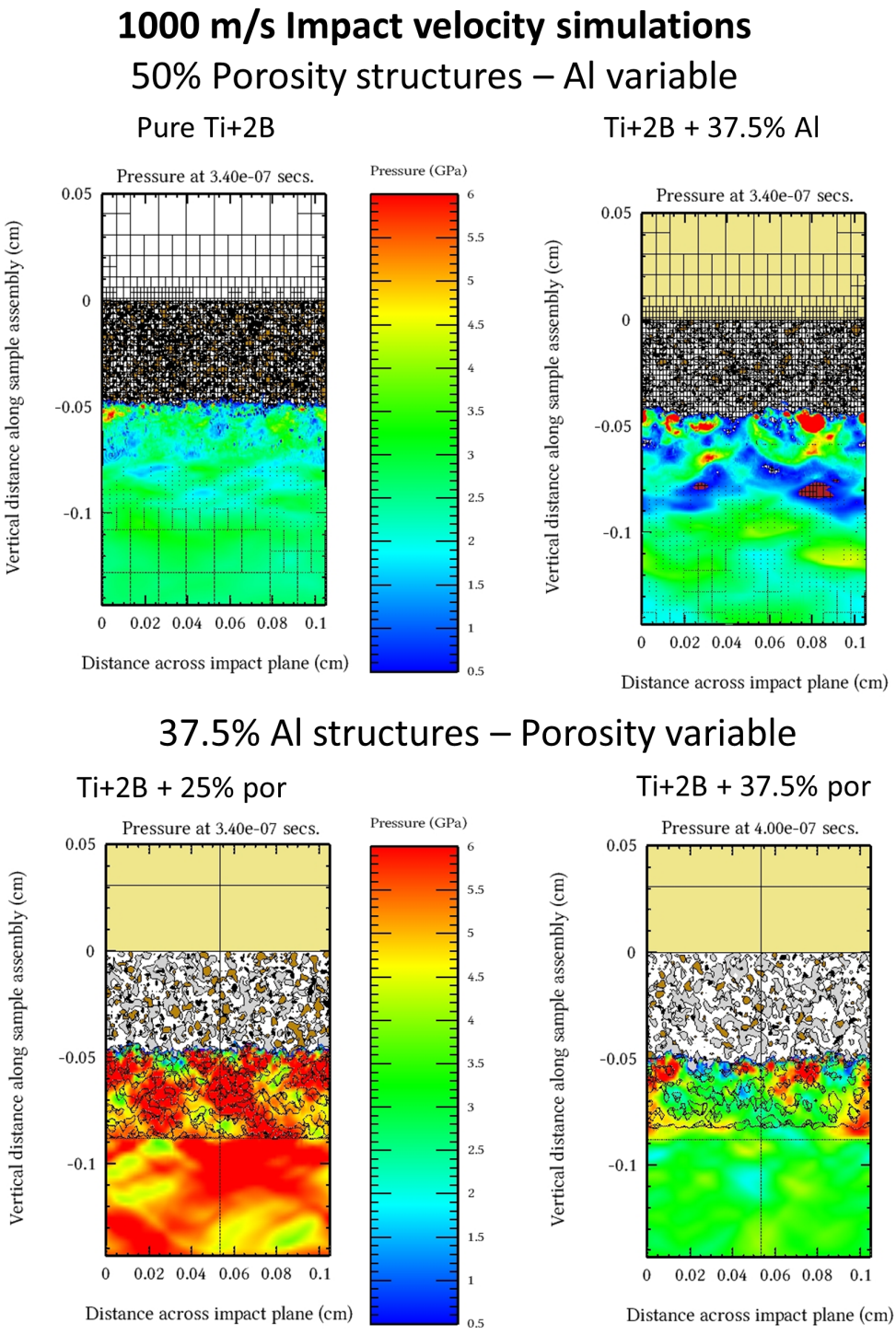

Figure 65: Pressure maps for 50% and 75% TMD structures with 37.5 by vol. Al%. This value was selected for ease of microstructure generation. The peak pressure is lower in higher porosity structures due to wave dispersion. The pressure is lower for Al-containing structures because of the impedance mismatch.

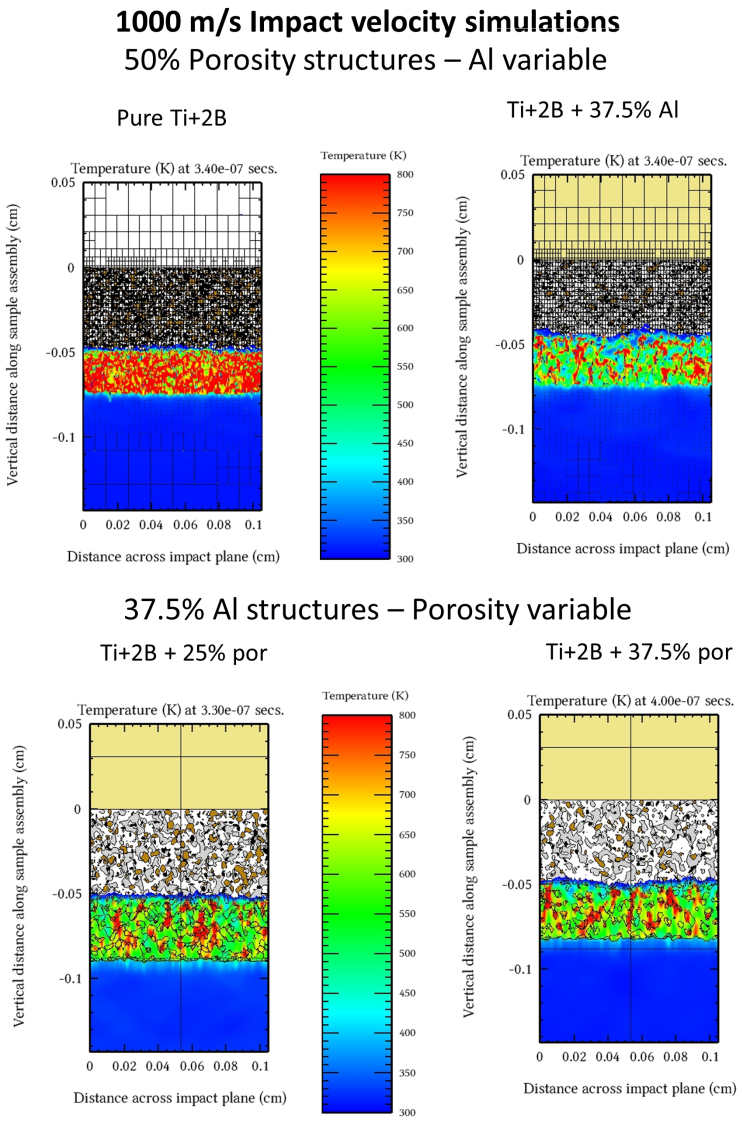

Figure 66: Shock compression simulation of the various microstructures initially considered (V_{impact} = 1000 m/s). (a.) Pressure maps reveal a greater pressure buildup with structures containing some Al with minimal porosity (i.e. 25% porosity with 37.5% Al). The shock is dispersed as a result of the microstructural heterogeneity. Greater pore space creates release pockets and further decreases the pressure buildup. (b.) Temperature maps show lower temperatures for Al-containing structures, mainly localized in bands parallel to the shock propagation direction. The greatest heat buildup occurs in larger porosity simulations while the temperatures do not seem to alter much at higher Al content for denser structures.

The initial shock compression simulations performed on microstructures of variable porosity and Al content also confirm the essential role that porosity plays in shock-induced plastic heating, as shown in figure 66 for an impact velocity of 1000 m/s. Pore space also

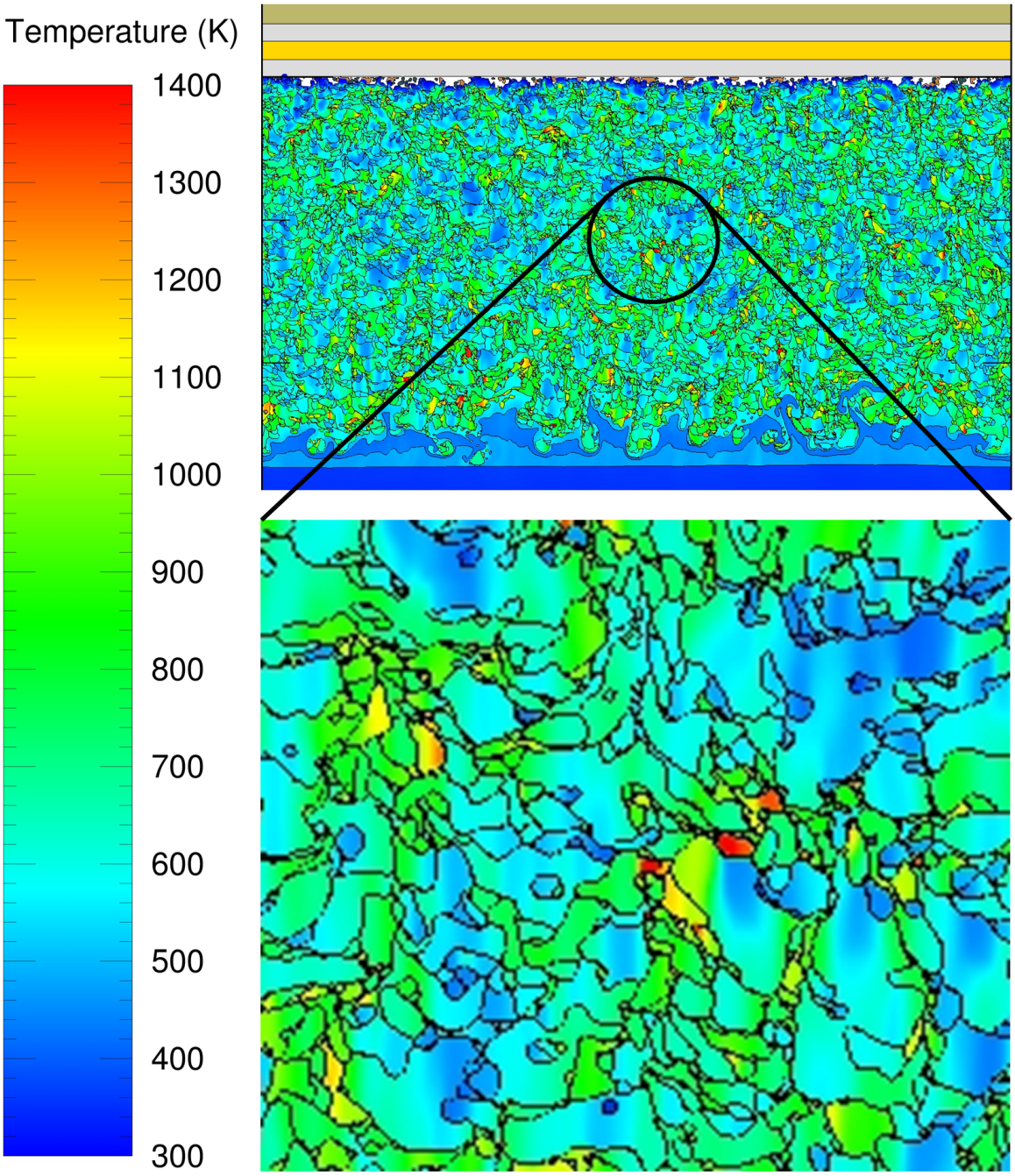

Figure 67: Temperature distribution in a 50% TMD microstructure of Ti+2B shock compressed with a Cu flyer impact at 1000 m/s. A random distribution of highly strained regions and high temperature hotspots are observed, along with highly deformed particles. Confined boron particles heat up more due to greater plastic deformation and friction.

provides an area for components to mix during shock densification. The temperature fields in Al-deficient mixtures (Ti+2B microstructures) show a random distribution of hotspot

regions at temperatures above 1400 K as well as highly deformed particles as shown in figure 67. The role of porosity is to support material mixing during compression. However, the simulations do not show the same pore-collapse behavior as molecular explosives due to the increased pressure of entrapped gases within the pores. This distinguishes the metal-powder mixtures from the molecular explosives in that the interparticle friction and plastic deformation will mediate large temperature generation. The optimal microstructural distribution is sought which prioritizes shock heating along with preferential comminution and contact of reactants. The effects of extrinsic microstructural variables have only been superficially explored in prior works without quantification. Quantifying their evolution remains key in identifying the optimum microstructure that leads to reactivity.

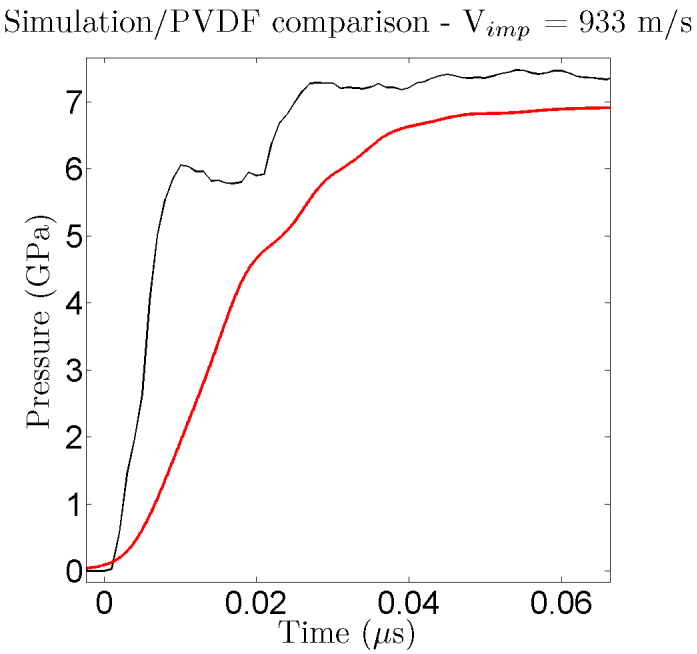

Figure 68: Simulated (black) stress trace compared with measured PVDF trace (red). The stresses predicted by the meso-scale simulation many times over-predict the peak pressure measured by the PVDF gauge. This may be due to premature gauge failure leading to a reduced active area, and thus reduced predicted pressure.

The recent simulations incorporating a simulated gauge package provided the stresses, velocities, and temperatures along various points in the simulation domain and are directly comparable with experiments. A number of recorded stress traces at the backer gauge

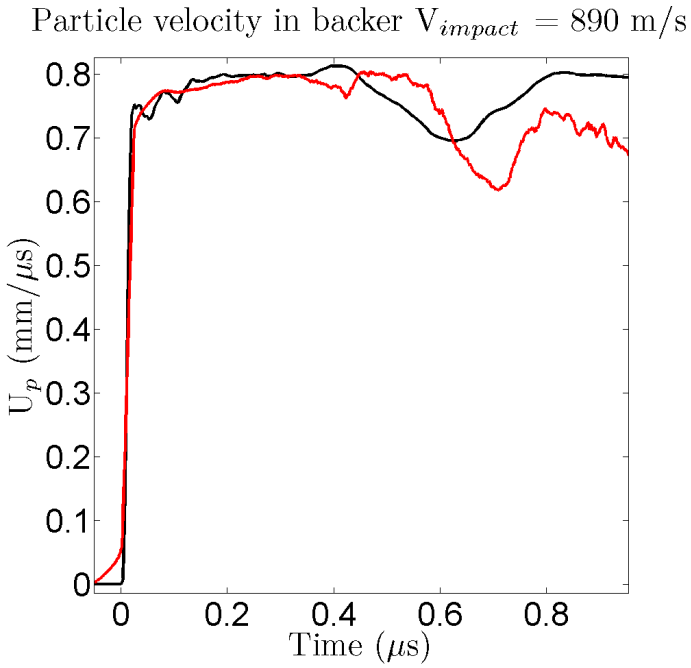

Figure 69: Simulated (black)compared with real VISAR (red) trace from shot 1314. The meso-scale simulation employing an average of ten tracer points at the propagated gauge was able to capture the rise, peak, and even release characteristics of a VISAR trace.

showed a dispersed "two-wave" structure, potentially due to differences in arrival times of the more loosely-bound particles near the surface of the PVDF gauge and the succeeding particle "avalanche." The avalanching particles move at a group velocity impedance-matched with the Cu driver and move slower than the initial jagged front. This initial front creates an initial shock compression of the gauge which rings up to pressure for about 10-20 ns, subsequently equilibrating with the more sluggish particles that follow. This is confirmed by simulations which reproduce the same behaviors (cf. figure 68).

Figure 68 compares the output of the propagated PVDF gauge for shot 1310 and the corresponding simulation for the same impact conditions. While the simulation captures the salient features rather well, the peak pressure is over-predicted, possibly due to premature gauge failure. The simulations also correlate extremely well with VISAR traces as shown in figure 69, capturing the peak velocity and even release-wave events, providing an initial validation for the simulation scheme and physical models employed.

CHAPTER VII

DISCUSSION

The high-strain-rate (uniaxial stress) and shock compression (uniaxial strain) loading experiments showed two distinct processes governing the heating and mixing/deformation of the constituents in the Ti/Al/B powder mixture compacts considered in this work. Under uniaxial stress, the geometry of the loading created preferential shear which led to agglomeration and fracture of the smaller, harder B particles in the case of the experiments on the Ti+2B powder mixtures. Adding Al powders seemed to improve reaction response (based on light emission evidence) and meso-scale simulations showed a more uniform mixing, although a much lower (yet still significant) bulk temperature. Further addition of Al powders, however, proved detrimental to reaction initiation under uniaxial stress loading, pointing to an optimal stoichiometry that enhances reaction initiation. Whether the Ti+Al or Ti+B reaction pathway was favored is not known and further spectroscopic evidence is necessary.

The chemical reaction between Ti and B to form TiB_2 under uniaxial strain will essentially be a dynamic equilibrium and if indeed the reaction occurs within the shock front, this dynamic equilibrium can be assessed by the methods of equilibrium thermodynamics, assuming that local equilibrium and mechanical equilibrium in the small neighborhood of the powders within the wave front (which is really a compaction front) is maintained. It is possible that a non-equilibrium approach as in Truesdell [1] is necessary for closure of the chemical reaction with the Rankine-Hugoniot (R-H) conditions, at least in the portion of the material where the R-H conditions are rigorously satisfied. Both reactants and products may be present within this equilibrium, and there may come a moment where this equilibrium is perturbed (that is, it is metastable) and the reaction proceeds further. This is

hypothesized to be the case in shock compression where the turbulent mixing continually cleanses surfaces and heat from the reaction is in constant supply.

In addition, the loading methods greatly influence the reaction mechanisms. The uniaxial strain loading configuration inherent in a shock compression experiment, for example, involves very little bulk straining, with particle-level transport and deformation processes dominating the bulk response. Extrinsic morphological properties, mechanical properties of constituents, and their physical properties such as shock impedance affect shock wave propagation and shock compaction of the powders. Local rates of deformation depend on these constitutive and acoustic properties. The deformation is confined and the volume reduction is ultimately based on void closure and particle deformation and fracture. Therefore, the mechanisms which generate heat and lead to chemical reactions depend on meso-scale phenomena [12].

7.1 Strain-induced reactions under uniaxial stress loading

The go/no-go results presented in figure 46 reveal an optimal stoichiometry at 50%-Al for a similar %TMD, and meso-scale simulations (see Figure 49) confirm that while Ti+2B compacts generate more heat in shear bands, the Ti+2B+50%-Al compacts produce more strain in the sample with a microstructure that has topologically-connected Al, leading to better mixing of the constituents. A zoomed-in view of the deformed powder mixture for both the Ti+2B and Ti+2B+50%-Al microstructures illustrating these effects is shown in figure 50 for the same impact velocity. The agglomerates in the shear bands for the Ti+2B microstructure show that much of the straining is spent pulverizing the hard boron particles, whereas the Ti+2B+50%-Al microstructure shows uniform heating/straining in the topologically-connected Al-matrix. This straining is further facilitated by the presence of the Ti/B particles, which force the Al to deform around the larger Ti particles. Since much of the straining takes place within the Al-matrix, there are fewer boron agglomerates dispersed within the shear bands. Less straining is used in dissipative fracture, and thus the

constituent mixing and heating is more efficient in the Ti+2B+50%-Al microstructure.

Plastic dissipation in Ti is much greater than in Al, leading to greater heating in the Ti+2B microstructure near the agglomerated regions. However, the overall bulk heating is lower in this structure, as shown in figure 50. Many areas throughout the microstructure remain at low temperatures, whereas the shear bands show significant temperatures (> 1400 K). However, these temperatures may not be significant enough to induce a chemical reaction in a microstructure with only Ti+2B as the constituents. Even though the temperatures in the banded regions are much lower in the 50% Al structure, the temperatures in Al is still significant (> 1000 K), indicating that a potential liquid-phase mechanism may mediate chemical reactivity in Al-containing structures [176] if the Al reached the melting point. The homologous temperature is quite significant ($> 0.8T_H$ in most cases) in much of the Al for this stoichiometry, and the temperatures and strains become significant when the copper rod begins to participate (after full densification) in the impact process. This may account for the reduced threshold velocity for reaction initiation as evidenced from light emission observed in the Ti+2B+50%-Al powder mixture rod-on-anvil impact experiments.

Furthermore, the harder boron particles in the Ti+2B microstructure easily agglomerate due to their size. They are also easy to pulverize due to their high strength and limited ductility. The relatively small size of the particles forces them to agglomerate into bands, as seen in Figures 48 and 50, entrapping them and causing the pulverizing shear and concomitant friction, thereby increasing temperature. However, the dissipative fracture process of the hard (and small) boron particles likely inhibits reactivity, due to lack of mixing between the B and Ti constituents.

Even though the temperatures are much greater in the Ti+2B compacts, the rapid quenching from the surrounding media likely inhibits sustained reactions. Moreover, while the temperatures in the Ti+2B+50%-Al structure are lower, the *bulk* areas around the shear bands are hotter, leading to a greater overall thermal conductivity through the structure, as shown in figure 50. The overall heating of the structure determines whether it is more

likely to react and is directly related to the plastic straining and friction generated during the deformation. This straining is more efficient when Al is present in the materials. The topological connectivity of the Al-containing microstructures (see Figure 50) enables the shear banded regions to have better constituent mixing. Coupled with the relatively high temperatures (relative to Al), the structure that promotes the greatest mixing and mutual plastic deformation between constituents seems to promote reactivity, manifested as a lower threshold for impact-induced reaction. The Ti+2B (0%-Al) structure, while displaying larger temperatures in the shear bands, does not show the same amount of mutual plastic deformation across constituents. The presence of Al appears to restrict the clustering and agglomeration of B, thereby promoting mixing of constituents and facilitating chemical reactions under the condition of uniaxial stress loading.

The rod-on-anvil impact configuration (**uniaxial stress**) involves unconfined bulk deformation, which leads to excessive straining and transport of constituents. Strain localization is expected due in part to material instability and unmitigated shear deformation. This can lead to extensive particle entrapment, deformation, fracture, and even agglomeration of smaller particles as was observed in this system. The microstructural state of the mixture again affects the bulk response, but the bulk heating then depends on material instability and particle straining. Particle transport must be such that constituents strain sufficiently to heat up, while maintaining intimate mixing and contact between reactants. This was again found to be inhibited by the use of small boron particles due to their agglomeration. The relatively low compact density (i.e. 75% TMD) provides free volume for mixing as well as potential void collapse sites (i.e. hot spot locations). However, the addition of a softer reactive material (Aluminum) was found to be critical in promoting reactivity when added to the stoichiometric Ti+2B mixture at 50% by Vol. This optimal stoichiometry demonstrates that there is indeed an optimal microstructural configuration that promotes reactivity. The binary Ti+2B microstructures, while showing higher temperatures for the same impact velocity, likely do not react because of the dissipative fracture and agglomeration processes,

and lower mutual plastic straining and mixing between boron and titanium.

The later-stage copper rod/sabot interaction with the reactive pellet and anvil in the rod-on-anvil impact configuration certainly plays a role inducing chemical reactivity. The highly strained material goes through a bulk-deformation stage, wherein the fully dense (yet highly strained) compact rings up to pressure with the copper rod. The re-shock event precipitously shocks the material which likely serves as the catalyst for the reaction. However, even accounting for this effect, the pure Ti+2B compact shows reactivity at higher impact conditions than the Ti+2B+50%-Al mixture. This is a direct consequence of the partition of kinetic energy to chemical reaction energy, which is facilitated when enough pre-strain (pre-activation) is imparted to the compact during stage 1 (when the compact is initially densifying) of the compaction. Figure 49 shows this effect in the early stages of the compaction. The added aluminum in the 50%-Al mixture (Mixture C) likely inhibits aggregation of the boron particles and promotes mixing to ensure consistent reactivity at lower velocities, as shown in the simulations illustrated in figures 48– 50.

The key feature remains the large strains facilitated by unconfined deformation and geometric/material instability inherent in uniaxial stress loading. Ames [10] observed similar features in conventional explosives tested in a rod-on-anvil impact configuration, and concluded that the shear instabilities are essential precursors to reaction initiation under uniaxial stress loading, although the issue of constituent mixing is not relevant in explosives. The chemical reactions observed in reactive mixtures under uniaxial stress loading depend on facilitated straining and mutual plastic deformation of topologically-connected material. Such reactions can therefore be labeled as *Strain-induced reactions*, wherein large amounts of strain is essential to promote shear instability and thus, mutual straining and mixing of the constituents remains the driving force inducing chemical reactions under uniaxial stress dynamic loading.

7.2 *Shock-induced chemical reactivity under uniaxial strain loading*

Figures 55 – 57 showing plots of $U_s - U_p$, $U_s - P$, and $P - V$, were created by impedance-matching the measured shock speed U_s with the impactor (of known EOS) velocity V_{imp} to obtain the final shock state. This assumes that an ideal shock wave is imparted into the powder mixture and travels without attenuating[1]. It can be seen that there is no obvious trend observed due to the large scatter in data, which is inherent when considering dispersion of shock waves as they propagate through powder mixtures. Data in $P - V$-space in particular shows the greatest amount of scatter because of the dual dependence of the volume on measured and calculated values of the shock state variables. Hence, the inert and reaction-product EOS predictions derived in section 6.3.5 may be considered to determine if the data (which was calculated assuming ideal conditions) shows any obvious trends when comparing with predicted EOS models.

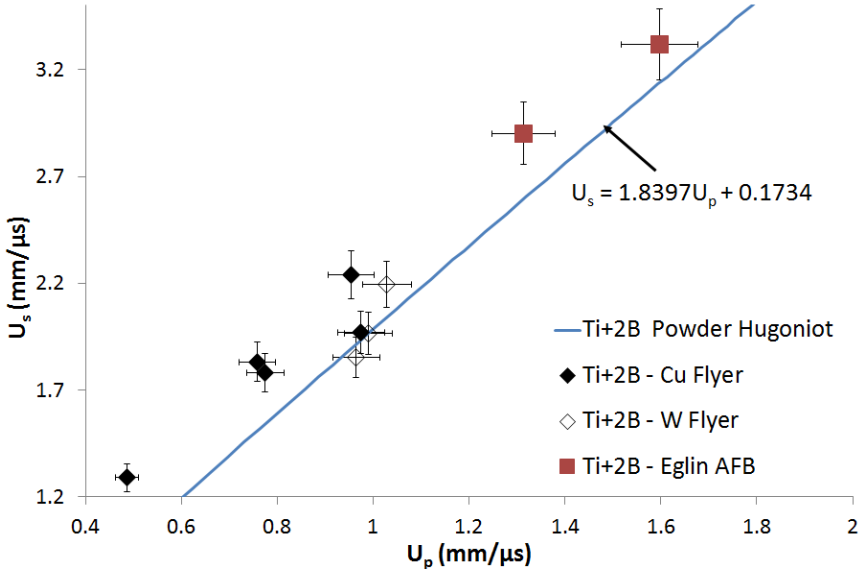

Figure 70: The experimental data for Ti+2B compared with the inert Hugoniot prediction in $U_s - U_p$ space.

Comparison of the uniaxial strain experimental data plotted in thermodynamic $U_s - U_p$, $U_s - P$, and $P - V$ spaces with the inert predicted EOS models using the McQueen mixture

[1] Attenuation in the wave traveling through the powder is mitigated by using large aspect ratio targets as discussed in chapter 4.

theory are shown in figures 70, 71, and 72, respectively. It can be seen that the low and high pressure data points lie off of the inert mixture line, indicating a faster-than-expected shock speed for the corresponding impedance-matched particle velocity or pressure in $U_s - U_p$ and $U_s - P$ plots, respectively. The off-Hugoniot data manifest as expanded states in the $P - V$ plot. The lower pressure data in $P - V$ space approaches the inert line at $\sim$ 3.5 GPa, which defines the dynamic crush-strength for the Ti+2B powder mixture.

The lower pressure points on the $P-V$ plot thus correspond to incomplete densification, since they follow the $P-\alpha$ densification curve plotted for a 3.5 GPa crush-strength powder. It should be noted that the shock velocity for the data points corresponding to the partially-densified (distended) states is also expected to be higher than the predicted inert Hugoniot, which assumes a zero-pressure crush-strength. Hence, the three low pressure data points in the $U_s - U_p$ and $U_s - P$ plots are observed to be above the predicted curve for the inert mixture.

The two higher pressure data points in figures 70 – 72 also deviate from the inert trend calculated by both the McQueen mixture model and Wu-Jing EOS (shown in $P - V$ space in Figure 72), which can possibly be due to shock-induced reaction. Considering the possibility of such shock-induced chemical reactions, the calculated TiB_2 reaction-product Hugoniot ($\Delta H_{rxn} = -320$ kJ/mol), described in section 6.3.5 and plotted in figures 59 – 62, were superimposed with the experimental data.

The combination of the inert mixture curves and the calculated Ballotechnic predictions of the possible Ti+2B=TiB_2 reaction-product plotted along with the experimental data is shown in figures 73 ($U_s - U_p$), 74 ($U_s - U_p$), and 75 ($P - V$). The calculated Ballotechnic curve acts as an upper-bound to the high pressure data corresponding to the state of the shock-induced reaction-product. It can be seen that the high pressure data points correspond to higher shock velocity and expanded states, and lie along the calculated reaction-product curve for TiB_2. The evidence of an expanded state is consistent with the Ballotechnic hypothesis, caused by the heat of reaction from a shock-induced chemical

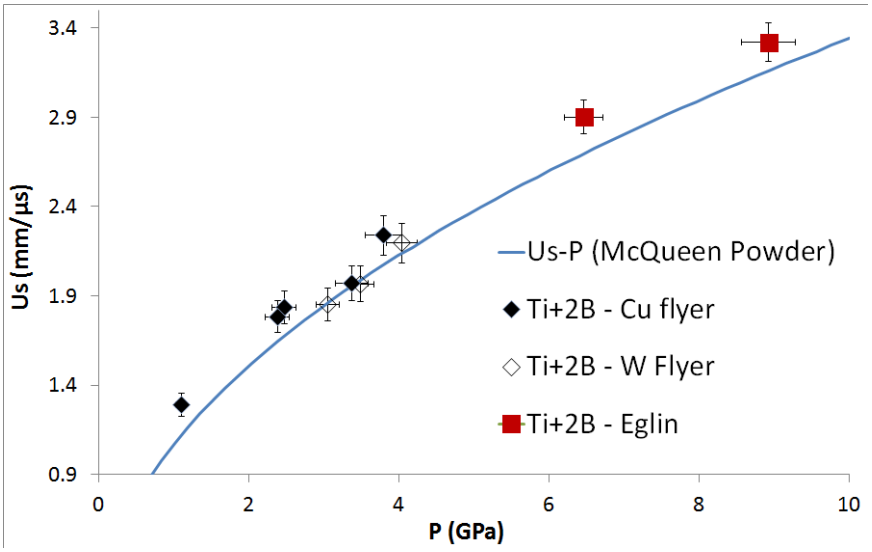

Figure 71: The experimental data for Ti+2B compared with the inert Hugoniot prediction in $U_s - P$ space. Again, many data points lie above the inert mixture line.

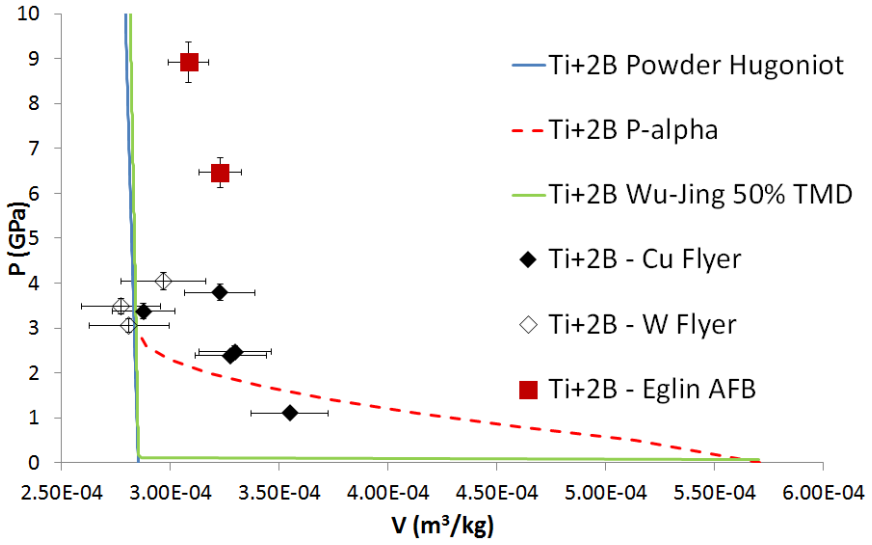

Figure 72: The experimental data for Ti+2B compared with the inert Hugoniot prediction in $P - V$ space. Around four data points cluster around the inert mixture line upon reaching full densification. The high pressure points lie to the expanded side of the Hugoniot.

reaction. It should be noted that the inert mixture and reaction-product Ballotechnic curves are first-order approximations using available EOS models for boron. The data nevertheless explains the possible reasoning for the deviation in experimentally obtained data points at lower and higher pressures. While the experimental data points by themselves do not reveal an anomalous trend, considering the results in the context of the predicted states for

the inert and fully reacted products provides possible scenarios for shock-induced chemical reactions, consistent with results obtained in previous works (See chapter 2).

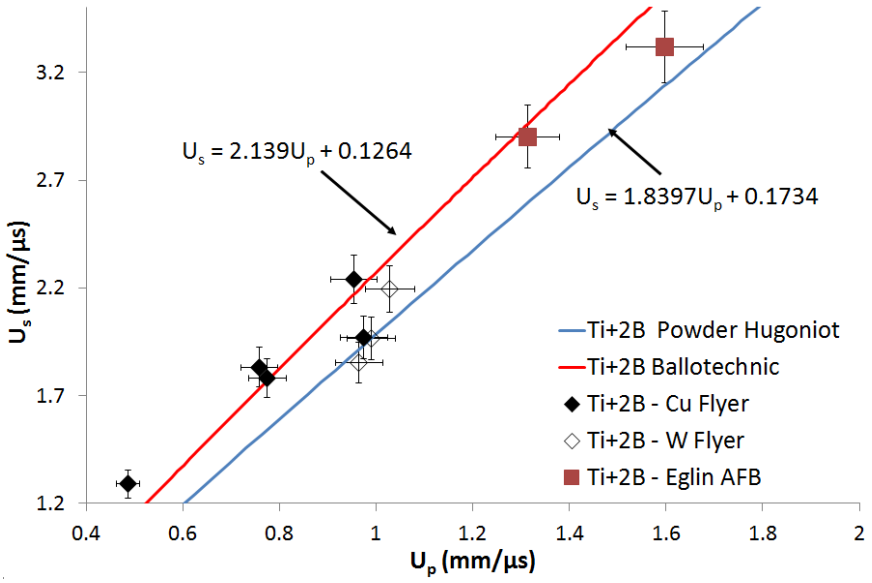

Figure 73: The P-V Hugoniot for Ti/Al/B with the P-α prediction and Ballotechnic. The Wu-Jing EOS approaches the Mie-Grüneisen porous Hugoniot. Many data points lie along the Ballotechnic, hinting at a potential shock-induced chemical reaction.

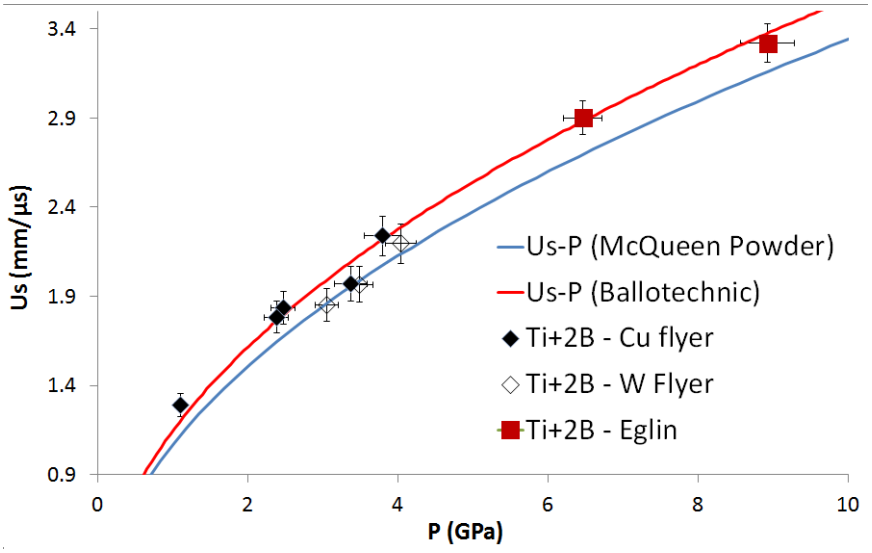

Figure 74: The U_s-P Hugoniot for Ti/Al/B reveals the expanded state in a clearer fashion. Both low pressure and high pressure data clearly fall along the TiB_2 reaction product curve.

The Hugoniot data approaching the expanded state, and higher shock speeds producing the expanded volume point to shock-induced chemical reactions at pressures above ~ 6

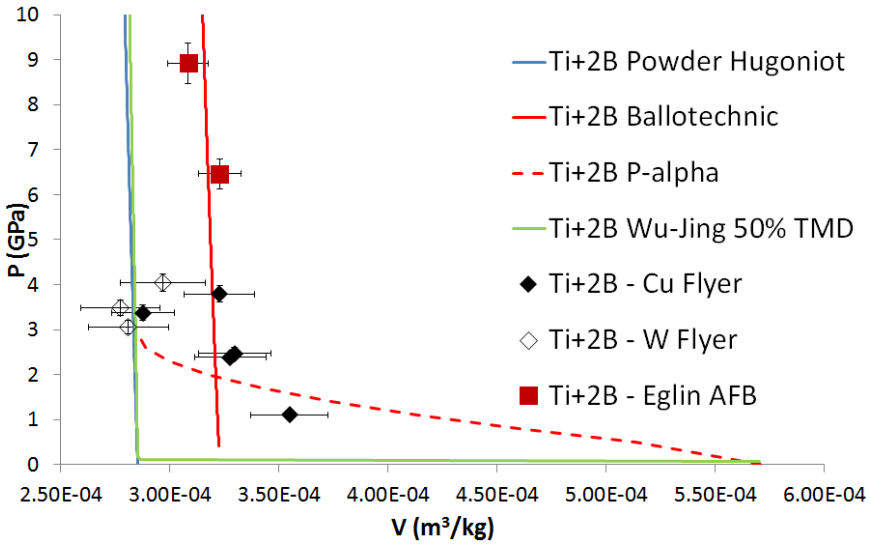

Figure 75: The P-V Hugoniot for Ti/Al/B with the P-α prediction and Ballotechnic. The Wu-Jing EOS approaches the Mie-Grüneisen porous Hugoniot. Many data points lie along the Ballotechnic, hinting at a potential shock-induced chemical reaction.

GPa. Experiments at pressures up to $\sim$ 3.5 GPa correspond to anomalous densification processes [42], due to the high crush-strength of the Ti+2B powder mixture. The data points between $\sim$ 3.5 GPa and $\sim$ 6 GPa are in good correspondence with the inert mixture line, indicating shock compression of the dense, inert reactive mixture state at intermediate shock pressures.

When considering the ternary Ti+2B+50% Al mixture, all of the data points in the $\sim$ 3.5 to 6 GPa range indicate no evidence of an expanded state or higher shock velocity, as shown in the $U_s - P$ plot in figure 76. The data lies near the inert mixture line for all experiments, indicating no obvious evidence of shock-induced reaction. It should be noted that the uniaxial stress experiments illustrated that the addition of Al was more beneficial to reaction initiation. Hence, a similar beneficial effect of Al addition in the Ti+2B mixture was anticipated even with uniaxial strain experiments. It is uncertain if the lack of reaction in the ternary mixture under uniaxial strain loading is due to the need for higher pressures ($>$ 6 GPa) similar to that needed for the Ti+2B mixture, or if the unconfined geometry in the uniaxial stress configuration allows greater straining of a topologically-connected

material like aluminum. The bulk compressibility of the densified material in a uniaxial strain geometry limits straining in the soft Al phase, thereby limiting mixing and heating of the materials. Further experiments are needed in the ternary mixture at higher pressures to indeed establish the role of the Al-additions to Ti+2B under uniaxial strain loading.

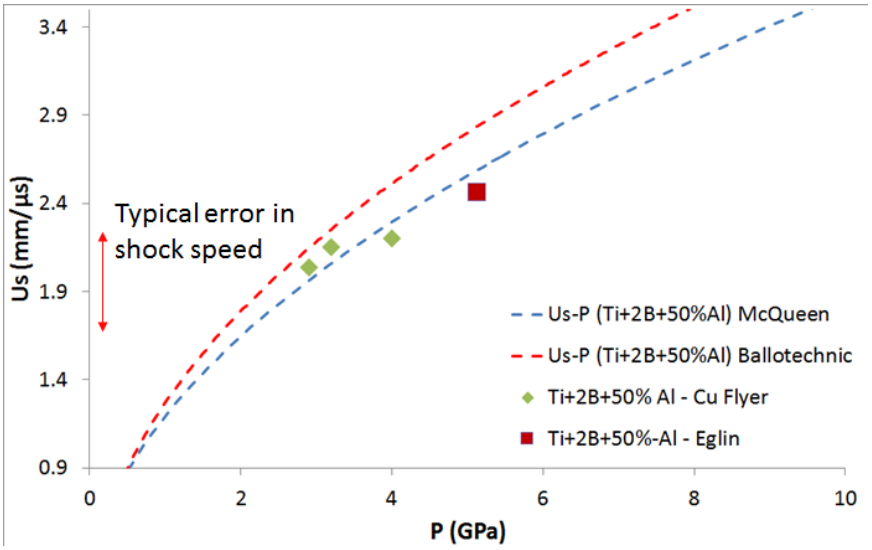

Figure 76: The U_s-P Hugoniot for Ti/Al/B reveals the expanded state in a clearer fashion. Both low pressure and high pressure data clearly fall along the TiB_2 reaction product curve.

In the case of **uniaxial strain** experiments, addition of Al seems to increase the measured stress at the propagated gauge (a larger back-pressure) due to impedance differences in the constituents, as shown in table 1. A comparable peak stress in the ternary mixture at an impact velocity of 716 m/s (Shot 1405) was observed when comparing with a similar experiment at an even greater velocity (818 m/s, Shot 1227) for the binary mixture (3.8 GPa in the ternary mixture and 4.1 GPa for the binary mixture), indicating a larger back-pressure (see figure 77, which shows the propagated PVDF stress trace for shot 1405). However, there is insufficient data to fully ascertain the influence of the impedance-mismatch on wave propagation characteristics, and as a corollary, its influence on shock-induced chemical reactivity. Further simulations using microstructures at the Ti+2B+50% stoichiometry and 50% TMD considered in the uniaxial strain experiments are necessary to confirm this effect.

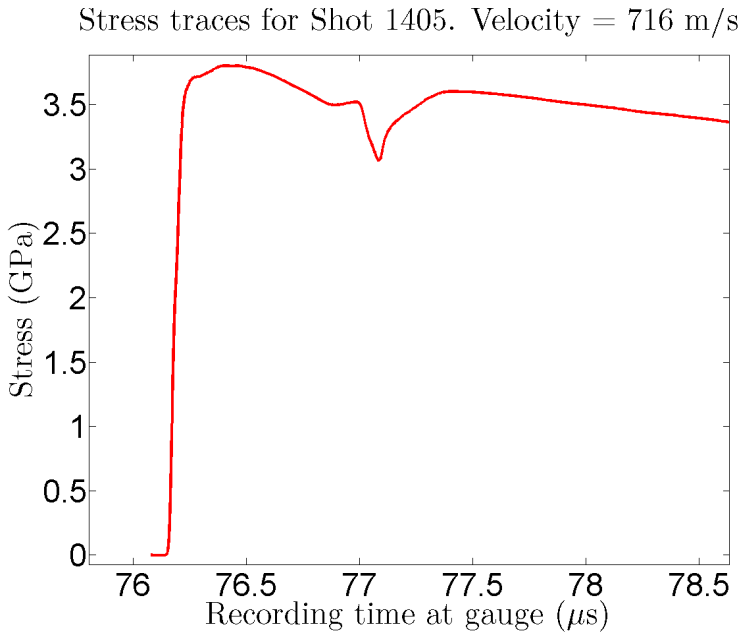

Figure 77: Propagated PVDF stress trace for Shot 1405 - Ti+2B+50%Al, 50%TMD. The peak stress in the ternary mixture for an impact velocity of 716 m/s (3.8 GPa) is comparable to that in the binary Ti+2B mixture at 818 m/s (~ 4.1 GPa, see table 6), indicating a comparable pressure of the propagated wave to the higher-impedance mixture (the binary Ti+2B) in the dense state.

7.3 Heterogeneity manifesting bulk response

Spatial variations in the compaction media reveal themselves as an averaged response (they are "smeared") by the sensors over the active sensing area and therefore the response at the particle size scale may be lost in the averaged response. However, when the heterogeneity is commensurate with the sensor active area, the spatial variations in the compaction become relevant and the observed response becomes a function of where the measurement was taken, making the result completely stochastic. This was observed in simulations as well as experiments and will be discussed further. The major heterogeneity in this work was the property disparity between the constituents, specifically between the boron and titanium particles.

Meso-scale simulations using precise microstructural representations reveal the character of the compaction process as the powders are shock compressed. A jagged wave front is observed when the first layer of loose particles at the rear surface become disturbed by

rapidly advancing wave fronts, mainly in the form of boron force chains. The disparate size distribution and the strength disparities between the boron particles and titanium particles leads to the piercing of the gauge package by the faster moving, higher strength boron agglomerates as shown in Figure 78a. Experiments at intermediate impact velocities (V = 700 – 1100 m/s using Cu flyers) showed rise-time structures in the form of "humps" (Figure 78b). These "humps" are typical of experiments at this velocity range and are due to the inhomogeneous loading of the PVDF gauge active area, which captures the early compaction process

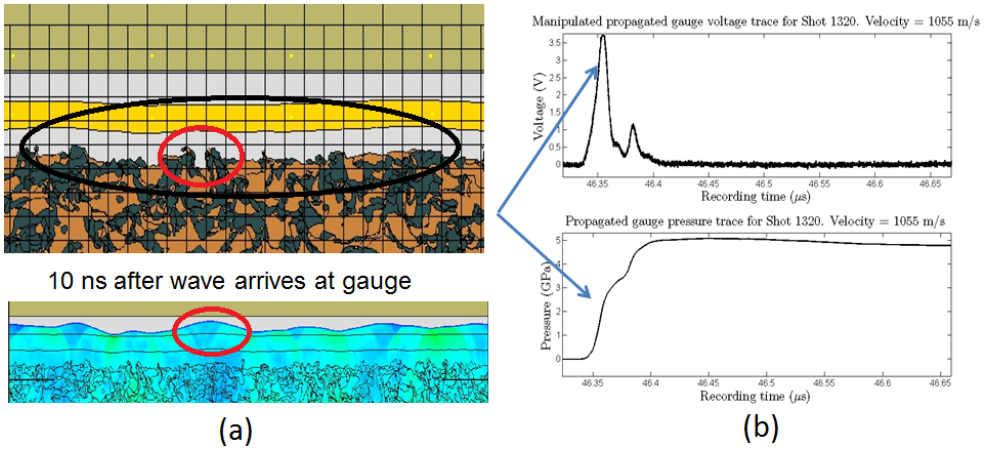

Figure 78: (a) Meso-scale simulations show a tortuous wave front due to localized heterogeneities, namely boron particle chains transmitting forces at greater velocities than the surrounding Ti-rich regions. (b) The rise-time "humps" observed in typical experiments between about V_{imp} = 700 – 1100 m/s impact velocities are due to these localized heterogeneities being averaged over the gauge active area. Distinct voltage signatures (top figure) are captured at time scales corresponding to reverberations in the gauge package, which are exacerbated by the natural heterogeneity in the powder mixture.

The high crush-strength (~ 3.5 GPa) of the Ti+2B mixture is partially responsible for the observed dispersion in the wave as well as the rise-time signature. The compaction process duration is extended due to agglomeration of the boron particles. These boron agglomerates interact with the gauge surface first and are likely responsible for the early time signatures; this highly depends on the local heterogeneity. Further plastic deformation in the Ti particles serves to flatten the wave front as it propagates through the powder.

The simulated output from the individual tracer points reveals a large amount of variability both in arrival-time signature and stress levels achieved during the shock compression of the powders, as shown in figure 79. This variability in measured stress levels is a function of the local heterogeneity in the mixture and is a meso-scale feature that cannot be captured without direct simulation of the particle geometries and structure. Individual tracer points reflect the local stress state upon wave transit and can be more easily matched to the measured response in a smaller-area probe, such as VISAR. However, there is a large variation in time-of-arrival signatures which may differ by as much as 20-40 ns. The non-uniform loading of the gauge active area directly influences the arrival of these signatures. Reverberations within the gauge package during the equilibration process disperse the wave further, but it is the multiple wave interactions from the arrival of faster moving regions that can account for the greatest source of dispersion.

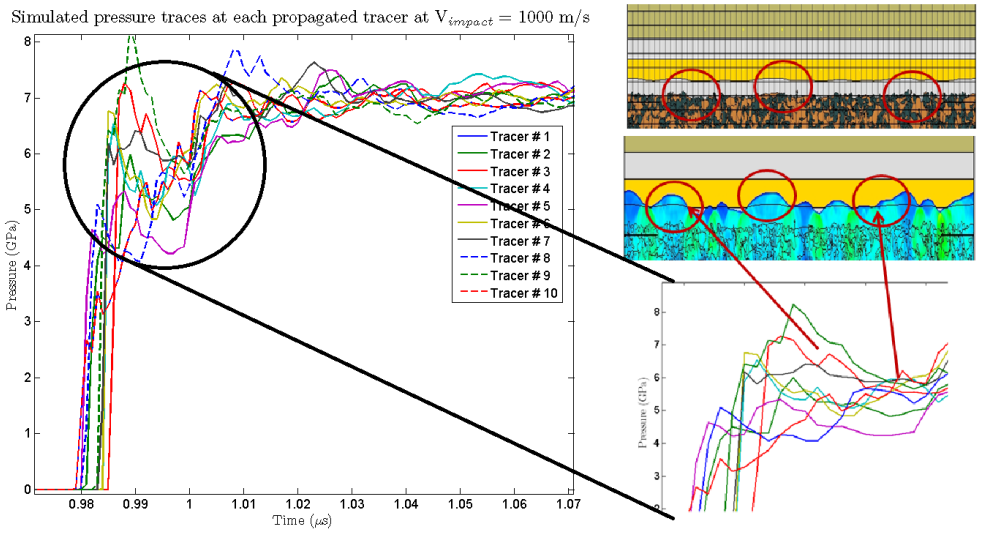

Figure 79: The simulated stresses measured at each individual tracer point show a wide variability in both arrival-time signature and stress level. Averaging the stresses naturally leads to the observed characteristic "hump," which was reproduced by simulations. This is captured due to the inhomogeneous loading of the PVDF gauge.

In fact, the very probes used to measure the stresses and velocities (i.e. PVDF and VISAR) will smear and average the heterogeneities (figure 80). Thus, the measured response will include these effects, manifested as the rise-time "humps," due to the inherent

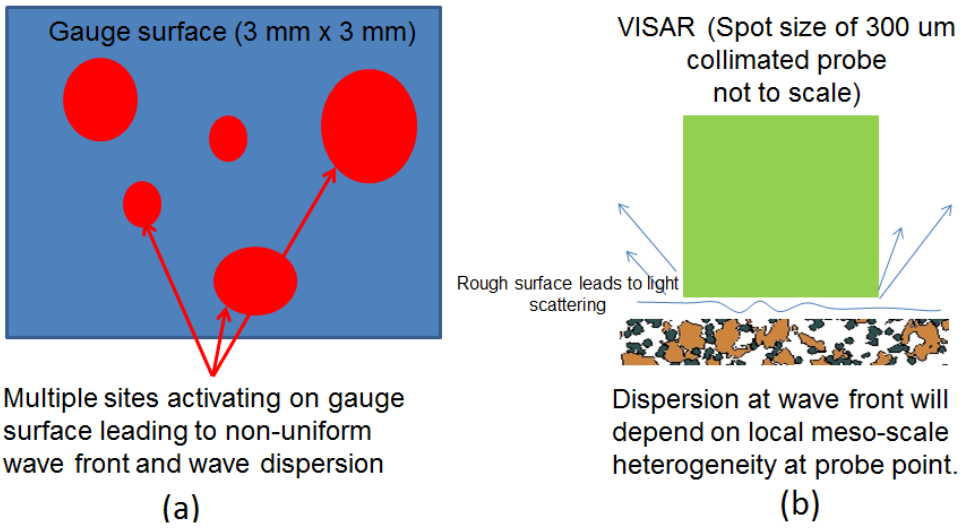

Figure 80: The probe area smears the heterogeneous response in the material.

averaging. Prior methodologies adopted for reporting wave speeds is to take the time of arrival from the 10%, 50%, and 90% of the peak stress values between the input and propagated stress gauges and either average these times, or report a single time-of-arrival value. The transit time measured when the particles fully crush up at peak stress (around the 90% peak level) is likely a better measurement for comparison with thermodynamic models for shock-induced chemical reactivity in powder mixtures. However, this measurement can be confounded by a highly dispersed wave, so measuring from the toe of the wave (the first arrival time of a disturbance) gives a consistent means of measuring wave transit time. It is therefore important to distinguish the method used to determine the shock speed if adequate comparison is to be made with thermodynamic models for shock-induced reactivity.

A possible rationale for the rise-time signatures and wave structures observed when shock compressing Ti+2B mixtures may be due to the compaction response. The natural heterogeneity in these mixtures combined with the high crush strength of the boron powders led to a highly dispersed wave front observed at the rear surface of the powder. Meso-scale simulations showed a large variability in stresses depending on the tracer location, demonstrating the meso-scale effect on the bulk shock response. The rise-time wave structure is due to inhomogeneous loading of the PVDF gauge surface by agglomerated

boron particles, and is a function of the local heterogeneity in the mixture. The simulations were able to capture the measured shock profile after averaging the stress values at each tracer point. Further analysis is necessary to fully determine the shock-induced reactivity response in this mixture. Wave speed measurements must account for this natural dispersion to be comparable with thermodynamic models for reactivity in powder mixtures.

7.4 Experimental and computational challenges in probing the shock compression behavior of Ti/Al/B

A series of important questions were posed in chapter 1 which motivated the present work exploring the microstructural tailorability of Ti/Al/B reactive powder mixtures. This section explores experimental and computational challenges unique to the Ti/Al/B mixtures and how these challenges affected the outcome of these questions. The highly heterogeneous nature of this multi-component system exacerbates the normal challenges of studying powder compacts under shock compression. The high hardness of boron and the disparate mechanical properties between the constituents of this mixture created problems in analyzing the PVDF stress gauge data. These problems were linked to the heterogeneities in the compaction process being captured by the very sensitive PVDF gauge. The random nature of these heterogeneous compaction processes led to uncertainties in the measured shock speed and peak stress at the rear of the powder compact. Details about the experimental setup are provided in chapter 4.

7.4.1 Unique experimental challenges - Can chemical reaction signatures be captured by stress profiles?

Powder mixtures form highly heterogeneous microstructures with complex topologies. Prior work has shown the efficacy of using the PVDF gauge to obtain equilibrated stress profiles for gauges attached directly onto the powder surface (cf. Chapter 2). The only shielding available for the gauges in these works were the PTFE encapsulating layers, ~50 μm in total thickness. Past works investigating powder mixtures using Manganin gauges

have used thick buffer materials to ensure transient fast rise-time events would not damage the gauge and to ensure that the incident wave was fully developed. The thickness of the buffer was selected so that attenuation was minimized. This ensures that interfacial shear between the gauge and backer/buffer is minimized and that much of the stress is due to the spherical component of the shock compression.

The chosen experimental setup for the present work relied on the past success of using PVDF stress gauges in direct contact with the powders. The gauges allow for the transient compaction phenomena to be captured and for the direct characterization of the resulting wave structure, as shown in figure 52. However, prior experiments focused on high Al-containing mixtures such as Ni+Al. The morphologies of the powders also promoted a steepening of the wave front [22], thus leading to lower interfacial shear stresses at the gauge. The present work focused on characterizing powders which consisted of very small amorphous boron particles which form agglomerates during pressing. Many of the PVDF recorded traces from the input stress gauge showed spurious results, which indicated premature gauge failure, eventually confirmed by meso-scale simulations, as shown in figure 67 which illustrates the remnants of a torn PVDF stress gauge package at the input side. Equilibrated stress at the input PVDF gauge were thus not obtained and the gauges were thus used primarily as time-of-arrival measurement devices.

The heterogeneous nature of the mixture also provided an additional layer of complexity because there was uncertainty even in measuring the arrival time of the shock wave. This has been identified by Borg and Vogler [178] who used meso-scale simulations employing idealized geometries to describe monodispersed WC spheres under shock compression. Many of the resulting propagated PVDF gauge traces showed delayed rise-times and interesting wave structures that are attributable to the compaction phenomenon. The high hardness (and therefore high crush strength) of the powders and their complex geometry increases the uncertainty, creating difficulties in interpreting data in the thermodynamic Hugoniot space.

While no direct evidence of shock-induced reactions is attributable to a gauge signature[2], the gauges provide a time-of-arrival. Therefore, the challenge in employing a direct-contact method of measurement such as the PVDF stress gauges makes it difficult to discern a unique chemical reaction signature measured directly by the gauge. Evidence of shock-induced chemical reactions is indirectly provided by comparing experimental data with predictions assuming idealized inert and reaction-product EOS models. These conventional techniques can be judiciously applied to heterogeneous reactive powder mixtures, but do not provide a causal description of the mechanochemical origins of the chemical reaction signature. A true meso-scale diagnostic combined with meso-scale simulations is the next possible step in the search for the mechanistic origins of shock-induced reactivity.

7.4.2 Rankine-Hugoniot jump conditions applied to powders - Are single-point thermodynamic properties sufficient?

Distended solids and powder mixtures are particularly challenging to probe under shock compression because a true shock may not be formed in a rigorous sense. The shock wave must be stable in nature to be able to take transit time measurements [118]. It is likely that the force-chaining phenomena described in chapter 2 leads to large rise times and dispersed waves. The Ti+2B powders showed rise times of greater than 100 ns at lower shock pressures, with reduced rise times at pressures greater than 2 GPa. Greater scatter is therefore expected in data obtained for highly-dispersed waves. However, using the "toe" value of the wave (as discussed in chapter 4) provides a good first-order approximation to how an ideal shock would propagate through the powder mixtures.

Higher shock pressures produced rise times on the order of 40 ns, but with transitional regions within the rise-to-peak showing characteristic "humps." Shock speed calculations that depend on voltage signal recording times, or on the perceived start of the wave-equilibration event, or on measurements of various points along the rise-to-peak (10%, 50%, 90%, etc. of peak value) will invariably produce a wide variation of shock

[2]The rise-time effects were confirmed to be heterogeneous meso-scale effects, as discussed in section 7.3

speed values. There will not be a "true" shock speed unless there is a true shock wave. Ergo, only a "wave speed" is derivable in this situation and the Rankine-Hugoniot jump conditions will not be rigorously satisfied. Any wave speed value used to compare with thermodynamic models for shock-induced chemical reactivity will merely be a first-order approximation. Still, in the present work, the term "shock speed" is used interchangeably with "wave speed" without loss of rigor upon recognizing this fact.

The size and strength disparity between the amorphous boron powders and titanium powders created agglomeration zones as discussed in chapter 5, which can serve to disperse the wave during compaction. These agglomerates are a natural consequence of the isostatic compaction of the powders and will produce sample-to-sample variations which are difficult to quantify. The variations can affect the recorded wave profiles, and thus may further affect the scatter in experimental data as well as the applicability of the Rankine-Hugoniot conditions. Nevertheless, the thermodynamic assessment of shock-induced reactivity is attempted in this framework as the rise times are within 100 ns – a reasonable regime to consider full applicability of the Rankine-Hugoniot jump conditions. For the purposes of the present work, the single point thermodynamic property U_s is considered sufficient to describe possible expanded states, but cannot describe the unique meso-scale processes observed in uniaxial strain loading.

7.4.3 Modeling mechanical response using simulated microstructures - The need for accurate microstructural representations

The modeling of chemical reactions, coupling high-strain-rate mechanical behavior, is an extraordinarily complex topic. Researchers are seeking methods which will address the multi-scale behavior of chemical reactivity and couple the meso- and macro-scale behaviors that might be driving this phenomena, which at its core starts at the atomistic level. Of course, the success of these efforts depends on proper microstructural representations, as well as physics-based constitutive models which capture the meso-scale response.

The present work opts for a coupled experimental and computational approach, whereby

the mechanical response is modeled with continuum-level constitutive models, but which employ very precise geometrical descriptions of the meso-scale structure. This is in stark contrast with prior works, such as Do and Benson's chemical reaction modeling [115], Baer's modeling of explosive materials using simple polygons [179], and Borg and Vogler's work modeling WC, [180] which all utilized simple geometries in their modeling schemes. While bulk-level information may be obtained by considering microstructures modeled with idealized shapes, the local particle-level deformation response will be lost. As was discussed in section 7.3, this particle-level response mediates the observed bulk response and is directly responsible for the observed wave dispersion in the uniaxial strain configuration. Some information can be captured as a first approximation using idealized shapes, but there may be substantial variations from the real response. Compaction and space-filling limitations inherent with idealized shapes obscure the true character of the evolving and resulting deformed, compacted microstructure. Thus, highly-resolved microstructure-based simulations which incorporate actual particle shapes are necessary if the local particle-level interactions and their effects on evolving heterogeneities play an important role in the shock compression response.

There are also morphological and topological considerations that must be explored to fully probe the meso-scale effects on bulk response. Particle morphology and individual particle complexity will influence the global topology of the material as deformation evolves. Indeed, the evolving heterogeneity and resulting topology from high-strain-rate deformation processes will drive the observed macro-scale response. The microstructure-based computations presented in this work were conducted in a 2D plane-strain configuration; the individual particles acted as prismatic cylinders in 3D. The configuration, connectivity, and resulting topological variability in a real system must consider both the particle-level topological complexity, as well as the global topological complexity in 3D. The present work showed the utility in the 2D plane-strain calculations in probing the meso-scale effects on the observed dynamic response of powder mixtures. However, the resulting

topological response must be explored in three-dimensional simulations using real particles due to its dependence on 3D particle-level topology, and compaction and space-filling limitations of 2D representations.

The microstructural descriptions, once validated, can provide a look into the meso-scale effects. Creating such validated and detailed microstructural representations is a laborious task, and even more laborious if done manually using conventional metallography. The microstructure-based simulations can, however, become limited by the simulation methods and constitutive models employed. Constitutive models are usually continuum-level models that do not include elements of substructure; thus important physics may be lost in the simulations. There can be a point of diminishing returns when employing highly-resolved microstructures, especially if the constitutive models or equations of state are inadequate. However, validating microstructure-based simulations employing continuum-level or physics-based models with diagnostic measurements is essential to lend confidence to the predicted microstructural states, which can provide valuable clues in assessing the meso-scale effects on the bulk response.

Simulations involving chemical reaction and matter exchange, retaining the current level of microstructural detail, were not performed and remain beyond the scope of the current work. Even so, the inferences gleaned from the qualitative observations in the highly-resolved microstructure-based simulations employed in the present work helped identify the crucial microstructural elements that lead to higher heat buildup, constituent mixing, and eventual reactivity in the time scale of shock compression. Quantitative microstructural metrics, such as reactant surface area per unit volume S_v, or two-point correlation functions for the deforming constituents of the microstructure, can further clarify these observations by identifying how these metrics evolve (i.e. how agglomeration changes the straining of the Ti and thus the plastic heating) over the simulation time. Quantitative characterization should be explored in future work to further elucidate the role each extrinsic microstructural variable plays in the deformation processes under uniaxial stress loading.

The challenges addressed in the present work instead showcased the utility of the highly-refined microstructure-based simulations in helping to pinpoint the possible processes leading to an observed bulk response influencing shock propagation and constituent deformation. The simulations revealed the importance of mutual plastic deformation between the constituents under uniaxial stress loading to promote reaction initiation. The simulations were able to capture meso-scale effects and were also able to match the experimentally-measured velocity and stress profiles for a number of experiments, as discussed in section 6.4. The meso-scale simulations may be refined by employing physics-based constitutive models that can better capture the mesomechanical response.

7.4.4 Appropriate equations of state for distended solids - Do "hot-spots" matter in the same way as in explosives?

Porosity and distension leads to complicated meso-scale behavior which manifests dispersion in the bulk shock response of a material. The final shocked state is reckoned as an equilibrium state where the thermodynamic path is taken along Rayleigh line connecting the initial state to the final state in the thermodynamic P-V space. An equation of state describes the relationship between thermodynamic state variables. However, these equations cannot properly include the meso-scale behavior, which is lumped into the continuum-level compaction model such as the P-α model.

In a porous solid, the pore collapse and frictional thermal contributions can be substantially higher than the compression contributions, which led Boslough to lump these terms into the equation of state along with the heat of reaction [72], assuming that the reaction went to completion (a consequence of the stability analysis he performed). The reaction then behaved as a detonation and reached thermodynamic equilibrium at the end state of the shock (the Hugoniot). Therefore, the underlying meso-scale structure cannot come into play. Any meso-level phenomena which leads to chemical reaction somehow must be connected to the continuum scale, perhaps as an internal state variable to the EOS model.

The meso-scale microstructure-based simulations presented in section 6.4 show that,

indeed the bulk response observed in experiments, as well as its meso-scale origins, are reproducible. However, in the absence of direct observation of shock-induced chemical reactions, the simulations cannot establish a causal link between so-called "hot-spots" and the reaction initiation in the powder mixtures under uniaxial stress or strain loading configurations. However, these simulations remain a powerful tool in helping elucidate the possible configurations that promote chemical reactivity in heterogeneous reactive powder mixtures.

CHAPTER VIII

CONCLUSIONS AND RECOMMENDATIONS FOR FUTURE RESEARCH

This work explored the mechanochemistry in Ti/Al/B reactive powder mixtures. The powder mixtures took the form of isostatically-compressed compacts and were studied under two distinct forms of dynamic loading, viz. uniaxial stress and uniaxial strain. The two load regimes represent the extremes of uniaxial dynamic loading. Most practical situations will involve some form of triaxiality, i.e. a mixture of these load conditions, and indeed the very nature of these powders produces heterogeneous stress/strain states (i.e. the aforementioned triaxiality) which are likely precursors for dynamically-induced chemical reactivity at ultra-fast time scales.

The following statements summarize the results of this work:

- Uniaxial stress loading experiments (reactive pellet-mounted rod-on-anvil experiments) showed enhanced reactivity for Al-containing stoichiometries at a controlled density. This was theorized to be due to the potential enhanced reactivity and mixing of Al synergistically aiding further reaction of the titanium and boron. Microstructure-based simulations confirm these findings and reveal enhanced mixing and straining of the constituents. Thus, these "strain-induced" reactions depend on a microstructure that can enhance straining and mixing for the uniaxial stress loading condition. The extreme straining leading to localization phenomena in the uniaxial stress loading condition is likely the main precursor to chemical reaction.

- Highly-resolved microstructure-based simulations were able to capture the rise-time anomalies observed in the propagated gauge stress traces in shock compression.

These anomalies arise from multiple compaction during the crush-up of the powder. The two-dimensional plane strain simulations reveal the effects of boron agglomeration in both the uniaxial stress and strain loading configurations. Simulations using actual particle shapes help capture the boron agglomeration and its effect on the measured bulk response under uniaxial strain loading.

- An expanded state consistent with the Ballotechnic hypothesis was observed in the Ti+2B powder mixture at high shock pressures (above 6 GPa). The highly complex compaction phenomena preceding full densification in the shock compression experiments likely inhibits reactivity through dissipative mechanisms. However, there seems to be enough mixing/straining to heat and react the Ti+2B mixture, as expanded states were obtained for high shock pressures. The ternary Ti+2B+50%Al did not display an expanded state. This is likely due to bulk compressibility of the densified powder mixture limiting straining and heat generation and constituent mixing.

- While strain plays an important role in promoting chemical reactions under dynamic loading due to the enhanced mixing it facilitates, it remains the chief mediator in promoting reactivity under uniaxial stress loading. The Al-additions in the uniaxial stress case served to increase straining and transport of the smaller, harder boron particles. This likely led to the greater reactivity observed in the 50%-Al mixture. However, strain seems to play an auxiliary role under uniaxial strain shock compression conditions. Inhibiting compaction-induced dissipation seems to be the most important factor when considering high crush strength mixtures. However, the soft-Al matrix in the ternary mixture likely inhibited shock-induced reactivity due to the lack of mixing and bulk straining. Therefore, the reaction mechanism is highly dependent on the loading condition (i.e. strain-induced v.s. shock-induced).

- The size and strength disparity of the particles relative to the constituents in these

mixtures act as an exogenous source of heterogeneity which convolutes the analysis of data. An EOS was estimated for boron as a good first-order approximation to compare Hugoniot data.

- Microstructure-based simulations using real particle shapes captured the size and strength disparity of the boron particles. The particle morphology affects the resulting global topology of the deformed material, and therefore can affect reactant configuration and influence reactivity under shock compression and high-strain-rate loading. Highly-resolved microstructure-based simulations are essential in probing the evolving heterogeneity and how this plays a role in the shock compression response of reactive powder mixtures.

This work also detailed the unique challenges in investigating a ternary mixture of Ti/Al/B. The expectation that the reactivity would be aided through a synergistic mechanism in the ternary mixture was demonstrated under uniaxial stress loading, but was inconclusive for the uniaxial strain condition. The Ti+2B mixture showed highly dispersed wave structures owing to their high crush strength and transient compaction effects identified through meso-scale simulations. This shows that the phenomenon of dynamic reactivity is highly context-dependent. Further work is necessary to identify the microstructural variables essential in promoting chemical reactivity for different contexts (i.e. load conditions, microstructural conditions, etc.).

8.1 Recommendations for future research

This work builds upon the efforts of prior researchers in the field of reactive materials under dynamic loading, furthering the research by showing the utility of a highly-resolved meso-scale simulation platform to investigate its influence on bulk response. However, as mentioned previously, boron is the only common element whose ground state thermodynamic phase was a mystery until very recently. Its astonishing properties in both the amorphous and crystalline forms begs the analysis of the shock Hugoniot at lower shock

pressures (i.e. the weak shock regime). Further work in any boron-containing mixture must follow a rigorous study of the boron equation of state.

The current work showed the utility of highly-resolved meso-scale simulations in capturing both the bulk response of the Ti+2B powder mixtures to shock compression, and its mesomechanical origins. However, the effects of the meso-scale evolution as the microstructure changes during deformation remains to be assessed. It is important to explore the microstructural evolution of the powder mixtures under both uniaxial stress and strain loading by assessing stereological metrics such as surface area per unit volume S_V and two-point correlation functions. This information shows how topology is influenced as deformation progresses and how it can be affected by load configuration. A statistical study of how these metrics evolve at different stages of the deformation process will be invaluable to quantifying the microstructural effect on both the bulk mechanical and reactive response in reactive powder mixtures.

A mechanistic study of shock-induced chemical reactivity in simple mixtures of Ti+B under shock compression is recommended to isolate the microstructural variables essential to reactivity in particular stoichiometries of Ti+B. The stoichiometric 1:2 mixture of Ti:B was already studied in this work, and its closure can be brought about through the systematic study of boron in its many forms. Having built a sound understanding of the thermodynamic properties of boron under shock compression, a logical extension would be to explore various stoichiometries of Ti and B. A 2^k full-factorial design of experiments exploring the effects extrinsic microstructural variables such as boron morphology, microstructural distributions, and particle mechanical properties can be performed. This research can help further pinpoint the optimal stoichiometry necessary for reaction at a specific load configuration in mixtures of Ti/Al/B. It can also help discern the existence of a collaborative effect between constituents in promoting the optimal microstructural deformation state that is necessary for mechanochemistry in the Ti/Al/B system, and if this can be extended to other reactive powder mixtures.

APPENDIX A

RAW PVDF GAUGE EXPERIMENTAL DATA

This appendix includes the experimentally-recorded PVDF (when available) traces in their raw state. The current output is included, along with the corresponding stress trace, labeled according to the shot #, impact velocity, and measured U_s (labeled on the propagated PVDF gauge caption). The PVDF gauges were connected to a Power Tee which effectively split the current in half, generating both low, and high sensitivity output signals. The low sensitivity signal captures the peaks of the voltage/current, whereas the high-sensitivity signal smooths the data. The final signal (shown in the figures) is a recombination of the low and high sensitivity signals, after doubling their values to obtain the final combined signal. This prompts the "manipulated" label shown on each figure, to distinguish that these signals are the combined low/high sensitivity signals. The stress trace is derived from the combined manipulated signals.

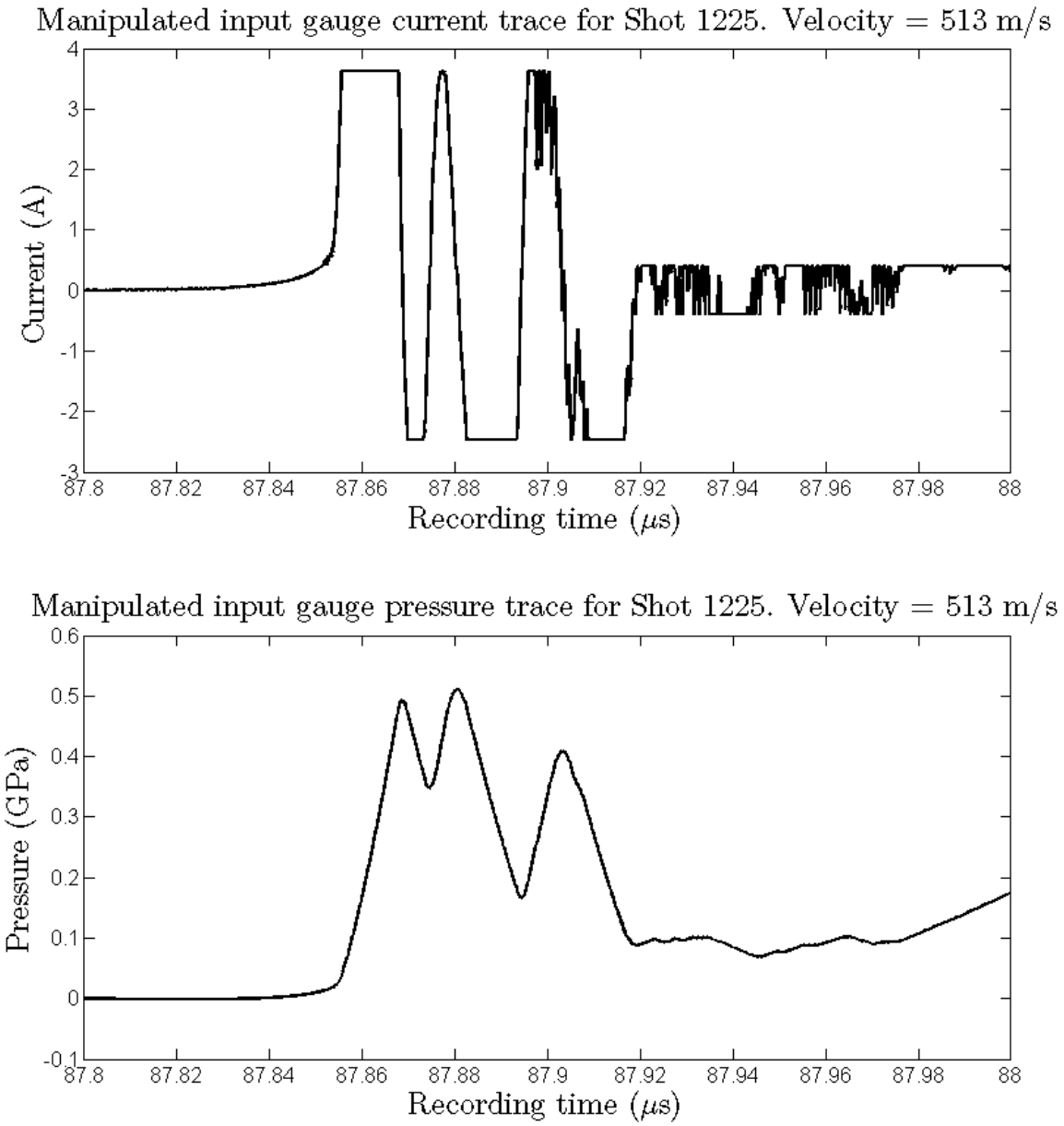

Figure 81: Input PVDF gauge output. Shot 1225, V_{imp} = 0.513 mm/μs, Cu-Flyer.

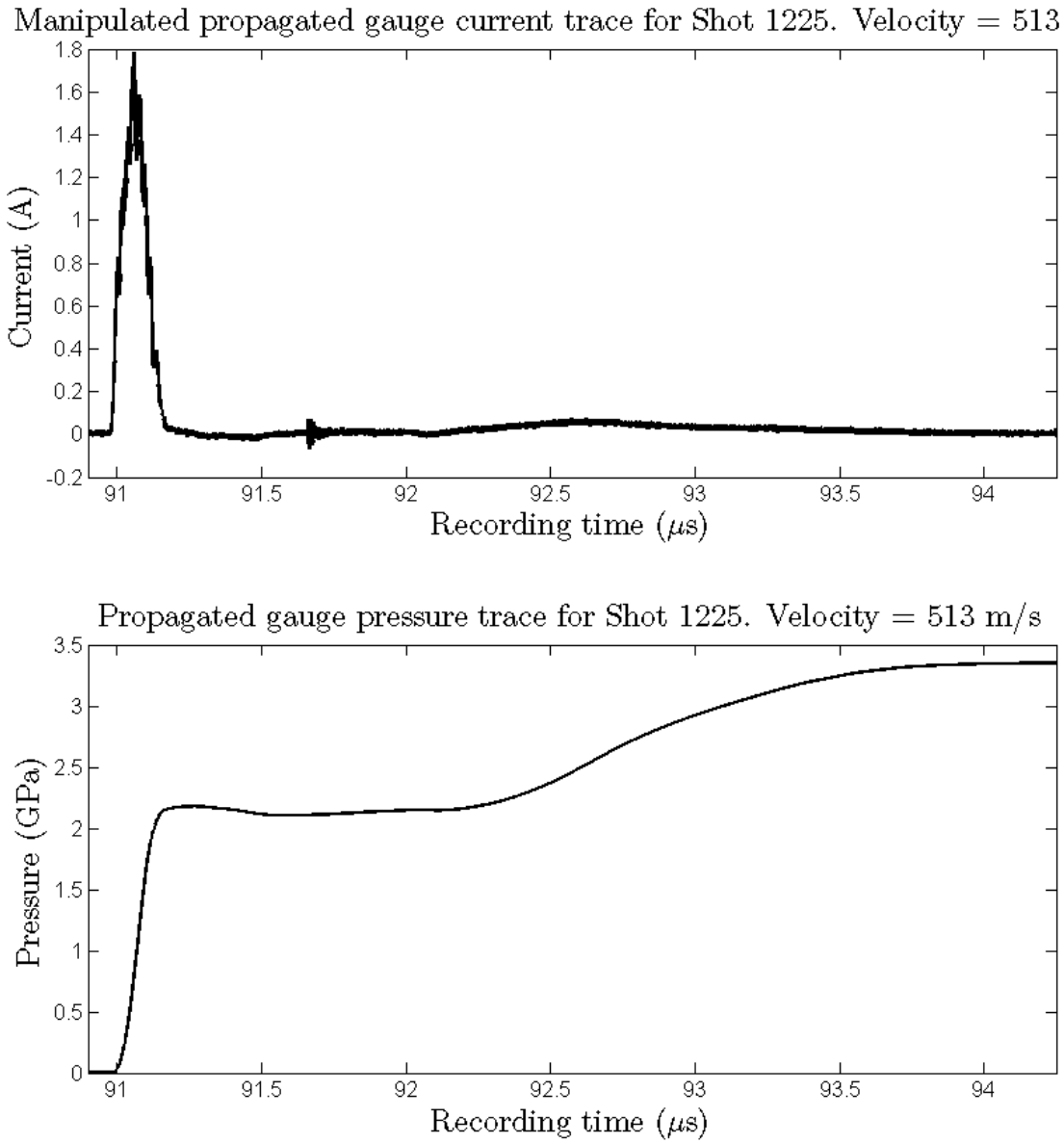

Figure 82: Propagated PVDF gauge output. Shot 1225, V_{imp} = 0.513 mm/μs, Cu-Flyer. U_s = 1.29 mm/μs.

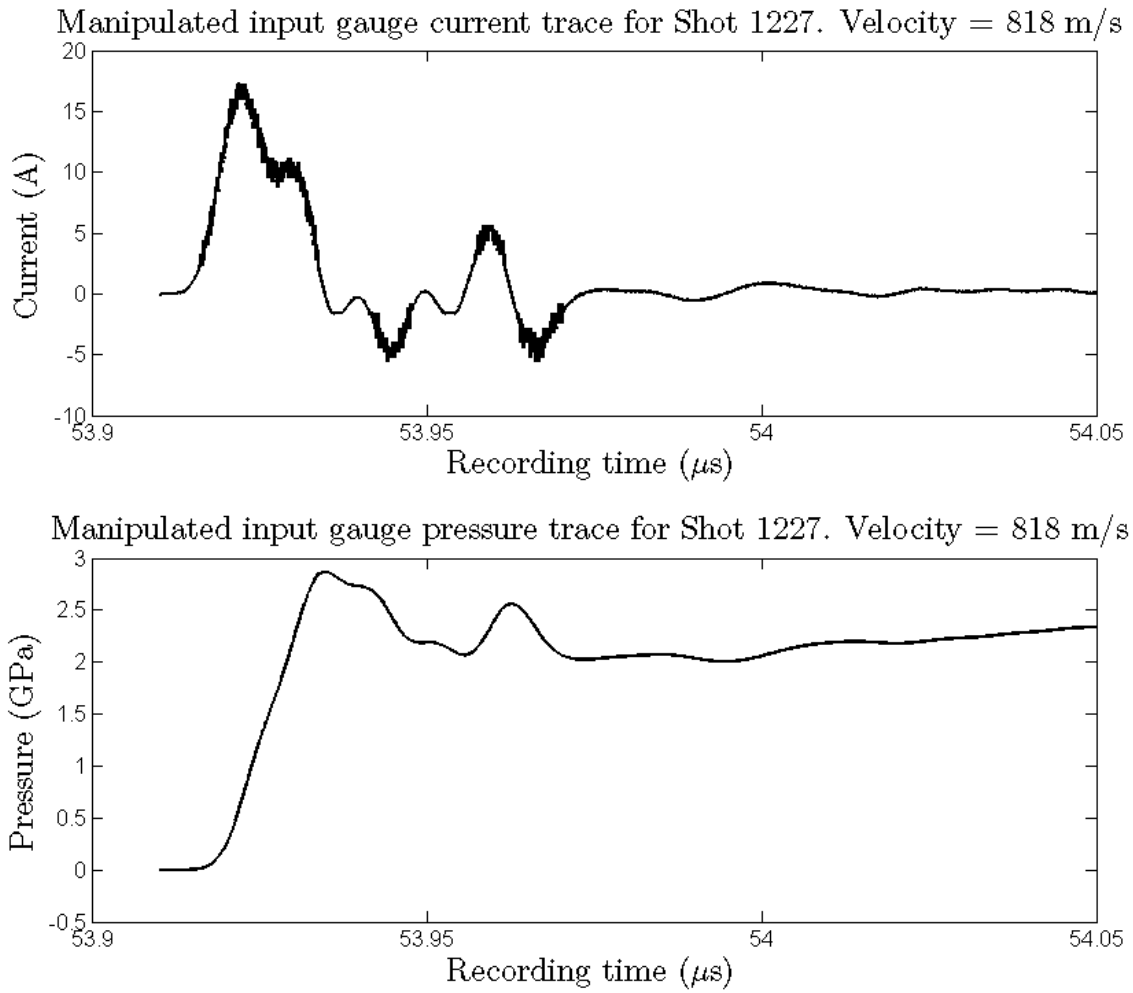

Figure 83: Input PVDF gauge output. Shot 1227, V_{imp} = 0.818 mm/μs, Cu-Flyer.

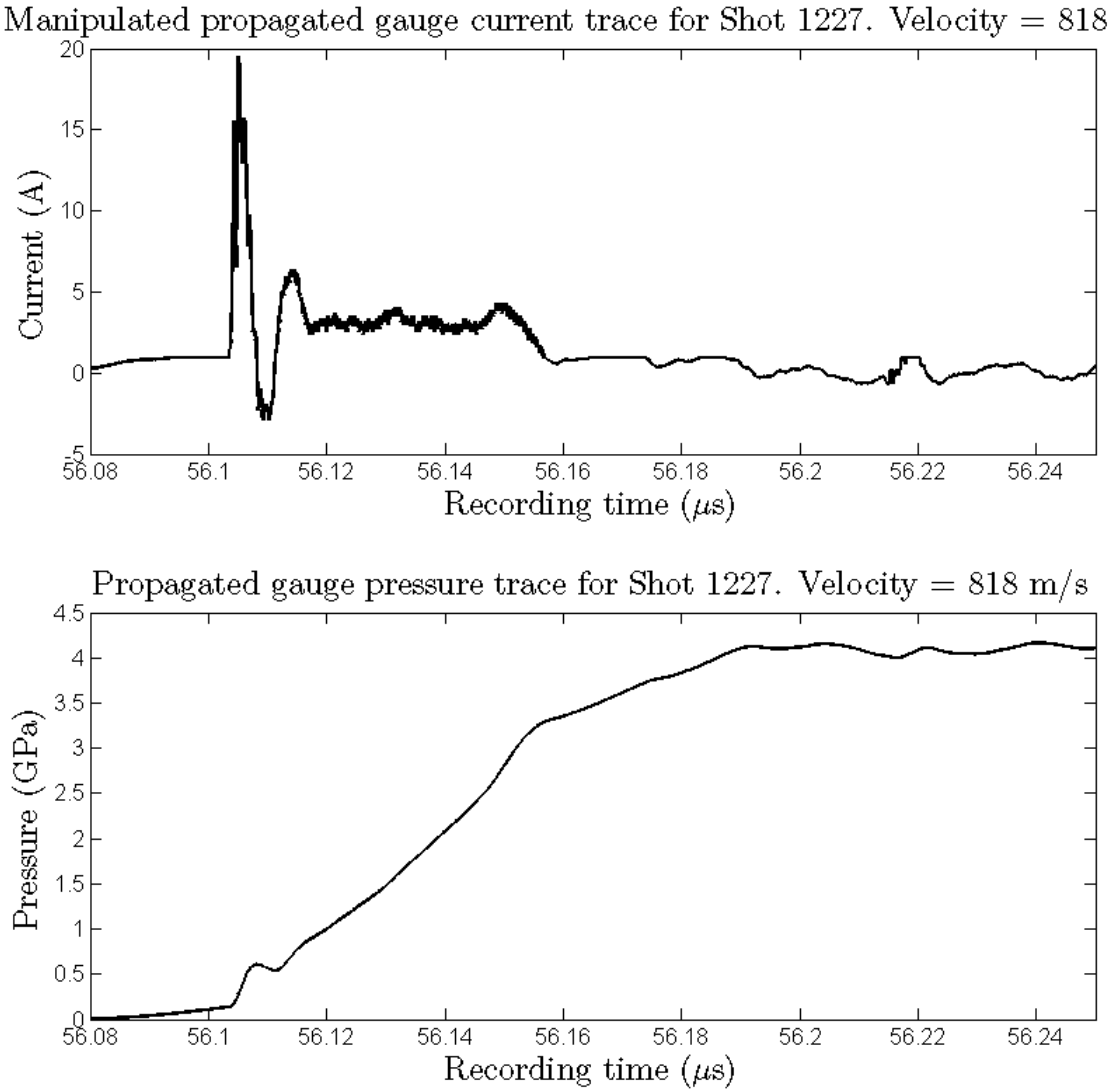

Figure 84: Propagated PVDF gauge output. Shot 1227, V_{imp} = 0.818 mm/μs, Cu-Flyer. U_s = 1.83 mm/μs.

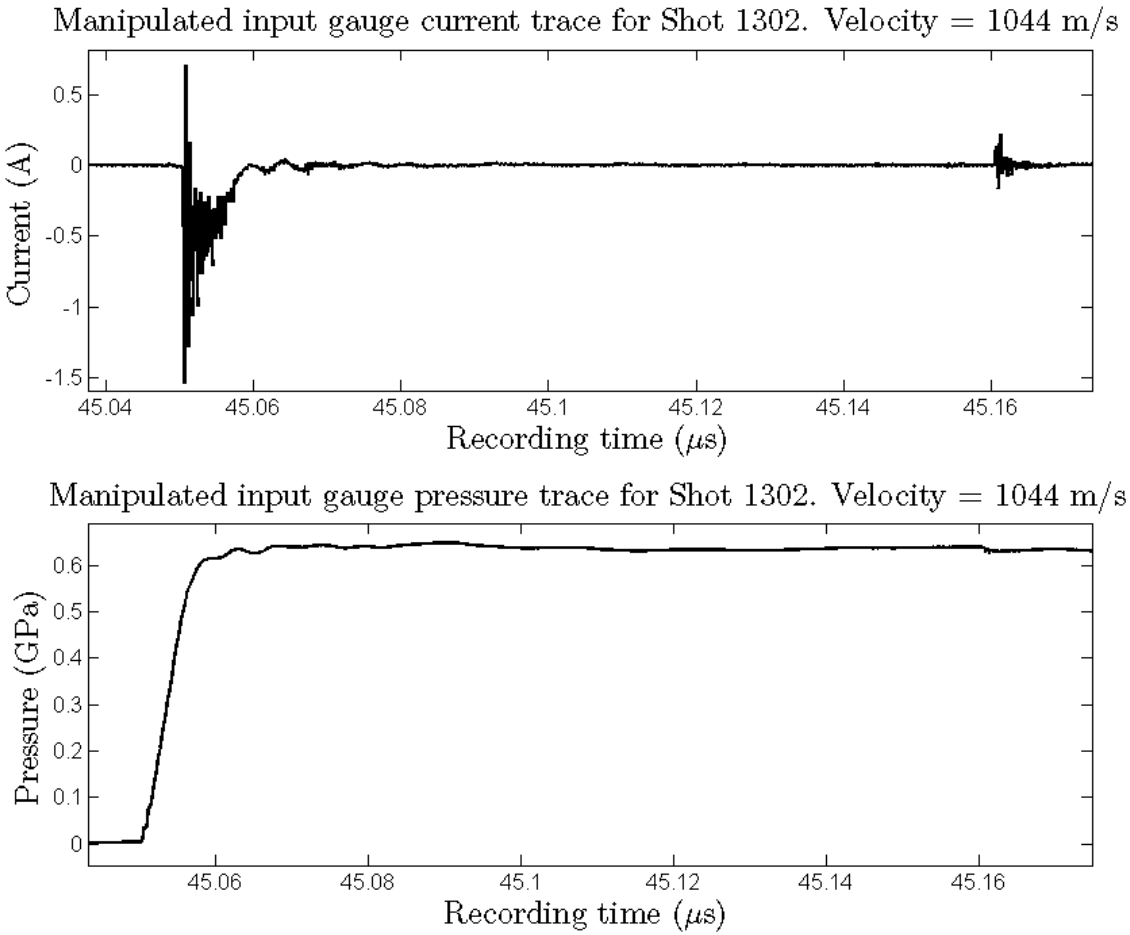

Figure 85: Input PVDF gauge output. Shot 1302, V_{imp} = 1.044 mm/μs, Cu-Flyer.

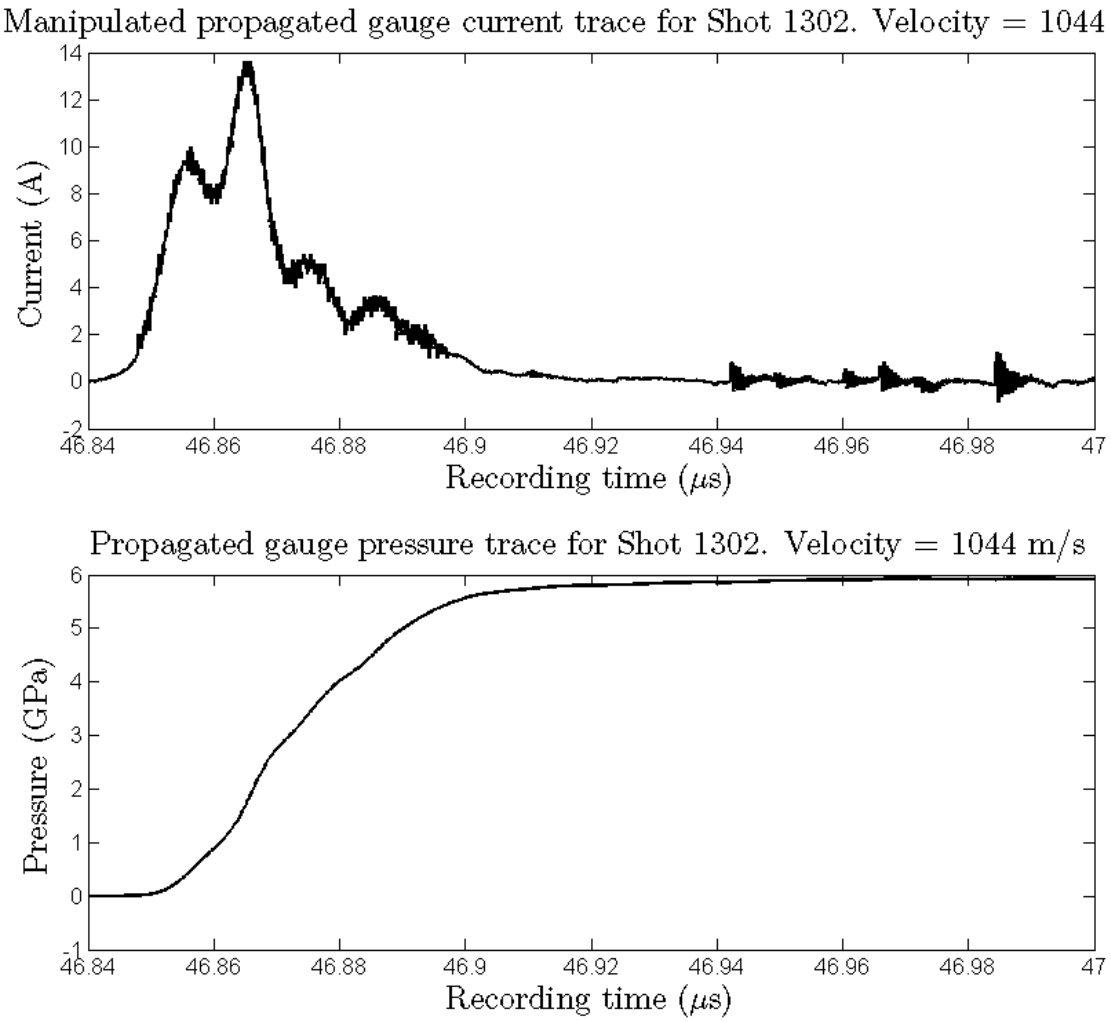

Figure 86: Propagated PVDF gauge output. Shot 1302, V_{imp} = 1.044 mm/μs, Cu-Flyer. U_s = 2.24 mm/μs.

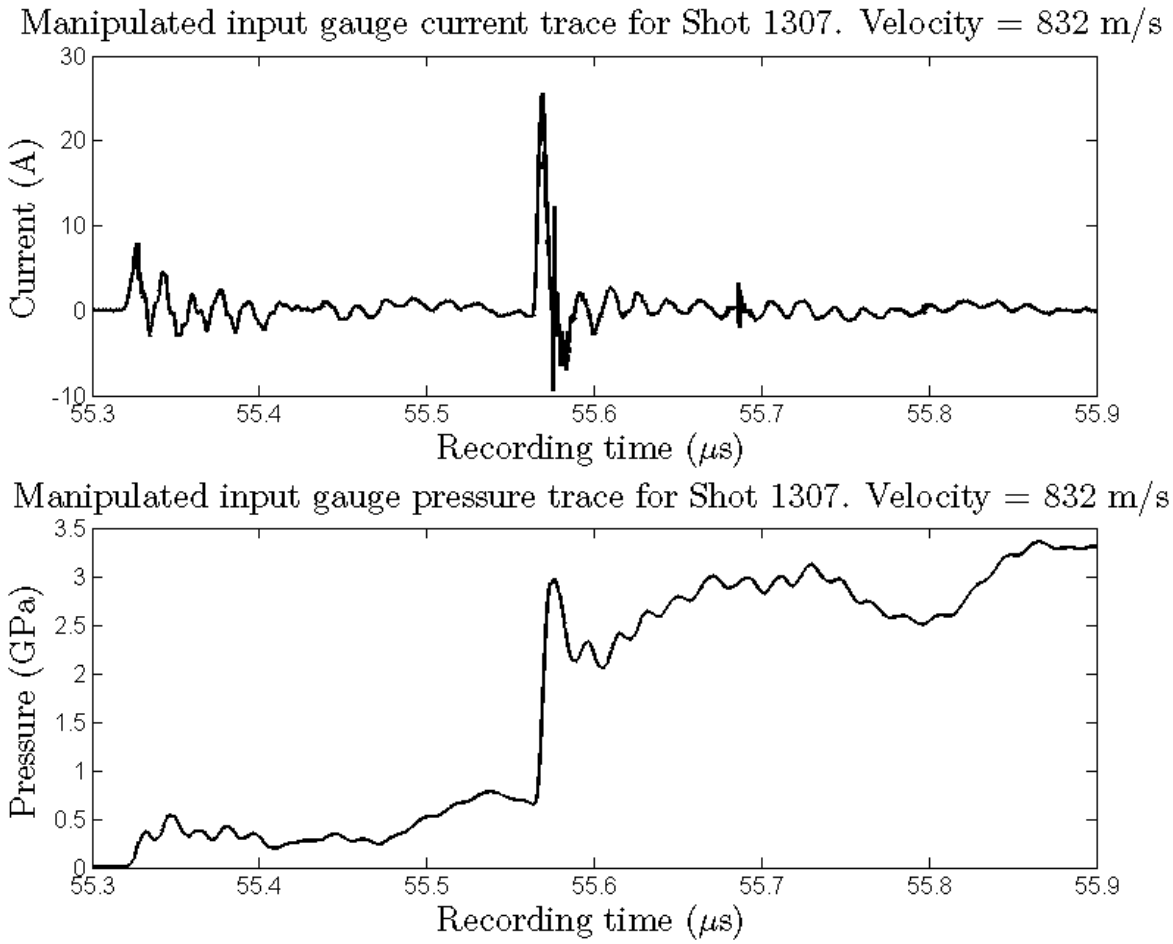

Figure 87: Input PVDF gauge output. Shot 1307, V_{imp} = 0.832 mm/μs, Cu-Flyer.

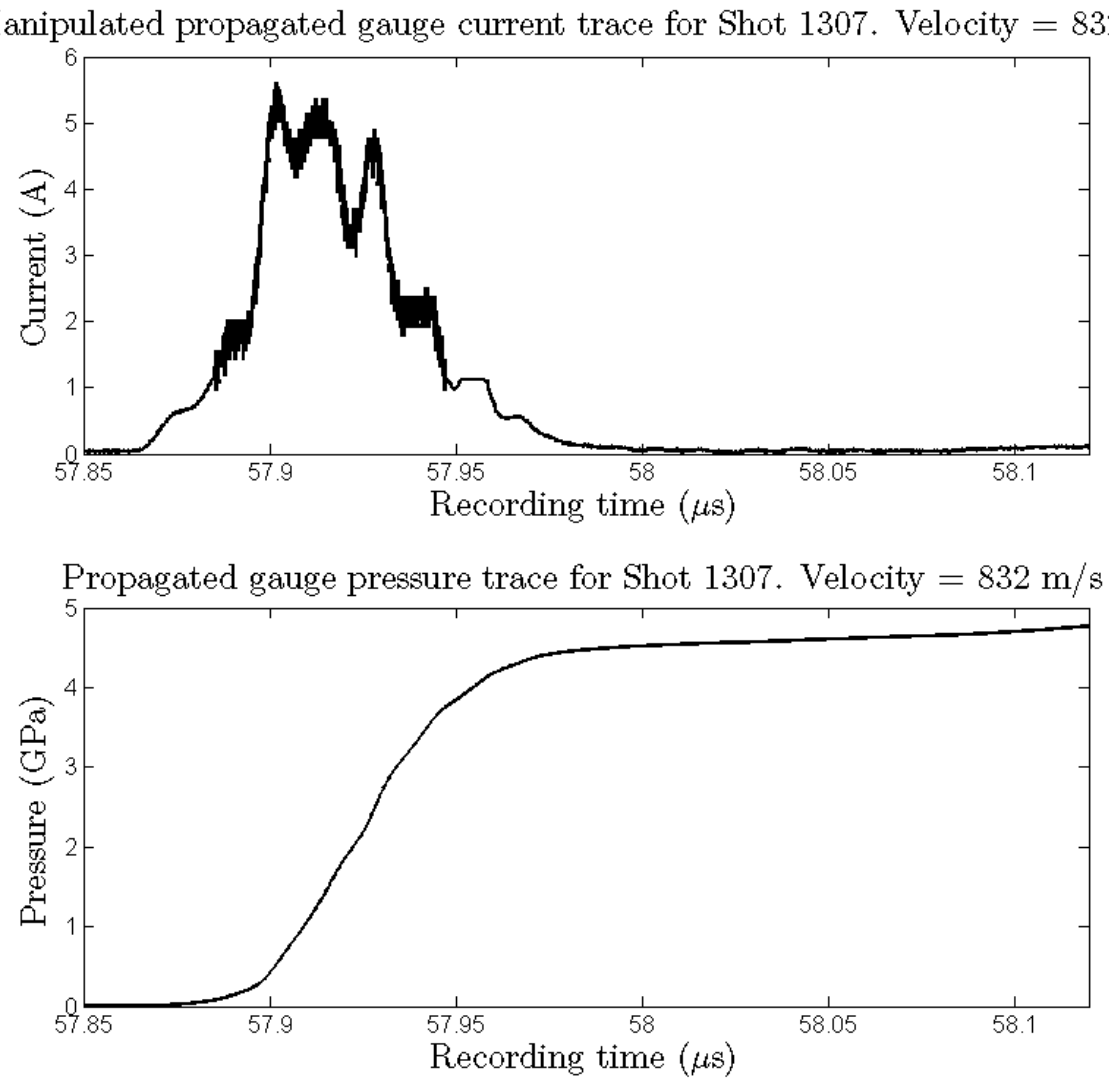

Figure 88: Propagated PVDF gauge output. Shot 1307, V_{imp} = 0.832 mm/μs, Cu-Flyer. U_s = 1.78 mm/μs.

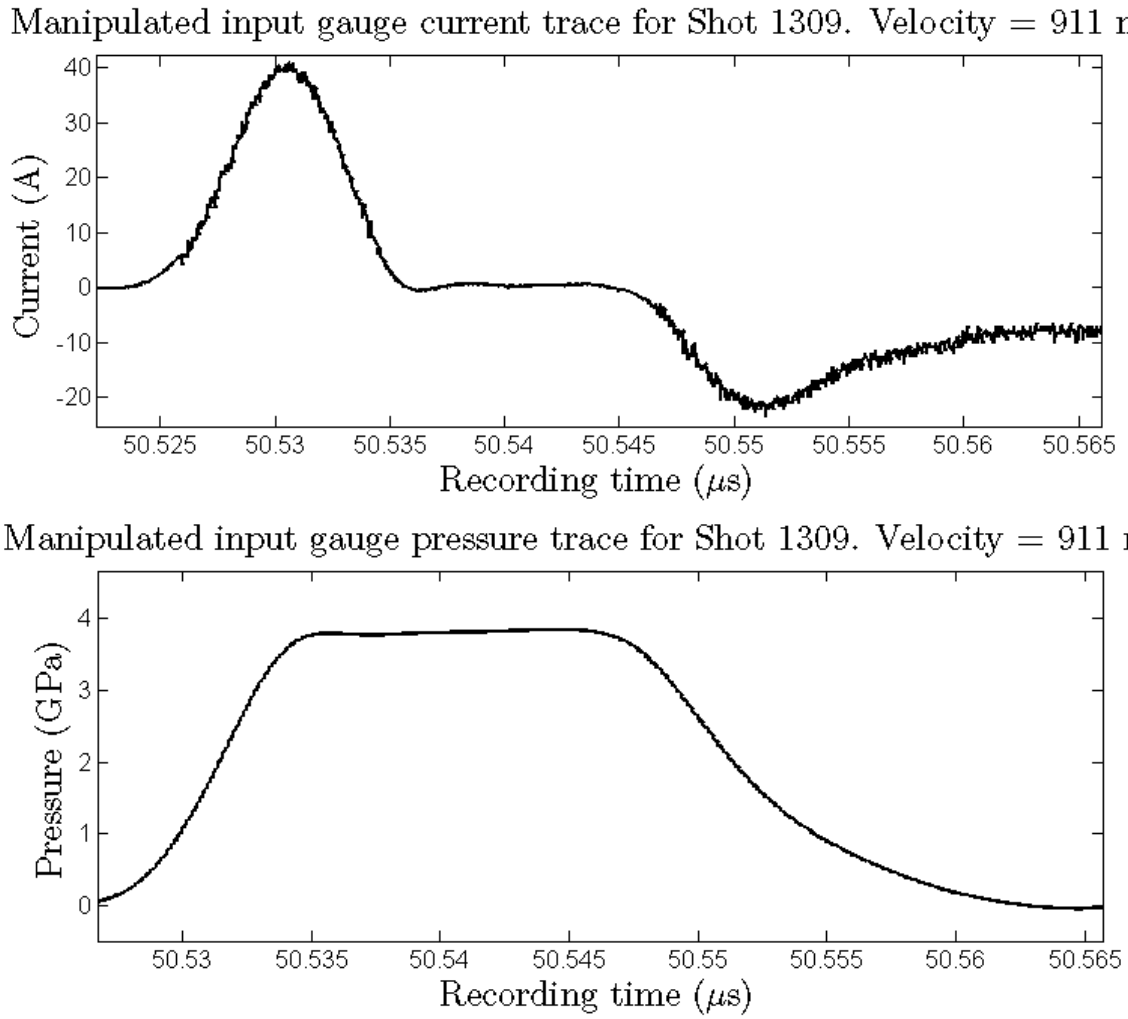

Figure 89: Input PVDF gauge output. Shot 1309, V_{imp} = 0.911 mm/μs, WHA-Flyer.

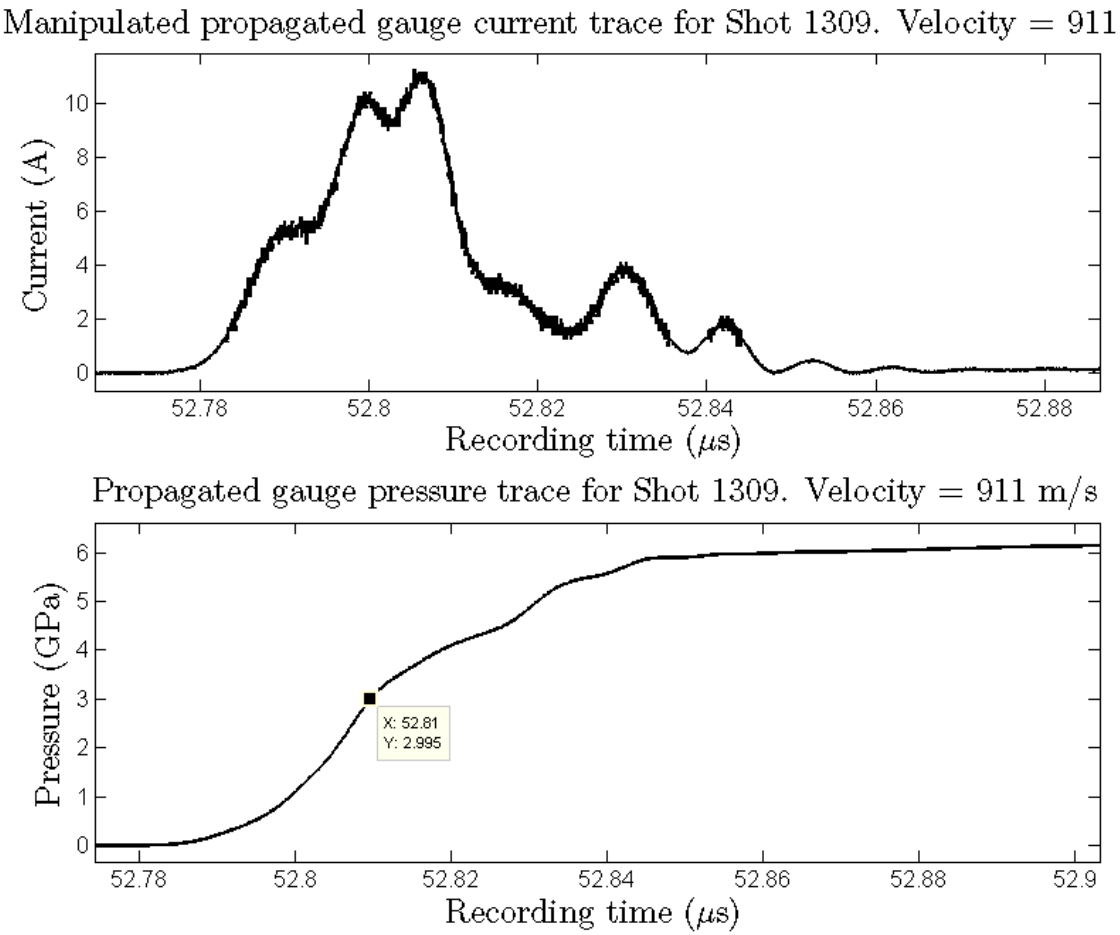

Figure 90: Propagated PVDF gauge output. Shot 1309, V_{imp} = 0.911 mm/μs, WHA-Flyer. U_s = 1.85 mm/μs.

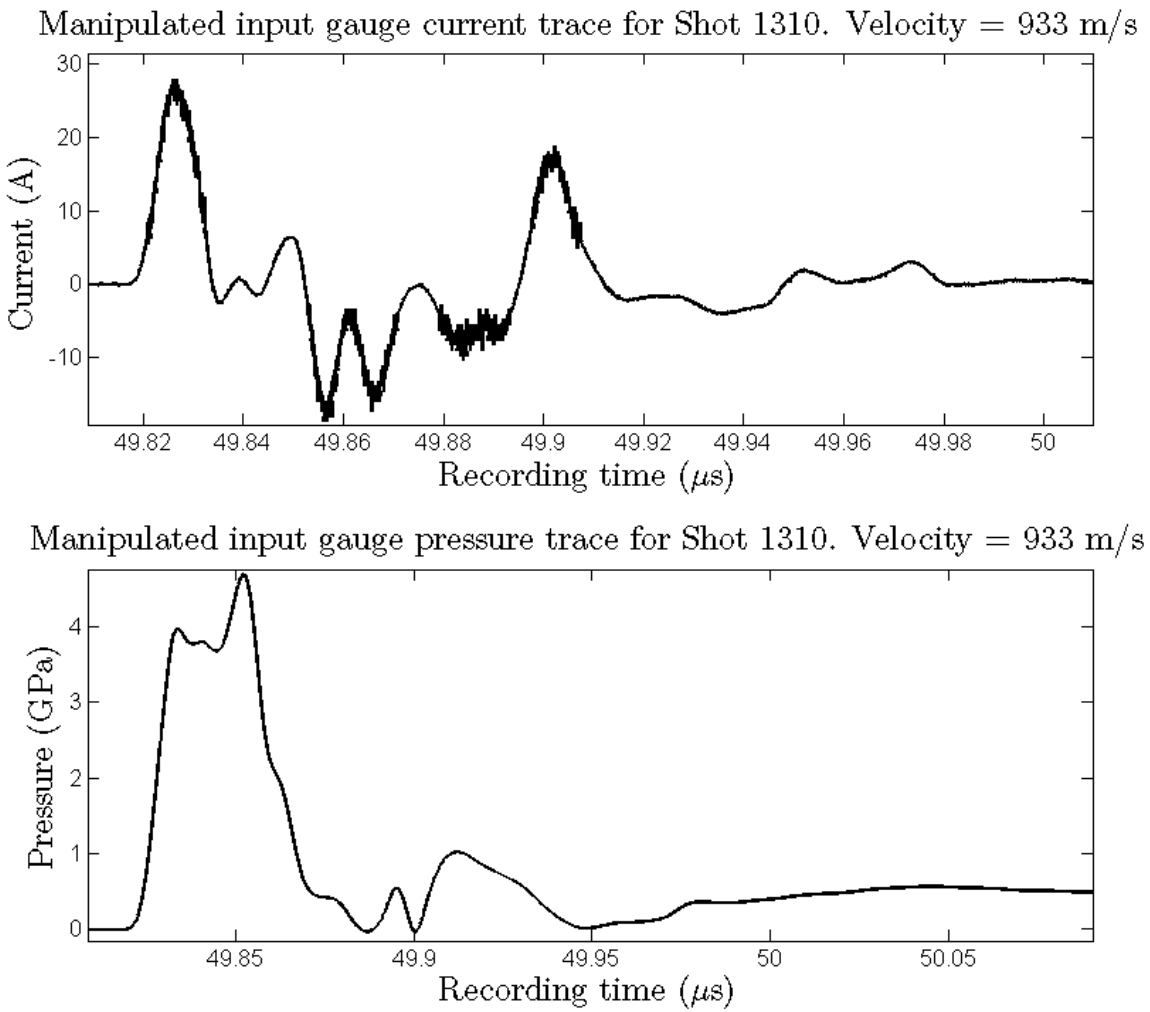

Figure 91: Input PVDF gauge output. Shot 1310, V_{imp} = 0.933 mm/μs, W-Flyer.

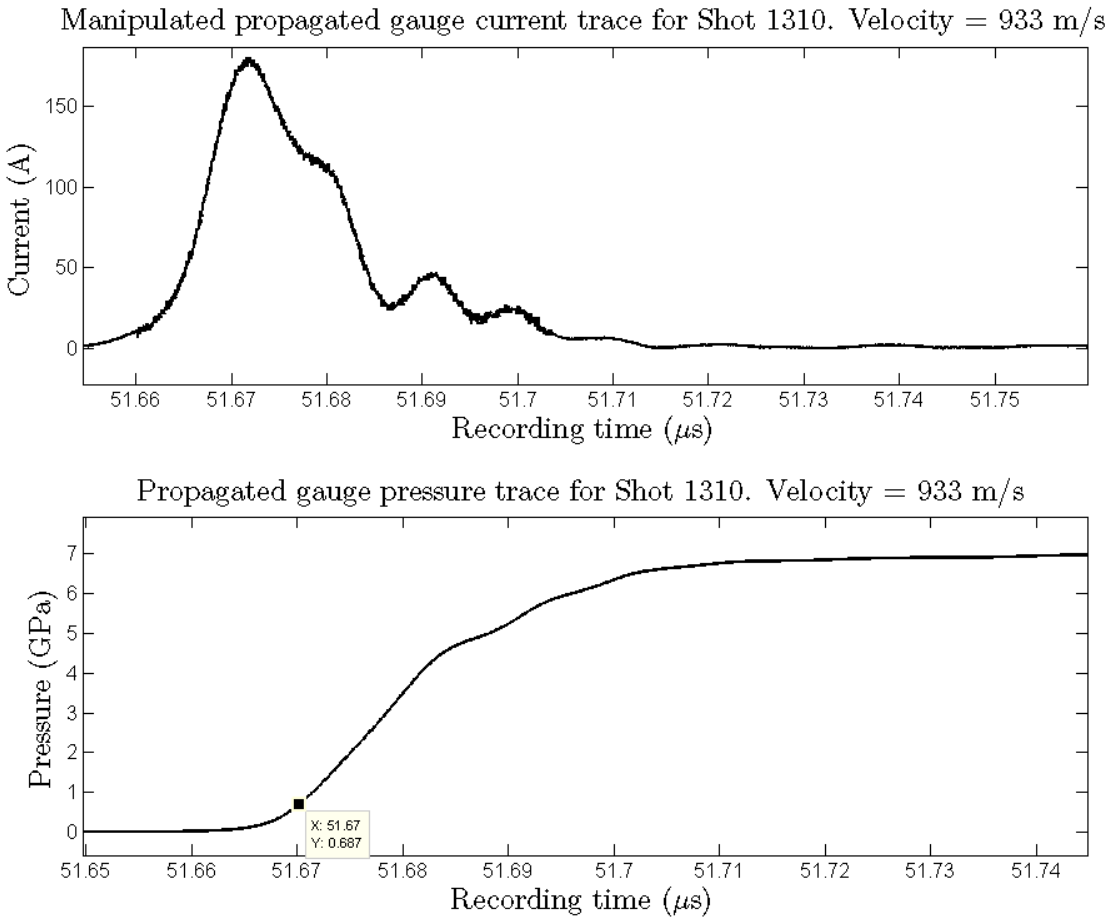

Figure 92: Propagated PVDF gauge output. Shot 1310, V_{imp} = 0.933 mm/μs, W-Flyer. U_s = 2.19 mm/μs.

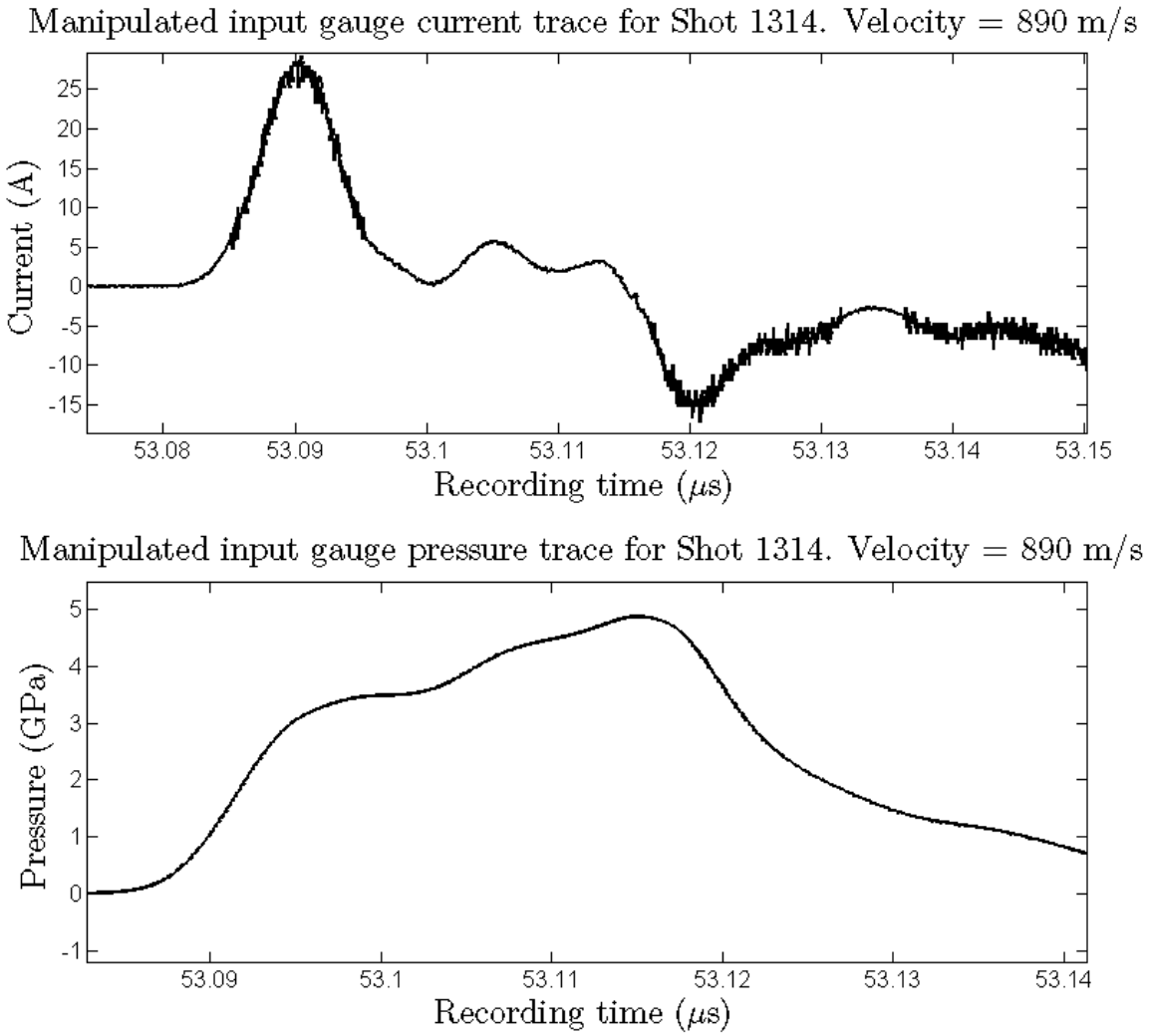

Figure 93: Input PVDF gauge output. Shot 1314, V_{imp} = 0.890 mm/μs, W-Flyer.

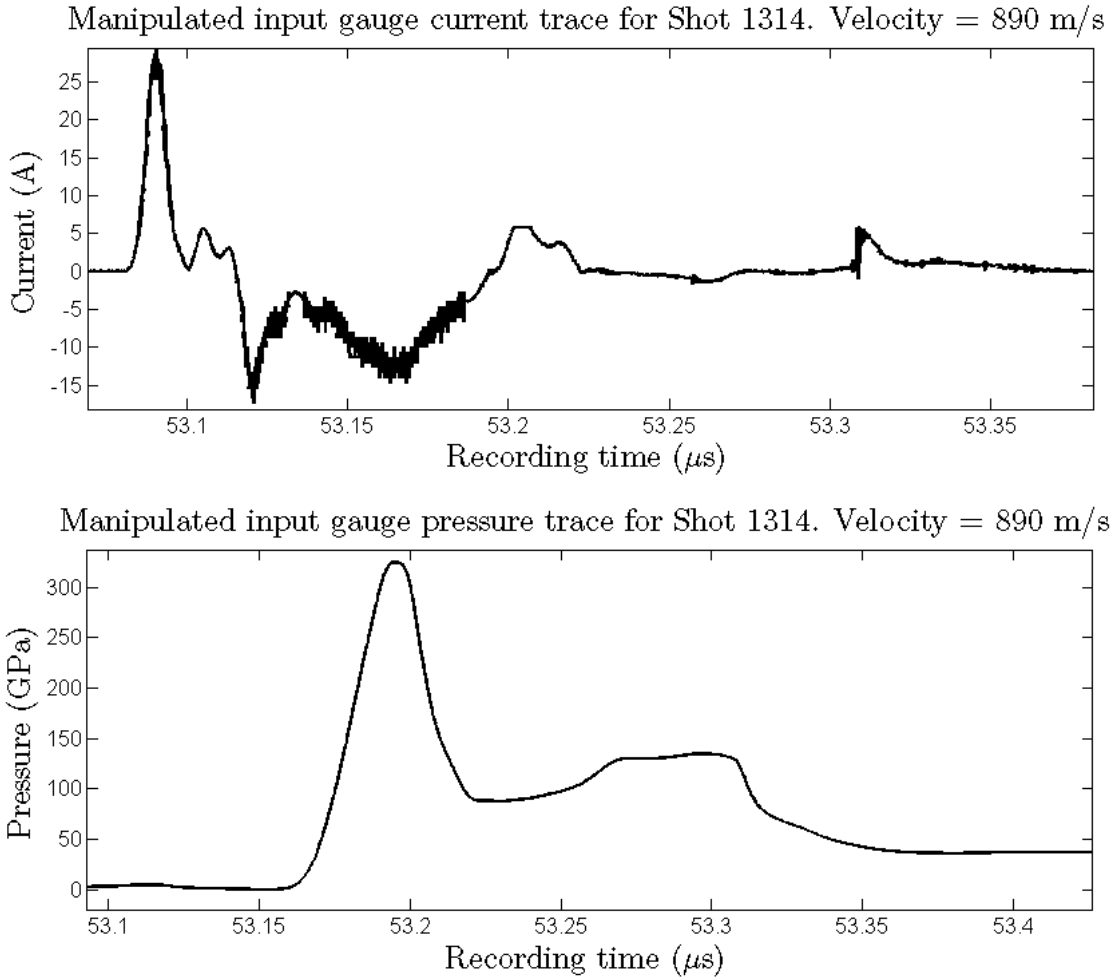

Figure 94: Propagated PVDF gauge output. Shot 1314, V_{imp} = 0.890 mm/μs, W-Flyer. U_s = 1.97 mm/μs.

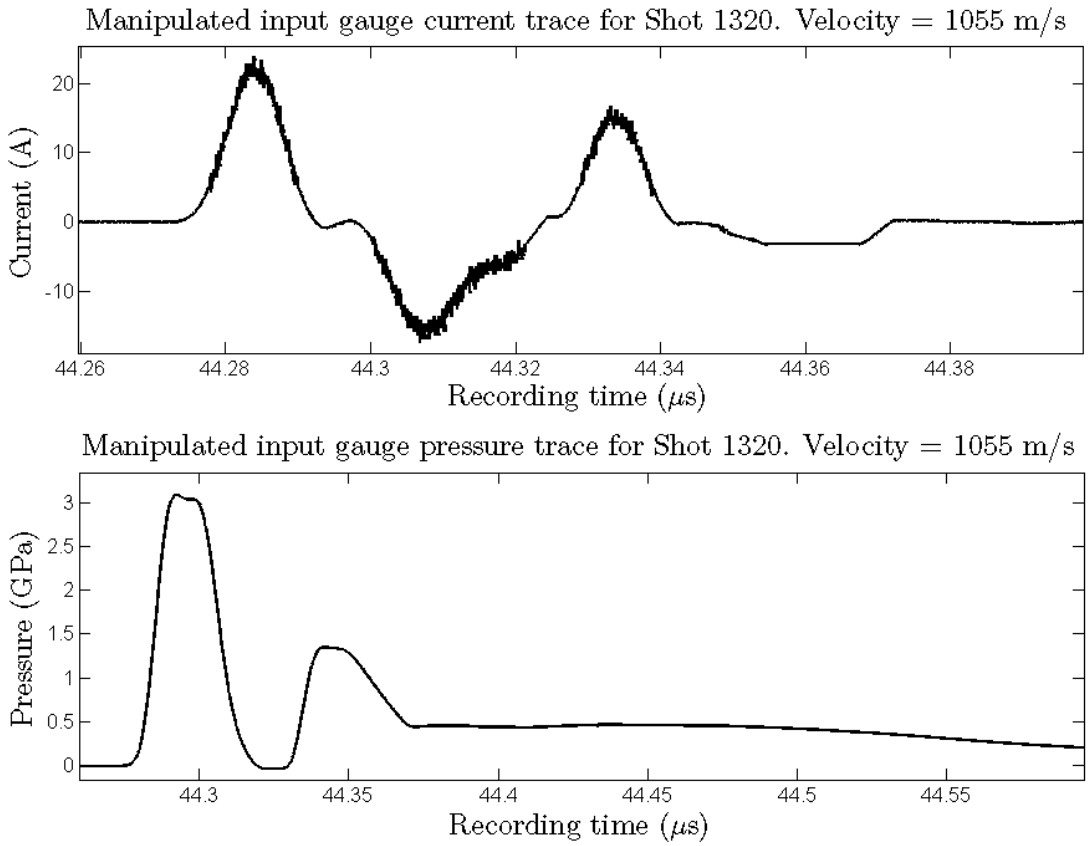

Figure 95: Input PVDF gauge output. Shot 1320, V_{imp} = 1.055 mm/μs, Cu-Flyer.

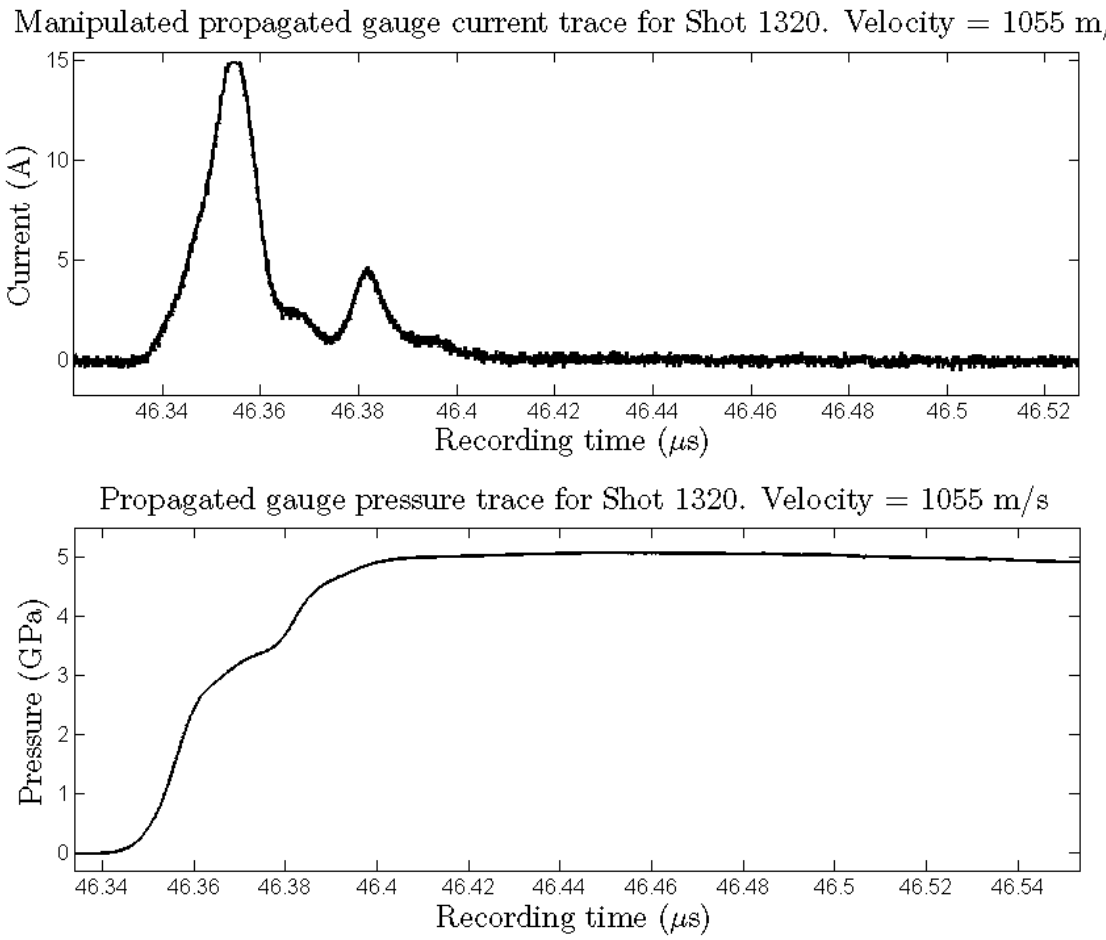

Figure 96: Propagated PVDF gauge output. Shot 1320, V_{imp} = 1.055 mm/μs, Cu-Flyer. U_s = 1.97 mm/μs.

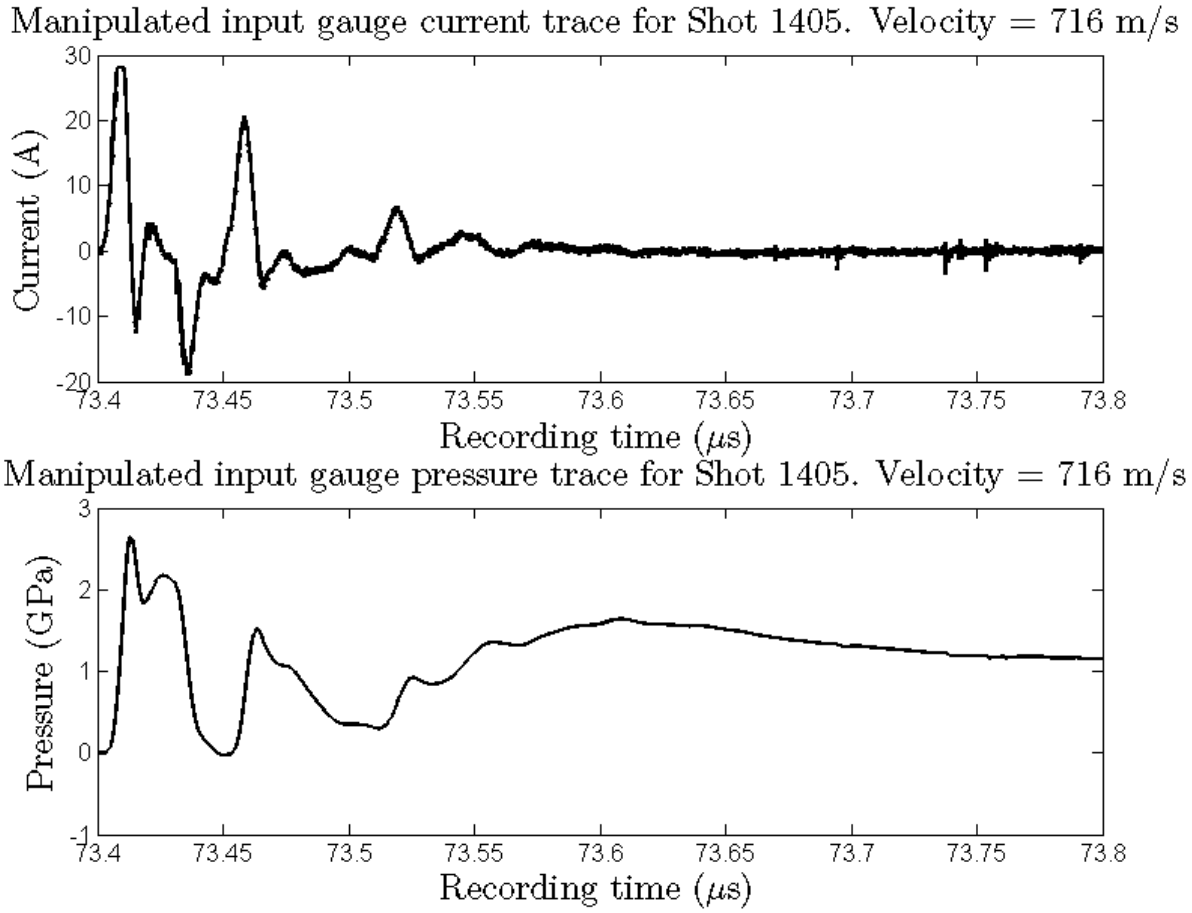

Figure 97: Input PVDF gauge output. Shot 1405, V_{imp} = 0.716 mm/μs, Cu-Flyer.

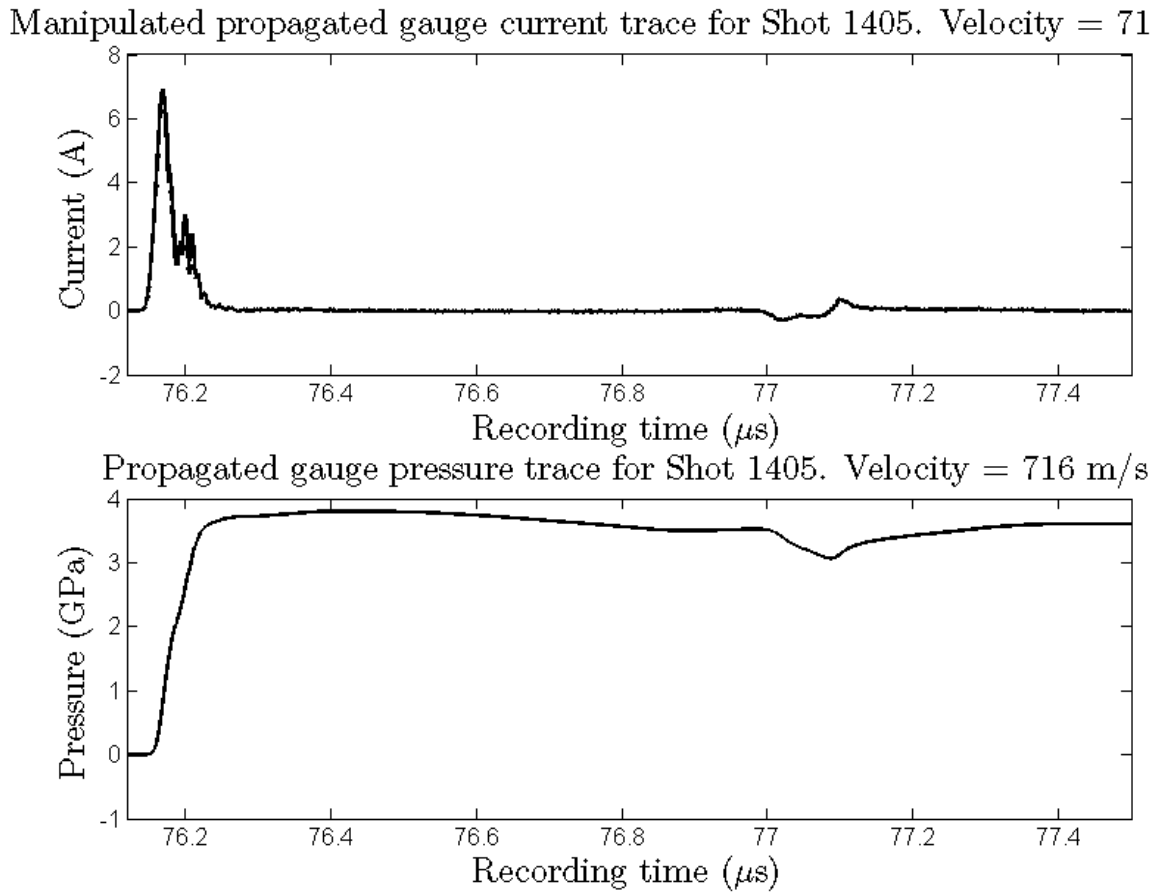

Figure 98: Propagated PVDF gauge output. Shot 1405, V_{imp} = 0.716 mm/μs, Cu-Flyer. U_s = 2.15 mm/μs.

REFERENCES

[1] C. Truesdell, *Rational Thermodynamics*. Springer-Verlag, 1984.

[2] J.-P. Bouchaud, P. Claudin, and M. O. Levine, "Force chain splitting in granular materials: A mechanism for large scale pseudo-elastic behaviour." arXiv:cond-mat/0011213v2, Nov 2000.

[3] M. A. Meyers, *Dynamic Behavior of Materials*. John Wiley and Sons, 1994.

[4] R. M. Nedderman, *Statics and Kinematics of Granular Materials*. Cambridge University Press, 1992.

[5] J. P. Wittmer, P. Claudin, M. E. Cates, and J.-P. Bouchaud, "An explanation for the central stress minimum in sand piles," *Nature*, vol. 382, no. 6589, pp. 336 – 338, 1996.

[6] M. E. Cates, J. P. Wittmer, J.-P. Bouchaud, and P. Claudin, "Jamming, force chains, and fragile matter," *Phys. Rev. Lett.*, vol. 81, no. 9, p. 1841, 1998.

[7] V. Nesterenko, *Dynamics of Heterogeneous Materials*. Springer, 2001.

[8] T. Mura, *Micromechanics of Defects in Solids*. Kluwer Academic Publishers, 1991.

[9] N. N. Thadhani, "Shock-induced chemical reactions and synthesis of materials," *Progress in Materials Science*, vol. 37, pp. 117–226, 1993.

[10] R. G. Ames, "Energy release characteristics of impact-initiated energetic materials," in *Mater. Res. Soc. Symp. Proc.*, vol. 896, Materials Research Society, 2006.

[11] C. Bedford, "Are we there yet? Explosives through the centuries or How to make that last calorie of energy mean something." Gordon Research Conference on Energetic Materials, June 2012.

[12] N. N. Thadhani, "Shock-induced and shock-assisted solid-state chemical reactions in powder mixtures," *J. Appl. Phys.*, vol. 76, pp. 2129 – 2138, August 1994.

[13] D. E. Eakins and N. N. Thadhani, "Shock compression of reactive powder mixtures," *International Materials Reviews*, vol. 54, no. 4, p. 181, 2009.

[14] L. S. Bennett, F. Y. Sorrell, I. K. Simonsen, Y. Horie, and K. Iyer, "Ultrafast chemical reactions between nickel and aluminum powders during shock loading," *Appl. Phys. Lett.*, vol. 61, no. 5, pp. 520–521, 1992.

[15] I. Song and N. N. Thadhani, "Shock-induced chemical reactions and synthesis of nickel aluminides," *Metall. Trans.*, vol. 23A, p. 41, 1992.

[16] Y. Horie and A. B. Sawaoka, *Shock compression chemistry of materials*. KTK, Tokyo, 1993.

[17] Y. Horie, "Computational modeling of shock-induced chemical reactions in powder mixtures," *AIP Conf. Proc.*, vol. 309, pp. 1235–1238, 1993.

[18] N. N. Thadhani, S. Work, R. Graham, and W. F. Hammetter, "Shock-induced reaction synthesis (SRS) of nickel aluminides," *J. Mater. Res.*, vol. 7, no. 5, p. 1063, 1992.

[19] D. E. Eakins and N. N. Thadhani, "Role of constituent configuration on shock-induced reactions in a Ni+Al powder mixture," in *Mater. Res. Soc. Symp. Proc. Vol. 896*, 2006.

[20] D. Eakins, *Role of Heterogeneity in the Chemical and Mechanical Shock-Response of Nickel and Aluminum Powder Mixtures*. PhD thesis, Georgia Institute of Technology, 2007.

[21] D. E. Eakins and N. N. Thadhani, "Mesoscale simulation of the configuration-dependent shock-compression response of Ni+Al powder mixtures," *Acta Materialia*, vol. 56, pp. 1496–1510, 2008.

[22] D. E. Eakins and N. N. Thadhani, "Shock-induced reaction in a flake nickel + spherical aluminum powder mixture," *J. Appl. Phys.*, vol. 100, p. 113521, 2006.

[23] Y. Horie and M. E. Kipp, "Modeling of shock-induced chemical reactions in powder mixtures," *J. Appl. Phys.*, vol. 63, no. 12, p. 5718, 1988.

[24] L. S. Bennett and Y. Horie, "Shock-induced inorganic reactions and condensed phase detonations," *Shock Waves*, vol. 4, p. 127, 1994.

[25] R. A. Austin, D. L. McDowell, and D. J. Benson, "Mesoscale simulation of shock wave propagation in discrete Ni/Al powder mixtures," *J. Appl. Phys.*, vol. 111, p. 123511, 2012.

[26] E. B. Herbold, N. N. Thadhani, and J. L. Jordan, "Observation of a minimum reaction initiation threshold in ball-milled Ni+Al under high-rate mechanical loading," *J. Appl. Phys.*, vol. 109, p. 066108, 2011.

[27] M. Gonzales, A. Gurumurthy, A. M. Gokhale, and N. N. Thadhani, "Computational study of the meso-scale effects on the dynamic behavior of heterogeneous Ti+Al+B reactive powder mixtures," in *Gordon Research Conference - Energetic Materials*, (Mt. Snow Resort, VT), June 2012.

[28] M. Gonzales, A. Gurumurthy, A. M. Gokhale, and N. N. Thadhani, "Meso-scale simulations of strain-induced reaction mechanisms in Ti/Al/B heterogeneous systems," in *Shock Compression of Condensed Matter - 2011* (M. Elert et al., ed.), (Chicago, IL), American Institute of Physics, June 2011.

[29] A. R. Oganov, V. L. Solozhenko, C. Gatti, O. O. Kurakevych, and Y. Le Godec, "The high-pressure phase of boron, γ-B28: Disputes and conclusions of 5 years after discovery," *ArXiv e-prints*, Sept. 2011.

[30] A. Tewari, A. M. Gokhale, and R. M. German, "Effect of gravity on three-dimensional coordination number distribution in liquid phase sintered microstructures," *Acta Materialia*, vol. 47, pp. 3721–3734, 1999.

[31] Y. Mao, A. M. Gokhale, and J. Harris, "Computer simulations of realistic microstrucures of coarse constituent particles in a hot-rolled aluminum alloy," *Comput. Mater. Sci*, vol. 37, pp. 543–556, 2006.

[32] J. M. Walsh and R. M. Christian *Phys. Rev.*, vol. 97, p. 1544, 1955.

[33] F. S. Minshall *Bull. APS*, vol. 29, p. 23, 1954.

[34] M. H. Rice, R. G. McQueen, and J. M. Walsh, "Compression of solids by strong shock waves," in *Solid State Physics* (F. Seitz and D. Turnbull, eds.), vol. VI, pp. 1–63, Academic Press, New York, 1958.

[35] P. DeCarli and J. C. Jamieson *Science*, vol. 133, p. 1821, 1961.

[36] Y. Horie, R. Graham, and I. Simonsen, "Synthesis of nickel aluminides under high-pressure shock loading," *Materials Letters*, vol. 3, no. 9-10, pp. 354 – 359, 1985.

[37] I. Simonsen, Y. Horie, and R. Graham, "Shock synthesis of nickel aluminides," in *Shock Waves in Condensed Matter – 1985* (Y. Gupta, ed.), pp. 743–748, New York: Plenum, 1986.

[38] Y. Horie and M. Kipp, "Modeling of chemical reactions in the mixture of Al-Ni powders under shock-wave compression," in *Shock Waves in Condensed Matter - 1987* (S. Schmidt and N. Holmes, eds.), pp. 387–390, Amsterdam: Elsevier, 1988.

[39] L. Bennett, K. Iyer, F. Sorrell, and Y. Horie, "Shock induced exothermic reactions in powder mixtures," in *Shock Compression of Condensed Matter - 1991* (S. Schmidt, R. Dick, J. Forbes, and D. Tasker, eds.), pp. 605–608, Amsterdam: Elsevier, 1992.

[40] E. Dunbar, N. N. Thadhani, and R. A. Graham *J. Mater. Sci.*, vol. 28, no. 11, pp. 2903–14, 1993.

[41] N. Thadhani, E. Dunbar, and R. Graham, "Characteristics of shock-compressed configuration of Ti and Si powder mixtures," in *High Pressure Science and Technology 1993* (S. Schmidt, J. Shaner, G. Samara, and M. Ross, eds.), pp. 1307–1310, New York: American Institute of Physics, 1994.

[42] N. N. Thadhani, R. A. Graham, T. Royal, E. Dunbar, M. U. Anderson, and G. T. Holman *J. Appl. Phys.*, vol. 82, no. 3, p. 1113, 1997.

[43] J. McGlaun, F. Zeigler, and S. Thompson, "CTH: A three-dimensional, large deformation deformation, shock wave physics code," in *Shock Waves in Condensed Matter - 1987* (S. Schmidt and N. Holmes, eds.), pp. 717–720, Amsterdam: Elsevier, 1988.

[44] M. Anderson, R. Graham, and D. Wackerbarth, "Prediction and data analysis of current pulses from impact loaded piezoelectric polymers (PVDF)," in *Shock Compression of Condensed Matter - 1989* (S. Schmidt, J. Johnson, and L. Davison, eds.), pp. 805–808, Amsterdam: Elsevier, 1990.

[45] F. Bauer, "Behavior of ferroelectric ceramics and PVF2 polymers under shock loading," in *Shock Waves in Condensed Matter – 1981* (W. Nellis, L. Seaman, and R. Graham, eds.), pp. 251–267, New York: American Institute of Physics, 1982.

[46] F. Bauer, "Piezoelectric and electric properties of PVF2 polymers under shock wave action: Application to shock transducers," in *Shock Waves in Condensed Matter - 1983* (J. Asay, R. Graham, and G. Straub, eds.), pp. 225–228, Amsterdam: North-Holland, 1984.

[47] O. T. Strand, L. V. Berzins, D. R. Goosman, W. W. Kuhlow, P. D. Sargis, and T. L. Whitworth, "Velocimetry using heterodyne techniques," in 26^{th} *International Congress on High-Speed Photography and Photonics – 2004* (D. L. Paisley, ed.), vol. 5580, p. 593, SPIE, 2005.

[48] G. E. Duvall and R. A. Graham, "Phase transitions under shock-wave loading," *Reviews of Modern Physics*, vol. 49, no. 3, p. 523, 1977.

[49] H. Schardin *Jahrbuch Der Deutsche Akademie Der Luftfahrtforschung*, p. 314, 1941.

[50] P. W. Bridgman *Phys. Rev.*, vol. 48, p. 825, 1935.

[51] P. W. Bridgman *Proc. Am. Acad. Arts Sci.*, vol. 71, p. 9, 1937.

[52] P. W. Bridgman *J. Chem. Phys.*, vol. 15, p. 311, 1947.

[53] P. W. Bridgman, *The Physics of high pressure*. Bell, London, 1949.

[54] E. Teller, "On the speed of reactions at high pressures," *J. Chem. Phys.*, vol. 16, pp. 901–903, 1962.

[55] M. A. Meyers, S. S. Batsanov, S. M. Gavrilkin, H. C. Chen, J. C. LaSalvia, and F. D. S. Marquis, "Effect of shock pressure and plastic strain on chemical reactions in Nb-Si and Mo-Si systems," *Materials Science and Engineering A*, vol. 201, pp. 150–158, 1995.

[56] D. Bancroft, E. L. Peterson, and F. S. Minshall *J. Appl. Phys.*, vol. 27, p. 291, 1957.

[57] W. J. Nellis, "P. W. Bridgman contributions to the foundations of shock compression of condensed matter." arXiv:0906.0106.

[58] L. V. Al'tshuler *Zh. Eksp. Teor. Fiz.*, vol. 54, p. 785, 1968.

[59] D. Holloway, "How the bomb saved Soviet physics," *Bulletin of the Atomic Scientists*, vol. 50, no. 6, pp. 46–55, 1994.

[60] G. A. Adadurov, I. M. Barkalov, V. I. Gol'danskii, A. N. Dremin, T. N. Ignatovich, A. N. Mikhailov, V. L. Tal'roze, and P. A. Yampol'skii *Polym. Sci. USSR*, vol. 7, p. 196, 1965.

[61] L. V. Al'tshuler *Sov. Phys.-Usp.*, vol. 8, p. 52, 1965.

[62] S. S. Batsanov, A. . A. Deribas, E. V. Dulepov, M. G. Ermakov, and V. M. Kudinov *Combust. Explos. Shock Waves*, vol. 1, pp. 47–49, 1965.

[63] Y. N. Ryabinin *Soviet Phys. Tech., Phys.*, vol. 1, p. 2575, 1956.

[64] A. N. Dremin and O. N. Breusov, "Processes occurring in solids under the action of powerful shock waves," *Russ. Chem. Rev.*, vol. 37, p. 392, 1968.

[65] S. S. Batsanov, G. E. Blokhina, and A. A. Deribas *J. Struct. Chem.*, vol. 6, p. 209, 1965.

[66] N. L. Coleburn and J. W. Forbes *J. Chem. Phys.*, vol. 48, p. 555, 1968.

[67] J. Kimura *Jpn. J. Appl. Phys.*, vol. 2, p. 312, 1963.

[68] Y. Horiguchi and Y. Nomura *Carbon*, vol. 36, pp. 2113–2118, 1965.

[69] Y. Horiguchi and Y. Nomura *Chem. Ind. London*, pp. 1791–1792, Oct. 1965.

[70] R. A. Graham, *Solids Under High-Pressure Shock Compression*. Springer-Verlag, 1993.

[71] M. Baer, "Computational modeling of heterogeneous reactive materials at the mesoscale," in *Shock Compression of Condensed Matter - 1999* (M. Furnish, L. Chhabildas, and R. Hixson, eds.), pp. 27–33, Melville, New York: American Institute of Physics, 2000.

[72] M. B. Boslough, "A thermochemical model for shock-induced reactions (heat detonations) in solids," *J. Chem. Phys.*, vol. 92, no. 3, p. 1839, 1990.

[73] L. E. Murr and K. P. Staudhammer, "Shock wave sensitization, shock-induced reactivity, and new materials fabrication," in *Shock waves for industrial applications* (L. E. Murr, ed.), ch. 12, pp. 441–472, Noyes Publications, 1988.

[74] S. S. Batsanov, V. A. Bakhmutskaya, A. A. Deribas, and E. N. Zalivina *Combust. Explos. Shock Waves*, vol. 3, p. 94, 1967.

[75] H. Schneider, W. Klee, and U. Horneman *J. Mater. Sci.*, vol. 15, p. 154, 1980.

[76] Y. Horie, R. A. Graham, and I. K. Simonsen in *Metallurgical Applications of Shock-Wave and High-Strain-Rate Phenomena* (L. E. Murr, K. P. Staudhammer, and M. A. Meyers, eds.), p. 1023, Mercel Dekker, Inc., 1986.

[77] S. S. Batsanov, G. S. Doronin, S. V. Klochkov, and A. I. Teut *Combust. Explos. Shock Waves*, vol. 22, p. 765, 1986.

[78] R. A. Graham, B. Morosin, E. L. Venturini, and M. J. Carr, "Materials modification and synthesis under high pressure shock compression," *Annu. Rev. Mater. Sci.*, vol. 16, p. 315, 1986.

[79] R. A. Graham, "Sandia Laboratories Report SAND88-1055," tech. rep., Sandia National Laboratory, 1988.

[80] R. A. Graham, M. U. Anderson, Y. Horie, S.-K. You, and G. T. Holman, "Pressure measurements in chemically reacting powder mixtures with the Bauer piezoelectric polymer gauge," *Shock Waves*, vol. 3, pp. 79–82, 1993.

[81] R. Reed, R. Graham, L. Moore, L. Lee, D. Fogelson, and F. Bauer, "The Sandia standard for PVDF shock sensors," in *Shock Compression of Condensed Matter – 1989* (S. Schmidt, J. Johnson, and L. Davison, eds.), pp. 825–828, Amsterdam: Elsevier, 1990.

[82] F. Bauer, "Ferroelectric properties of PVDF polymer and WF2/C2F3H copolymers: high pressure and shock response of PVDF gauge," *Ferroelectrics*, vol. 115, pp. 247–266, 1991.

[83] F. Bauer, R. Graham, M. Anderson, H. Lefebvre, L. Lee, and R. Reed, "Response of the piezoelectric polymer PVDF to shock compression greater than 10 GPa," in *Shock Compression of Condensed Matter - 1991* (S. Schmidt, R. Dick, J. Forbes, and D. Tasker, eds.), pp. 887–890, Amsterdam: Elsevier, 1992.

[84] R. Graham, M. Anderson, F. Bauer, and R. Setchell, "Piezoelectric polarization of the ferroelectric polymer PVDF from 10 MPa to 10 GPa: Studies of loading path dependence," in *Shock Compression of Condensed Matter - 1991* (S. Schmidt, R. Dick, J. Forbes, and D. Tasker, eds.), pp. 883–886, Amsterdam: Elsevier, 1992.

[85] S. S. Batsanov, G. S. Doronin, S. V. Klochkov, and A. I. Teut, "Synthesis reactions behind shock fronts," *Fiz. Goreniya Vzryva*, vol. 22, pp. 765–768, 1987.

[86] L. H. Yu and M. A. Meyers, "Shock synthesis and synthesis-assisted shock consolidation of silicides," *J. Mat. Sci*, vol. 26, p. 601, 1991.

[87] M. B. Boslough, "Thermochemical model for shock induced chemical reactions in porous thermite: The heat detonation model," in *Shock Compression of Condensed Matter - 1989* (S. Schmidt, J. Johnson, and L. Davison, eds.), pp. 671–674, Amsterdam: Elsevier, 1990.

[88] E. Dunbar, R. Graham, G. Holman, M. Anderson, and N. Thadhani, "Time-resolved pressure measurements in chemically reacting powder mixtures," in *High Pressure Science and Technology 1993* (S. Schmidt, J. Shaner, G. Samara, and M. Ross, eds.), pp. 1303–1306, New York: American Institute of Physics, 1994.

[89] K. Vandersall and N. N. Thadhani, "Dynamic densification of Mo-Si powder compacts for reactive solid state processing," in *Shock Compression of Condensed Matter - 1997* (S. Schmidt, D. Dandekar, and J. Forbes, eds.), pp. 647–650, Woodbury, New York: American Institute of Physics, 1998.

[90] K. Vandersall and N. N. Thadhani, "Shock compression of Mo-Si powder mixtures using recovery and instrumented experiments," in *Shock Compression of Condensed Matter - 1999* (M. Furnish, L. Chhabildas, and R. Hixson, eds.), pp. 763–766, Melville, New York: American Institute of Physics, 2000.

[91] K. Vandersall and N. N. Thadhani, "Investigation of shock-induced chemical reactions in Mo-Si powder mixtures using instrumented experiments with PVDF stress gauges," in *Shock Compression of Condensed Matter – 2001* (M. Furnish, N. Thadhani, and Y. Horie, eds.), pp. 1109–1112, Melville, NY: American Institute of Physics, 2002.

[92] K. S. Vandersall and N. N. Thadhani *J. Appl. Phys.*, vol. 94, p. 1575, 2003.

[93] K. S. Vandersall and N. N. Thadhani, "Investigation of "shock-induced" and "shock-assisted" chemical reactions in Mo + 2Si powder mixtures," *Metall. Mater. Trans. A*, vol. 34, no. 1, pp. 15 – 23, 2003.

[94] K. S. Vecchio, L. H. Yu, and M. A. Meyers, "Shock synthesis of silicides I - Experimentation and microstructural evolution," *Acta Metall. Mater.*, vol. 42, p. 701, 1994.

[95] M. A. Meyers, L. H. Yu, and K. S. Vecchio, "Shock synthesis of silicides II - Thermodynamcs and Kinetics," *Acta Metall. Mater.*, vol. 42, p. 715, 1994.

[96] X. Xu and N. N. Thadhani, "Investigation of shock-induced reaction behavior of as-blended and ball-milled Ni+Ti powder mixtures using time-resolved stress measurements," *J. Appl. Phys.*, vol. 96, no. 4, pp. 2000–2009, 2004.

[97] B. Aydelotte and N. N. Thadhani, "A comparison of different Ni+Al structural energetic materials," in *Symposium OO – Properties, Processing and Applications of Reactive Materials*, vol. 1521 of *MRS Online Proceedings Library*, 2013.

[98] V. F. Nesterenko, M. A. Meyers, H. C. Chen, and J. C. LaSalvia *Appl. Phys. Lett.*, vol. 65, p. 3069, 1994.

[99] B. R. Krueger and T. J. Vreeland, "Correlation of Shock Initiated and Thermally Initiated Chemical Reactions in a 1:1 Atomic Ratio Nickel-Silicon Mixture," *J. Appl. Phys.*, vol. 70, p. 5362, 1991.

[100] B. R. Krueger and T. J. Vreeland, "Shock Initiated Chemical Reactions in a 1:1 Atomic Percent Nickel-Silicon Powder Mixture," in *Shock Waves and High-Strain Rate Phenomena in Materials*, Marcel Dekker, Inc., 1991.

[101] S. Du and N. Thadhani, "Impact initiation of pressed Al-based intermetallic forming powder mixtures," in *Shock Compression of Condensed Matter - 2009* (M. Elert, W. Buttler, M. Furnish, W. Anderson, and W. Proud, eds.), pp. 470–473, Melville, NY: American Institute of Physics, 2009.

[102] A. Gavens, D. Van Heerden, A. Mann, M. Reiss, and T. Weihs, "Effect of intermixing on self-propagating exothermic reactions in Al/Ni nanolaminate foils," *J. Appl. Phys.*, vol. 87, no. 3, pp. 1255–1263, 2000.

[103] L. E. Murr, *Interfacial Phenomena in Metals and Alloys*. Addison-Wesley, 1975.

[104] G. E. Duvall, "Shock compression chemistry in materials synthesis and processing," tech. rep., National Academy of Sciences, National Research Council, National Materials Advisory Broad, National Academy Press, Washington, 1984.

[105] E. Dunbar, R. A. Graham, G. T. Holman, M. U. Anderson, and N. N. Thadhani in *Proceedings of AIRAPT/APS High Pressure Science and Technology Conference* (S. C. Schmidt, ed.), (Colorado Springs, CO), AIRAPT/APS, 28 June to 2 July 1993.

[106] R. A. Graham in *Proceedings of the 3rd International Symposium on Dynamic Pressures*, (La Grande Motte, France), June 5-9 1989.

[107] D. E. Maiden, G. Bianchini, B. Holt, H. Hornig, and D. Kingman, "Chemical shock synthesis of TiB_2," in *Materials Processing by High-Temperature Synthesis of Materials (SHS)* (K. A. Gabriel, S. G. Wax, and J. W. McCauley, eds.), no. Report No. MTL-SP-87-3, (Daytona Beach, Florida), pp. 359–377, DARPA/ARMY SHS Symposium Proc., 21-23 October 1985.

[108] G. L. Nutt, "Thermodynamics of reactive flow model," Tech. Rep. Report no. UCID 20277, Lawrence Livermore National Laboratory, 1984.

[109] D. E. Maiden and G. L. Nutt in *Proceedings of the 11th Int'l. Pyrotechnics Seminar*, (Vail, Colorado), p. 813, 1986.

[110] N. S. Enikolopyan, A. A. Khzarzhyan, E. E. Gasparyan, and V. B. Vol'eva *Academy Nauk, USS, Procs. Phys. Chem.*, vol. 294, p. 567, 1987.

[111] P. A. Taylor, M. B. Boslough, and Y. Horie in *Shock Waves in Condensed Matter - 1987* (S. C. Schmidt and N. C. Holmes, eds.), p. 395, North-Holland, Amsterdam, 1988.

[112] H. Kunishige, Y. Oya, Y. Kukuyama, S. Watanabe, H. Tamura, A. B. Sawaoka, T. Taniguchi, and Y. Horie, "Report of the Research Laboratory of Engineering Materials," Tech. Rep. 15, Tokyo Institute of Technology, 1990.

[113] W. Hermann *J. Appl. Phys.*, vol. 40, p. 2490, 1969.

[114] B. R. Krueger, A. H. Muntz, and T. J. Vreeland, "Shock Induced Reactions in 5:3 Atomic Ratio Titanium/Silicon Powder Mixtures," *Metall. Trans.*, vol. 23A, p. 55, 1991.

[115] I. P. H. Do and D. J. Benson, "Micromechanical modeling of shock-induced chemical reactions in heterogeneous multi-material powder mixtures," *International Journal of Plasticity*, vol. 17, no. 4, pp. 641–668, 2001.

[116] R. J. Kee, F. M. Rupley, E. Meeks, and J. A. Miller, "Chemkin III: A fortran chemical kinetics package for the analysis of gas phase chemical and plasma kinetics," Technical Report SAND96-8216, Sandia National Laboratory, University of California, 1996.

[117] L. E. Malvern, *Introduction to the Mechanics of a Continuous Medium*. Prentice-Hall Inc., 1969.

[118] J. W. Forbes, *Shock Wave Compression of Condensed Matter - A Primer*. Springer, 2012.

[119] G. I. Kerley, "The linear $U_s - U_p$ relation in shock-wave physics," Tech. Rep. KTS06-1, Kerley Technical Services, Appomattox, VA 24522-0709, 2006.

[120] C. H. P. Lupis, *Chemical Thermodynamcs of Materials*. Prentice Hall Inc., 1983.

[121] D. R. Gaskell, *Introduction to the Thermodynamics of Materials*. Taylor & Francis, 2003.

[122] R. G. McQueen, S. P. Marsh, J. W. Taylor, J. N. Fritz, and W. J. Carter, "The equation of state of solids from shock wave studies," in *High velocity impact phenomena* (R. Kinslow, ed.), p. 230, New York: Academic Press, 1970.

[123] S. K. Garg and J. W. Kirsh *J. Comp. Materials*, vol. 5, p. 428, 1971.

[124] M. M. Carroll and A. C. Holt *J. Appl. Phys.*, vol. 43, p. 1626, 1972.

[125] B. M. Butcher and C. H. Karnes *J. Appl. Phys.*, vol. 40, p. 2967, 1969.

[126] H. F. Fischmeister and E. Artz *Powder Metall.*, vol. 26, p. 82, 1983.

[127] Q. Wu and F. Jing, "Thermodynamic equation of state and application to Hugoniot predictions for porous materials," *J. Appl. Phys.*, vol. 80, p. 4343, 1996.

[128] G. A. Simons and H. H. Legner *J. Appl. Phys.*, vol. 53, p. 943, 1982.

[129] M. Rice and J. Walsh, "Dynamic compression of liquids from measurements on strong shock waves," *J. Chem. Phys.*, vol. 26, p. 824, 1957.

[130] D. Grady, G. Fenton, and T. Vogler, "Equation of state and evidence of enhanced phase transformation for the shock compression of distended compounds," *Procedia Engineering*, vol. 58, pp. 110 – 116, 2013.

[131] M. Baer, "A mixture model for shock compression of porous multi-component reactive materials," in *High Pressure Science and Technology 1993* (S. Schmidt, J. Shaner, G. Samara, and M. Ross, eds.), pp. 1247–1250, New York: American Institute of Physics, 1994.

[132] C. Dai, D. Eakins, and N. Thadhani, "On the applicability of analytical models to predict hugoniot of nano-sized powder compacts," in *Shock Compression of Condensed Matter - 2007* (M. Elert, M. Furnish, R. Chau, N. Holmes, and J. Nguyen, eds.), pp. 35–38, Melville, NY: American Institute of Physics, 2007.

[133] C. D. Dai, D. E. Eakins, and N. N. Thadhani, "Dynamic densification behavior of nanorion powders under shock compression," *J. Appl. Phys.*, no. 9, p. 093503, 2008.

[134] Y. B. Zel'dovich and Y. P. Raizer, *Physics of shock waves and high-temperature hydrodynamic phenomena*. Dover Publications, 2002.

[135] M. B. Boslough and R. A. Graham, "Submicrosecond shock-induced chemical reactions in solids: First real-time observations," *Chem. Phys. Lett.*, vol. 121, no. 4, 5, pp. 446–452, 1985.

[136] Y. Horie, D. Hoy, I. Simonsen, R. Graham, and B. Morosin, "Shock-wave synthesis of titanium aluminides," in *Shock Waves in Condensed Matter – 1985* (Y. Gupta, ed.), pp. 749–754, New York: Plenum, 1986.

[137] R. Courant and K. O. Friedrichs, *Supersonic Flow and Shock Waves*. New York: Springer, 1976.

[138] X. F. Zhang, A. S. Shi, J. Zhang, Y. Qiao, and Y. He, "Thermochemical modeling of temperature controlled shock-induced chemical reactions in multifunctional energetic structural materials under shock compression," *J. Appl. Phys.*, vol. 111, p. 123501, 2012.

[139] X. Xu and N. Thadhani, "Investigation of shock-induced chemical reactions in Ni-Ti powder mixtures using instrumented experiments," in *Shock Compression of Condensed Matter - 2001* (M. Furnish, N. Thadhani, and Y. Horie, eds.), pp. 1123–1126, Melville, NY: American Institute of Physics, 2002.

[140] D. E. Eakins and N. N. Thadhani, "Investigation of shock-induced reactions in a Ni+Al powder mixture," in *Shock Compression of Condensed Matter - 2005* (M. D. Furnish, M. Elert, T. P. Russell, and C. T. White, eds.), pp. 1153 – 1156, 2005.

[141] Y. Beers, *Introduction to the theory of error*. Addison-Wesley, 1957.

[142] A. C. Mitchell and W. J. Nellis, "Shock compression of aluminum, copper, and tantalum," *J. Appl. Phys.*, vol. 52, p. 3363, 1981.

[143] J. P. Holman, *Experimental Methods for Engineers*. McGraw-Hill, 7^{th} ed., 2001.

[144] T. Belytschko, W. K. Liu, and B. Moran, *Nonlinear Finite Elements for Continua and Structures*. John Wiley & Sons, 2000.

[145] D. M. Levine, P. P. Ramsey, and R. K. Smidt, *Applied Statistics for Engineers and Scientists*. Prentice-Hall Inc., 2001.

[146] S. P. Marsh, *LASL Shock Hugoniot Data*. University of California Press, 1980.

[147] T. Machaladze, M. Samkharadze, N. Kakhidze, and M. Makhviladze, "Crystallization of amorphous boron by the calorimetric method," *Open Journal of Inorganic Chemistry*, vol. 4, pp. 18–20, 2014.

[148] G. Parakhonskiy, N. Dubrovinskaia, E. Bykova, R. Wirth, and L. Dubrovinsky, "Experimental pressure-temperature phase diagram of boron: resolving the long-standing enigma," *Scientific Reports*, vol. 1, no. 96, p. 1.

[149] E. Rudy and S. Windisch, "Ternary phase equilibria in transition metal-boron-carbon-silicon systems (Part I)," tech. rep., Ohio: Air Force Materials Laboratory - Wright-Patterson Air Force Base, 1966.

[150] H. Duschanek and P. Rogl, "The Al-B (Aluminum-Boron) System," *Journal of Phase Equilibria*, vol. 15, no. 5, p. 543, 1994.

[151] G. Tsagareishvili, D. Tsagareishvili, and A. Khvedelidze, "Estimation of some thermoelastic properties of β rhombohedral boron in wide ranges of temperature and pressure," *J. Less-Common Met.*, vol. 75, pp. 141–145, 1980.

[152] D. Tsagareishvili, G. Tsagareishvili, I. Omiadze, J. Jobava, V. Naumov, V. Nogteva, and I. Paukov, "Thermodynamic properties of α-rhombohedral boron from 16.05 to 714.5 K," *J. Less-Common Met.*, vol. 117, pp. 143–151, 1986.

[153] R. Uno, J. Ishigaki, and M. Sudou, "The electrical properties of β-rhombohedral boron," *J. Less-Common Met.*, vol. 47, pp. 125–128, 1976.

[154] P. A. Medwick, B. E. J. White, and R. O. Pohl, "Elastic properties of amorphous and crystalline $B_{1x}C_x$ and boron at low temperatures," *J. Alloys Compd.*, vol. 270, pp. 1–15, 1998.

[155] T. Lundström, B. Lönnberg, and J. Bauer, "Thermal expansion of β-rhombohedral boron," *J. Alloys Compd.*, vol. 267, pp. 54 – 58, 1998.

[156] R. J. Nelmes, R.s, J. S. Loveday, D. R. Allan, J. M. Besson, G. Hamel, P. Grima, and S. Hull, "Neutron- and X-Ray-diffraction measurements of the bulk modulus of boron," *Phys. Rev. B.: Condens. Matter*, vol. 47, pp. 7668–7673, 1993.

[157] F. E. Wawner and D. B. Satterfield, "Observations on the tensile strength of "amorphous" boron," *Appl. Phys. Lett.*, vol. 11, p. 192, 1967.

[158] F. E. Wawner in *Boron*, Plenum Press, 1965.

[159] C. P. Talley, L. E. Line Jr., and Q. D. Overman Jr. in *Boron synthesis, structure, and properties* (J. A. Kohn, W. F. Nye, and G. K. Gaule, eds.), Plenum Press, 1960.

[160] J. S. Gillespie Jr., "Crystallization of masmass amorphous boron," *J. Am. Chem. Soc.*, vol. 88, no. 11, pp. 2423–2425, 1966.

[161] S. Crockett, "Creating new equations of state for high strength materials (Boron and Boron Carbide)," tech. rep., Los Alamos National Laboratory, 2008.

[162] M. Meyers, L.-H. Yu, and K. Vecchio, "Shock synthesis of silicides," in *Shock Compression of Condensed Matter - 1991* (S. Schmidt, R. Dick, J. Forbes, and D. Tasker, eds.), pp. 629–632, Amsterdam: Elsevier, 1992.

[163] L. Yu, W. Nellis, M. Meyers, and K. Vecchio, "Shock synthesis of niobium silicides," in *High Pressure Science and Technology 1993* (S. Schmidt, J. Shaner, G. Samara, and M. Ross, eds.), pp. 1291–1294, New York: American Institute of Physics, 1994.

[164] A. Gurumurthy, M. Gonzales, A. M. Gokhale, and N. N. Thadhani, "Bulk orientational anisotropy without spatial anisotropy due to powder compaction in Al-Ti-B compacts," *Scr. Mater.*, vol. 86, pp. 28–31, 2014.

[165] A. Gurumurthy, *Simulation Methodologies for Multiphase Three-Dimensional Microstructures*. PhD thesis, Georgia Institute of Technology, 2014.

[166] K. A. Rakhmatulin *Appl. Math. Metch.*, vol. 9, 1945.

[167] G. I. Taylor, "The testing of materials at high rates of loading," *J. Inst. Civ. Engrs.*, vol. 26, p. 486, 1946.

[168] T. von Karman and P. Duwez *J. Appl. Phys.*, vol. 21, p. 987, 1950.

[169] J. Breidenich, *Impact-initiated combustion of Aluminum*. PhD thesis, Georgia Institute of Technology, 2015.

[170] F. Bauer and A. Lichtenberger, "Use of pvdf shock gauges for stress measurements in hopkinson bar," in *Shock Waves in Condensed Matter - 1987* (S. Schmidt and N. Holmes, eds.), pp. 631–634, Amsterdam: Elsevier, 1988.

[171] D. Fogelson, L. Lee, D. Gilbert, W. Conley, R. Graham, R. Reed, and F. Bauer, "Fabrication of standardized piezoelectric polymer shock gauges by the bauer method," in *Shock Waves in Condensed Matter - 1987* (S. Schmidt and N. Holmes, eds.), pp. 615–618, Amsterdam: Elsevier, 1988.

[172] L. Lee, D. Hyndman, R. Reed, and F. Bauer, "Pvdf applications in shock measurements," in *Shock Compression of Condensed Matter - 1989* (S. Schmidt, J. Johnson, and L. Davison, eds.), pp. 821–824, Amsterdam: Elsevier, 1990.

[173] B. Aydelotte, *Fragmentation and reaction of structural energetic materials*. PhD thesis, Georgia Institute of Technology, 2013.

[174] A. Gurumurthy, A. M. Gokhale, A. Godha, and M. Gonzales, "Montage Serial Sectioning: some finer aspects of practice," *Metallogr. Microstruct. Anal.*, vol. 2, pp. 364 – 371, 2013.

[175] G. I. Kerley, "Equation of State and Constitutive Models for Numerical Simulations of Dust Impacts on the Solar Probe," Tech. Rep. KTS09-1, Kerley Technical Services, August 2009.

[176] M. Gonzales, A. Gurumurthy, G. B. Kennedy, A. M. Gokhale, and N. N. Thadhani, "Microstructure-based simulations of the high-strain-rate response of heterogeneous Ti/Al/B reactive powder mixtures," in *Proceedings of the Fall 2012 meeting of the Materials Research Society*, (Boston, MA), MRS, November 2012.

[177] M. Gonzales, A. Gurumurthy, G. B. Kennedy, A. M. Gokhale, and N. N. Thadhani, "Shock compression response of Ti+B reactive powder mixtures," *J. Phys.: Conf. Ser.*, vol. 500, p. 052013, 2014.

[178] J. P. Borg and T. J. Vogler, "Mesoscale calculations of the dynamic behavior of a granular ceramic," *International Journal of Solids and Structures*, vol. 45, no. 6, p. 1676, 2008.

[179] M. Baer and W. Trott, "Mesoscale studies of shock loaded tin sphere lattices," in *Shock Compression of Condensed Matter - 2003* (M. Furnish, Y. Gupta, and J. Forbes, eds.), pp. 517–520, Melville NY: American Institute of Physics, 2004.

[180] J. Borg, T. Vogler, and A. Fraser, "A review of mesoscale simulations of granular materials," in *Shock Compression of Condensed Matter - 2009* (M. Elert, W. Buttler, M. Furnish, W. Anderson, and W. Proud, eds.), pp. 1331–1336, Melville, NY: American Institute of Physics, 2009.

VITA

Manny was born on May 2, 1984 in El Paso, Texas, the only child of his loving mother Leonila Gonzales. He was raised by his mother and aunts in a loving home, to which he will always be grateful. He developed a passion for teaching spurred by the support of Dr. Peter Golding and Dr. Stephen W. Stafford. He was afforded the opportunity to conduct research in additive manufacturing, computational mechanics, and engineering education while at UTEP, and earned a B.S. in Mechanical Engineering in 2005 and B.S. in Metallurgical Engineering in 2006. Manny earned his M.S. in 2010, conducting research applying Density Functional Theory (DFT) to assess mechanical properties of ceramics at ultra-high temperatures.

Under the tutelage of Professor Naresh Thadhani at Georgia Tech, Manny has discovered a new love for studying materials subjected to the most extreme environments, thus pushing their design envelope. Manny conducted research into the mechanochemistry of heterogeneous reactive powder mixtures of Ti+Al+B, and has presented his work in numerous peer-reviewed articles conferences proceedings.

Manny was married on March 21, 2015 to Rachel K. Gandy in a small ceremony in El Paso, TX. The SMART fellowship enabled Manny to accept a position at the Air Force Research Laboratory (AFRL), Wright-Patterson Air Force Base, OH, where he will be starting the next phase of his career.

Manny's personal interests include cooking, nutritional science, gardening, music and arts, ornithology, and the occasional old-school video game.